TUM

Technische Universität München

TUM School of Computation, Information and Technology

Stochastic Detection of Silver Nanoparticles for Sensing Applications

Lennart Jakob Konstantin Weiß

Abstract

Nanoelectrochemistry is a fascinating discipline that presents novel opportunities to investigate material structure and dynamic processes at the nanoscale. The present thesis focuses on the emerging branch of nanoimpact electrochemistry, which explores the interaction of colliding nanoparticles with electrodes of μm size. In case of silver nanoparticles, their collision upon an appropriately-biased electrode triggers a fast electron-transfer reaction, which is associated with a spike-shaped perturbation in the current trace. These current spikes exhibit an exceptionally high signal-to-noise ratio rendering nanoimpact electrochemistry an intriguing read-out technique for quantitative biosensing. Especially for very diluted species, the concept of *counting* discrete collision events within a specified time-frame could replace current state-of-the-art amplitude-based approaches.

The focus of the present work was to develop and implement reliable experimental protocols that ensure consistent and accurate responses from nanoimpact sensors, which are critical for the successful integration into (bio)sensing applications. To accomplish this, sensor chips that allow for parallel recordings from microelectrode arrays have been utilized, which ultimately lead to an improved statistical reliability compared to single-electrode experiments. Moreover, the present work highlights various strategies to enhance the nanoparticle detection yield by means of engineering the particle transport. Theoretical and practical aspects on this matter are covered in a review contribution. In the first experimental work, the issue of particle adsorption, common to chip-based measurements, was considered and counteracted by embedding a macroscopic electrode that surrounds the entire electrode array. This electrode can manipulate the electrostatic interactions in the region adjacent to the detection electrodes resulting in altered particle motion. The proposed sensor design was shown to increase the detection yield without necessitating local chemical surface modification, which is typically a challenging task.

Moreover, two different implementations of additional microfluidic support were investigated. For instance, by utilizing the previously described macroscopic electrode, electrokinetic transport phenomena can be induced. Their influence on the particle detection yield was thoroughly examined in a separate study, where on-chip micropumping was found to significantly enhance the collision rate by a combination of electroosmotic and electrophoretic effects. In a different study, paper-based wax-patterned microfluidic structures were employed to reliably detect nanoparticles – even under challenging point-of-care constraints. This work demonstrated that nanoparticle sensing, which is typically a delicate experiment that requires careful sample and sensor preparation, could also be performed in a lateral-flow architecture by using a simplified setup.

Last, a particle-based small-molecule biosensor was implemented for the model system of streptavidin/biotin. This was achieved by specifically functionalizing silver nanoparticles to act as redoxactive labels that could still specifically bind to receptor sites. A pH-assisted ligand exchange protocol was established to create a heterogeneous particle corona. The prototype assay operated in a classical competitive binding mode and was able to measure free biotin at concentrations as low as pM.

In summary, this work provides valuable insights into various aspects relevant for the development of nanoparticle-based (immuno)assays and could serve as starting point for future on-site detection and quantification of very dilute substances with unparalleled precision and accuracy.

Kurzfassung

Das Gebiet der Nanoelektrochemie ist eine faszinierende wissenschaftliche Disziplin, die neuartige Möglichkeiten bietet, Materialstrukturen und die Dynamik von Prozessen im Nanometerbereich zu untersuchen. Die vorliegende Arbeit konzentriert sich auf den relativ jungen Forschungsbereich der Kollisionselektrochemie, welcher die dynamischen Wechselwirkungen von Stößen elektroaktiver Nanopartikel an polarisierten Mikroelektroden untersucht. Im Fall von Silbernanopartikeln löst die Kollision mit einer Elektrodenoberfläche eine schnelle Elektronentransferreaktion aus, welche zu einem charakteristischen transienten Verlauf der Stromkurve führt. Dieses *diskrete* stochastische Signal weist ein außergewöhnlich hohes Signal-zu-Rausch-Verhältnis auf, so dass die Kollisionselektrochemie eine interessante Auslesetechnik für zukünftige (Bio)Sensorik-Anwendungen darstellt. Möglicherweise könnte das *Prinzip des Zählens* diskreter Kollisionsereignisse die aktuelle amplitudenbasierte Sensorik komplementieren, was vor allem für sehr niedrigkonzentrierte Analyten von Interesse ist.

Die vorliegende Arbeit konzentriert sich darauf, robuste experimentelle Protokolle zu etablieren, die eine zuverlässige und konsistente Messung von Silbernanopartikelkollisionen ermöglichen. Insbesondere chip-basierte Lösungen bieten eine erhöhte statistische Zuverlässigkeit, da mehrere Mikroelektroden durch parallele Messungen Redundanz erzeugen. Die vorliegende Arbeit nutzt verschiedene Optimierungsstrategien um die Kollisionsrate in solchen Experimenten zu erhöhen und bedient sich dabei klassischer Kontinuumsmodelle des Massenstransports. So wurde beispielsweise das Problem der Partikeladsorption an isolierenden Oberflächen reduziert, indem eine makroskopische Elektrode in den Chip integriert wurde. Diese ist, ebenso wie die Detektionselektroden, extern ansteuerbar. Es konnte gezeigt werden, dass induzierte elektrostatische Wechselwirkungen an der makroskopischen Elektrode die Kollisionsrate der Partikel an den Detektionselektroden beeinflusst. Diese induzierte Abschirmung ist eine einfache Methode die Anhaftung von Partikeln zu reduzieren und stellt damit eine interessante Alternative zu klassischen chemischen Oberflächenmodifikationen dar.

Darüberhinaus wurden in dieser Arbeit verschiedene Mikrofluidik-Strategien auf ihre Anwendbarkeit getestet. Dieser Aspekt ist von besonderer Relevanz, da der diffusive Transport kolloider Systeme über große Distanzen nicht effizient ist. Daher wurde ein zusätzlicher advektiver Partikeltransport auf zwei verschiedene Arten implementiert. Es wurde beispielsweise die zuvor beschriebene makroskopische Elektrode dafür genutzt, um zusätzliche elektrokinetische Transportphänomene zu induzieren. Hier konnte gezeigt werden, dass ein chip-basiertes elektrokinetisch-induziertes Durchmischen die Kollisionsrate signifikant erhöhen kann, wobei sowohl elektroosmotische als auch elektrophoretische Beiträge eine Rolle spielen.

Mit Blick auf den aktuellen Standard in der Point-of-Care Diagnostik wurde in einer weiteren Arbeit gezeigt, dass die Detektion von Nanopartikeln auch in einer klassischen lateral-flow Konfiguration möglich ist. Hierzu wurde eine papierbasierte Mikrofluidik auf einem Sensorchip implementiert und deren Einfluss auf die Partikeldetektion untersucht. Diese Arbeit war grundlegend für die darauf aufbauende Entwicklung eines Sensorprototypen, der eine kollisionsbasierte Auslese nutzt, um den Analyten Biotin im Modelsystem Biotin / Streptavidin zu quantifizieren. Hierfür ist eine spezifische Funktionalisierung der Silbernanopartikeln nötig, da die Partikel als redoxaktive Marker fungieren. Dies erfordert inbesondere, dass die Nanopartikel spezifisch und Rezeptorstellen binden können,

aber gleichzeitig noch detektierbar sind. In diesem Rahmen wurde ein Ligandenaustausch-Protokoll für die Nanopartikelfunktionalisierung etabliert. Der Sensorprototyp nutzt das kompetitive Binden von Biotin-Nanopartikeln und freiem Biotin und konnte freies Biotin im Bereich von pM-Konzentrationen nachweisen.

Insgesamt liefert die vorliegende Arbeit wertvolle Erkenntnisse zu verschiedenen Aspekten der Assay-Entwicklung und könnte als Ausgangspunkt für zukünftige point-of-care Detektion und Quantifizierung von extrem niedrigkonzentrierten Substanzen mit beispielloser Präzision und Genauigkeit dienen.

Table of Contents

1. Introduction

Nanoelectrochemistry is an exciting field that lies at the intersection of electrochemistry, material science, and nanotechnology. This multidisciplinary field has the potential to revolutionize the way we sense and manipulate matter at the nanoscale. At the core of nanoelectrochemistry is the understanding and control of electron transfer processes that occur at the interface between a solid electrode and a liquid electrolyte. It entails studying and manipulating chemical reactions and transport phenomena at the nanoscale, where the traditional rules of macroscopic electrochemistry do not always apply. The emerging field of nanoelectrochemistry offers new opportunities for probing the structure and dynamics of nanoscale materials and processes, leading to a broad range of applications from energy conversion to nanoelectronics and biosensing. The focus of this thesis is to characterize and utilize a nanoelectrochemical technique that examines the dynamic interactions of single (electroactive) entities upon collision with microelectrodes. Specifically, this work explores, how the stochastic detection of silver nanoparticles, unveiled by characteristic perturbations in the electronic signal, can be translated into reliable sensing schemes for other analytes. The forthcoming chapters in this dissertation are structured as follows:

- **Chapter 2** lays out fundamental concepts and the theoretical background pertinent to the topics addressed in subsequent chapters. The chapter begins by presenting the research field of stochastic impact electrochemistry, followed by a description of different phenomena affecting colloidal transport in typical stochastic impact experiments. Processes occurring at (electrified) solid-liquid interfaces are also examined. Furthermore, a basic model is provided to describe plasmonic effects in metallic nanoparticles. Last, the chapter considers receptor-ligand binding dynamics and their real-time observation via surface plasmon resonance measurements.

- **Chapter 3** focuses on the current state of research on impact-based electrochemistry with a specific focus on the detection of silver nanoparticles. It provides a comprehensive overview of various aspects that have been reported to play a critical role in such experiments. The chapter also recaps current research activities in the field of biosensing via impact electrochemistry.

- **Chapter 4** outlines the scientific contributions included in this dissertation. This encompasses a review article that highlights mass transfer aspects in impact experiments, an investigation on, how reduced particle adsorption enhances the particle detection yield on chip-based recordings, two experimental studies that examine the influence of forced advection via electrokinetic and capillary-based flows, and last, an experimental work, where a prototype impact-based lateral flow sensor was developed.

- **Chapter 5** provides a summary of the research contributions and offers an outlook on potential future research projects that could benefit from the scientific achievements presented in this thesis.

2. Fundamentals and Theoretical Background

2.1 Stochastic Impact Electrochemistry

Stochastic impact electrochemistry[§] investigates the dynamic interactions of single species upon their collision with electrodes of µm-size. The method is based on the detection and analysis of characteristic perturbations in the electronic signal resulting from the species colliding at the electrode. The *discrete* or *digital* nature of these perturbations sets them apart from the background signal in classical amperometric, potentiometric or impedance-based recordings.[1–3] Previous investigations have primarily focused on amperometric recordings in which the electrochemical reaction is controlled by its potential and the resulting current is analyzed. Specifically, these amperometric experiments can be classified into four categories based on the colliding species and the resulting current response, as depicted in Fig. 2.1,

- **blocking impacts**, where colliding microparticles hinder the constant flux of a redox mediator species by restricting the diffusional field of the electrode. The microparticle itself is not redoxactive and only reduces the background current. Irreversibly adsorbing particles lead to a current step, while fast-moving non-adsorbing microparticles create a blip response.

- **electrocatalytic amplification impacts**, where the metallic nanoparticles are catalysts for a characteristic reaction and their collisions lead to an increase in the total current, either by enabling the reaction or by expanding the likewise-catalytic electrode surface.

- **direct (dissolution / electrooxidation) impacts**, where nanoparticles themselves undergo a charge transfer reaction at the electrode. For example, metallic nanoparticles, such as silver or nickel particles, can be oxidized at a positive electrode potentials. Similarly, collisions of metal-oxide nanoparticles can be monitored at negative potentials by facilitating species reduction.

- **droplet / vesicle impacts**, where small volumes of liquid redoxactive substances are released and converted upon the collision of the vesicle with the electrode.

All of the methods mentioned above are based on two common features: First, the stochastic motion at the level of individual entities and their subsequent interaction with the electrified surface, which affects the or leads to a electrochemical conversion. In the following sections, the basic principles of particle transport and electrochemistry will be discussed, both with special emphasis on the detection of silver nanoparticles by their electrooxidative collisions.

[§] The field of study is also referred to as single-impact electrochemistry, single-entity electrochemistry, and stochastic (particle) collision electrochemistry.
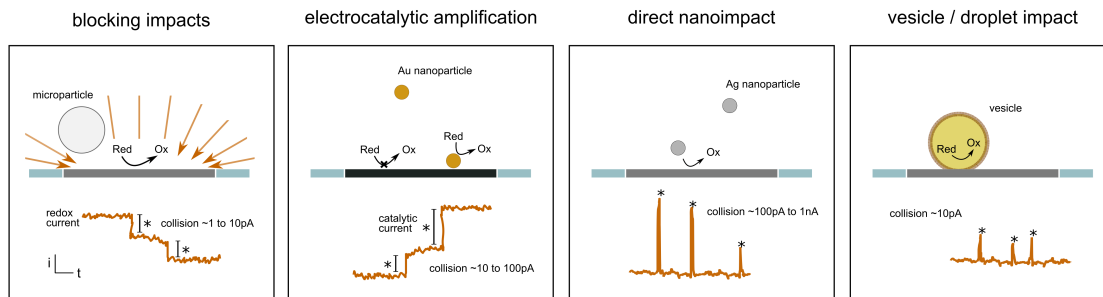
Figure 2.1   Different classes of stochastic impact electrochemistry and their typical response. In blocking impact experiments, the background redox current is partially blocked by microparticles entering the diffusion field of the microelectrode. In contrast, catalytic nanoparticles can be detected via electrocatalytic amplification, since they generate an additional current upon their collision. In direct nanoimpact experiments, metallic nanoparticles are oxidized and dissolved at an appropriately-biased electrode. If vesicles or droplets containing an electroactive substance collide with the electrode, their collision is resolved by a rapid conversion of the species released.[4,5]

2.2   Microscopic Particle Trajectories and Macroscopic Transport

2.2.1   Diffusion

Since stochastic impact electrochemistry is able to resolve the collision of individual entities, a fundamental understanding of their motion trajectory becomes increasingly relevant. This includes the motion of the species within the bulk volume, but also their behavior in the vicinity of the electrode. As a first approximation, their motion can be assumed to be governed solely by the thermal fluctuations of the surrounding medium, i.e. by the fundamental process of Brownian motion. At the particle-level, this phenomenon can be described as an unbiased random walk, where all directions are equally likely. Therefore, no directed motion is possible. However, as time passes, it becomes less likely that the particle will be close to its original position, thus the mean square displacement increases with time.

At the macroscopic level, Brownian motion leads to diffusion, causing a net species transport from a region of higher concentration to a region of lower concentration. This effect can be described in terms of classical field equations, specifically Fick's 1st and 2nd law.

$$\mathbf{j}_{\text{diff}}(\mathbf{x}, t) = -D\nabla c(\mathbf{x}, t) \tag{2.2.1}$$

$$\frac{\partial c(\mathbf{x}, t)}{\partial t} = D\nabla^2 c(\mathbf{x}, t) \tag{2.2.2}$$

Here in Fick's 1st law, $\mathbf{j}_{\text{diff}}$ is vectorial and denotes the diffusive particle flux (density) that balances the concentration gradient ∇c at position $\mathbf{x}$ and time t. Fick's 2nd law describes the temporal evolution of the concentration field c due to a local concentration imbalance. The proportionality constant, referred to as the diffusion coefficient D, can be related to the microscopic mobility of the species by using a hydrodynamic model proposed by Einstein and Smoluchowski.[6,7] The Einstein-Smoluchowski model is based on the assumption of a dilute quiescent solution at a uniform temperature in which the solute molecules are much larger in diameter than the solvent. In this model, the particle is treated as perceiving a continuum rather than a collection of discrete solvent molecules. This perspective is analogous to the hydrodynamic drag experienced by a solid body moving through a fluid. The resulting relationship between the diffusion coefficient and the microscopic mobility of the species is given by

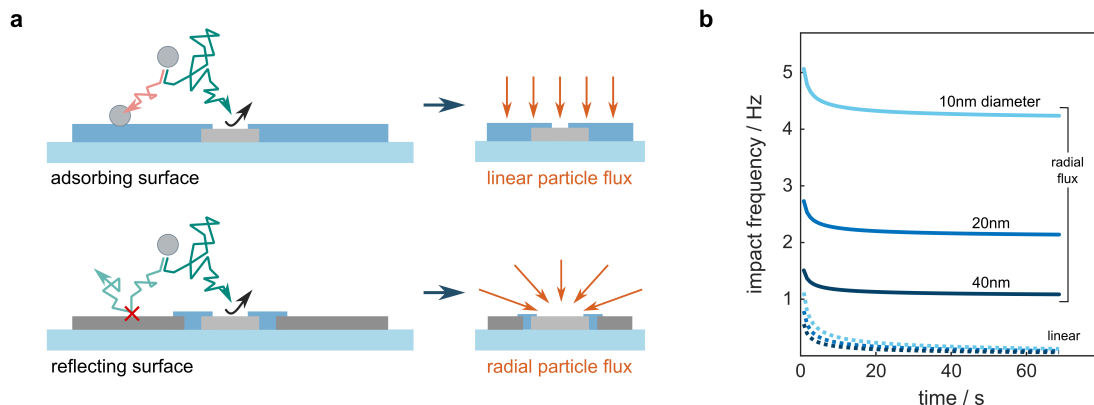$$D = \frac{k_{\text{B}}T}{6\pi\eta r_{\text{p}}}, \tag{2.2.3}$$

Figure 2.2 Predictions of the diffusion-limited particle impact frequency. (a) The two limit cases describe irreversible adsorption and perfect reflection at the surrounding passivation surface. **(b)** Impact rates obtained from the Shoup Szabo (solid) and the Cottrell (dashed) Equations for different particle sizes in case of a concentration of 10 pM and a disk electrode with a diameter of 8 μm.

where k_B is Boltzmann's constant, T is the absolute temperature, η is the dynamic viscosity and r_p is the radius of the particle. In general, the diffusion coefficient is inversely proportional to the particle size, resulting in very low values for nanoparticles. For example, at room temperature, the diffusion coefficient for a 20 nm-sized particle is $2.2 \times 10^{-11}\,\mathrm{m^2\,s^{-1}}$, which is two orders of magnitude lower than the diffusion coefficient of a typical small molecule in aqueous solution. Consequently, the nanoparticle could overcome a distance of $\sim 5\,\mathrm{\mu m}$ within 1 s, whereas a small molecule would travel $\sim 50\,\mathrm{\mu m}$ during the same time.

Although nanoparticle transport via diffusion is slow, its contribution can still play a significant role in nanoelectrochemical experiments, where both microscopic and macroscopic considerations have been used to interpret experimental observations.[8–10] For example, random walk simulations were employed to study noise characteristics in nm-scaled systems and to correlate particle trajectories in the proximity of the electrode with experimental current signals.[10–14] At the same time, classical field theory based on Fick's laws can be used as complementary tool for designing optimized sensor layouts, as it can reveal geometrical influences. Here, a nano-impact experiment is modeled as a diffusive transport problem, in which the concentration of silver nanoparticles in the bulk solution, $c = c_\infty$, is assumed to be constant and the concentration at the electrode surface is set to zero, $c = 0$. This Dirichlet boundary condition at the electrode refers to an infinitely fast oxidation reaction that consumes the colliding particles. The concept is illustrated in Fig. 2.2a, where two limit cases that yield analytical solutions for the particle collision rate are illustrated. The limit cases differ in the way the nanoparticles are supposed to interact with the insulating surface surrounding the disk electrode.

For example, the Cottrell Equation describes the total particle flux[§] toward a disk electrode of size πr^2, given the Dirichlet boundary condition $c = 0$ for the passivation surface as well.[15] It reads

$$j_{\mathrm{diff,C}} = \pi r^2 c_\infty \sqrt{\frac{D}{\pi t}} \quad \rightarrow \quad \frac{dn_{\mathrm{diff,C}}}{dt} = \pi r^2 c_\infty N_A \sqrt{\frac{D}{\pi t}} \qquad (2.2.4)$$

and can be converted to a prediction for the collision frequency dn/dt by multiplying Avogadro's constant N_A. The Cottrell Equation represents the particle flux resulting from a linear diffusion profile and is a minimum estimate for the particle collision frequency. In this scenario, the particles are assumed to be 'consumed' at both surfaces, either through oxidation at the electrode or

---

[§] The total or integrated particle flux $j_{\mathrm{diff,C}}$ for a given electrode geometry is a scalar and has units of $\mathrm{mol\,s^{-1}}$. It is obtained from integrating the vectorial particle flux density $\mathbf{j}$ in units of $\mathrm{mol\,s^{-1}\,m^{-2}}$ over the electrode area.

by irreversible adsorption on the passivation surface. In contrast, the Shoup Szabo Equation calculates the total particle flux towards a disk electrode with radius r that is enclosed by a reflecting surface.[16]

$$j_{\text{diff,SS}} = 4Drc_\infty \left[0.7854 + 0.8862\tau^{-1/2} + 0.2146e^{-0.7823\tau^{-1/2}} \right] \qquad \tau = 4D\frac{t}{r^2} \qquad (2.2.5)$$

Its transient term approaches 1 for $t \to \infty$ and the steady-state total particle flux is given by the Saito Equation[17]

$$j_{\text{diff,S}} = 4Drc_\infty. \qquad (2.2.6)$$

The Shoup Szabo and Saito Equations predict the theoretical maximum for the particle collision rate, when the diffusion profile is radial and there are no other competing particle sinks, as illustrated in Fig. 2.2a. The graph in Fig. 2.2b depicts exemplary theoretical predictions for a typical impact experiment. Here, radial diffusion profiles generate non-zero steady-state total particle fluxes, while the Cottrellian fluxes approaches zero. In general, the steady-state characteristic of the flux is preserved also for other electrode geometries, as long as they are surrounded by a reflecting passivisation. Then, the resulting particle flux varies only by a constant factor. For instance, the flux towards a hemispherical electrode reads[18,19]

$$j_{\text{diff,H}} = 2\pi Drc_\infty. \qquad (2.2.7)$$

This arises from the fact that the concentration field at reasonable distances is largely independent of the exact electrode geometry due to the Laplacian nature of Fick's 2nd law in the steady-state, $D\nabla^2 c = 0$.[20] So far, we have examined two extreme cases that model the influence of the insulating surface surrounding the electrode – total irreversible adsorption and perfect reflection – for purely diffusive mass transport. More specific adsorption characteristics, such as the Langmuir isotherm or the BET-model, can be included as a time-dependent boundary condition in a numerical framework for the diffusion equation.[21–23] Another interfering phenomenon that has been neglected so far is near-wall hindered diffusion, which arises from the limited degrees of freedom for particle motion close to a surface.[24,25] This effect slows down the diffusive particle motion at any surface and can be viewed as a form of (reversible) particle adsorption that may also significantly impede nano-impact experiments.[26–29]

2.2.2 Macroscopic Particle Transport Beyond Diffusion

While diffusion governs the particle trajectories at small time and length scales, its contribution reduces with increasing distances, due to its scaling $x \sim \sqrt{Dt}$. In impact experiments, three major phenomena can affect particle transport beyond diffusion: electrophoretic migration, electroosmotic fluid flow, and forced advection. The motion of particles within the fluid follows on average the general conservation law, which states that any change in concentration is due to either a difference in particle fluxes or a change in particle consumption/production rate R_V

$$\frac{\partial c(\mathbf{x}, t)}{\partial t} = -\nabla \cdot \mathbf{j}(\mathbf{x}, t) + R_V(\mathbf{x}, t). \qquad (2.2.8)$$

The bulk concentration of the particles is usually kept constant, which means that aggregation dynamics are ignored, hence the reaction term vanishes. For dilute solutions, the different transport effects are described independently and the superposition yields a combined flux density, which includes diffusion, electrophoretic migration, and advection arising from electroosmotic

flows and supporting microfluidics. Mathematically, this can be expressed as

$$\mathbf{j} = \mathbf{j}_{\text{diff}} + \mathbf{j}_{\text{ep}} + \mathbf{j}_{\text{adv}} = -D\nabla c + \left(\mathbf{u}_{\text{ep}} + \mathbf{u}_{\text{eo}} + \mathbf{u}_{\text{m}}\right) c, \tag{2.2.9}$$

with $\mathbf{u}_{\text{ep}}$ denoting the electrophoretic particle velocity, and $\mathbf{u}_{\text{eo}}$ and $\mathbf{u}_{\text{m}}$ describing the velocity of the fluid due to electroosmosis and forced advection, respectively. The complete transport problem for an arbitrary geometry can only be solved via numerical methods. However, the contribution of each phenomenon can be also predicted based on simpler reasoning.

Electrophoretic Migration

Electrophoretic migration describes the motion of a charged particle due to an electric field, $\mathbf{u}_{\text{ep}} = \mu_{\text{ep}}\mathbf{E}$. In general, a charged particle carries a shell of counterions when immersed in electrolyte solution. The extend of the shell can be estimated by the Debye length (see also Section 2.3.1)

$$\lambda_{\text{D}} = \sqrt{\frac{\varepsilon k_{\text{B}} T}{e_0^2 \sum_i z_i^2 c_i}} \tag{2.2.10}$$

where ε is the electric permittivity of the medium, e_0 is the elementary charge, and z_i and c_i are the valency and the concentration of the ion species i present in solution. The electrophoretic mobility μ_{ep} typically depends on the particle size (radius r_{p}) and the thickness of its surrounding shell λ_{D}.[30] In the limit of a thin screening shell, $r_{\text{p}} \gg \lambda_{\text{D}}$, the mobility is specified by the Helmholtz-Smoluchowski Equation[30]

$$\mu_{\text{ep}} = \frac{\varepsilon \zeta_{\text{p}}}{\eta}. \tag{2.2.11}$$

where the ζ-potential is considered as the voltage drop within the diffusive part of the electric double layer around the charged particle.[31] Interestingly, in this limit case the mobility depends only on properties of the medium and the surface charge of the particle, because the ζ-potential can be related to the bound surface charge density σ_{p} of the particle via[20]

$$\zeta_{\text{p}} = \frac{\lambda_{\text{D}} \sigma_{\text{p}}}{\varepsilon}. \tag{2.2.12}$$

The ζ-potentials for citrate-stabilized nanoparticles typically range from $-20\,\text{mV}$ to $-50\,\text{mV}$. Thus, the silver nanoparticles become electrophoretically attracted by the positive potential at the detection electrode during a nano-impact experiment, where ongoing background reactions generate a remaining electric field.

Unlike Brownian motion, electrophoretic migration is directional, which raises the question of which process dominates in particle-impact experiments. To answer this question, it is necessary to deduce the electric field generated by the biased electrode. Forcing the electrode-electrolyte interface to a potential different from its Nernst potential results in charge transfer reactions across the interface. These Faradaic processes create an electric field in solution as electrolyte ions must move to compensate for the injected charge. For the sake of simplicity, a hemispherical electrode is considered to compare electrophoretic and diffusive transport.[20,32] In steady-state, the radial electric field and the total electrophoretic particle flux for a hemispherical electrode yields

$$E_r(r) = -\frac{r_{\text{e}}}{r^2}\Delta\phi, \tag{2.2.13}$$

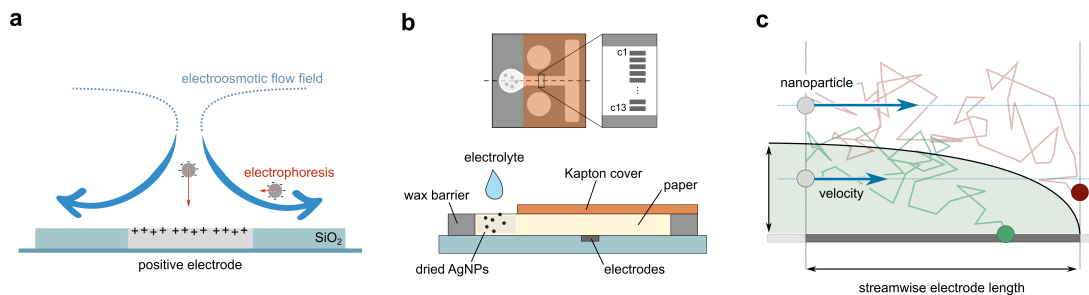$$j_{\text{ep}} = -2\pi c_\infty r_{\text{e}} \mu_{\text{ep}} \Delta\phi, \tag{2.2.14}$$

Figure 2.3 Transport phenomena in nanoparticle-impact experiments. (a) Electrically-induced particle transport mechanisms are electrophoresis and electroosmosis. Faradaic background reactions at the electrode lead to a three-dimensional electroosmotic flow field that superimposes with electrophoretic particle motion. **(b)** Paper-based microfluidics is a straightforward way to implement forced advection. **(c)** The supply of particles in flow-over sensors is restricted to lateral advection along the streamlines of the flow tangential to the surface; without the possibility of guiding them directly towards the electrode.

where r indicates the distance from the electrode and r_e describes the electrode radius. The potential difference $\Delta\phi$ across the solution from the reference to the working electrode, also known as ohmic drop, can be either described analytically by the limiting current of a redox mediator (for blocking experiments[20]) or in case of unknown background reactions (in direct nano-impact studies) by using the experimentally obtained current and the spreading resistance of the solution, which reads e.g. $\rho/2\pi r_e$ for a hemisphere and $\rho/4r_e$ for a disk microelectrode. In contrast to most other electrochemical studies, electrophoretic migration was reported to play an active role in nanoparticle-impact studies.[33–37] This is due to the fact that electrophoretic migration is largely independent of particle size, while diffusive transport is not.[20,32] Their relative influence can be estimated by the comparing the magnitudes of the two fluxes, given by Eqn. (2.2.7) and Eqn. (2.2.14). Electrophoretic migration is supposed to take over for an electric field strength associated with a potential drop inside the solution of

$$\Delta\phi > \frac{D}{\mu_{ep}} = \frac{k_B T}{6\pi\varepsilon|\zeta_p|r_p}, \tag{2.2.15}$$

which is e.g. for a 20 nm-sized particle with $\zeta_p = -30$ mV around 1 mV. Ohmic drops on this order would transfer to experimentally-observed background currents of ~ 5 nA, when we assume a 8 μm disk electrode immersed in 30 mM KCl solution, hence a spreading resistance on the order of $1.4 \times 10^5\,\Omega$.

Electroosmosis

The phenomena illustrated previously were all acting on the particles themselves and fluid motion was not taken into consideration. However, in electrochemical studies there is by nature a convective contribution: electroosmosis.[38,39] It describes the motion of a fluid in the vicinity of a charged surface due to the presence of an imposed electric field. When Faradaic reactions occur at the electrode, the remaining electric field exerts a force on the ions in solution. Within the bulk, the solutions obeys electroneutrality and there is no net ion transport. This is different in the proximity of a dielectric surface, where counter ions screen the surface charge of the solid and generate a (movable) net charge density with thickness λ_D. The motion of counter ions in the diffusive layer causes adjacent fluid elements to move via viscous forces. This results in a steady-state three-dimensional flow field. The contribution of electroosmosis is modeled by the

same equations, Eqn. (2.2.11) and Eqn. (2.2.13), as for electrophoresis, but with the opposite sign

$$u_{\mathrm{eo}} = -\frac{\varepsilon \zeta_{\mathrm{s}}}{\eta} E_{\parallel}. \tag{2.2.16}$$

Using this framework, it is possible to estimate particle transport via electroosmosis by evaluating the zeta potential of the surface ζ_{s} and the electric field component tangent and in close proximity to the dielectric surface $E_{\parallel}$. For a positively-biased microelectrode which is embedded in an SiO_2-surface with $\zeta_{\mathrm{s}} \sim -50\,\mathrm{mV}$, as shown in Fig. 2.3a, the ion cloud adjacent to the dielectric experiences a diverting force. This leads to a toroidal flow pattern that points outwards in the electrode plane, but delivers fresh volume from the bulk above the electrode. In blocking impact experiments at low ionic strength, considerably strong electric fields remain and very high velocities of microparticles can cause *near miss* events. These occur when particles approach the edge of the depletion layer, but are deviated from the electrode before they can be detected.[38]

Secondary Elektrokinetic Effects

Besides electrophoresis and electroosmosis that arise from a steady-state electric field, there have been attempts to study the influence of alternating electric fields and secondary effects due to Faradaic background reactions.[40,41] Such additional transport might stem from imposed concentration gradients of other species in solution, commonly referred to as diffusiokinetics.[42–45] Like its electric counterpart, the macroscopic concentration gradient of a solute affects both the ion shell around suspended particles (diffusiophoresis) and the double layer at dielectric surfaces (diffusioosmosis). Diffusiokinetic motion is governed by two mechanisms. First, an imposed electrolyte concentration gradient produces an electric field *in situ*, given its ion species have different diffusion coefficients. Second, there is a chemiphoretic contribution, since the nonuniform adsorption of counter ions inside the electrical double layer creates excess pressure. This ion motion always directs towards the lower electrolyte concentration. Since both phenomena do not necessarily point in the same direction, the resulting net motion highly depends on all species involved.[45] Moreover, a complete theoretical model for particle transport in impact experiments should consider all participating species, leading to various interdependencies of electro- and diffusiokinetic phenomena.[46–48]

Classical Microfluidics

Last, the motion of silver nanoparticles can be manipulated by forced advection in classical microfluidic devices.[49] Microfluidic setups are typically driven by external pumps or capillary forces, see Fig. 2.3b. The velocity distribution $\mathbf{u}_{\mathrm{m}}$ in the channel is governed by the Navier-Stokes Equation, a conservation law for the momentum, which reads in case of incompressible Newtonian fluids

$$\rho \left(\frac{\partial \mathbf{u}_{\mathrm{m}}}{\partial t} + \mathbf{u}_{\mathrm{m}} \cdot \nabla \mathbf{u}_{\mathrm{m}} \right) = -\nabla p + \eta \nabla^2 \mathbf{u}_{\mathrm{m}} + \sum_n \mathbf{f}_n.$$

where ρ describes the fluid's mass density, ∇p the pressure gradient, η the dynamic viscosity, and $\mathbf{f}_n$ the body forces acting on the fluid element. The confined space in microfluidic devices leads to a laminar flow pattern and the convective term vanishes. Under laminar flow conditions, pressure-driven systems typically exhibit a parabolic velocity profile.[50,51] For instance, the

velocity profile in a rectangular channel with height h can be estimated via

$$u(z) \approx -\frac{1}{2\eta}\frac{\partial p}{\partial x}z(h-z) \quad \text{for} \quad h \ll w \qquad (2.2.17)$$

with z denoting the vertical position in the channel.[52] Microfluidics are often used to supply 'fresh' analytes by counteracting the depletion that arises from slow diffusion. However, its positive impact on the detection yield might be drastically lower than expected.[53,54] The reason for this issue of *flow-over sensors* is a geometrical one: Forced advection can only supply particles from upstream regions along the streamlines of the flow tangential to the surface, but not in a direction perpendicular to it, as illustrated in Fig. 2.3c. This means, that the initial vertical distance between the particle and the electrode in the bottom of the channel has to be solely overcome by diffusion, which can be a slow process (neglecting migration). The collision of a particle is only possible if the time needed for downstream traveling and reacting is smaller than the time it takes to sweep the particle across the stream-wise length of the electrode. It has been shown, that there are different regimes under which such flow-over sensors can be operated depending on the channel height and electrode length, as well as the imposed flow rate.[53–56] However, these regimes either lead to a high particle flux or a high capture yield with a minimum of escaped particles – but not both at the same time. This problem has been (partially) addressed by implementing passive mixing units that enforce spiraling streamlines. The first and most famous example of such structures is the staggered herringbone mixing unit consisting of asymmetric groove patterns.[57,58]

2.3   Electrostatics and Electrochemistry

The previous section was concerned with the transport mechanisms that (may) influence particle transport in stochastic electrochemistry. Now, we focus on the effects occurring at the electrode surface. Regardless of the exact experiment, all stochastic impact methods involve an electrochemical reaction, which means that electrons are transferred between the metal and chemical species in solution. This can happen spontaneously or can be forced by an external potential that alters the reaction landscape. Before discussing such Faradaic processes in more detail, the focus will be on a dielectric surface in contact with an electrolyte solution.

2.3.1   Electrostatics at the Solid-Liquid Interface

When a dielectric surface comes into contact with an electrolyte, electrostatic interactions lead to a charged double layer at the solid-liquid interface.[59] As the solid phase carries a surface charge, the mobile ions in solution see an electric field and move accordingly. This ultimately leads to an excess of counter ions at the proximity of the dielectric surface. Helmholtz described this phenomenon first and considered the electrical double layer as a rigid monolayer of counter ions that balance the surface charges at the solid phase completely within the length scale of an ion radius. However, this description lacks the thermal motion of the ions in solution, which prohibits a static order on microscopic scales. When thermal fluctuations are considered, the rigid ion layer described by Helmholtz is either replaced or extended by a diffusive ion layer. The likelihood of a species being in an electric field at position x is dependent on the energy $q\phi(x)$ that is associated with this position/state. If Boltzmann statistics are applied for the distribution of ions i, their concentration profile reads

$$c_i(x) = c_{i,\infty}\exp\left(-\frac{z_i e_0 \phi(x)}{k_\mathrm{B}T}\right), \qquad (2.3.1)$$

with $c_{i,\infty}$ being the bulk concentration, $k_{\mathrm{B}}T$ denoting the thermal energy, and $z_i e_0 \phi(x)$ describing the potential energy in the electric field at position x. The concentration profile as a measure of the occupancy of this state depends exponentially on the electric potential $\phi(x)$. The potential at x, in turn, is determined by the joint contributions of all charged species in solution. By summarizing their effect on the resulting field via the Poisson Equation $\nabla^2 \phi = -\rho/\varepsilon$, one obtains the Poisson-Boltzmann Equation for the electric potential

$$\nabla^2 \phi = -\frac{e_0}{\varepsilon} \sum_i z_i c_{i,\infty} \exp\left(-\frac{z_i e_0 \phi(x)}{k_{\mathrm{B}}T}\right). \tag{2.3.2}$$

Considering a potential lower than the thermal voltage, $\phi \ll 25\,\mathrm{mV}$, the exponential term can be linearized, which leads to the Debye-Hückel approximation.[60] Then, the solution of the Poisson-Boltzmann Equation simplifies to an exponential decay of the potential

$$\phi(x) = \phi_0 e^{-\lambda_{\mathrm{D}} x} \quad \text{with} \quad \lambda_{\mathrm{D}} = \sqrt{\frac{\varepsilon k_{\mathrm{B}}T}{e_0^2 \sum_i z_i^2 c_i}} \tag{2.3.3}$$

characterized by its Debye length λ_{D}. The Debye length is a measure of the penetration depth of the electric field into the liquid and is a property of the solution. It ranges at room temperature between $0.3\,\mathrm{nm}$ for $1\,\mathrm{M}$ and $3\,\mathrm{nm}$ for $10\,\mathrm{mM}$ considering a monovalent symmetric electrolyte composition, such as NaCl or KCl.

2.3.2 The Electrode-Electrolyte Interface at Thermodynamic Equilibrium

In contrast to the charge separation at dielectric surfaces, it is possible for electrons to cross the energy barrier of an electrode – either from the metal to the liquid phase or vice versa. This is the core of electrochemical studies. Such transfer reactions can happen spontaneously but may also be induced by an external electric potential. Faradaic reactions arise, whenever the energy levels of the metal-phase and the liquid-phase are not equal. As long as an electrochemical potential gradient exists, electrons are driven across the interface. If we consider a redox couple with the oxidized (O) and the reduced species (R) being dissolved in an inert electrolyte, the charge transfer reaction is given by

$$\mathrm{O} + z\,\mathrm{e}^- \rightleftharpoons \mathrm{R}. \tag{2.3.4}$$

Both species are associated with different energy states and their occupancy depends on the thermal energy in the system. At thermodynamic equilibrium, the ratio of the concentrations $c_{\mathrm{red}}/c_{\mathrm{ox}}$ at the electrode obeys the Boltzmann statistics, too. The associated Nernst potential of the electrode-electrolyte interface reads

$$\phi^{\mathrm{eq}} = E^0 - \frac{k_{\mathrm{B}}T}{ze} \ln\left(\frac{c_{\mathrm{red}}}{c_{\mathrm{ox}}}\right), \tag{2.3.5}$$

where E^0 describes a reaction-specific potential§ using a standard hydrogen electrode (SHE) as reference and c_{red} and c_{ox} indicate the concentration of the reduced and oxidized species at the interface. Tab. 2.1 provides a selection of standard potentials for reactions that may occur during nano-impact experiments.

The Nernst Equation Eqn. (2.3.5) is at the core of electrochemistry, as it relates the potential across the interface to the concentrations of the species. For instance, it explains why an electrical current is measured when two compartments with different species composition are connected in

---

§ In electrochemical literature, electrode potentials are usually represented by the variable E. However, the potential E^0 should not be confused with the electric field mentioned in previous sections.

Table 2.1 Electrochemical standard potentials for selected redox processes that can occur during nanoparticle detection experiments, when Au or Pt electrodes are used.[61] The experiments in this thesis were typically carried out with a Ag/AgCl (3 M KCl) reference electrode with an offset potential of 0.21 V at 20 °C. The practically-relevant shifted redox potentials ϕ^{exp} are shown in the third column.

redox process	E^0 / V	ϕ^{exp} / V
$2\,H_2O + 2\,e^- \rightleftharpoons H_2 + 2\,OH^-$	-0.83	-1.04
$AgI + e^- \rightleftharpoons Ag + I^-$	-0.15	-0.36
$\mathbf{2\,H + 2\,e^- \rightleftharpoons H_2}$	0.00	-0.21
$AgBr + e^- \rightleftharpoons Ag + Br^-$	0.07	-0.14
$\mathbf{AgCl + e^- \rightleftharpoons Ag + Cl^-}$	0.22	0.1
$O_2 + H_2O + 4\,e^- \rightleftharpoons 4\,OH^-$	0.4	0.19
$Ag + e^- \rightleftharpoons Ag$	0.8	0.59
$[AuCl_4]^- + 3\,e^- \rightleftharpoons Au + 4\,Cl^-$	0.93	0.72
$[AuCl_2]^- + e^- \rightleftharpoons Au + 2\,Cl^-$	1.15	0.94
$Pt^{2+} + 2\,e^- \rightleftharpoons Pt$	1.19	0.98
$O_2 + 4\,H^+ + 4\,e^- \rightleftharpoons 2\,H_2O$	1.23	1.02

a galvanic cell. Vice versa, it describes what happens when the interface is forced to a potential out of equilibrium. Whenever the interfacial potential is lower than the standard potential, $\phi < E^0$, the reduction process is favored. In case of $\phi > E^0$, the system is driven towards oxidation. The latter mechanism is used for nanoimpact experiments, where the potential at the microelectrode catalyzes reactions to investigate single nanoparticles. When performing such experiments, it is important to consider that the electrolyte solution consists of multiple species and the applied potential can fuel side reactions as well. The list in Tab. 2.1 can be used to determine a potential range that accounts for unwanted interfering reactions. For instance, the potential should stay inside the water window ranging between $-0.83\,\text{V} < \phi < 1.23\,\text{V}$, when measured in aqueous solutions. Otherwise, hydrolysis might mask the signal of interest and introduce interfering phenomena. If a reference electrode different than the SHE is used, the standard potentials in Tab. 2.1 have to be shifted accordingly, for example by $-0.21\,\text{V}$ in case of a Ag/AgCl reference (3 M KCl).

2.3.3 Faradaic Background Currents at the Electrode

The Cottrell- and Saito Equations, Eqn. (2.2.4) and Eqn. (2.2.6), have been proven valuable to estimate the range at which nanoparticle collisions are expected. In contrast, additional background reactions that are induced by the electrode potential can be described by Butler-Volmer kinetics. The Butler-Volmer framework applies, when the reaction is not dominated by the species transport to the electrode, but by the potential at the electrode, since the species are present in large excess at the interface. The detection of silver nanoparticles is typically conducted in supporting electrolyte without any additional redox mediator, wherefore we are mainly concerned with reactions involving water, oxygen and hydrogen molecules – species that are present at high concentrations.

At equilibrium, the net exchange current at the electrode is zero. Nevertheless, redox species are constantly oxidized/reduced at the interface, but their oxidation/reduction currents are exactly balanced. The number of transferred electrons n is determined by the rate constants for the oxidation and reduction processes, k_{ox} and k_{red}, and the number of species available at the electrode surface being in the oxidized and reduced state (c_{ox} and c_{red}), which leads to

$$n = k_{ox}(\phi)\,c_{red} - k_{red}(\phi)\,c_{ox}. \tag{2.3.6}$$

The rate constants k_i are determined by the energy barrier that separates the two states – oxidized or reduced –, following the Arrhenius law

$$k_i = A_i \exp\left(-\frac{\Delta G_i(\phi)}{k_B T}\right) \quad i \in \{\text{ox}, \text{red}\} \tag{2.3.7}$$

with A_i representing a constant and ΔG_i denoting the activation energy required to cross the barrier. Thus, the rate constants are a function of the potential difference across the electrode-electrolyte interface. For a small deviation from the equilibrium potential ϕ^{exp}, the Gibb's free energy $\Delta G_i(\phi)$ can be approximated by a first-order Taylor series.

$$\Delta G_i(\phi) \approx \Delta G_i(\phi^{\text{exp}}) + (\phi - \phi^{\text{exp}}) \left.\frac{\partial \Delta G_i(\phi)}{\partial \phi}\right|_{\phi=\phi^{\text{exp}}} \tag{2.3.8}$$

If an external potential is applied, the energy landscape is altered, which ultimately results in a net exchange current at the interface. Combining the considerations above, the electron transfer rate in Eqn. (2.3.6) can be transformed in a potential-dependent exchange current density at the interface,

$$j = j_0 \left[\exp\left(\frac{ze_0\alpha(\phi - \phi^{\text{exp}})}{k_B T}\right) - \exp\left(\frac{-ze_0(1-\alpha)(\phi - \phi^{\text{exp}})}{k_B T}\right)\right] \quad \text{with} \quad \alpha = \frac{1}{ze_0} \left.\frac{\partial \Delta G_i(\phi)}{\partial \phi}\right|_{\phi=\phi^{\text{exp}}} \tag{2.3.9}$$

which is known as the Butler-Volmer Equation. Here, j_0 is defined as the anodic exchange current density at equilibrium, when $\phi = \phi^{\text{exp}}$ and α is the anodic charge transfer coefficient. The potential difference $\phi - \phi^{\text{exp}}$ is also known as overpotential η. The Butler-Volmer Equation is valid as long as the species depletion does not critically interfere with the reaction process, thus it describes a kinetically-limited reaction. However, a more general version of the Butler-Volmer Equation accounts for mass-transfer limitations as well by introducing prefactors related to the species concentrations for the anodic / cathodic reactions

$$j = j_0 \left[\frac{c_{\text{ox}}(0,t)}{c_{\text{ox},\infty}} \exp\left(\frac{ze_0\alpha(\phi - \phi^{\text{exp}})}{k_B T}\right) - \frac{c_{\text{red}}(0,t)}{c_{\text{red},\infty}} \exp\left(\frac{-ze_0(1-\alpha)(\phi - \phi^{\text{exp}})}{k_B T}\right)\right], \tag{2.3.10}$$

where e.g. $c_{\text{ox}}(0,t)$ is the oxidized species present at the interface at time t.

When the overpotential $|\phi - \phi^{\text{exp}}|$ is small, i.e. less than $10\,\text{mV}$, the exponential terms can be approximated as linear. In this case, the relationship between the applied potential and the exchange current density becomes proportional. This implies that the interface behaves similar to an ohmic resistor.

$$j = j_0 \left[1 + \frac{ze_0\alpha(\phi - \phi^{\text{exp}})}{k_B T} - 1 + \frac{(1-\alpha)ze_0(\phi - \phi^{\text{exp}})}{k_B T}\right] = j_0 \frac{ze_0(\phi - \phi^{\text{exp}})}{k_B T} \tag{2.3.11}$$

The other limit case involves high overpotentials, where $(\phi - E^0) \gg |k_B T/ze_0|$. In this so-called Tafel regime, either oxidation or reduction dominates the exchange current density

$$j_{\text{ox}} = j_0 \exp\left(\frac{ze_0\alpha(\phi - \phi^{\text{exp}})}{k_B T}\right) \tag{2.3.12}$$

$$j_{\text{red}} = -j_0 \exp\left(\frac{-ze_0(1-\alpha)(\phi - \phi^{\text{exp}})}{k_B T}\right). \tag{2.3.13}$$

2.4   Optical Properties of Silver Nanoparticles

Why do silver nanoparticle suspensions shine yellow, while a silver ring exhibits a metallic appearance? The reason for this discrepancy is the small size of the nanoparticles, which leads to localized surface plasmon resonance (LSPR). When an electromagnetic wave hits a metallic nanoparticle, the electric field acts on the free electrons available in the particle and causes a coherent displacement of the electrons. This coherent displacement of electrons away from the positively charged lattice creates a restoring force that pulls the polarized electrons back to the lattice, meaning that the nanoparticle acts much like a *nanoantenna*. The collective charge oscillation, called *plasmon*, is distributed over the entire volume of the particle, thus, it is *localized*. Its motion can be modeled as harmonic – mass-on-spring, dampened – oscillator in the Rayleigh approximation for particle sizes $d_p \ll \lambda$. In this case, a quasistatic description is valid and the electric field at any point in time is constant across the particle, see Fig. 2.4a. Then, the problem boils down to solving the Laplace Equation $\nabla^2 \phi = 0$ for this geometry. Under such conditions, the induced dipole moment $\mathbf{p}$ of the particle is proportional to the incoming wave $\mathbf{E}_0$, as $\mathbf{p} = \varepsilon_0 \varepsilon_m \alpha \mathbf{E}_0$. The polarizability

$$\alpha = 4\pi r_p^3 \frac{\varepsilon_p - \varepsilon_m}{\varepsilon_p + 2\varepsilon_m} \tag{2.4.1}$$

captures the resonance behavior, which depends on the dielectric permittivities of both the particle ε_p and the surrounding medium ε_m, respectively. The interaction is further dependent on the particle size, since $\alpha \propto r_p^3$. The quasistatic approximation rules out any phase-difference across the particle, therefore the solution is restricted to a dipole behavior, which is only valid for particle sizes up to $d_p = 100\,\text{nm}$ in case of visible light. Larger particles experience additional phase differences, which lead to retardation forces and the occurrence of higher modes, which are covered by the more rigorous Mie theory.[62]

Resonance characteristics relate to a polarizability of $\alpha > 1$, which occurs when the denominator in Eqn. (2.4.1) is minimum, also called Fröhlich condition

$$\text{Re}(\varepsilon_p) = -2\varepsilon_m \quad \text{for small } \text{Im}(\varepsilon_p). \tag{2.4.2}$$

The dielectric function $\varepsilon_p(\omega)$ for the metallic nanoparticle can be deduced from the Drude model, which describes the motion of free conducting electrons within the metal.[63] The model assumes that the material properties are homogenous and isotropic and accounts for the electric field and a friction term to describe the electron motion

$$m_e \frac{\partial^2 r}{\partial t^2} = -e_0 E - m_e \gamma \frac{\partial r}{\partial t}. \tag{2.4.3}$$

Here, m_e is the mass of an electron, e_0 its charge, $E = E_0 e^{-i\omega t}$ is the local electric field, and γ is the collision frequency of the electrons hitting the lattice atoms. The dampening term $\gamma = 1/\tau$ can be obtained from the relaxation time, which is on the order of $10^{-14}\,\text{s}$. This relaxation corresponds to the frequency of infrared light. The solution to the Drude model reads

$$r(\omega) = \frac{e_0}{m_e \left(\omega^2 + i\omega\gamma\right)} E \tag{2.4.4}$$

where $r(\omega)$ describes the magnitude of the electron displacement caused by the monochromatic electric field. By comparing the resulting dipole moment $\mathbf{p} = e_0 N r(\omega)$ with the macroscopic expression for the polarizability, one obtains the complex dielectric function that simplifies in the
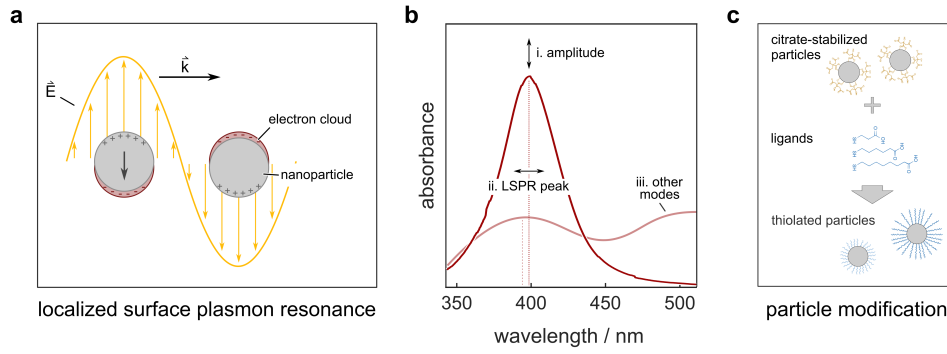
Figure 2.4 Localized surface plasmon resonance for noble metal particles. (a) Schematic for light-particle interaction. In case of a particle size smaller than the wavelength, the particle experiences approximately a constant electric field, leading to a dipole resonance behavior. **(b)** Schematic of an UV/Vis spectrum (dark red) of a nanoparticle suspension. Changes in the resonance wavelength can be attributed to changes in the dielectric environment, e.g. caused by the attachment of thiolated ligands. The amplitude of the absorbance scales with the number of particles in solution. The light red curve represents an instable colloid, since the amplitude of the initial resonance is drastically lower and additional higher-order resonance modes appear, which can be attributed to dissolution of the particle and cluster formation. **(c)** Particle modification via ligand exchange can be monitored by consecutive UV/Vis spectra of the colloid. This work used a pH-assisted method to exchange citrate molecules at the particle surface of commercially available suspensions.

limit of $\omega \ll \gamma$ to

$$\varepsilon_{\mathrm{p}}(\omega) = 1 + \frac{\omega_{\mathrm{p}}^2}{i\gamma\omega - \omega^2} \quad \rightarrow \quad \varepsilon(\omega) = \left[1 - \frac{\omega_{\mathrm{p}}^2}{\omega^2}\right] + i\left[\frac{\gamma\omega_{\mathrm{p}}^2}{\omega^3}\right] \quad \text{with} \quad \omega_{\mathrm{p}} = \sqrt{\frac{Ne_0^2}{m_e\varepsilon_0}}. \quad (2.4.5)$$

The plasma frequency ω_{p} is a material-specific value. It is determined by the electron density N in m^{-3} of the metal and depicts a turning point in its behavior – up to ω_{p} the electrons are able to follow the incident field, but beyond ω_{p} the electrons cannot move accordingly anymore. Although the Drude model ignores quantum phenomena, it captures the major features of metals: The real part of the permittivity remains negative for wavelengths corresponding to $\omega \ll \omega_{\mathrm{p}}$, which results in a reflective behavior. At wavelengths $\omega \gg \omega_{\mathrm{p}}$ the metal becomes transparent. The imaginary part of ε is associated with energy dissipation. Now, the resonance frequency of the particles can be calculated by using the real part of Eqn. (2.4.5) for the Fröhlich condition Eqn. (2.4.2)

$$\omega_{\mathrm{LSPR}} = \sqrt{\frac{\omega_{\mathrm{p}}}{1 + 2\varepsilon_{\mathrm{m}}}}. \quad (2.4.6)$$

The dependence on ω_{p} explains why Au and Ag particles of the same size exhibit different localized surface plasmon resonance (LSPR) peaks in the optical spectrum, as an increase in electron density in the metal causes a blue shift of the resonance. Additionally, ω_{LSPR} is strongly affected by the surrounding environment, where an increase in ε_{m} results in a red shift of the resonance. These properties make metallic nanoparticles ideal for optical sensing. Likewise, changes in the optical spectrum before and after ligand modification can be used to easily assess ligand binding, as shown in Fig. 2.4b and c.[64–66]
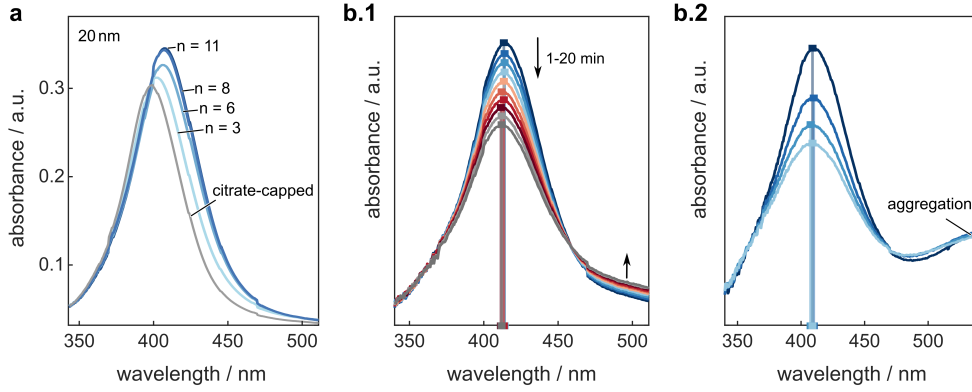
Figure 2.5   Exemplary UV/Vis spectra for silver nanoparticles. (a) Spectra of different nanoparticle suspensions after functionalization with differently-sized, $n \in \{3, 6, 8, 11\}$, alkanethiols. **(b.1, b.2)** Consecutive spectra of different 40 nm-sized particle suspensions immersed in phosphate-buffered saline. The changes in the spectra indicate colloid instability of different severity. The change in the optical density at 410 nm is caused by oxidative dissolution of the silver nanoparticles. At the same time, new resonance modes at higher wavelengths arise due to a clustering of the particles.

Considering a monochromatic planar wave hitting a sphere, its cross sections for scattering and absorption can be obtained from the Poynting vector for dipole radiation

$$\sigma_{\mathrm{sc}} = \frac{k^4}{6\pi} |\alpha|^2 = \frac{8\pi}{3} k^4 \, r_{\mathrm{p}}^6 \left| \frac{\varepsilon_{\mathrm{p}} - \varepsilon_{\mathrm{m}}}{\varepsilon_{\mathrm{p}} + 2\varepsilon_{\mathrm{m}}} \right|^2 \tag{2.4.7}$$

$$\sigma_{\mathrm{ab}} = k \, \mathrm{Im}(\alpha) = 4\pi k r_{\mathrm{p}}^3 \, \mathrm{Im}\left(\frac{\varepsilon_{\mathrm{p}} - \varepsilon_{\mathrm{m}}}{\varepsilon_{\mathrm{p}} + 2\varepsilon_{\mathrm{m}}} \right) \tag{2.4.8}$$

with $k = {}^{2\pi}/\lambda$. In the case of small particles with $r_{\mathrm{p}} \ll \lambda$, absorption is the dominant process as it scales with r_{p}^3 in contrast to scattering which scales with r_{p}^6. For metal nanoparticles, both cross sections σ_{sc} and σ_{ab} are resonantly enhanced when the Fröhlich condition Eqn. (2.4.6) is met. Therefore, the extinction spectra of silver nanoparticles experience a prominent peak, either caused by predominant absorption ($d_{\mathrm{p}} < 40$ nm) or scattering. In addition to the dependence on material and particle size, there is also a dependence on shape and assembly that can be utilized for plasmonic sensing applications.[67–70] For example, metallic rods show two extinction peaks in their spectrum that are associated with their different confinements in length and width. Moreover, nanoparticles clustering together typically lead to a redshift and the occurrence of additional resonant modes.[71,72] In the present work, LSPR characteristics have been extensively used to assess the success and quality of ligand exchange procedures, as shown in Fig. 2.5a, and also to test the colloidal stability of the particles in different measurement buffers, see also Fig. 2.5b.

2.5 Assessing Receptor-Ligand Interactions for (Bio)Sensing

A biosensor measures biological reactions by generating readout signals that are proportional to the concentration of an analyte. First, this involves the specific binding of the analyte to a recognition element. In a subsequent step, the specific binding event is transduced into a read-out signal, which can be e.g. optical or electrochemical. Regardless of the exact transduction mechanism, all biosensing concepts have to account for the initial step of (specific) ligand capture. The binding is associated with a conformational change of the receptor (protein or oligonucleotide), which is a function of charge, hydrophobicity, and molecular structure. Typically, binding refers to (reversible) intermolecular interactions stemming from Coulomb forces, hydrogen bond formation, and Van der Waals forces.

2.5.1 Modeling Receptor-Ligand Kinetics

Simplified dynamics of such a bimolecular reaction between receptor (R) and ligand (L) molecules can be modeled via chemical rate equations. The receptors are considered to be pre-immobilized with a fixed amount on the sensor surface, thus, there is only a limited number of binding sites available. Then, ligands/analytes are flushed over the surface in order to bind to the receptors. Ideally, the concentration of L is constant during binding, which essentially means that diffusive transport is sufficient to counteract the depletion of molecules close to the binding sites. Under this assumptions, the capturing can be modeled by a two-state system, referring to the receptor R being free or occupied,

$$\mathrm{R} + \mathrm{L} \underset{k_{\mathrm{off}}}{\overset{k_{\mathrm{on}}}{\rightleftharpoons}} \mathrm{RL} \tag{2.5.1}$$

where k_{on} and k_{off} are the association and dissociation rate constants in units of $(\mathrm{Ms})^{-1}$ and s^{-1}, respectively. The association rate constant reflects, how many RL-complexes are formed per second inside a mixture of $1\,\mathrm{M}$ R and L species. In contrast, the dissociation constant reflects the stability of the RL-complex and describes the fraction of complex decays per second. Typically, k_{on} ranges from 10^3 to $10^7\,(\mathrm{Ms})^{-1}$ and k_{off} from 10^{-1} to $10^{-6}\,\mathrm{s}^{-1}$ for biological species. Similar to Section 2.3.3, the reaction rate is connected to the difference in the Gibbs free energy that separates the free and bound state. The frequency of overcoming the energy barrier is again modeled by the Arrhenius law, see Eqn. (2.3.7). Given the bimolecular process above, the number of occupied receptors $[RL]$ obeys

$$\frac{d[RL]}{dt} = k_{\mathrm{on}}[R][L] - k_{\mathrm{off}}[RL] \tag{2.5.2}$$

with $[L]$ and $[R]$ denoting the concentration of free ligands and unoccupied receptors, respectively. In equilibrium, the rate of unbinding equals the rate of binding and one obtains a so-called dissociation constant

$$K_{\mathrm{d}} = \frac{k_{\mathrm{off}}}{k_{\mathrm{on}}} = \frac{[R][L]}{[RL]}. \tag{2.5.3}$$

in units of M. K_{d} is a characteristic value that indicates the ligand concentration, where half of the receptors are occupied. Hence, strong receptor-ligand binding is characterized by small dissociation constants. For instance, the interaction of streptavidin and biotin – known as the strongest binding couple in nature – yields a $K_{\mathrm{d}} \sim 10^{-14}\,\mathrm{M}$. Eqn. (2.5.2) can be simplified by

considering a constant total number of receptors leading to $[R_t] = [R] + [RL]$. Then the steady-state fraction of occupied receptors $f_R = [RL]/[R_t]$ as a function of the ligand concentration $[L]$ reads

$$f_R = \frac{[L]}{K_d + [L]}. \tag{2.5.4}$$

This can be used to determine the equilibrium concentration of occupied receptors via

$$[RL] = \frac{[R_t][L]}{K_d + [L]}. \tag{2.5.5}$$

Besides the equilibrium occupancies, the reaction dynamics are of crucial importance in sensing applications. In first approximation, the temporal evolution of a receptor-ligand binding follows an exponential relaxation given by

$$f_R(t) = \frac{K_d}{[R_t]} \left[1 - e^{-(k_{on}[L]+k_{off})(t-t_0)} \right] \qquad \text{during association with } [L] \gg [R_t] \tag{2.5.6}$$

$$f_R(t) = \frac{K_d}{[R_t]} e^{-k_{off}(t-t_0)} \qquad \text{during dissociation with } [L] = 0. \tag{2.5.7}$$

2.5.2   Real-time Monitoring Using Surface Plasmon Resonance

During (bio)assay development, the real-time monitoring of association and dissociation is an extremely helpful tool to determine K_d, k_{on}, and k_{off}. Especially surface plasmon resonance-based (SPR) analysis has proven to provide valuable information regarding binding kinetics. This spectroscopic technique exploits the resonance at a metal-dielectric interface and is very similar to the LSPR in metallic nanoparticles described earlier. A typical SPR device, see Fig. 2.6a, consists of a p-polarized infrared light source, a detector, a thin Au film attached in contact with a glass prism, and a flow cell, where the analyte can be delivered and flushed out. Specific coatings of the Au film allow to immobilize receptor species, for instance, antibodies or aptamers. After preparation of the capture layer, the analyte is supplied under a continuous flow to study ligand-receptor interactions in real time. Therefore, SPR is able to monitor association and dissociation profiles of various analyte concentrations to infer binding kinetics and other parameters of interest in the field of bioassay development, see Fig. 2.6b and c.

In the so-called Kretschmann configuration, as illustrated in Fig. 2.6a, the incident light beam travels through a glass prism with a high dielectric constant before it hits the thin metal film in contact with the liquid phase. The light beam is directed under an angle beyond the critical angle (using Snell's law, $\sin(\theta_c) = n_m/n_d$) to the metal-dielectric interface. This results in total internal reflection and causes a collective motion of surface charges at the liquid-metal interface via light tunneling through the metal. The resonant coupling generates an electromagnetic wave traveling along the surface, a *surface plasmon polariton* (SPP), that involves both, collective oscillations of the electrons in the metal and an electromagnetic wave in the (liquid) dielectric.

More precisely, the resonant coupling is a consequence of momentum conservation. Although the incident wave is totally reflected, it is able to periodically generate surface charges between the metal and the dielectric, which have associated radiation fields. These evanescent fields decay exponentially in amplitude and extend orthogonal to the interface. If we consider momentum

conservation, which essentially means that components of the wave vectors parallel to the interface have to match, the condition for plasmonic resonance reads

$$k_{\text{SPP}}(\omega) = \frac{\omega}{c}\sqrt{\frac{\varepsilon_{\text{d}}\varepsilon_{\text{m}}}{\varepsilon_{\text{d}} + \varepsilon_{\text{m}}}}, \tag{2.5.8}$$

where ε_{m} and ε_{d} are the permittivities of the metal and the dielectric. Resonant coupling is achieved for $\varepsilon_{\text{d}} + \varepsilon_{\text{m}} = 0$, which requires the real part of one of the two dielectric functions to be negative. Using again the Drude model in Eqn. (2.4.5) for the ε_{m}, the resonance frequency is given by

$$\omega_{\text{SPP}} = \frac{\omega_{\text{p}}}{\sqrt{1 + \varepsilon_{\text{d}}}} \tag{2.5.9}$$

where ω_{p} describes again the plasma frequency of the metal, see Eqn. (2.4.5). If the wavelength of the light and the angle of the incident beam in the prism matches, light tunneling leads to an excitation of a SPP at the liquid-metal interface. Therefore, SPR sensors in Kretschmann configuration use Au layers with a thickness $< 50\,\text{nm}$ to make this process efficient. As the amplitude of the evanescent field in the liquid chamber decays exponentially, the sensitive region where changes in the dielectric function affect the read-out signal lies within a distance of $300\,\text{nm}$.

The SPR device is able to monitor changes in the dielectric constant of the liquid phase and temporal variations in the electron density at the metal surface. For instance, binding of thiolated molecules or the attachment of other metal nanoparticles shifts the SPP peak towards longer wavelengths. Yet, also any change in the environment close to the metal surface leads to changes in the SPP spectrum. These changes can arise from exchanging buffers with different refractive indices, or from the (specific) binding of species to the receptor-modified metal surface. An exemplary SPR signal is depicted in Fig. 2.6b, where a biotinylated Au chip was first exposed to streptavidin and subsequently flushed with biotinylated particles to study their binding on the latter. As the changes in the SPR signal scale with the local change in the dielectric function, the binding of larger structures with higher masses are ideal study objects for SPR sensors. In contrast, the specific binding of small ligands is mostly beyond the device's capability. This work employed SPR measurements during the entire development process of a nanoparticle-based bioassay, as it yields insights regarding various aspects, such as the optimum surface coverage of receptors as illustrated in Fig. 2.6c, the effect of different buffer compositions, the quality of the ordered biological species, *et cetera*.
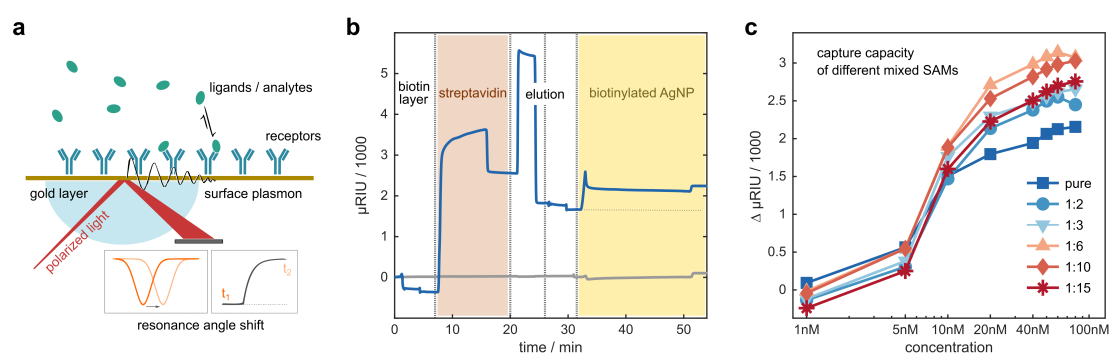
Figure 2.6   Real-time monitoring via surface plasmon resonance. (a) Schematic of a SPR sensor in Kretschmann configuration. A shift in the resonance angle indicates changes in the electric permittivity close to the gold surface, which can be associated with ligand binding. **(b)** Exemplary sensorgram, where the SPR signal associated with the location of resonance angle at the detector is monitored over time. The biotinylated Au-chip (blue) was first flushed with NaOH to remove residual molecules. Then, streptavidin was injected leading to a stark increase in signal during association. During dissociation, the signal decreased rapidly, but plateaued at a high level, indicating the initial shift in the refractive index due to the absence of free streptavidin and subsequent the successful capture of streptavidin on the chip. Afterwards, different buffers that decrease the electrostatic interactions were used for elution. Last, 40 nm-sized, biotin-coated particles were flushed over, which resulted in a small overall shift in the resonance. This could be attributed to a very weak, probably, nonspecific interaction. The gray curve corresponds to a biotinylated Au-chip that was exclusively flushed with biotinylated silver nanoparticles. In this case, electrostatic repulsion should prevent their attachment. **(c)** The capture capacity of mixed self-assembled monolayers (SAM) with different ratios of mercaptoundecanoic acid spacers and protruding PEG-biotin alkanethiolate molecules. The data was acquired for chips differently coated prior to the study, where streptavidin at increasing concentrations was injected to assess binding saturation.

3. State of the Art

3.1 Single-Impact Electrochemistry of Silver Nanoparticles

The charge transfer from silver nanoparticles upon their collision with an electrode is conceptually different from the steady-state electrochemical conversion of bulk redox species, because the former is not a continuous but a discrete process. Recent advances in fabrication technology and measurement science enabled to study such dynamic interactions at the level of single entities. Although pioneering research was done in the mid-20th century,[73–75] the field of impact electrochemistry is relatively new, starting in 2004 with Lemay and co-workers who reported blocking impacts from microparticles that collide with microelectrodes.[76] Then in 2011, Compton and colleagues used stochastic collisions to detect and size silver nanoparticles in solution by their electrochemical conversion at a microelectrode.[77] Nowadays, the oxidation of silver nanoparticles is among the most studied subjects in impact electrochemistry.[78] In contrast to other impact-based methods, the particle *itself* is converted upon collision whenever the externally applied potential exceeds the Nernst potential of the redox couple. Depending on the electrolyte composition, different reaction pathways are possible.[79–81] For example, the silver nanoparticle can be oxidized directly to AgO_x at high positive potentials, but in the presence of halides, lower potentials are also possible, with the charge transfer being mediated by the anion of the salt, see also Tab. 2.1.

The oxidation reaction includes several substeps and is still under investigation.[12,13,82–85] Especially, the extended size of the nanoparticle adds another level of complexity, because its motion trajectory is crucial to the dynamic processes occurring at the electrode, as shown in Fig. 3.1. There has been substantial research in the past to explore such interfacial effects and their impact on the particle detection.[78] In this regard, the complementary information from simultaneous optical/spectroscopic and electrical readouts has provided valuable insights.[40,86–88] In a simplified picture, the nanoparticle moves in solution by virtue of Brownian motion and may approach the biased electrode. Once it reaches the tunneling distance of the electrode, the particle (instantaneously) undergoes oxidation and dissolves. Assuming complete oxidation, the number of transferred electrons is equal to the number of silver atoms in the particle, allowing to estimate the particle size from the obtained charge via

$$d_{\mathrm{p}} = 2 \cdot \sqrt[3]{\frac{3QM_{\mathrm{Ag}}}{4\pi F \rho_{\mathrm{Ag}}}}, \tag{3.1.1}$$

where Q is the measured charge, M_{Ag} is the molar mass of Ag and ρ_{Ag} its density. However, this relationship may not always hold true. Recent studies have shown that silver nanoparticles with diameters smaller than 30 nm typically undergo complete oxidation, whereas larger particles are typically subject to multiple partial oxidations.[13,82,83] The observation of such incomplete oxidation events aligns well with the particle motion inside the tunneling distance. Depending on the bandwidth and the sampling rate of the amplifier system, such particle motion can be resolved.
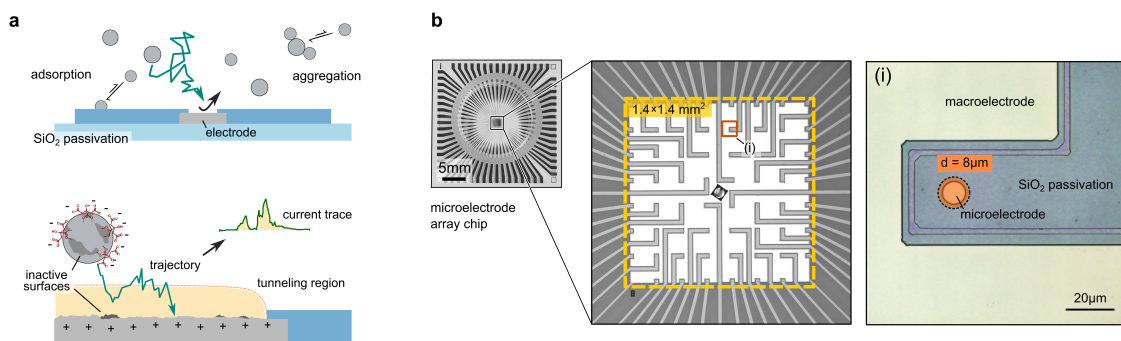
Figure 3.1   Nano-impacts at microelectrodes. (a) The particle collision is influenced by a variety of macroscopic and microscopic effects. Adsorption and aggregation lead to temporal changes in the underlying bulk concentration. Inactive electrode- and particle surfaces may lead to silent particles, if the electric potential is not sufficient to overcome the increased energy barrier for electron tunneling. **(b)** Optical and microscopic images of a microelectrode array chip used in this work. The chip is fabricated by classical clean-room techniques and consists of 8×8 Pt electrodes surrounded by a stack of five alternating SiO_2 and Si_3N_4 layers and a macroscopic shield electrode to manipulate electrostatic repulsion.

Especially the filter stage of the amplifier can lead to a broadening of the current peak, as the measured current peak is a convolution of the initial charge injection with the response of the measurement system.[89–92]

Advanced setups allowed experimental designs that aim to better understand the governing processes at the interface. For instance, there has been substantial work on the effect of the electrode potential.[93–95] Extended and stronger electric fields do not only alter the energy landscape to favor the reaction, but also affect the particles' trajectories.[40,87,96] Moreover, the rule – the more, the better – is not unlimited, as high overpotentials can trigger additional background reactions, which might impede the particle oxidation. Such reactions can critically interfere with the particle oxidation, as they induce local changes in the buffer composition, or may alter the particle transport, but most severely, they can change the state of the electrode surface. For instance, Au and Pt are typically used as electrode material and become oxidized at high potentials, which effectively decreases the electroactive area or results in a higher energy barrier that has to be overcome during impact. This is only one example of how the electrode surface can influence the particle oxidation. The same applies for the particle surface. Targeted surface modifications at the electrode and defects on the nanoparticle surface were reported to alter the oxidation reaction significantly.[78,95,97,98] In summary, particle oxidation across an increased energy barrier, e.g. introduced via long-chained alkanethiols, is still possible, if the particle adsorption onto this surface is energetically favored.[78] Therefore, particle impacts were measured across a long-chain layer with a positive end group but not with a negatively charged one.[99]

Beyond the surface status of the metal surfaces, the electrolyte plays a major role. It has been shown that a low concentration of co-reactands (e.g. Cl^-, Br^-, NO_3^-) impedes a fast reaction, because the diffusive flux of ions towards the particle/electrode is limited.[89,100,101] Likewise, the same was found for water/alcohol mixtures, where the bulkier solvation molecules restricted the influx of anions causing a broadening of the current peak.[102] The oxidation was further shown to be affected by the pH value of the electrolyte. Here, alkaline solutions lead to a drastic increase the detection yield by lowering the particle adsorption energy at the electrode and supporting the dissolution of the reaction products.[94] In contrast, incomplete dissolution can contaminate the electrode surface with residual AgO_x or $AgCl$ thereby affecting subsequent particle oxidation.[97,103–105]

In a typical detection experiment, the silver nanoparticles are suspended at pM concentrations
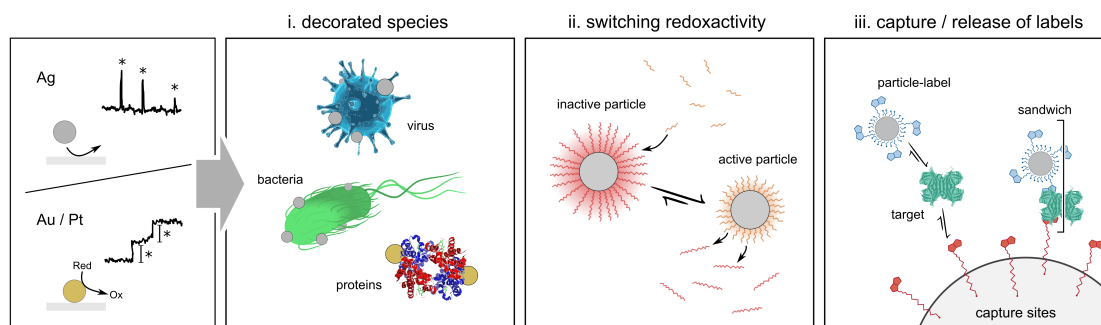
Figure 3.2 Strategies to transfer stochastic impact electrochemistry into biosensing concepts. Metallic nanoparticles offer spike-shaped (Ag, Ni, Cu) and step-like responses (Au, Pt, Pd) upon their collision with a microelectrode. There are basically three different methods, how to use nanoparticle-based detection as read-out method for other analytes: **(i)** The species of interest is decorated with the electroactive particles and its collision causes the particles to react. In these cases, the particles were mostly non-specifically adsorbed and act as simple labels. **(ii)** The particles are specifically coated, such that in case of an interaction with the analyte the redoxactivity of the particles is either switched on or off. Ligand exchange or particle aggregation upon analyte presence are typical schemes falling into this category. Here, the presence of the analyte is identified by a characteristic temporal change in the impact frequency. **(iii)** The particles are specifically coated, yet the coating is not altered when the analyte is present. Such particles can be integrated in classical assay, as they are able to specifically attach to the analyte (sandwich assay) or the receptor species (competitive assay). The concentration of the analyte is inferred from the left-over or competitively displaced particles hitting the electrodes.

within a electrolyte solution of moderate ionic strength, mostly between 20 mM and 30 mM. Decreasing the concentration of negatively charged anions in the electrolyte can adversely affect the detection yield, while high concentrations of anions can cause the nanoparticles to irreversibly aggregate and adsorb to surfaces.[106–108] The narrow range of optimal salt concentration results in a low bulk conductivity of the electrolyte, leading to a significant potential drop in the solution, which was shown to affect the impact rate.[89]

TSilver nanoparticles have become a well-known species in the field of stochastic electrochemistry, with many studies using this model system to investigate basic mechanisms at the electrode-particle interface. With a growing understanding about its governing processes, researchers have started to apply stochastic – *discrete* – sensing of nanoparticles to other analytes.

3.2 (Bio)Sensing via Stochastic Electrochemistry

To date, the majority of biosensors continue to rely on amplitude-based techniques for quantifying species concentrations in solution. However, this approach comes with several challenges, primarily due to a low signal-to-noise ratio. For instance, the limit of detection is often poor, because a few analyte molecules can be obscured by background noise in the signal amplitude. In contrast, stochastic electrochemical sensing offers in theory a high signal-to-noise ratio, an exceedingly low limit of detection, and a high sensitivity.[4,109]

In the absence of an electroactive species, the amperometric current signal exhibits only a background current noise. For instance, this work typically measured background noise on the order of 10 pA peak-to-peak for disk electrodes with a diameter of $\sim$ 10 μm and an amplifier system with 3.4 kHz bandwidth. The presence of a species is discernible, when a single entity collides with the microelectrode, as it induces a distinctive current perturbation. The magnitude of the perturbation resulting from an particle collision scales with its size, yielding a current signal of $\sim$ 1 nA for a 40 nm particle, thereby being 100 times higher than the background noise. In this context, quantifying species concentrations essentially means *counting* discrete events. Since particle collisions follow on average continuum mass-transfer laws, their number of collisions within a given time frame yields a concentration estimation. Interestingly, higher statistical validity can
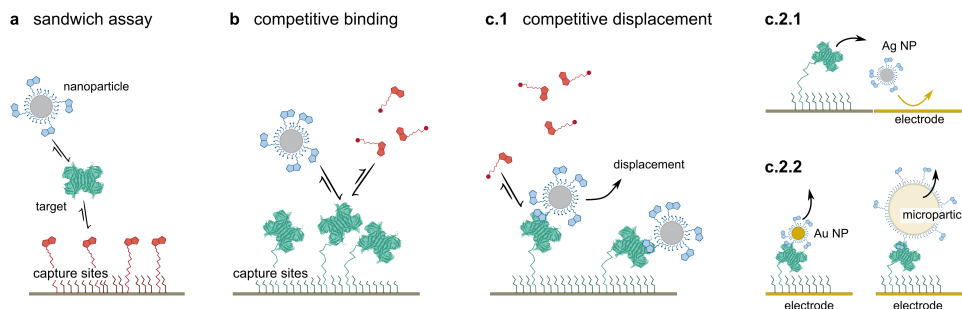
Figure 3.3   **Integration of impact-electrochemistry using specifically-coated particles (a)** The nanoparticle acts as a label for the receptor-target complex. The impacts from left-over particles can be used to construct a calibration curve. **(b)** In a competitive binding assay, the particle-label and the target molecule are both present in solution and compete for a fixed number of binding sites. **(c.1)** Whereas in a competitive displacement assay, the particle is bound at the receptor prior to the detection. Then, target molecules from solution can displace the particle labels. In general, the particle-based immunoassays are not restricted to the detection of silver nanoparticles. The readout of the displacement could be done by three different impact methods, for instance. **(c.2.1)** Via silver nanoparticles. The released silver nanoparticle moves in solution and gets detected at nearby detection electrodes. **(c.2.1)** Via the release of either catalytic nanoparticles or blocking spheres. The displacement of the label is monitored directly, if the receptor is immobilized on an electrode surface. Then, current steps at this electrode can be associated with the displacement event of the label. Here, the release of the catalytic gold nanoparticle leads to decreasing current steps, whereas the release of the blocking sphere would result in increasing ones.

be gained by simply extending the measurement time. In principle, even concentrations of very dilute species could be determined via first passage statistics.[19,33]

Given the promising capabilities of stochastic electrochemical sensing, it comes as no surprise that an increasing number of researchers have begun exploring its potential for detecting targets beyond the realm of nano- and microparticles.[110,111] Currently, stochastic electrochemistry is integrated into sensing applications primarily via four strategies:

(i) **Direct detection**

Species that are inherently electroactive or blocking can be detected by monitoring the induced perturbations upon their collision. This method has been successfully demonstrated for a diverse range of entities, including soft emulsion particles,[112] vesicles,[113] polymers,[114] thrombocytes,[115] cancer cells,[116] bacteria,[117–119] and viruses,[120] among others. Furthermore, characteristic perturbations in electrical signals have been observed for proteins,[121–123] and even DNA origami structures.[124] Particularly noteworthy is the detection of single enzymatic molecules based on their catalytic impacts.[125–129]

(ii) **Nonspecific decoration**

The species of interest is decorated with metallic nanoparticles that lead to the typical step- or spike-shaped signal. This strategy commonly involves only pristine particles that are non-specifically attached to the target, for example to a virus, bacteria, or cell.[130,131] Upon contact with the electrode surface, the reacting nanoparticles unveil the presence of the target entity.

(iii) **Switching redoxactivity**

Most attempts focused on modified nanoparticles, whose redoxactivity is either switched on or off, when the analyte is present. This works particularly well for the detection of miRNA or ssDNA using Au, Pt, or Pd nanoparticles being specifically functionalized with oligonucletides.[132–136] Here, the highly charged, sufficiently long oligonucleotide chains in the shell help to stabilize the particle such that it can be utilized as redox probe under physiological buffer conditions. Another example is the detection of perfluoralkyl species by their specific interaction with native citrate-capped silver particles.[137] Similar target-induced shell modifications have also been reported for other analytes, such as proteins

and viruses.[138–141] Typically, the redox activity of the nanoparticles is modulated via strand displacement, conformational changes of the ligands upon analyte-binding, or simple particle aggregation.

(iv) **Nanoparticle labels for classical assays**

An alternative strategy aims to integrate redoxactive nanoparticle-labels in traditional immunoassays, as depicted in Fig. 3.3. The nanoparticles are modified to enable them to selectively bind to and/or be released from the target species. In contrast to the previous method, the nanoparticle shells do not undergo any structural changes, but the particles are either captured or released in response to external stimuli.[142] Such particles could act as label or as competitor in sandwich and competition assays. The competitive assays are particularly interesting for the detection of small analytes. However, the design of nanoparticle labels is challenging as they have to support efficient binding and detection at the same time.

In summary, there has been growing interest in utilizing nanoelectrochemistry for sensing applications in recent years. With a deepened understanding of the fundamental principles of detection, colloidal stability, and particle functionalization, researchers have made remarkable strides in the design of ultra-sensitive sensors capable of detecting ultra-low concentrations of analytes.

4. Contributions

Over the past decade, there has been significant progress in understanding how individual nm-sized entities interact with electrified interfaces. Advanced setups combining optical or spectroscopic analysis with electrochemical readouts have helped to gain insight into the motion and transformation of single species in the vicinity of polarized electrodes. This promoted growing interest in utilizing impact electrochemistry as ultrasensitive technique to detect the presence or absence of specific species. However, a reliable detection requires optimal detection conditions concerning the electrolyte composition, the sensor design, and the species of interest.

The main focus of this research is to translate the concept of single-impact electrochemistry into a reliable sensing technique by identifying advantageous operating conditions and exploring how stochastic sensing can be integrated into existing assays. While the focus is on detecting silver nanoparticles, the achievements and findings of this work can be applied to other methods as well. First, a review of the challenges and opportunities of particle-based sensing is provided. Then, different engineering strategies for an improved detection yield are presented. Finally, the use of digital signals for biosensing applications is demonstrated within a prototype lateral flow architecture. The following chapter summarizes the main contributions for each of the publications included in this dissertation. The related Supplementary Materials to these publications can be found in Appendices A.1 to A.4. Furthermore, additional collaborative first-author contributions that are not part of this dissertation are provided in Appendices B.1 to B.3.

Opportunities and Challenges of Translating Direct Single Impact Electrochemistry to High-Throughput Sensing Applications

L.J.K. Weiß, P. Rinklin, B. Wolfrum

Synopsis

Stochastic impact electrochemistry is a promising method for analyzing very dilute species in situ. This review focuses on detecting silver nanoparticles and discusses the opportunities and challenges of applying this technique in high-throughput scenarios. Advances in clean-room technology now allow for parallel nanoelectrochemical studies by using arrays of individually-addressable electrodes ranging from micrometers to nanometers. This provides increased statistical validity and allows for multiplexed sensing. The particle collision rate is a key parameter in such experiments and it is greatly affected by the mass transfer towards the electrodes. This review highlights engineering approaches to increase the collision rate and the reliability of the experiment with particular emphasis on two aspects: particle adsorption and forced advection. Particle adsorption is problematic for chip-based measurements, because adhered nanoparticles are ultimately lost for detection. Microfluidic support is often used to improve transport towards surface-embedded sensing sites, but the positive effect might be overestimated for the classic microfluidics used in flow-over geometries. Due to the laminar flow profile, the trade-off between maximizing particle flux towards the electrodes and the capture efficiency across the channel's cross-section can be partially solved by creative design and advanced fabrication approaches. Last, this work outlines the requirements for translating an ultrasensitive electrochemical technique performed under laboratory conditions to a robust sensing method with specific purpose. Critical factors, such as colloidal stability, electrolyte composition, incomplete oxidation events, and instrumental requirements, are reviewed.

Individual Contribution

conceptualization of the work, literature review, data collection, leading role in composition and writing of the manuscript

Review Article

Opportunities and challenges of translating direct single impact electrochemistry to high-throughput sensing applications

Lennart J. K. Weiß, Philipp Rinklin and Bernhard Wolfrum

Abstract

In this review, we address the opportunities and challenges of single impact electrochemistry as a detection framework applicable beyond the research laboratory. Focusing on the direct detection of nanoparticles, we discuss several aspects essential to the transfer of this technique into applications for ultralow concentration sensing. We cover particle size–dependent sensor performance and engineering approaches for improving mass transfer via microfluidics. Furthermore, we address interfering phenomena such as aggregation, adsorption, and the effect of electrolyte composition.

Addresses

Neuroelectronics Group, Department of Electrical and Computer Engineering, Munich School of Bioengineering, Technical University of Munich, D-85748, Garching, Germany

Corresponding author: Wolfrum, Bernhard (bernhard.wolfrum@tum.de)

Keywords

Single impact electrochemistry, Direct nanoimpact method, Silver nanoparticles, Mass transfer.

Introduction

Originating from their confined dimensions, nanoparticles (NPs) exhibit special properties that render them of great interest for many applications — especially in the field of life sciences, where they have been applied, for example, in diagnosis, bioimaging, and drug delivery [1,2]. In general, a variety of techniques (optical spectroscopy, X-ray fluorescence, transmission and scattering electron microscopy, mass spectroscopy) have been used to probe the properties and interactions of NPs with their surrounding, which are essentially determined by the NPs' composition, size, shape, and concentration [3,4]. Apart from routine optical techniques that measure ensemble characteristics (e.g. dynamic light scattering and optical spectroscopy) and electron microscopy, single impact electrochemistry features a powerful framework to study NPs on a single-entity level, thus, being able to reveal information that is inaccessible to other techniques. In addition, single impact electrochemistry can be implemented in high-throughput applications because of its potential for massive upscaling by using integrated circuits.

In general, single impact electrochemistry comprises any electrochemical detection of single NPs colliding with an electrode surface. This research field rapidly gained interest in the last decade and is currently divided into four main approaches: probing NPs via direct impacts, current-blocking impacts, current-amplification impacts, and mediated faradaic impacts [5–9]. In this review, we focus on the direct nanoimpact method, where a characteristic reaction of single NPs is detected. This method is particularly interesting for the determination of ultralow concentrations because each colliding entity causes a discrete signal. The rate of impacts reflects the concentration and is usually less affected by background drift or interference compared with concentration measurements that rely on the amplitude of the signal. The signal-to-noise ratio is mainly governed by the acquisition time, and lower limits of detection can be achieved by extending the duration of the measurement or optimizing the particle flux toward the electrodes.

To perform a direct nanoimpact measurement, an electrode in contact with a sample solution is biased to a potential where reduction/oxidation takes place. Although other approaches are possible [10,11], the potential is commonly selected such that the reaction is mass transfer controlled. Microscopically, the NP firstly reaches the electron tunneling distance and subsequently a Faradaic reaction causes a measurable charge transfer. The resulting current signal, refer Figure 1 A and B, can be analyzed to estimate the underlying NP concentration by counting the number of recorded spikes (Figure 1 C). In addition, the integration of each spike yields a charge distribution that can be converted

Figure 1
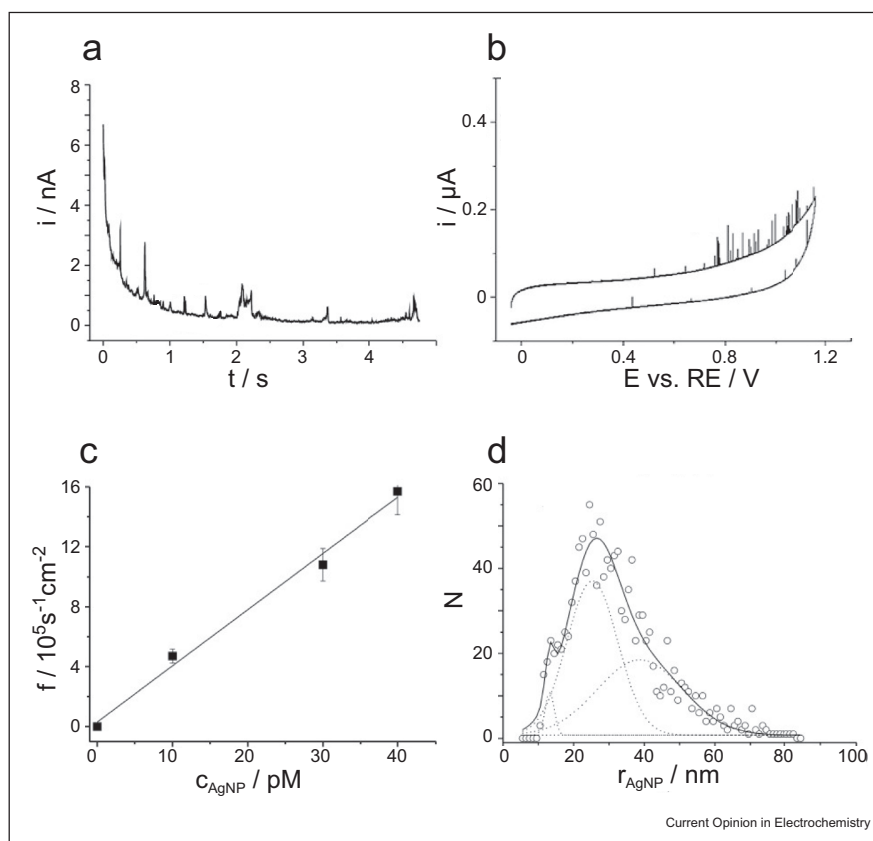
Direct nanoimpact method. **(a)** Chronoamperometric detection of silver nanoparticles (AgNPs) in citrate solution at a glassy carbon electrode with r_{el} = 11μm. **(b)** AgNP impacts in a cyclic voltammetry measurement for c_p = 12Pm in 20 mm KCl at a carbon microdisk with r_{el} = 20.5μm and a scan rate of 10 mVs^{-1}. **(c)** Calibration curve showing the impact frequency as a function of NP concentration for experiments conducted as in (a). **(d)** Distribution of NP radii for experimental data from (a). (a), (c), and (d): Modified and reprinted with the permission from the study by Zhou et al [12]. Copyright 2011, Wiley-VCH. (b): Modified and reprinted with permission from the study by Ngamchuea et al [10]. Copyright 2017, Wiley-VCH. NP, nanoparticle.

to a NP size distribution (Figure 1 D) using the following formula if spherical NPs are assumed:

$$r_p = \sqrt[3]{\frac{3 M_p Q}{4\pi z F \rho_p}} \qquad (1)$$

Here, r_p is the radius of the NP, M_p the molar mass of its constituents, Q the measured charge, z the valency of the converted species, F Faraday's constant, and ρ_p the particle's mass density. Depending on the NP species, the characteristic reaction is either an oxidation, for example, for metals (Ag [12], Au [13], Ni [14], Cu [15], Pt [16], and so on), or a reduction, for example, in case of metal oxides (Fe_3O_4 [17], $LiMn_2O_4$ [18]) and halides (AgCl [19]). The method is also applied to metal complexes (prussian blue [20]), organic nanoparticles (C60 [21], indigo [22]), and redox-tagged carbon nanotubes [23] demonstrating its broad range of possible applications.

Opportunities

The direct nanoimpact method offers great potential to be transferred into high-throughput sensors beyond the laboratory: Here, electrochemical techniques could make use of microelectrode arrays [24,25] in combination with integrated circuits that allow cost-efficient, highly parallelized recordings. Implemented in biomedical [26–30] and point-of-care applications, the direct method could be, for example, used as an onsite sensing mechanism to detect pathogens [31,32] or proteins. In such scenarios, the NPs are either linked to the target species and thereby present an electroactive label or the target species itself is electroactive.

Another application is to probe the contamination of water by metal and metal oxide NPs. This opportunity is particularly interesting in the case of silver nanoparticles (AgNPs). As a result of their favorable antibacterial and anti-inflammatory activity, they have been widely used, for example, in textiles, household items, food

packaging, and biomedical applications [33]. Consequently, they are released into the environment in large quantities every year with still unidentified consequences [33]. First, attempts toward a contaminant sensor have already been made by Cheng et al [34], Stuart et al [35], and Li et al [36], who performed experiments with AgNP-spiked sea and tap water. In principle, the nanoimpact method allows inferring the NP type via sampling its characteristic redox potential. This facilitates entirely new multicontaminant detection platforms in which multiple electrodes within an array biased to different potentials enable the simultaneous detection of different contaminants.

Such a sensor requires both basic research and engineering science: Fundamental research will help to identify conditions and limitations for the applicability of the nanoimpact method by deciphering the relevant processes at the single-entity level. In addition, engineering strategies that optimize the mass transfer toward the electrodes will increase the sensor performance. We will focus on these strategies in the following and discuss the potential of specifically engineered microfluidics. Initially, we present approaches to control the NP impact rate in an ideal case. Subsequently, we discuss interfering phenomena such as adsorption, aggregation, and partial reactions, which likely affect real-world measurements.

Engineering mass transfer

Albeit rooted in an inherently stochastic process, the mean collision frequency obtained from a nanoimpact experiment follows an ensemble average predicted by classical mean-field theory. In general, the mass transfer of NPs is determined by the following formula with the superposition of diffusion, electrophoresis, and forced advection:

$$\frac{\partial c_p(x,t)}{\partial t} = -\nabla \cdot \left(j_{diff} + j_{ep} + j_{ad} \right)$$
$$= \nabla \cdot \left(D\nabla c_p - \mu_{ep}c_p\nabla\phi - c_p u_{ad} \right) \quad (2)$$

Here, c_p, j_i, D, μ_{ep}, ϕ, and u_{ad} are the particle concentration, the respective fluxes, the diffusion coefficient, the electrophoretic mobility, the applied potential, and the fluid velocity, respectively. Usually, experiments are performed at high electrolyte concentrations. This results in Debye lengths on the order of nm and hence electrophoretic effects can be neglected, that is, $j_{ep} = 0$ in the absence of externally applied fields. Without an external flow actuation, $j_{ad} = 0$ and the movement of the NPs is exclusively governed by diffusion. The average number of impacts N_{imp} at a single microdisk with radius r_{el} is given by the following equation [37], assuming purely diffusive transport and a mass transfer-limited reaction.

$$N_{imp}(\tau) = c_p N_A r_{el}^3 \left[\tau + 1.437\sqrt{\tau} + 6.567 \cdot 10^{-2}\ln(\tau) \right.$$

$$\left. + \frac{3.425 \cdot 10^{-2}}{\sqrt{\tau}} - \frac{3.349 \cdot 10^{-3}}{\tau} \right],$$

$$with \ \tau = 4D\frac{t_m}{r_{el}^2} \ and \ D = \frac{k_B T}{6\pi\eta r_p},$$

$$(3)$$

Here, t_m, N_A, k_B, T, and η are the duration of the measurement, Avogadro's constant, Boltzmann's constant, the absolute temperature, and the dynamic viscosity, respectively. As shown in Figure 2 A, the impact number is highly dependent on the particle size (approx. $N_{imp} \propto \frac{1}{r_p}$). Because smaller particles move faster than larger ones, similar concentrations of differently sized NPs are not detectable with the same signal-to-noise ratio SNR $= \sqrt{N_{imp}}$ [37]. However, this causes further ambiguities (Figure 2 B and C): Usually, the underlying NP concentrations in laboratory experiments are well known (Figure 1 C and D), and therefore, it is easy to fit the resulting distribution. But what happens if we do not know the concentration and size distribution in the sample? Then, data binning becomes important as each particle size has its own calibration curve, refer Figure 2 B, inlay. Consequently, a coarse binning required in case of only few events can lead to large estimation errors.

If we imagine a sensor designed to detect concentrations in the range of fM to pM and particle sizes from 10 nm to 100 nm [38,39], the required measurement time t_m for a fixed SNR is determined by the largest particles. But how long will such a measurement take? At relevant silver concentrations of 100ngL^{-1} [33], for instance, even fast-moving particles with $r_p = 10$nm would require $t_m > 97$hr for a SNR ≥ 2 (assuming a single microdisk with $r_{el} = 50|\mu$m). Apparently, a reliable SNR exceeds any practical measurement times for such concentrations. Clean-room and nowadays even additive manufacturing technologies allow the fabrication of microelectrode arrays which can drastically increase the sensitivity [24,40,41]. But even parallel recordings from ∼100 microelectrodes would reduce the required time only to 53min (assuming nonoverlapping depletion fields). To further push the electrode count, complementary metal−oxide−semiconductor fabrication can be used to record electrochemical signals from thousands of electrodes in parallel [42]. These architectures, however, are only beneficial as long as the individual electrodes have nonoverlapping depletion regions within the measurement time. Otherwise, they act similar to a macroscopic electrode in terms of mass transfer.

Figure 2
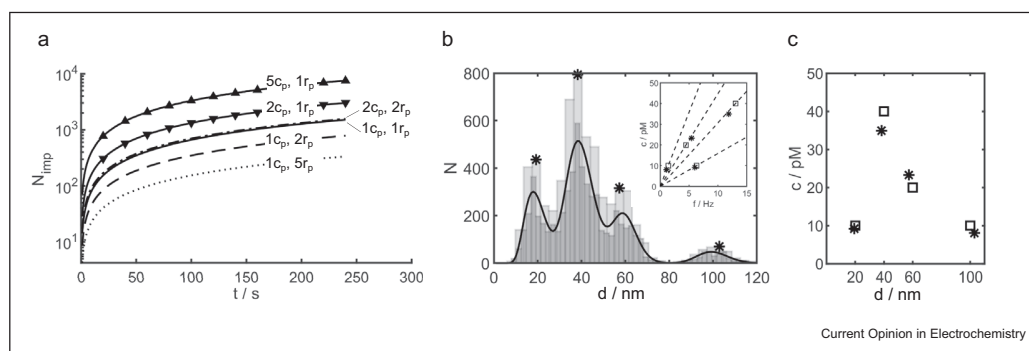
Issues in size and concentration estimation for a heterogeneous NP population. **(a)** Average number of impacts $N_{imp}(t)$ at a microdisk with $r_{el} = 10\mu m$ according to Equation (3) for different particle sizes and concentrations ($r_p = 10nm$, $c_p = 10Pm$). **(b)** Size distribution of a randomly drawn NP ensemble for two different numbers of data bins shown as light ($N_{bins} = 30$) and dark gray ($N_{bins} = 50$) columns. *Inlay* calibration curves for the data bins (*) according to Equation (3). ($t_m = 240s$, log-normal distributions, with NP diameters $d_p \in \{20, 40, 60, 100\}$ nm and concentrations $c_p \in \{10, 40, 20, 10\}$ Pm). **(c)** Estimation error of (b). The deviations between the ground truth (□) and the estimation based on B (*) arise from binning. NP, nanoparticle.

Another idea to enhance the SNR is to introduce additional particle guiding phenomena, for example, magnetism [43,44] and/or microfluidics [13,45−47]. The concept of using microfluidics to increase mass transport is not unique to single impact electrochemistry but a general strategy that has been investigated in the sensor community. Here, flow-over sensors comprising a rectangular channel and a detection site on the bottom surface, refer Figure 3 A, are very common because of their straightforward design and well-known characteristics. Advection, however, might not always be as effective as one would intuitively think: There is a trade-off between sensitivity and efficiency as — in this configuration — advection is not able to guide the particles directly toward the electrode. The last few μm typically have to be covered by diffusion. Depending on the geometry and the flow rate, there are different operational regimes according to the diffusion−advection length scale that relates the sensor-to-channel aspect ratio λ to the Peclét number Pe [48,49].

$$\zeta = \frac{l_s}{h_c} \frac{D}{u_c h_c} = \frac{\lambda}{Pe}, \tag{4}$$

Here, l_s, h_c, and u_c are the length of the electrode in flow direction, the height of the microchannel, and the average velocity, respectively. A thin depletion layer (Figure 3 B bottom) arises if $\zeta \ll 1$, for example, for a high flow rate and a small electrode. In this case, the impact frequency only scales with $f_{imp} \sim u_c^{\frac{1}{3}}$ as most of the NPs travel past the electrodes without being detected. The resulting low yield of detected NPs might be unproblematic for a water contamination sensor where the sample volume is not critical. However, a low yield can be prohibitive in case of

Figure 3
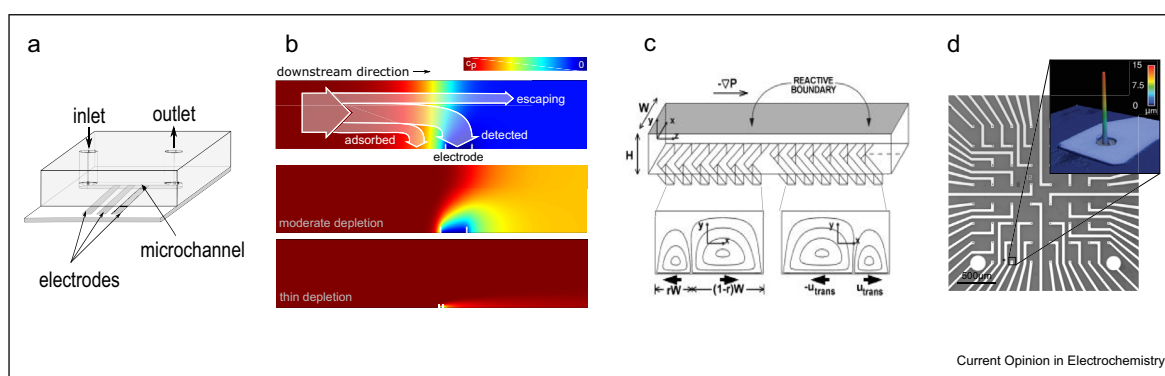
Engineered mass transfer. **(a)** Schematic of a flow-over sensor system. **(b)** Flow-over sensors can operate in different depletion regimes ranging from high efficiency (top) to high sensitivity (bottom) [48,49]. **(c)** Herringbone structures help to overcome the trade-off between efficiency and sensitivity by introducing chaotic mixing. Modified and reprinted from the study by Kirtland et al [50], with the permission of AIP Publishing. **(b)** Microelectrode arrays and three-dimensional geometries are promising approaches to enhance the sensor performance. Modified and reprinted with the permission from the study by Grob et al [40]. Copyright 2019, Wiley-VCH.

biosensor applications where only small volumes are available. The opposite holds true for an extended depletion regime, $\zeta \gg 1$ (Figure 3 B top): The absolute number of impacts is very small, but almost all particles that enter the channel will be detected — at the expense of a notably longer acquisition time.

To overcome this trade-off, passive mixing structures such as the herringbone mixer depicted in Figure 3 C can be used [51]. Their asymmetric design introduces Lagrangian chaos and leads to an extended depletion in the channel [50]. In addition, novel nanofabrication and microfabrication techniques render, for example, three-dimensional electrode arrays [40,52], refer Figure 3 D, or sieve electrodes as interesting alternatives to flow-over configurations. Furthermore, finite element simulations can be used to find an optimal set of parameters with respect to SNR and detection yield, for example, suitable ranges for the flow rate, the channel height, and the electrode dimensions [53,54].

Challenges beyond mass transfer

The framework of Equation (2) provides guidance for new sensor geometries but is based on an idealized scenario: The reaction kinetics are considered to be infinitely fast and any particle–particle or particle–wall interaction is ignored. The following section will present interfering phenomena that require consideration to implement the nanoimpact method successfully in sensing applications.

Temporal changes in the underlying NP concentration

The clustering of particles via aggregation and agglomeration is highly critical for a concentration sensor, as the total number of NPs that are available for detection will be decreased (Figure 4 A) [55]. In addition, it effectively shifts the size distribution toward larger NPs. Commonly, such colloidal instabilities are induced by a high electrolyte concentration and should be prevented or at least monitored to be accounted for in the subsequent data analysis.

Figure 4
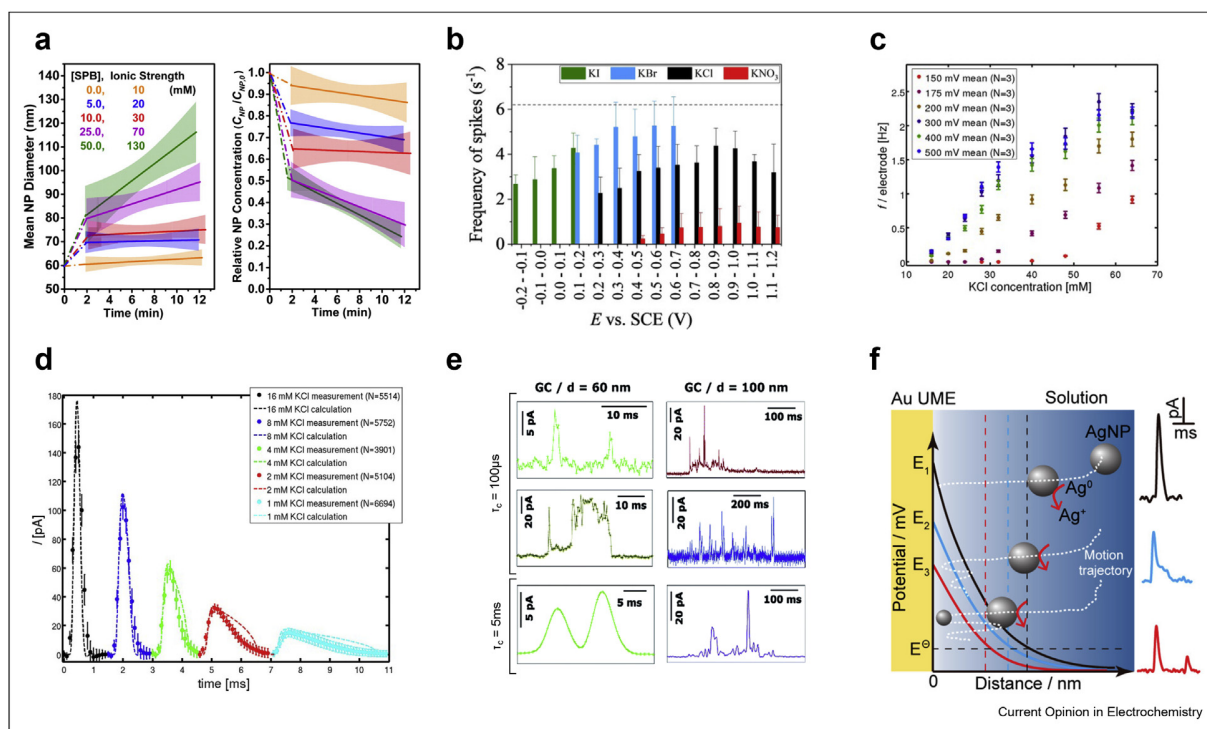
Interfering phenomena. **(a)** An increasing ionic strength leads to colloid instability. The particle size and the relative concentration of PtNPs change with respect to different concentrations of sodium phosphate buffer. **(b)** The electrolyte type affects the impact frequency of AgNPs within a cyclic voltammetry experiment ($c_p = 12$pM, $r_{el} = 20.5\mu m$, $c_e = 20$mM). **(c)** The electrolyte concentration and the oxidation potential influence the impact frequency of AgNPs ($c_p = 130$pM, $r_{el} = 12\mu m$). **(d)** The concentration of the electrolyte affects the dissolution kinetics altering the shape of the oxidation spikes ($c_p = 130$pM, $r_{el} = 12\mu m$, $c_{KCl} + c_{KNO_3} = 80$mM, $E = 0.4$V vs. Ag/AgCl). **(e)** and **(f)** Multiple partial oxidations of AgNPs at a glassy carbon electrode (GC). The current spikes are highly affected by the electronic equipment (e) and the applied potential (f). Representative current transients for NPs with $d_p = 40$nm (left) and $d_p = 100$nm (right) for different time constants τ_c of the readout circuit ($E = 0.6$V vs. Ag/AgCl, $c_{NaNO_3=50mM}$). (a): Reprinted with permission from the study by Robinson et al [55]. Copyright 2016 American Chemical Society. (b): Reprinted with permission from the study by Ngamchuea et al [10]. Copyright 2017, Wiley-VCH. (c), (d): Reprinted with permission from the study by Krause et al [59]. Copyright 2017, Wiley-VCH. (e): Reprinted under the terms of the Creative Commons Attribution 3.0. Unported Licence from the study by Ustarroz et al [60]. Copyright 2017, The Royal Society of Chemistry. (f): Reprinted and adapted with permission from the study by Ma et al [61]. Copyright 2018, American Chemical Society.

In addition to the temporal changes within the NP ensemble, adsorption of NPs can also interfere: Bound to the sensor walls, these NPs are lost for detection [56]. This drastically decreases the impact rate and can alter the sensor performance in an unpredictable fashion. While direct adsorption on the wall can be prevented by surface modifications, near-wall hindered diffusion affects the measurements in a similar way [57]. Here, the random motion of NPs close to the wall is slowed down due to their limited degrees of freedom. Similar to bulk diffusion, near-wall hindered diffusion is size-dependent in that larger particles are slowed down more effectively. Overall, the influence of such surface phenomena can be reduced by approaches that position the sensing surface in the center of the microchannel. In addition, the implementation of a sheath fluid allows focusing the NP stream [58], for example, toward the tips of 3D electrodes or to the center of a sieve electrode.

Effect of electrolyte and size-dependent reaction kinetics

The supporting electrolyte composition [10] and its concentration [59] were shown to affect the impact rate at the electrode for a given potential, refer Figure 4 B and C. In the presented experiment, higher salt contents generate higher impact rates (Figure 4 C). At the same time, however, high electrolyte concentrations can drive the system toward colloid instability. As such, a future nanoimpact-based sensor might need an upstream mixing unit that adjusts the relevant properties of the sample volume to yield efficient but stable detection. Figure 4 D illustrates how an appropriate salt concentration promotes a fast dissolution reaction [59,62], which in turn avoids the masking of NP spikes by background currents.

Starting in 2015, several groups conducted experiments that seek to unravel the reaction itself on a single-entity level: The application of ultrafast electronic readouts (Figure 4 E) and parallel optical measurements provides a deeper understanding of the processes at the interface [63−68]. These findings will ultimately help to design sensor systems because they allow, for example, adjusting the flow rate to the expected reaction rates. Nevertheless, recent work [60−70] showed that the basic assumption rendering the direct nanoimpact method so promising is indeed not always true: Depending on their size and the electrode's potential [71,61,72], the AgNPs do not always oxidize fully but undergo multiple partial oxidation events at the electrode, refer Figure 4 F. Most likely, AgNPs with a diameter $d_p < 50$nm oxidize completely during a single event, whereas larger particles experience multiple oxidations and are not converted completely [73]. Depending on hardware (Figure 4 E) [74,60] and data analysis, these partial oxidations can remain unaccounted for resulting in a major limitation of the method for fM concentration sensing.

Conclusions

The direct nanoimpact method offers a promising tool that can potentially be applied in future high-throughput applications, whenever fM concentrations are of interest. It poses high demands on read-out electronics in terms of sensitivity, noise, and sampling rate, but integrated circuits and microelectrode arrays allow highly parallelized measurements leading to reliable results within reasonable times. Furthermore, the detection limit and time scale of such measurements can be decreased by advection. In this scenario, 3D electrodes and mixing structures provide means to enhance the detection yield even further. However, the overall sensor performance is extremely sensitive to particle−particle and particle−wall interactions. Mitigating these requires an appropriate design of electrolyte composition and fluid transport. Ultimately, the straightforward analysis of individual impacts could be leveraged as an ultrasensitive method to detect arbitrary NP-labeled analytes.

Declaration of Competing Interest

The authors declare that they have no known competing financial interests or personal relationships that could have appeared to influence the work reported in this paper.

Acknowledgement

References

1. McNamara K, Tofail SAM: **Nanoparticles in biomedical applications**. *Adv Phys X* 2017, **2**:54−88, https://doi.org/10.1080/23746149.2016.1254570.

2. De M, Ghosh PS, Rotello VM: **Applications of nanoparticles in biology**. *Adv Mater* 2008, **20**:4225−4241, https://doi.org/10.1002/adma.200703183.

3. Modena MM, Rühle B, Burg TP, Wuttke S: **Nanoparticle characterization: what to measure?** *Adv Mater* 2019, **31**:1901556, https://doi.org/10.1002/adma.201901556.

4. Mourdikoudis S, Pallares RM, Thanh NTK: **Characterization techniques for nanoparticles: comparison and complementarity upon studying nanoparticle properties**. *Nanoscale* 2018, **10**:12871−12934, https://doi.org/10.1039/C8NR02278J.

5. Quinn BM, van't Hof PG, Lemay SG: **Time-resolved electrochemical detection of discrete adsorption events**. *J Am Chem Soc* 2004, **126**:8360−8361, https://doi.org/10.1021/ja0478577.

6. Xiao X, Bard AJ: **Observing single nanoparticle collisions at an ultramicroelectrode by electrocatalytic amplification**. *J Am Chem Soc* 2007, **129**:9610−9612, https://doi.org/10.1021/ja072344w.

7. Sokolov SV, Eloul S, Kätelhön E, Batchelor-McAuley C, Compton RG: **Electrode-particle impacts: a users guide**. *Phys Chem Chem Phys* 2017, **19**:28−43, https://doi.org/10.1039/C6CP07788A.

8. Xu W, Zou G, Hou H, Ji X: **Single particle electrochemistry of collision**. *Small* 2019, **15**:1804908, https://doi.org/10.1002/smll.201804908.

9. Goines S, Dick JE: **Electrochemistry's potential to reach the ultimate sensitivity in measurement science**. *J Electrochem Soc* 2020, **167**, 037505, https://doi.org/10.1149/2.0052003JES.

10. Ngamchuea K, Clark ROD, Sokolov SV, Young NP, Batchelor-McAuley C, Compton RG: **Single oxidative collision events of silver nanoparticles: understanding the rate-determining chemistry**. *Chemistry â€" A European Journal* 2017, **23**: 16085–16096, https://doi.org/10.1002/chem.201703591.

11. Figueiredo PG, Grob L, Rinklin P, Krause KJ, Wolfrum B: **On-chip stochastic detection of silver nanoparticles without a reference electrode**. *ACS Sens* 2018, **3**:93–98, https://doi.org/10.1021/acssensors.7b00559.

12. Zhou Y-G, Rees NV, Compton RG: **The electrochemical detection and characterization of silver nanoparticles in aqueous solution**. *Angew Chem Int Ed* 2011, **50**:4219–4221, https://doi.org/10.1002/anie.201100885.

13. Ogończyk D, Gocyla M, Andryszewski T, Opallo M: **Continuous electrochemical detection of gold nanoparticles in flow**. *Electroanalysis* 2017, **29**:1934–1940, https://doi.org/10.1002/elan.201700188.

14. Zhou Y-G, Haddou B, Rees NV, Compton RG: **The charge transfer kinetics of the oxidation of silver and nickel nanoparticles via particle–electrode impact electrochemistry**. *Phys Chem Chem Phys* 2012, **14**:14354–14357, https://doi.org/10.1039/C2CP42940C.

15. Haddou B, Rees NV, Compton RG: **Nanoparticle–electrode impacts: the oxidation of copper nanoparticles has slow kinetics**. *Phys Chem Chem Phys* 2012, **14**:13612–13617, https://doi.org/10.1039/C2CP42585H.

16. Jung SY, Joo JW, Kwon SJ: **Observation of blip response in a single Pt nanoparticle collision on a Cu ultramicroelectrode**. *Bull Kor Chem Soc* 2016, **37**:349–354, https://doi.org/10.1002/bkcs.10682.

17. Tschulik K, Haddou B, Omanović D, Rees NV, Compton RG: **Coulometric sizing of nanoparticles: cathodic and anodic impact experiments open two independent routes to electrochemical sizing of Fe$_3$O$_4$ nanoparticles**. *Nano Research* 2013, **6**:836–841, https://doi.org/10.1007/s12274-013-0361-3.

18. Zampardi G, Batchelor-McAuley C, Kätelhön E, Compton RG: **Lithium-ion-transfer kinetics of single LiMn$_2$O$_4$ particles**. *Angew Chem Int Ed* 2017, **56**:641–644, https://doi.org/10.1002/anie.201610485.

19. Yakushenko A, Mayer D, Buitenhuis J, Offenhäusser A, Wolfrum B: **Electrochemical artifacts originating from nanoparticle contamination by Ag/AgCl quasi-reference electrodes**. *Lab Chip* 2014, **14**:602–607, https://doi.org/10.1039/C3LC51029H.

20. Zampardi G, Sokolov SV, Batchelor-McAuley C, Compton RG: **Potassium (de-)insertion processes in prussian blue particles: ensemble versus single nanoparticle behaviour**. *Chemistry A European Journal* 2017, **23**:14338–14344, https://doi.org/10.1002/chem.201703175.

21. Stuart EJE, Tschulik K, Batchelor-McAuley C, Compton RG: **Electrochemical observation of single collision events: fullerene nanoparticles**. *ACS Nano* 2014, **8**:7648–7654, https://doi.org/10.1021/nn502634n.

22. Cheng W, Batchelor-McAuley C, Compton RG: **Organic nanoparticles: mechanism of electron transfer to indigo nanoparticles**. *ChemElectroChem* 2014, **1**:714–717, https://doi.org/10.1002/celc.201300233.

23. Holdynski M, Dolinska J, Opallo M: **Electrochemical behaviour of suspended redox-tagged carbon nanotubes at a rotating disc electrode**. *Electrochem Commun* 2019, **99**:32–35, https://doi.org/10.1016/j.elecom.2018.12.014.

24. Krause KJ, Yakushenko A, Wolfrum B: **Stochastic on-chip detection of subpicomolar concentrations of silver nanoparticles**. *Anal Chem* 2015, **87**:7321–7325, https://doi.org/10.1021/acs.analchem.5b01478.

25. Moazzenzade T, Huskens J, Lemay SG: **Stochastic electrochemistry at ultralow concentrations: the case for digital sensors**. *Analyst* 2020, **145**:750–758, https://doi.org/10.1039/C9AN01832H.

26. Lin C, Kätelhön E, Sepunaru L, Compton RG: **Understanding single enzyme activity via the nano-impact technique**. *Chem Sci* 2017, **8**:6423–6432, https://doi.org/10.1039/C7SC02084H.

27. Karimi A, Hayat A, Andreescu S: **Biomolecular detection at ssdna-conjugated nanoparticles by nano-impact electrochemistry**. *Biosens Bioelectron* 2017, **87**:501–507, https://doi.org/10.1016/j.bios.2016.08.108.

28. Andreescu D, Kirk KA, Narouei FH, Andreescu S: **Electroanalytic aspects of single-entity collision methods for bioanalytical and environmental applications**. *ChemElectroChem* 2018, **5**:2920–2936, https://doi.org/10.1002/celc.201800722.

29. Albrecht T, Horswell S, Allerston L, Rees N, Rodriguez P: **Electrochemical processes at the nanoscale**. *Current Opinion in Electrochemistry* 2018, **7**:138–145, https://doi.org/10.1016/j.coelec.2017.11.016.

30. Castañeda AD, Robinson DA, Stevenson KJ, Crooks RM: **Electrocatalytic amplification of dna-modified nanoparticle collisions via enzymatic digestion**. *Chem Sci* 2016, **7**:6450–6457, https://doi.org/10.1039/C6SC02165D.

31. Sepunaru L, Tschulik K, Batchelor-McAuley C, Gavish R, Compton RG: **Electrochemical detection of single e. coli bacteria labeled with silver nanoparticles**. *Biomaterials Sci* 2015, **3**:816–820, https://doi.org/10.1039/C5BM00114E.

32. Dick JE: **Electrochemical detection of single cancer and healthy cell collisions on a microelectrode**. *Chem Commun* 2016, **52**:10906–10909, https://doi.org/10.1039/C6CC04515D.

33. McGillicuddy E, Murray I, Kavanagh S, Morrison L, Fogarty A, Cormican M, Dockery P, Prendergast M, Rowan N, Morris D: **Silver nanoparticles in the environment: sources, detection and ecotoxicology**. *Sci Total Environ* 2017, **575**:231–246, https://doi.org/10.1016/j.scitotenv.2016.10.041.

34. Cheng W, Stuart EJE, Tschulik K, Cullen JT, Compton RG: **A disposable sticky electrode for the detection of commercial silver NPs in seawater**. *Nanotechnology* 2013, **24**:505501, https://doi.org/10.1088/0957-4484/24/50/505501.

35. Stuart EJE, Tschulik K, Omanović D, Cullen JT, Jurkschat K, Crossley A, Compton RG: **Electrochemical detection of commercial silver nanoparticles: identification, sizing and detection in environmental media**. *Nanotechnology* 2013, **24**: 444002, https://doi.org/10.1088/0957-4484/24/44/444002.

36. Li X, Batchelor-McAuley C, Compton RG: **Silver nanoparticle detection in real-world environments via particle impact electrochemistry**. *ACS Sens* 2019, **4**:464–470, https://doi.org/10.1021/acssensors.8b01482.

37. Eloul S, Kätelhön E, Batchelor-McAuley C, Tschulik K, Compton RG: **Diffusional impacts of nanoparticles on microdisc and microwire electrodes: the limit of detection and first passage statistics**. *J Electroanal Chem* 2015, **755**:136–142, https://doi.org/10.1016/j.jelechem.2015.07.042.

38. Bartlett TR, Sokolov SV, Compton RG: **Electrochemical nanoparticle sizing via nano-impacts: how large a nanoparticle can be measured?** *ChemistryOpen* 2015, **4**:600–605, https://doi.org/10.1002/open.201500061.

39. Nasir MZM, Pumera M: **Impact electrochemistry on screen-printed electrodes for the detection of monodispersed silver nanoparticles of sizes 10-107 nm**. *Phys Chem Chem Phys* 2016, **18**:28183–28188, https://doi.org/10.1039/C6CP05463C.

40. Grob L, Yamamoto H, Zips S, Rinklin P, Hirano-Iwata A, Wolfrum B: **Printed 3D electrode arrays with micrometer-scale lateral resolution for extracellular recording of action potentials**. *Advanced Materials Technologies* 2019:1900517doi, https://doi.org/10.1002/admt.201900517.

41. Martín-Yerga D: **Electrochemical detection and characterization of nanoparticles with printed devices**. *Biosensors* 2019, **9**: 47, https://doi.org/10.3390/bios9020047.

42. Dudina A, Frey U, Hierlemann A: **Carbon-nanotube-based monolithic cmos platform for electrochemical detection of neurotransmitter glutamate**. *Sensors* 2019, **19**, https://doi.org/

10.3390/s19143080. URL, https://www.mdpi.com/1424-8220/19/14/3080.

43. Yoo JJ, Kim J, Crooks RM: **Direct electrochemical detection of individual collisions between magnetic microbead/silver nanoparticle conjugates and a magnetized ultra-microelectrode**. *Chem Sci* 2015, **6**:6665–6671, https://doi.org/10.1039/C5SC02259B.

44. Robinson DA, Yoo JJ, Castañeda AD, Gu B, Dasari R, Crooks RM, Stevenson KJ: **Increasing the collision rate of particle impact electroanalysis with magnetically guided Pt-decorated iron oxide nanoparticles**. *ACS Nano* 2015, **9**:7583–7595, https://doi.org/10.1021/acsnano.5b02892.

45. Alligrant TM, Anderson MJ, Dasari R, Stevenson KJ, Crooks RM: **Single nanoparticle collisions at microfluidic microband electrodes: the effect of electrode material and mass transfer**. *Langmuir* 2014, **30**:13462–13469, https://doi.org/10.1021/la503628h.

46. Sokolov SV, Bartlett TR, Fair P, Fletcher S, Compton RG: **Femtomolar detection of silver nanoparticles by flow-enhanced direct-impact voltammetry at a microelectrode array**. *Anal Chem* 2016, **88**:8908–8912, https://doi.org/10.1021/acs.analchem.6b02670.

47. Cunningham JC, Kogan MR, Tsai Y-J, Luo L, Richards I, Crooks RM: **Paper-based sensor for electrochemical detection of silver nanoparticle labels by galvanic exchange**. *ACS Sens* 2016, **1**:40–47, https://doi.org/10.1021/acssensors.5b00051.

48. Squires T, Messinger R, Manalis S: **Making it stick: convection, reaction and diffusion in surface-based biosensors**. *Nat Biotechnol* 2008, **26**:417–426, https://doi.org/10.1038/nbt1388.

49. Amatore C, Pebay C, Sella C, Thouin L: **Mass transport at microband electrodes: transient, quasi-steady-state, and convective regimes**. *ChemPhysChem* 2012, **13**:1562–1568, https://doi.org/10.1002/cphc.201100942.

50. Kirtland JD, McGraw GJ, Stroock AD: **Mass transfer to reactive boundaries from steady three-dimensional flows in micro-channels**. *Phys Fluids* 2006, **18**, 073602, https://doi.org/10.1063/1.2222389.

51. Stroock AD, Dertinger SKW, Ajdari A, Mezić I, Stone HA, Whitesides GM: **Chaotic mixer for microchannels**. *Science* 2002, **295**:647–651, https://doi.org/10.1126/science.1066238.

52. Fritzsche J, Albinsson D, Fritzsche M, Antosiewicz TJ, Westerlund F, Langhammer C: **Single particle nanoplasmonic sensing in individual nanofluidic channels**. *Nano Lett* 2016, **16**:7857–7864, https://doi.org/10.1021/acs.nanolett.6b04124.

53. Lynn NS, Homola J: **(Bio)sensing using nanoparticle arrays: on the effect of analyte transport on sensitivity**. *Anal Chem* 2016, **88**:12145–12151, https://doi.org/10.1021/acs.analchem.6b03002.

54. Forbes TP, Kralj JG: **Engineering and analysis of surface interactions in a microfluidic herringbone micromixer**. *Lab Chip* 2012, **12**:2634–2637, https://doi.org/10.1039/C2LC40356K.

55. Robinson DA, Kondajji AM, Castañeda AD, Dasari R, Crooks RM, Stevenson KJ: **Addressing colloidal stability for unambiguous electroanalysis of single nanoparticle impacts**. *J Phys Chem Lett* 2016, **7**:2512–2517, https://doi.org/10.1021/acs.jpclett.6b01131.

56. Eloul S, Compton RG: **Shielding of a microdisc electrode surrounded by an adsorbing surface**. *ChemElectroChem* 2014, **1**:917–924, https://doi.org/10.1002/celc.201400005.

57. Eloul S, Kätelhön E, Compton RG: **When does near-wall hindered diffusion influence mass transport towards targets?** *Phys Chem Chem Phys* 2016, **18**:26539–26549, https://doi.org/10.1039/C6CP05716K.

58. Xuan X, Zhu J, Church C: **Particle focusing in microfluidic devices**. *Microfluid Nanofluidics* 2010, **9**:1–16, https://doi.org/10.1007/s10404-010-0602-7.

59. Krause KJ, Brings F, Schnitker J, Kätelhön E, Rinklin P, Mayer D, Compton RG, Lemay SG, Offenhäusser A, Wolfrum B: **The influence of supporting ions on the electrochemical detection of individual silver nanoparticles: understanding the shape and frequency of current transients in nano-impacts**. *Chemistry A European Journal* 2017, **23**:4638–4643, https://doi.org/10.1002/chem.201605924.

60. Ustarroz J, Kang M, Bullions E, Unwin PR: **Impact and oxidation of single silver nanoparticles at electrode surfaces: one shot versus multiple events**. *Chem Sci* 2017, **8**:1841–1853, https://doi.org/10.1039/C6SC04483B.

61. Ma W, Ma H, Yang Z-Y, Long Y-T: **Single Ag nanoparticle electro-oxidation: potential-dependent current traces and potential-independent electron transfer kinetic**. *J Phys Chem Lett* 2018, **9**:1429–1433, https://doi.org/10.1021/acs.jpclett.8b00386.

62. Kätelhön E, Feng A, Cheng W, Eloul S, Batchelor-McAuley C, Compton RG: **Understanding nano-impact current spikes: electrochemical doping of impacting nanoparticles**. *J Phys Chem C* 2016, **120**:17029–17034, https://doi.org/10.1021/acs.jpcc.6b04289.

63. Patel AN, Martinez-Marrades A, Brasiliense V, Koshelev D, Besbes M, Kuszelewicz R, Combellas C, Tessier G, Kanoufi F: **Deciphering the elementary steps of transport-reaction processes at individual ag nanoparticles by 3D superlocalization microscopy**. *Nano Lett* 2015, **15**:6454–6463, https://doi.org/10.1021/acs.nanolett.5b02921.

64. Brasiliense V, Berto P, Combellas C, Tessier G, Kanoufi F: **Electrochemistry of single nanodomains revealed by three-dimensional holographic microscopy**. *Accounts of Chemical Research* 2016, **49**:2049–2057, https://doi.org/10.1021/acs.accounts.6b00335.

65. Percival SJ, Zhang B: **Fast-scan cyclic voltammetry allows determination of electron-transfer kinetic constants in single nanoparticle collision**. *J Phys Chem C* 2016, **120**:20536–20546, https://doi.org/10.1021/acs.jpcc.5b11330.

66. Hao R, Fan Y, Zhang B: **Imaging dynamic collision and oxidation of single silver nanoparticles at the electrode/solution interface**. *J Am Chem Soc* 2017, **139**:12274–12282, https://doi.org/10.1021/jacs.7b06431.

67. Wonner K, Evers MV, Tschulik K: **Simultaneous opto- and spectro-electrochemistry: reactions of individual nano-particles uncovered by dark-field microscopy**. *J Am Chem Soc* 2018, **140**:12658–12661, https://doi.org/10.1021/jacs.8b02367.

68. Patrice FT, Qiu K, Ying Y-L, Long Y-T: **Single nanoparticle electrochemistry**. *Annu Rev Anal Chem* 2019, **12**:347–370, https://doi.org/10.1146/annurev-anchem-061318-114902.

69. Oja SM, Robinson DA, Vitti NJ, Edwards MA, Liu Y, White HS, Zhang B: **Observation of multipeak collision behavior during the electro-oxidation of single Ag nanoparticles**. *J Am Chem Soc* 2017, **139**:708–718, https://doi.org/10.1021/jacs.6b11143.

70. Robinson DA, Liu Y, Edwards MA, Vitti NJ, Oja SM, Zhang B, White HS: **Collision dynamics during the electrooxidation of individual silver nanoparticles**. *J Am Chem Soc* 2017, **139**:16923–16931, https://doi.org/10.1021/jacs.7b09842.

71. Saw EN, Kratz M, Tschulik K: **Time-resolved impact electro-chemistry for quantitative measurement of single-nanoparticle reaction kinetics**. *Nano Research* 2017, **10**:3680–3689, https://doi.org/10.1007/s12274-017-1578-3.

72. Mun SK, Lee S, Kim DY, Kwon SJ: **Various current responses of single silver nanoparticle collisions on a gold ultra-microelectrode depending on the collision conditions**. *Chemistry â€" An Asian Journal* 2017, **12**:2434–2440, https://doi.org/10.1002/asia.201700770.

73. Little C, Li X, Batchelor-McAuley C, Young N, Compton R: **Particle-electrode impacts: evidencing partial versus complete oxidation via variable temperature studies**. *J Electroanal Chem* 2018, **823**, https://doi.org/10.1016/j.jelechem.2018.06.050.

74. Kanokkanchana K, Saw EN, Tschulik K: **Nano impact electro-chemistry: effects of electronic filtering on peak height, duration and area**. *ChemElectroChem* 2018, **5**:3000–3005, https://doi.org/10.1002/celc.201800738.

Engineering Electrostatic Repulsion of Metal Nanoparticles for Reduced Adsorption in Single-Impact Electrochemical Recordings

L.J.K. Weiß, E. Music, P. Rinklin, L. Straumann, L. Grob, D. Mayer, B. Wolfrum
ACS Applied Nano Materials, Volume 4, July 2021
Reprinted with permission. Copyright 2021 American Chemical Society.

Synopsis

In single-impact experiments, the parameter of interest is typically the number of particle collisions registered within a given time. Thus, for very diluted species, recordings from single electrodes are subject to high uncertainty due to the stochastic nature of particle collisions. To address this issue, parallel recordings from microelectrode arrays (MEAs) can provide additional statistical validity. Nonetheless, nonspecific particle adsorption at the electrodes' surrounding can interfere with detection. One conventional method to reduce adsorption is to modify the insulating surfaces with molecules that prevent adherence by entropic effects or electrostatic interactions. However, surface functionalization that is both local and specific is challenging. The present study compares a conventional microelectrode array design with a so-called shield MEA that has an additional tunable macroscopic (shield) electrode embedded. This shield electrode surrounds all microelectrodes for detection and its tunable surface can be used to exploit electrostatic repulsion by applying an appropriate shield potential to create reflecting boundaries. The proposed concept is experimentally validated by demonstrating that the collision rate of silver nanoparticles varies for different conditions at the surrounding surface. A conventional chip using a SiO_2-layer and two shield conditions – floating and a negative potential of $-200\,\mathrm{mV}$ – were tested for negatively charged citrate-stabilized particles. The negative shield potential resulted in the highest number of impacts, whereas the floating shield electrode showed the lowest collision rate. This result can be explained by different surface charges present on the shield electrode surface. Thus, the relative differences agree well with our hypothesis. However, the experimental data substantially deviates from theoretical predictions in terms of absolute values. The analytical model based on purely diffusive transport, instantaneous reaction kinetics and non-sticky surfaces at insulating surfaces, expects two times higher collision rates. We attribute this discrepancy to impurities at the electrode surface in addition to electrolyte- and size-dependent reaction dynamics, which might affect the particle yield as well, yet are not considered in the model. In summary, the present work demonstrates that externally-controlled electrostatic repulsion can enhance the particle yield in nano-impact recordings. The implementation of a tunable surface could be an efficient and simple method to increase the performance of future impact-based sensors. Supplementary Material to this work is provided in Appendix A.1.

Individual Contribution

conceptualization of the study, data acquisition, data processing and analysis, data interpretation, leading role in composition and writing of the manuscript

Article

Engineering Electrostatic Repulsion of Metal Nanoparticles for Reduced Adsorption in Single-Impact Electrochemical Recordings

Lennart J. K. Weiß, Emir Music, Philipp Rinklin, Lea Straumann, Leroy Grob, Dirk Mayer, and Bernhard Wolfrum*

Read Online

ACCESS | Metrics & More | Article Recommendations | Supporting Information

ABSTRACT: Stochastic impact electrochemistry is a promising concept to detect ultralow concentrations of nanoparticles in solution. However, statistically reliable sensor outputs require an appropriate number of observed nanoparticle collision events. Here, arrays of individually addressable electrodes allow increasing the effective detection area, and thereby the number of collision events, without sacrificing the signal-to-noise ratio. At the same time, however, these measurements typically increase the surface-to-volume ratio of the system, leading to a stronger influence of adsorption on the number of available particles. We address this issue of nanoparticle adsorption by controlling the electrode−electrolyte interface close to the detection electrodes. We use a direct nanoimpact experiment to demonstrate that a negatively charged surface leads to electrostatic repulsion, which results in a 2.5-fold increase in the number of detected collision events. Adding to this improved sensor performance, a tunable shield electrode offers a versatile tool to study nanoparticle adsorption at the solid−liquid interface.

KEYWORDS: silver nanoparticles, stochastic single-entity electrochemistry, direct nanoimpact method, digital sensors, adsorption, electrostatic repulsion
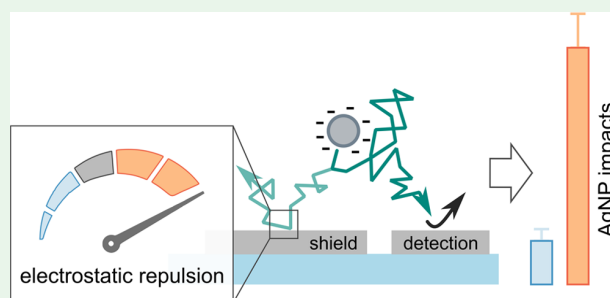
INTRODUCTION

By providing individual entities at a nm scale to be measured in situ, analytical chemistry enters the field of digital sensing with ultimate sensitivity and lowest limits of detection (LOD).[1,2] In digital sensors, the presence of a species is indicated by distinct perturbations in the signal stemming from stochastic collisions of the species with an electrode surface. Digital sensors feature several interesting properties compared with amplitude-based sensors. They offer, for instance, a clear distinction between the signal and background, a theoretical LOD of a single entity, and an increasing precision with recording time.[1] Hence, stochastic electrochemistry-based sensors could open up entirely new opportunities and may provide calibration curves at subfemtomolar levels in the future.[3−6] Recently, various groups successfully applied the concepts of stochastic electrochemistry in environmental and biosensing applications.[7−17] Particularly in diagnostics, the early detection of very dilute disease markers is of outstanding interest. However, to apply stochastic electrochemistry as a reliable digital (bio)sensor, several issues have to be addressed.[18] Strategies to incorporate specificity, for instance, are currently limited.[19] Similarly, the physicochemical properties of single nanoentities and their interaction with (metal) surfaces have to be understood to develop detection protocols and design structures that allow statistically valid outputs.[20−26] However, the absolute number of detected collisions within a typical experiment is usually limited since ultra-micro-electrodes are required to resolve individual collisions. To overcome this issue, microelectrode arrays (MEAs) that support high-density parallel recordings can be used to increase the number of collisions within a given timeframe.[27] Nevertheless, even in this case, the sensor performance depends on an efficient mass transport toward the detection sites. This can be partially achieved by providing a high supply of species from the bulk, e.g., via microfluidics or magnetic guidance.[6,28,29] Furthermore, one has to ensure that no species gets lost to detection by adhering to other surfaces. In fact, previous findings highlight the critical role of adsorption.[30,31]

Within this work, we present an innovative strategy to reduce unwanted adsorption of silver nanoparticles (AgNPs) by altering the surface charge at the solid−liquid interface close to the detection electrodes, as depicted in Figure 1a. As AgNPs exhibit a (usually negative) surface charge, their trajectory in
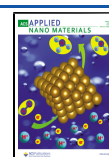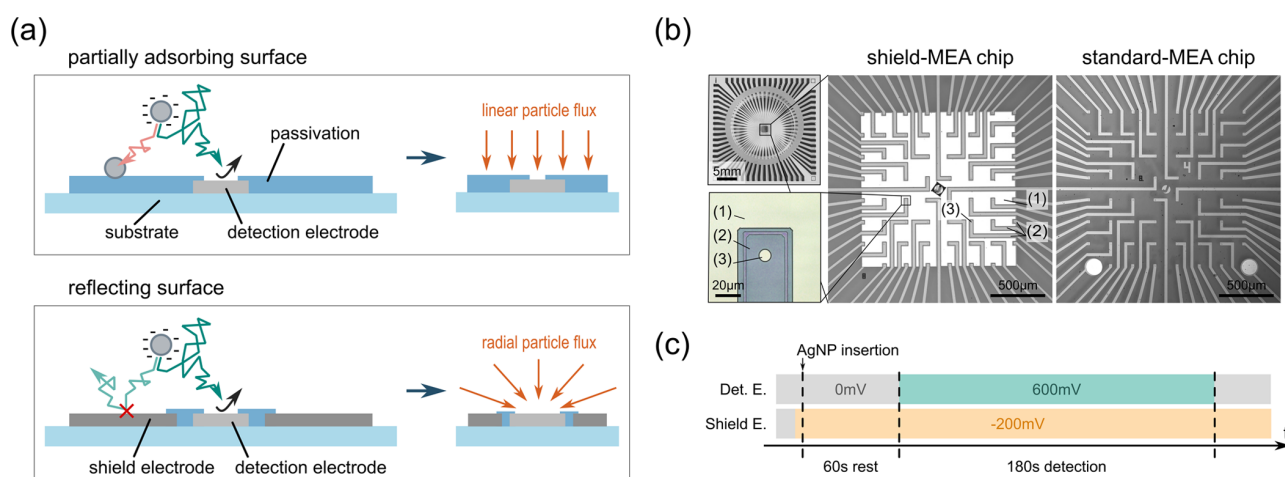
Figure 1. (a) Concept of a tunable surface that prevents the adsorption of AgNPs to yield a radial diffusive mass transport in contrast to a chip with adsorbing passivation resulting in a linear diffusion profile. (b) Images of a shield-MEA and a standard-MEA chip each consisting of 62 detection electrodes with a diameter of 8 μm. In the case of the shield-MEA chip, the detection electrodes (3) are surrounded by a 1.7×1.7 mm^2 shield electrode (1) with a 3 μm gap in between them. The gap as well as the feedlines are covered by the passivation layer (2). (c) Timeline of the experiment for a biased shield electrode.

the proximity of surfaces can be influenced by tailored coatings[32−36] that, e.g., enable electrostatic repulsion and/or steric hindrance. However, selective surface functionalization that ensures clean detection electrodes poses a challenge; in particular since in stochastic electrochemistry even minute impurities can have drastic effects.[37] Moreover, structural defects in the self-assembled monolayers, and their degradation over time, limit their positive impact on nanoparticle detection experiments. As an alternative to chemical surface modifications, an addressable metal surface can be used to control the surface potential externally. Bohn and co-workers previously reported a strong influence of static electric fields on the trajectories of AgNPs in a confined space.[38]

Here, we introduce a tunable surface by embedding an additional electrode, called the shield electrode, which surrounds the detection electrodes, as shown in Figure 1a. Thus, we are able to alter the surface charge close to the detection sites, which allows us to investigate and modulate particle adsorption. To demonstrate this effect, we record stochastic impacts of AgNPs using microelectrode arrays, as depicted in Figure 1b. Here, the random collision of a AgNP and its subsequent oxidation at an appropriately biased electrode generates a characteristic current transient.[39] Our experiment is carried out with a high-throughput amplifier system that allows recordings of 64 electrodes in parallel.[27] Furthermore, we used two different types of chips, standard-MEA chips and shield-MEA chips (see Figure 1b), each consisting of 62 platinum detection electrodes with a diameter of 8 μm.

EXPERIMENTAL SECTION

Chemicals. Acetone ($\geq$99.5%) and 2-propanol ($\geq$99.5%) were purchased from Carl Roth (Karlsruhe, Germany). Poly-(dimethylsiloxane) (PDMS) SYLGARD 184 (mixed at 10:1 w/w base/curing agent) was bought from Dow Corning (Wiesbaden, Germany). Nitric acid (HNO$_3$, 70%), potassium hydroxide (KOH, $\geq$85%), sulfuric acid (H$_2$SO$_4$, 95.0−98.0%), and silver nanoparticles (AgNPs, 0.02 mg/mL in aqueous solution, average size 20 nm, confirmed by transmission electron microscopy) were obtained from Sigma-Aldrich (St. Louis, MO). Ammonium hydroxide (NH$_4$OH,

28%) was purchased from VWR Chemicals, Fontenay-sous-Bois, France. Potassium chloride (KCl) was bought from Merck (Wiesbaden, Germany). Phosphate-buffered saline (PBS, 1$\times$) was purchased from Biochrom (Berlin, Germany) and deionized water (conductivity 0.054 μS/cm) was taken from a BerryPURE purification system (Berrytec, Harthausen, Germany).

Chip Fabrication. Both chip types (see Figure 1b) were fabricated based on standard photolithography as reported elsewhere.[40] Briefly, a stack of metal layers (5 nm Ti/200 nm Pt/5 nm Ti) was deposited onto a 500 μm-thick borosilicate wafer (SCHOTT AG, Mainz, Germany) via electron beam evaporation to create the electrode structures and feedlines. In the case of a shield-MEA chip, both the detection electrodes and the shield electrode are located in the same layer. Subsequently, the feedlines are selectively passivated with a stack of five alternating SiO$_2$ (200 nm) and Si$_3$N$_4$ (100 nm) layers (O−N−O−N−O) by plasma-enhanced chemical vapor deposition. Lastly, the detection electrodes with an 8 μm diameter are fabricated by reactive ion etching. Glass rings with a diameter of 17 mm were glued onto the chips using PDMS to serve as an electrolyte reservoir.

Single-Impact Electrochemistry Experiments. The detection of AgNPs is performed with an in-house-built 64-channel transimpedance amplifier in a two-electrode configuration as reported previously.[27] An additional potentiostat (VSP-300, BioLogic) was used to control the potential at the shield electrode in a three-electrode setup (same Ag/AgCl reference electrode, 3 M NaCl, RE-6 from BASi, coiled platinum wire as the counter electrode). The detection experiments were performed in 700 μL of 25 mM KCl electrolyte solution containing 42 pM AgNP with a diameter of 20 nm. At the beginning of each experiment (see Figure 1c) the potential at the shield electrode was set to the desired value. In the case of standard and floating shield chips, there was no potential control. Subsequently, the AgNPs were inserted and mixed three times via pipetting 500 μL in and out. After a 60 s rest time, the potential at the detection electrodes was set to 600 mV vs Ag/AgCl for 180 s.

Chip Cleaning Procedure. All other electrochemical measurements were performed with a three-electrode setup in a shielded environment using a VSP-300 potentiostat (BioLogic Instruments, France), a Ag/AgCl reference electrode (3 M NaCl, RE-6 from BASi, West Lafayette, ID), and a coiled platinum wire as the counter electrode. Prior to all detection experiments, the chips were electrochemically activated via chronoamperometry in 100 mM KOH (potential at −1.3 V vs Ag/AgCl for 120 s), followed by cyclic voltammetry in 200 mM H$_2$SO$_4$ (potential range from −0.2 to 1.5 V vs Ag/AgCl, 200 mV/s scan rate, 10 cycles). Furthermore, after each
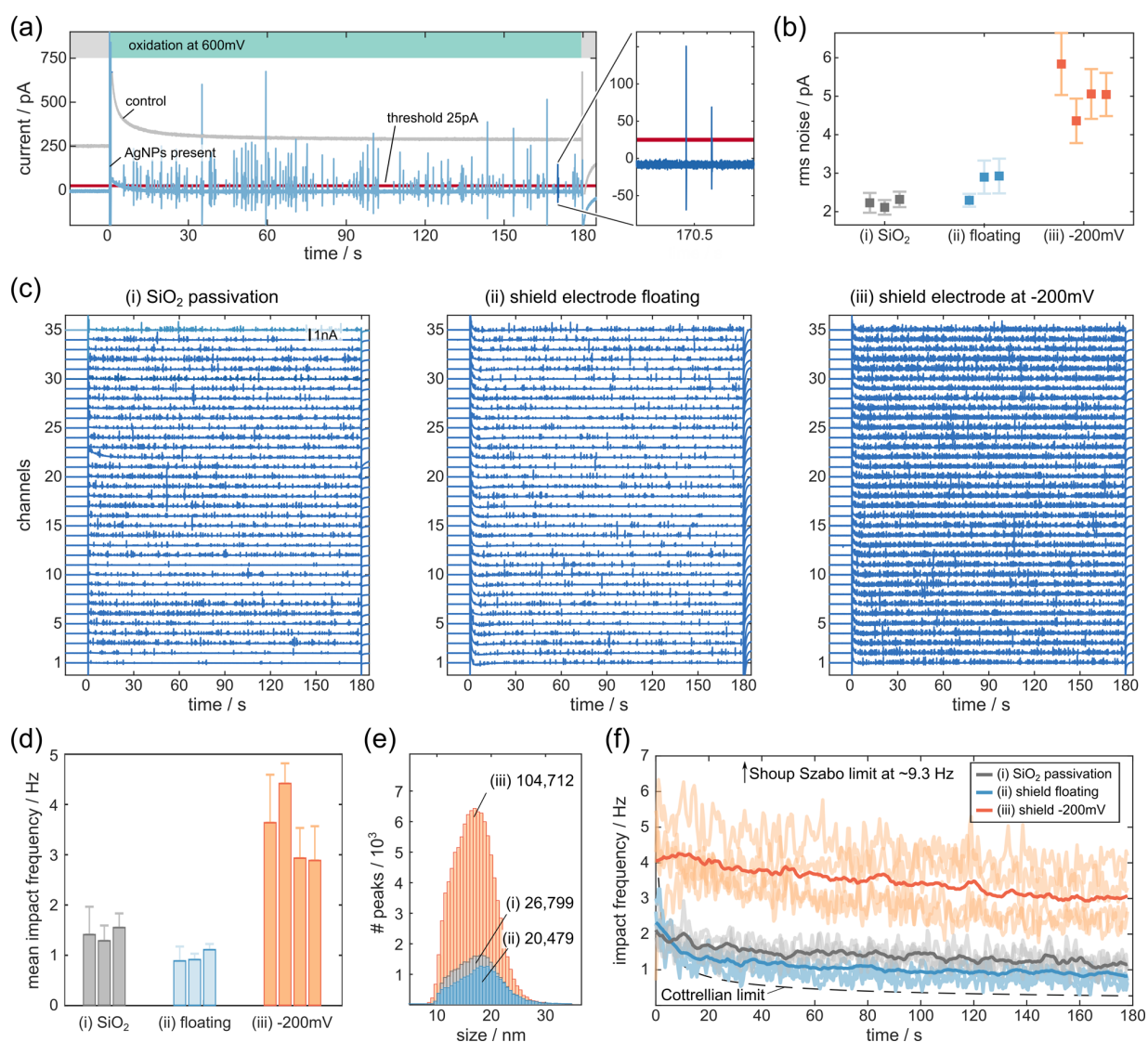
Figure 2. AgNP detection experiments using a chip with (i) SiO$_2$ passivation, (ii) a floating shield electrode, and (iii) a shield electrode at −200 mV vs Ag/AgCl. The experiments were carried out in a 25 mM KCl solution containing 43 pM AgNPs with a diameter of 20 nm. (a) Current traces of a single 8 μm electrode biased to 600 mV vs Ag/AgCl in a pure electrolyte solution (gray, offset by 250 pA for clarity) and in the presence of AgNPs (blue). All current peaks exceeding 25 pA (red) are considered as AgNP impacts. (b) Average noise levels of the detection electrodes measured at 0 mV vs Ag/AgCl. (c) Exemplary current traces of 35 microelectrodes for all three conditions. (d) Mean AgNP impact frequency per channel based on the 30 best-performing channels. (e) Summarized size distributions for all conditions shown in (d). (f) Mean temporal change in the AgNP impact frequency per channel for each condition (solid) and each trial (translucent). Each data point in (b) and (d), as well as each translucent trace in (f), corresponds to a single experiment with recordings from 30 individual electrodes. Error bars in (b) and (d) indicate standard deviations.

AgNP detection experiment, the chips were immersed in 28% NH$_4$OH and in 70% HNO$_3$ for 3 min each to remove silver chloride and silver residues.

Data Processing. The data was processed in MATLAB with a custom detection algorithm: First, nonconductive electrodes (noise below 3 pA, measured as root-mean-square current at 0 mV vs Ag/AgCl) as well as noisy channels (noise above 7 pA) were canceled and the current traces were detrended to account for the exponential relaxation. Subsequently, all current peaks exceeding 25 pA were considered further in the analysis. The absolute threshold, being larger than two times the maximum peak-to-peak noise, was chosen to reduce the influence of fabrication variations and to account for different noise levels across conditions. Additionally, a minimum interpeak distance of 25 ms was introduced to avoid amplifier-related artifacts—visible as ringing after the initial charge injection (see zoom

in Figure 2a)—from being accidentally included. For all further analyses, the 30 best-performing channels exhibiting the highest number of detected peaks were used in each experiment to minimize the effects of fabrication variations.

The AgNP sizes are calculated as follows. The deposited charge is obtained via integration of the peak with respect to the noise floor. Assuming a spherical shape, the size can be estimated via

$$r_{\mathrm{p}} = \sqrt[3]{\frac{3\,M_{\mathrm{Ag}}Q}{4\pi z F \rho_{\mathrm{Ag}}}} \tag{1}$$

where r_{p} is the radius of the AgNP, M_{Ag} is the molar mass of Ag, Q is the delivered charge, z is the valency of Ag, F is the Faraday constant, and ρ_{Ag} is the mass density of Ag.

Theoretical mass transfer limits are based on the diffusion coefficient D of the nanoparticle with a radius r_p of 10 nm. An upper bound can be determined using the Stokes−Einstein relation

$$D = \frac{k_B T}{6\pi\eta r_p} \tag{2}$$

where k_B is the Boltzmann constant, T is the absolute temperature (293 K), and η is the dynamic viscosity of the solution (1 mPas). Using eq 2, the diffusion coefficient for the AgNP is calculated to be $\sim 2.15 \times 10^{-11}$ m^2 s^{-1}.

The instantaneous impact frequency per channel was determined with a 1 s time window and a 50% overlap for each trial (translucent graphs in Figure 2f). The resulting time traces across all trials for each condition (solid graphs) were obtained by averaging across recordings and using a moving mean filter with a 20 s window. All error bars shown in the graphs indicate standard deviations. Moreover, all statements in the text regarding ensemble values refer to ensemble means and standard deviations.

■ RESULTS AND DISCUSSION

To investigate the effect of electrostatic repulsion, we compared detection experiments using a standard-MEA chip with a SiO$_2$-passivation layer on top (i) to experiments with a shield-MEA chip where the shield electrode is a floating one (ii) and where the potential is held at −200 mV vs Ag/AgCl (iii). The recordings were performed as follows (see Figure 1c). Initially, the chip was immersed in an electrolyte and, if required, the potential at the shield electrode was set. Subsequently, AgNPs were inserted and mixed, resulting in a solution finally containing 43 pM 20 nm AgNPs and 25 mM KCl. After 60 s of rest, the potential of the detection electrodes was stepped from 0 to 600 mV vs Ag/AgCl and the current was measured for 180 s. Exemplary recordings of a single microelectrode in the presence of AgNPs (blue) and in a pure electrolyte (gray, offset by 250 pA for clarity) are presented in Figure 2a.

Figure 2c depicts the i−t traces of 35 individual channels for all three conditions (i−iii). Apparently, the raw traces show a drastic increase of AgNP impacts for the shield electrode held at −200 mV vs Ag/AgCl (iii), whereas there is no clear difference between a chip with SiO$_2$ passivation (i), and a floating shield electrode (ii). Although a second electric circuit introduces a significant background noise (see Figure 2b), we ensure by a current threshold of 25 pA that the evaluated impacts can be ascribed to colliding AgNPs. We find the effect of a steered shield to be robust across different trials, as visualized in Figure 2d, where the mean impact frequency per electrode is shown. Here, a standard-MEA chip (i) leads to impact frequencies of 1.4 ± 0.1 Hz, followed by a floating electrode (ii) with slightly lower impact frequencies of 0.9 ± 0.1 Hz. In stark contrast, the frequency for a shield potential at −200 mV is 3.5 ± 0.7 Hz. Hence, the surrounding microenvironment plays indeed a critical role. We observe a clear enhancement for the shield potential at −200 mV (iii) and conclude that the negative surface charge repels the AgNPs being close to its surface. In the case of a SiO$_2$ passivation (i), we would expect a slightly negative surface charge,[41,42] whereas the floating shield electrode (ii) should initially present positive surface charges due to its open-circuit potential (OCP) at ~210 mV vs Ag/AgCl (see Supporting Information Figure S1). Consequently, the lower impact rates for a floating shield can be attributed to a loss of AgNPs in solution. This is in line with previous data, which confirms the adsorption of AgNPs on electrode surfaces via optical and electrochemical methods.[31,33] Moreover, the AgNPs might initially even become oxidized on the shield electrode, as its OCP can be higher than the oxidation potential of Ag in the electrolyte solution.[21,43] The OCP recordings in the Supporting Information Figure S1 show a drastic change from 210 to −150 mV within 300 s, indicating that the AgNPs interact with the floating shield, either via adsorption and/or oxidation.

Interestingly, this is not the case for the shield electrode under potential control in condition (iii). A stripping voltammetry recording (see Supporting Information Figure S2) subsequent to a detection experiment revealed that there was no significant electrodeposition of Ag$^+$ ions on the shield electrode surface. This finding indicates a passive role of the shield electrode.

The effect of an electrostatic repulsion for negative shield potentials is further supported by Figure 2e, depicting the AgNP size distributions obtained via integration of the delivered charge in each current spike and using eq 1, across all trials for each condition. Further statistical information of the experiments on amplitudes, durations, and the charge is provided in the Supporting Information Figure S3. Here, the mean sizes measured with a standard-MEA chip (i), a floating shield electrode (ii), and a negatively biased shield-MEA chip (iii) are 17.5 ± 3.6 nm (n = 26 799), 18.2 ± 4.3 nm (n = 20 479), and 17.0 ± 3.6 nm (n = 104 712), respectively. For the slight decrease (significance test, see the Supporting Information) in the mean particle size in the case of a negative shield potential, there are three possible reasons: First, the higher noise levels in (ii) and (iii) make it more likely that the current peak of a small AgNP exceeds the threshold as the currents superpose. Second, the higher surface charge to mass ratio could render electrostatic repulsion more effectively for smaller particles. Additionally, differently sized AgNPs do not experience the same diffusive mass transport toward the electrode because the diffusivity is reciprocal to the particle size (see eq 2 and Supporting Information Figure S4). Hence, the effect of a repelling surface would be more prominently visible for smaller particles.

Lastly, Figure 2e highlights that even small differences in the mean impact frequency (shown in Figure 2d) can lead to a substantial deviation in the absolute numbers of detected peaks, and this effect becomes considerably stronger for longer measurement times. For instance, even for a moderate experimental duration of 3 min, we observed more than 25 000 impacts for a negative shield electrode (iii), compared to ~8800 for SiO$_2$ passivation (i).

In theory, the mass transfer toward the detection electrodes can be estimated by the Shoup−Szabo equation,[44−46] which leads to the impact rate of colliding particles, dn/dt, on a disk electrode with radius r_e under diffusion-limited conditions

$$\frac{dn}{dt} = 4Dcr_e N_A f(\tau) \tag{3}$$

with

$$\tau = 4Dt r_e^{-2}$$

and

$$f(\tau) = 0.7854 + 0.8862\,\tau^{-1/2} + 0.2146\,e^{-0.7854\tau^{-1/2}}$$

where D is the diffusion coefficient, c is the species concentration, N_A is Avogadro's number, and τ is the

nondimensional time. However, its underlying assumptions of infinitely fast reaction kinetics and a nonsticky passivation render it only a theoretical upper limit.[46] Contrarily, for a fully adsorbing passivation, the Cottrell equation can be used to predict the impact rate of colliding particles

$$\frac{dn}{dt} = c\pi r_e^2 N_A \sqrt{\frac{D}{\pi t}} \qquad (4)$$

Hence, we expect a mean impact rate of ∼9.3 Hz in the case of a nonsticky and ∼0.5 Hz for a fully adsorbing passivation. As provided in Figure 2f, the impact frequency for all experiments ranges between these theoretical limits throughout the recordings. Even in the case of a floating shield electrode (ii) where we assume particle consumption, we find the mean frequency of ∼1 Hz to be higher than the Cottrellian limit. This difference could be caused by additional mass transfer phenomena, such as convection, electromigration, and diffusiophoresis, which might lead to a preconcentration of nanoparticles.[47,48] Contrarily, the measured impact frequency for a negative shield potential (iii) with ∼4 Hz is only half as high as that predicted by Shoup and Szabo. A possible contribution for the deviation in this case might be overlapping diffusion fields. However, we find the mean displacement of a 20 nm AgNP to be ∼70 μm for 240 s and the electrodes feature a spacing of 200 μm. Furthermore, the discrepancy may be explained by our simplified models, since there are a variety of processes governing the individual trajectories and redox characteristics of AgNPs, which are not covered.[49,50] Among others, near-wall hindered or limited diffusion, slower reaction kinetics, and transport phenomena of the supporting ions were shown to have a substantial influence on the outcome by altering the impact rate.[21,23,25,38,51−57] Interestingly, the instantaneous impact frequency for a negative shield electrode (iii) also decreases with time, indicating again that either the shield is not fully repelling or a second mechanism renders AgNP oxidation less likely. Indeed, it has been reported that barely soluble residues of AgCl and AgO$_x$ stemming from previous collisions or unreacted AgNPs may stay on the electrode surface.[21,55,58] This could decrease the electroactive area during the experiment (see also Figure S5).[59] Lastly, although small, a slight drift toward aggregation might also affect the impact rate at a longer time duration (see Figure S6).[60]

CONCLUSIONS

In conclusion, we demonstrated that the mass transport of AgNP toward the detection electrodes is highly affected by the surrounding microenvironment. By the integration of a tunable shield electrode, we are able to create negative surface charges at nondetection sites, which allows us to increase the mean impact frequency by a factor of 2.5 for a negative shield electrode compared to a chip with standard SiO$_2$ passivation. Herein, we could detect more than 25 000 peaks within a single 3 min experiment showing the great potential of an engineered electrode−electrolyte interface. However, results deviating from simple mass transfer models indicate that AgNP impacts are governed by complex interactions of several phenomena. Ultimately, high-throughput recordings and tailored mass transport may provide means to push the performance of digital sensors toward previously unattained areas.

ASSOCIATED CONTENT

Supporting Information

The Supporting Information is available free of charge at https://pubs.acs.org/doi/10.1021/acsanm.1c01507.

Additional details are provided as mentioned below: open-circuit potential (OCP) measurements of a floating shield electrode; anodic stripping voltammetry recordings for a shield electrode after the detection experiment; statistical information on peak amplitudes, durations, and charge; significance test for size distributions acquired from different passivation conditions; particle-size-dependent diffusive mass transfer; effect of silver chloride residues on cleaning procedure and AgNP detection experiments; and UV−vis and DLS measurements of AgNPs in KCl solution (PDF)

AUTHOR INFORMATION

Corresponding Author

Bernhard Wolfrum − *Neuroelectronics, Munich School of Bioengineering, Department of Electrical and Computer Engineering, Technical University of Munich, 85748 Garching, Germany;* orcid.org/0000-0003-4438-3755; Email: bernhard.wolfrum@tum.de

Authors

Lennart J. K. Weiß − *Neuroelectronics, Munich School of Bioengineering, Department of Electrical and Computer Engineering, Technical University of Munich, 85748 Garching, Germany;* orcid.org/0000-0002-6943-737X

Emir Music − *Neuroelectronics, Munich School of Bioengineering, Department of Electrical and Computer Engineering, Technical University of Munich, 85748 Garching, Germany;* orcid.org/0000-0002-1583-7597

Philipp Rinklin − *Neuroelectronics, Munich School of Bioengineering, Department of Electrical and Computer Engineering, Technical University of Munich, 85748 Garching, Germany;* orcid.org/0000-0003-1063-8342

Lea Straumann − *Neuroelectronics, Munich School of Bioengineering, Department of Electrical and Computer Engineering, Technical University of Munich, 85748 Garching, Germany;* orcid.org/0000-0003-4939-8526

Leroy Grob − *Neuroelectronics, Munich School of Bioengineering, Department of Electrical and Computer Engineering, Technical University of Munich, 85748 Garching, Germany;* orcid.org/0000-0002-2696-7725

Dirk Mayer − *Institute of Biological Information Processing, Bioelectronics (IBI-3), Forschungszentrum Jülich, 52425 Jülich, Germany;* orcid.org/0000-0003-1296-8265

Complete contact information is available at:
https://pubs.acs.org/10.1021/acsanm.1c01507

Author Contributions

L.J.K.W., P.R., and B.W. designed the study. L.J.K.W., L.S., and E.M. carried out the experiments. L.J.K.W. wrote the manuscript with support from P.R., D.M., and B.W. All authors provided critical feedback and helped shape the research.

Notes

The authors declare no competing financial interest.

■ ABBREVIATIONS

KCl, potassium chloride
AgNP, silver nanoparticles
SiO_2, silicon dioxide
MEA, microelectrode array
AgCl, silver chloride
AgO_x, silver oxide
NH_4OH, ammonium hydroxide
HNO_3, nitric acid
H_2SO_4, sulfuric acid
KOH, potassium hydroxide

■ REFERENCES

(1) Goines, S.; Dick, J. E. Review—Electrochemistry's Potential to Reach the Ultimate Sensitivity in Measurement Science. *J. Electrochem. Soc.* **2019**, *167*, No. 037505.

(2) Moazzenzade, T.; Huskens, J.; G Lemay, S. Stochastic Electrochemistry at Ultralow Concentrations: The Case for Digital Sensors. *Analyst* **2020**, *145*, 750−758.

(3) Yoo, J. J.; Anderson, M. J.; Alligrant, T. M.; Crooks, R. M. Electrochemical Detection of Insulating Beads at Subattomolar Concentration via Magnetic Enrichment in a Microfluidic Device. *Anal. Chem.* **2014**, *86*, 4302−4307.

(4) Yoo, J. J.; Kim, J.; Crooks, R. M. Direct Electrochemical Detection of Individual Collisions between Magnetic Microbead/Silver Nanoparticle Conjugates and a Magnetized Ultramicroelectrode. *Chem. Sci.* **2015**, *6*, 6665−6671.

(5) Boika, A.; Bard, A. J. Time of First Arrival in Electrochemical Collision Experiments as a Measure of Ultralow Concentrations of Analytes in Solution. *Anal. Chem.* **2015**, *87*, 4341−4346.

(6) Sokolov, S. V.; Bartlett, T. R.; Fair, P.; Fletcher, S.; Compton, R. G. Femtomolar Detection of Silver Nanoparticles by Flow-Enhanced Direct-Impact Voltammetry at a Microelectrode Array. *Anal. Chem.* **2016**, *88*, 8908−8912.

(7) Dick, J. Electrochemical Detection of Single Cancer and Healthy Cell Collisions on a Microelectrode. *Chem. Commun.* **2016**, *52*, 10906−10909.

(8) Dick, J. E.; Hilterbrand, A. T.; Strawsine, L. M.; Upton, J. W.; Bard, A. J. Enzymatically Enhanced Collisions on Ultramicroelectrodes for Specific and Rapid Detection of Individual Viruses. *Proc. Natl. Acad. Sci. U.S.A.* **2016**, *113*, 6403−6408.

(9) Dick, J. E.; Renault, C.; Bard, A. J. Observation of Single-Protein and DNA Macromolecule Collisions on Ultramicroelectrodes. *J. Am. Chem. Soc.* **2015**, *137*, 8376−8379.

(10) Castañeda, A. D.; Brenes, N. J.; Kondajji, A.; Crooks, R. M. Detection of MicroRNA by Electrocatalytic Amplification: A General Approach for Single-Particle Biosensing. *J. Am. Chem. Soc.* **2017**, *139*, 7657−7664.

(11) Sepunaru, L.; Plowman, B. J.; Sokolov, S. V.; Young, N. P.; Compton, R. G. Rapid Electrochemical Detection of Single Influenza Viruses Tagged with Silver Nanoparticles. *Chem. Sci.* **2016**, *7*, 3892−3899.

(12) Couto, R. A. S.; Chen, L.; Kuss, S.; Compton, R. G. Detection of Escherichia Coli Bacteria by Impact Electrochemistry. *Analyst* **2018**, *143*, 4840−4843.

(13) Karimi, A.; Hayat, A.; Andreescu, S. Biomolecular Detection at SsDNA-Conjugated Nanoparticles by Nano-Impact Electrochemistry. *Biosens. Bioelectron.* **2017**, *87*, 501−507.

(14) Narouei, F. H.; Andreescu, D.; Andreescu, S. Rapid Characterization of Arsenic Adsorption on Single Magnetite Nanoparticles by Collisions at Microelectrodes. *Environ. Sci.: Nano* **2020**, *7*, 1999−2009.

(15) Andreescu, D.; Kirk, K. A.; Narouei, F. H.; Andreescu, S. Electroanalytic Aspects of Single-Entity Collision Methods for Bioanalytical and Environmental Applications. *ChemElectroChem* **2018**, *5*, 2920−2936.

(16) Stuart, E. J. E.; Rees, N. V.; Cullen, J. T.; Compton, R. G. Direct Electrochemical Detection and Sizing of Silver Nanoparticles in Seawater Media. *Nanoscale* **2013**, *5*, 174−177.

(17) Neves, M. M. P. S.; Nouws, H. P. A.; Delerue-Matos, C.; Martín-Yerga, D. Electrochemical Detection and Characterization of Nanoparticles: A Potential Tool for Environmental Purposes. *Curr. Opin. Electrochem.* **2020**, *22*, 58−64.

(18) Sekretareva, A. Single-Entity Electrochemistry of Collision in Sensing Applications. *Sens. Actuators Rep.* **2021**, *3*, No. 100037.

(19) Iglesias-Mayor, A.; Amor-Gutiérrez, O.; Costa-García, A.; de la Escosura-Muñiz, A. Nanoparticles as Emerging Labels in Electrochemical Immunosensors. *Sensors* **2019**, *19*, 5137.

(20) Krause, K. J.; Brings, F.; Schnitker, J.; Kätelhön, E.; Rinklin, P.; Mayer, D.; Compton, R. G.; Lemay, S. G.; Offenhäusser, A.; Wolfrum, B. The Influence of Supporting Ions on the Electrochemical Detection of Individual Silver Nanoparticles: Understanding the Shape and Frequency of Current Transients in Nano-Impacts. *Chem. - Eur. J.* **2017**, *23*, 4638−4643.

(21) Ngamchuea, K.; Clark, R. O. D.; Sokolov, S. V.; Young, N. P.; Batchelor-McAuley, C.; Compton, R. G. Single Oxidative Collision Events of Silver Nanoparticles: Understanding the Rate-Determining Chemistry. *Chem. - Eur. J.* **2017**, *23*, 16085−16096.

(22) Ustarroz, J.; Kang, M.; Bullions, E.; Unwin, P. R. Impact and Oxidation of Single Silver Nanoparticles at Electrode Surfaces: One Shot versus Multiple Events. *Chem. Sci.* **2017**, *8*, 1841−1853.

(23) Oja, S. M.; Robinson, D. A.; Vitti, N. J.; Edwards, M. A.; Liu, Y.; White, H. S.; Zhang, B. Observation of Multipeak Collision Behavior during the Electro-Oxidation of Single Ag Nanoparticles. *J. Am. Chem. Soc.* **2017**, *139*, 708−718.

(24) Saw, E. N.; Kratz, M.; Tschulik, K. Time-Resolved Impact Electrochemistry for Quantitative Measurement of Single-Nanoparticle Reaction Kinetics. *Nano Res.* **2017**, *10*, 3680−3689.

(25) Sundaresan, V.; Monaghan, J. W.; Willets, K. A. Visualizing the Effect of Partial Oxide Formation on Single Silver Nanoparticle Electrodissolution. *J. Phys. Chem. C* **2018**, *122*, 3138−3145.

(26) Ma, H.; Chen, J.-F.; Wang, H.-F.; Hu, P.-J.; Ma, W.; Long, Y.-T. Exploring Dynamic Interactions of Single Nanoparticles at Interfaces for Surface-Confined Electrochemical Behavior and Size Measurement. *Nat. Commun.* **2020**, *11*, No. 2307.

(27) Krause, K. J.; Yakushenko, A.; Wolfrum, B. Stochastic On-Chip Detection of Subpicomolar Concentrations of Silver Nanoparticles. *Anal. Chem.* **2015**, *87*, 7321−7325.

(28) Alligrant, T. M.; Anderson, M. J.; Dasari, R.; Stevenson, K. J.; Crooks, R. M. Single Nanoparticle Collisions at Microfluidic Microband Electrodes: The Effect of Electrode Material and Mass Transfer. *Langmuir* **2014**, *30*, 13462−13469.

(29) Robinson, D. A.; Yoo, J. J.; Castañeda, A. D.; Gu, B.; Dasari, R.; Crooks, R. M.; Stevenson, K. J. Increasing the Collision Rate of Particle Impact Electroanalysis with Magnetically Guided Pt-Decorated Iron Oxide Nanoparticles. *ACS Nano* **2015**, *9*, 7583−7595.

(30) Eloul, S.; Compton, R. G. Shielding of a Microdisc Electrode Surrounded by an Adsorbing Surface. *ChemElectroChem* **2014**, *1*, 917−924.

(31) Lemineur, J.-F.; Stockmann, T. J.; Médard, J.; Smadja, C.; Combellas, C.; Kanoufi, F. Optical Nanoimpacts of Dielectric and Metallic Nanoparticles on Gold Surface by Reflectance Microscopy: Adsorption or Bouncing? *J. Anal. Test.* **2019**, *3*, 175−188.

(32) Stuart, E. J. E.; Tschulik, K.; Ellison, J.; Compton, R. G. Improving the Rate of Silver Nanoparticle Adhesion to 'Sticky Electrodes': Stick and Strip Experiments at a DMSA-Modified Gold Electrode. *Electroanalysis* **2014**, *26*, 285−291.

(33) Tschulik, K.; Palgrave, R. G.; Batchelor-McAuley, C.; Compton, R. G. 'Sticky Electrodes' for the Detection of Silver Nanoparticles. *Nanotechnology* **2013**, *24*, No. 295502.

(34) Krause, K. J.; Adly, N.; Yakushenko, A.; Schnitker, J.; Mayer, D.; Offenhäusser, A.; Wolfrum, B. Influence of Self-Assembled Alkanethiol Monolayers on Stochastic Amperometric On-Chip Detection of Silver Nanoparticles. *Anal. Chem.* **2016**, *88*, 3632−3637.

(35) Cai, H.; Wind, S. J. Improved Glass Surface Passivation for Single-Molecule Nanoarrays. *Langmuir* **2016**, *32*, 10034−10041.

(36) Eklöf, J.; Gschneidtner, T.; Lara-Avila, S.; Nygård, K.; Moth-Poulsen, K. Controlling Deposition of Nanoparticles by Tuning Surface Charge of SiO2 by Surface Modifications. *RSC Adv.* **2016**, *6*, 104246−104253.

(37) Kätelhön, E.; Cheng, W.; Batchelor-McAuley, C.; Tschulik, K.; Compton, R. G. Nanoparticle-Impact Experiments Are Highly Sensitive to the Presence of Adsorbed Species on Electrode Surfaces. *ChemElectroChem* **2014**, *1*, 1057−1062.

(38) Fu, K.; Han, D.; Crouch, G. M.; Kwon, S.-R.; Bohn, P. W. Voltage-Gated Nanoparticle Transport and Collisions in Attoliter-Volume Nanopore Electrode Arrays. *Small* **2018**, *14*, No. 1703248.

(39) Sokolov, S. V.; Eloul, S.; Kätelhön, E.; Batchelor-McAuley, C.; Compton, R. G. Electrode−Particle Impacts: A Users Guide. *Phys. Chem. Chem. Phys.* **2017**, *19* (1), 28−43.

(40) Yakushenko, A.; Schöps, V.; Mayer, D.; Offenhäusser, A.; Wolfrum, B. On-Chip Fast Scan Cyclic Voltammetry for Selective Detection of Redox Active Neurotransmitters: Cyclic Voltammetry for Selective Detection of Redox Active Neurotransmitters. *Phys. Status Solidi A* **2014**, *211*, 1364−1371.

(41) Kokot, G.; Bespalova, M. I.; Krishnan, M. Measured Electrical Charge of SiO2 in Polar and Nonpolar Media. *J. Chem. Phys.* **2016**, *145*, No. 194701.

(42) Lowe, B. M.; Skylaris, C.-K.; Green, N. G.; Shibuta, Y.; Sakata, T. Calculation of Surface Potentials at the Silica−Water Interface Using Molecular Dynamics: Challenges and Opportunities. *Jpn. J. Appl. Phys.* **2018**, *57*, No. 04FM02.

(43) Figueiredo, P. G.; Grob, L.; Rinklin, P.; Krause, K. J.; Wolfrum, B. On-Chip Stochastic Detection of Silver Nanoparticles without a Reference Electrode. *ACS Sens.* **2018**, *3*, 93−98.

(44) Shoup, D.; Szabo, A. Chronoamperometric Current at Finite Disk Electrodes. *J. Electroanal. Chem. Interfacial Electrochem.* **1982**, *140*, 237−245.

(45) Stuart, E. J. E.; Zhou, Y.-G.; Rees, N. V.; Compton, R. G. Determining Unknown Concentrations of Nanoparticles: The Particle-Impact Electrochemistry of Nickel and Silver. *RSC Adv.* **2012**, *2*, 6879−6884.

(46) Eloul, S.; Kätelhön, E.; Batchelor-McAuley, C.; Tschulik, K.; Compton, R. G. Diffusional Impacts of Nanoparticles on Microdisc and Microwire Electrodes: The Limit of Detection and First Passage Statistics. *J. Electroanal. Chem.* **2015**, *755*, 136−142.

(47) Patel, A. N.; Martinez-Marrades, A.; Brasiliense, V.; Koshelev, D.; Besbes, M.; Kuszelewicz, R.; Combellas, C.; Tessier, G.; Kanoufi, F. Deciphering the Elementary Steps of Transport-Reaction Processes at Individual Ag Nanoparticles by 3D Superlocalization Microscopy. *Nano Lett.* **2015**, *15*, 6454−6463.

(48) Boika, A.; Bard, A. J. Electrophoretic Migration and Particle Collisions in Scanning Electrochemical Microscopy. *Anal. Chem.* **2014**, *86*, 11666−11672.

(49) Ma, W.; Ma, H.; Chen, J.-F.; Peng, Y.-Y.; Yang, Z.-Y.; Wang, H.-F.; Ying, Y.-L.; Tian, H.; Long, Y.-T. Tracking Motion Trajectories of Individual Nanoparticles Using Time-Resolved Current Traces. *Chem. Sci.* **2017**, *8*, 1854−1861.

(50) Lu, S.-M.; Peng, Y.-Y.; Ying, Y.-L.; Long, Y.-T. Electrochemical Sensing at a Confined Space. *Anal. Chem.* **2020**, *92*, 5621−5644.

(51) Defnet, P. A.; Anderson, T. J.; Zhang, B. Stochastic Collision Electrochemistry of Single Silver Nanoparticles. *Curr. Opin. Electrochem.* **2020**, *22*, 129−135.

(52) Eloul, S.; Kätelhön, E.; Compton, R. G. When Does Near-Wall Hindered Diffusion Influence Mass Transport towards Targets? *Phys. Chem. Chem. Phys.* **2016**, *18*, 26539−26549.

(53) Robinson, D. A.; Liu, Y.; Edwards, M. A.; Vitti, N. J.; Oja, S. M.; Zhang, B.; White, H. S. Collision Dynamics during the Electrooxidation of Individual Silver Nanoparticles. *J. Am. Chem. Soc.* **2017**, *139*, 16923−16931.

(54) Wonner, K.; Evers, M. V.; Tschulik, K. Simultaneous Opto- and Spectro-Electrochemistry: Reactions of Individual Nanoparticles Uncovered by Dark-Field Microscopy. *J. Am. Chem. Soc.* **2018**, *140*, 12658−12661.

(55) Hao, R.; Fan, Y.; Zhang, B. Imaging Dynamic Collision and Oxidation of Single Silver Nanoparticles at the Electrode/Solution Interface. *J. Am. Chem. Soc.* **2017**, *139*, 12274−12282.

(56) Brasiliense, V.; Patel, A. N.; Martinez-Marrades, A.; Shi, J.; Chen, Y.; Combellas, C.; Tessier, G.; Kanoufi, F. Correlated Electrochemical and Optical Detection Reveals the Chemical Reactivity of Individual Silver Nanoparticles. *J. Am. Chem. Soc.* **2016**, *138*, 3478−3483.

(57) Giorgi, F.; Coglitore, D.; Curran, J. M.; Gilliland, D.; Macko, P.; Whelan, M.; Worth, A.; Patterson, E. A. The Influence of Inter-Particle Forces on Diffusion at the Nanoscale. *Sci Rep* **2019**, *9*, No. 12689.

(58) McKelvey, K.; Robinson, D. A.; Vitti, N. J.; Edwards, M. A.; White, H. S. Single Ag Nanoparticle Collisions within a Dual-Electrode Micro-Gap Cell. *Faraday Discuss.* **2018**, *210*, 189−200.

(59) Batchelor-McAuley, C.; Ellison, J.; Tschulik, K.; L Hurst, P.; Boldt, R.; G Compton, R. In Situ Nanoparticle Sizing with Zeptomole Sensitivity. *Analyst* **2015**, *140*, 5048−5054.

(60) Robinson, D. A.; Kondajji, A. M.; Castañeda, A. D.; Dasari, R.; Crooks, R. M.; Stevenson, K. J. Addressing Colloidal Stability for Unambiguous Electroanalysis of Single Nanoparticle Impacts. *J. Phys. Chem. Lett.* **2016**, *7*, 2512−2517.

On-Chip Electrokinetic Micropumping for Nanoparticle Impact Electrochemistry

L.J.K. Weiß, E. Music, P. Rinklin, M. Banzet, D. Mayer, B. Wolfrum

Synopsis

The current investigation builds upon earlier work by exploring the impact of transport phenomena, which have not been studied previously. The proposed chip layout (of a macroscopic electrode surrounding the detection electrodes) was used to manipulate macroscopic and microscopic electrokinetic effects and examine their influence on particle trajectories. Electrokinetic transport is expected to play an active role in impact experiments, as it directly affect the particles' trajectories in solution. In this study, we demonstrate the ability to control and decouple macroscopic flows from particle detection. Our experimental setup enabled us to simultaneously monitor silver nanoparticle impacts at the detection electrodes, while altering the macroscopic flow field with the shield electrode potential. Studies with insulating microbeads revealed that the overall effect is governed by both electroosmosis and electrophoresis. Electroosmosis creates macroscopic vortices whose directional rotation is determined by the potential at the shield electrode, while electrophoresis can lead to a focusing of particles towards the detection electrodes. Thus, the overall impact of the imposed flow pattern depends on the particle's position with respect to the sensor layout. Optical data and impact recordings demonstrated that negative shield potentials caused a lateral particle supply from the adjacent area parallel to the passivation surface, which resulted in significantly enhanced collision rates for high potentials. Here, detection electrodes at the boundaries of the array exhibited the highest detection yields. On the other hand, a positive shield potential reversed the flow pattern, and particles were supplied from the bulk solution above the electrodes. At sufficiently high positive shield potentials, the shield electrode impedes detection by oxidizing the particles as well. Furthermore, the influence of the shield potential is not limited to particle transport, as it also affects the distribution of co-reactants. Interfering background reactions, such as oxygen reduction at negative potentials, can cause persistent changes in the local electrolyte composition near the electrode. In electrolytes with low ionic strength, the anion influx is critical, and secondary dependencies may be particularly significant. This study demonstrates that engineered electrokinetic flows are feasible, nonetheless, challenging to optimize. The associated Supplementary Material is provided in Appendix A.2.

Individual Contribution

conceptualization of the study, data collection via experimental work and simulation, data processing and analysis, data interpretation, leading role in composition and writing of the manuscript

On-Chip Electrokinetic Micropumping for Nanoparticle Impact Electrochemistry

Lennart J. K. Weiß, Emir Music, Philipp Rinklin, Marko Banzet, Dirk Mayer, and Bernhard Wolfrum*

Read Online

ACCESS | Metrics & More | Article Recommendations | Supporting Information

ABSTRACT: Single-entity electrochemistry is a powerful technique to study the interactions of nanoparticles at the liquid−solid interface. In this work, we exploit Faradaic (background) processes in electrolytes of moderate ionic strength to evoke electrokinetic transport and study its influence on nanoparticle impacts. We implemented an electrode array comprising a macroscopic electrode that surrounds a set of 62 spatially distributed microelectrodes. This configuration allowed us to alter the global electrokinetic transport characteristics by adjusting the potential at the macroscopic electrode, while we concomitantly recorded silver nanoparticle impacts at the microscopic detection electrodes. By focusing on temporal changes of the impact rates, we were able to reveal alterations in the macroscopic particle transport. Our findings indicate a potential-dependent micropumping effect. The highest impact rates were obtained for strongly negative macroelectrode potentials and alkaline solutions, albeit also positive potentials lead to an increase in particle impacts. We explain this finding by reversal of the pumping direction. Variations in the electrolyte composition were shown to play a critical role as the macroelectrode processes can lead to depletion of ions, which influences both the particle oxidation and the reactions that drive the transport. Our study highlights that controlled on-chip micropumping is possible, yet its optimization is not straightforward. Nevertheless, the utilization of electro- and diffusiokinetic transport phenomena might be an appealing strategy to enhance the performance in future impact-based sensing applications.
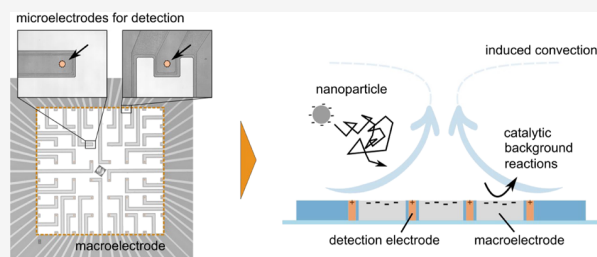
INTRODUCTION

Single-entity electrochemistry offers great opportunity to explore physicochemical characteristics at the solid−liquid interface that are typically neglected in mean-field analyses.[1−3] In particular, combined optical-electrochemical and high-resolution recordings from micro- and nanoelectrodes were able to reveal the complexity of nanoparticle (NP) interactions upon collision.[4−11] A key parameter to all impact-electrochemistry studies is the potential at the electrode interface.[12,13] It governs not only the electron-transfer kinetics within the tunneling region but also the particle trajectories in the vicinity of the electrode.[3,14−16] Here, non-negligible Faradaic processes at the electrode establish an electric field in solution and can thereby substantially influence micro- and macroscopic mass transport beyond diffusion. In general, the extent of any electric field in solution is determined by the ionic strength because the electrolyte concentration dictates both the Ohmic drop at the electrode as well as the static electrical double layer at dielectric surfaces. Electrokinetic transport becomes increasingly relevant for low-electrolyte conditions but may also affect measurements at moderate ionic strengths.[17] Especially, electrophoresis and electroosmosis are two mechanisms that may be primarily considered for a typical (nano-impact) experiment under constant potential control.[18−22] However, the background reaction at the electrode can also drive secondary phenomena, for example, diffusiopho-resis, diffusioosmosis, or catalytic micropumping, by altering the electrolyte composition close to the surface.[6,17,23−26] The complex interplay due to an intrinsic coupling by the electrical double layer is most strongly encountered in electrochemical measurements within confined spaces, and there have been attempts to facilitate enhanced signal responses via external modulation.[27−31] For instance, Bohn and co-workers investigated the impact of electroosmotic flow and externally controlled migration on analyte and particle transport within nanopore electrode arrays.[32,33] Likewise, Lemay and co-workers recently studied trajectories of insulating microparticles approaching a biased microelectrode and demonstrated that their motion is dominated by electroosmosis.[21] Although electrokinetic phenomena are proven to play an active role, they are not often utilized in analytical electrochemistry because associated ion migration and electrolysis are typically interfering.[6] However, especially in single-entity electrochemistry, it might be an appealing strategy to control
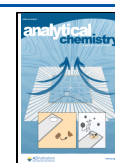
the electrokinetic transport and thus to increase the number of collisions of the species under study.[34] So far, most nano-impact studies in this regard were carried out at mediator/electrolyte concentrations ≤1 mM and investigated transport that came along with the potential used for detection.[18,21]

Complementary to the existing studies, we investigate the effect of electrokinetic transport at an intermediate ionic strength of 25 mM KCl solution. We study the occurrence and shape of electro-oxidative nano-impacts of silver nanoparticles (AgNPs) based on parallel recordings from 62 micro-electrodes. This enables us to compute ensemble character-istics that reveal information potentially hidden when considering only the motion of single particles.

The experimental control over particle transport can be realized by physically decoupling the flow control from particle detection. To this end, we introduce a second macroscopic electrode (ME, with size 1.4×1.4 mm^2) that surrounds the entire microelectrode array (MEA) and is supposed to dominate the macroscopic particle transport via its background reactions. This allows us to manipulate the electrokinetic transport via potential control of the ME while we concomitantly record nanoparticle impacts at the detection electrodes. Previous work reported a positive effect of such a ME via its ability to reduce nanoparticle adsorption typically limiting the performance of surface-based sensors.[35] The goal of the present work is to complement existing studies that focus on electrokinetically driven particle motion in low-electrolyte solution. We illustrate that, even at moderate ionic strength, electrokinetic processes do play an active role. Moreover, the concept of micropumping that is presented here could find application in digital sensors to enhance the collision rate by simple means.

■ EXPERIMENTAL SECTION

Single-Impact Electrochemistry Experiments. The MEA features 62 disk electrodes (8 μm in diameter) and a surrounding square electrode with 1.4 mm side length; see Figure S1. The electrodes are made of platinum, and the top insulating layer is SiO$_2$. Further experimental details are provided in the Supporting Information.

Prior to the impact experiments, the chips were electro-chemically cleaned in a four-step routine, which allows multiple usage of the same chip. The status of the electrodes during cleaning was assessed via cyclic voltammetry in mild H$_2$SO$_4$ solution (see Figure S2), which ensures consistent detection performance for electrodes sharing similar character-istics (see the Supporting Information).

The AgNP impact experiments were recorded with a low-noise transimpedance amplifier-system (10 kHz sampling rate per channel, 3.4 kHz bandwidth), which features parallel measurements from 62 detection electrodes in a two-electrode configuration. The potential at the ME was controlled using an additional potentiostat (VSP-300, BioLogic) in a three-electrode setup. Both systems used the same Ag/AgCl reference electrode; see Supporting Information Figure S3. If not otherwise stated, 700 μL of 25 mM KCl solution containing 100 pM AgNP (diameter of 20 nm) were used. As previously assessed, particle aggregation was not critical for our conditions.[35] Typically, the ME potential was set to an initial value of -200 mV prior to the AgNP insertion in order to reduce the effect of irreversible adsorption.[35] After 60 s of resting time, the potential at the detection electrodes was stepped to an oxidation potential of 600 mV. While concomitantly recording AgNP impacts, the ME potential was altered to modulate the background reactions, which in turn affect the macroscopic transport characteristics.

The detection experiments that were conducted under different step potentials were performed in direct succession with the following order for the ME potential steps: 0, -100, -300, -500, 50, 200, -700, -900, and 600 mV. All experiments with varying supporting electrolyte concentration were also performed in 700 μL solution volume. The alkaline solution (25 mM KCl, pH 9) was prepared by adding 5 μL of 100 mM KOH solution.

Data Processing and Analysis. The data were processed in Matlab, similar to a previous study.[35] In short, the analysis includes (i) the rejection of noisy and not well-connected electrodes, (ii) the detrending of the exponential decay after potential steps, and (iii) a peak-detection method that is based on channel-specific thresholds. To this end, the peak-to-peak noise at 0 mV, i_{pk}, was evaluated for each channel, and all current peaks that exceed the limit $0.5\ i_{pk} + 10$ pA were considered as AgNP impacts. Additional to the first current peak, the current traces show subsequent negative peaks (ringing artifacts) introduced by the amplifier system. Therefore, a minimum inter-peak distance of 10 ms was implemented to avoid misclassification. To account for fabrication differences, all further evaluations are based on a reduced dataset created from a subset of channels that typically provided the highest number of AgNP impacts (if not otherwise stated). The analysis for different ME potentials is based on a fixed subset of 18 electrodes containing equal number of inner and outer channels.

■ RESULTS AND DISCUSSION

Externally Induced Electrokinetic Transport. If we consider a typical nano-impact experiment, the oxidative dissolution of AgNPs is thermodynamically favored at potentials beyond 200 mV vs Ag/AgCl in the presence of chloride ions.[36,37] The electrode potential, however, does not only control the reaction of interest but can also influence reactions of other species — for example in aqueous solutions the reduction of dissolved oxygen, the onset of metal oxidation, and the electrolysis of water at (higher) potentials.[6,38−40] These interfering Faradaic reactions are commonly ignored as they only lead to small background currents in most cases. However, they cause an electric field in solution and thus unintentionally drive additional mass transport phenomena beyond diffusion.[6,19] For instance, Tarach and co-workers observed a substantial electroosmosic transport generated as a side effect from detection.[20] Furthermore, Lemay and co-workers illustrated the effect of *self-induced* convection on microparticle trajectories in low-electrolyte solutions.[21]

As a complement to these studies, we aim to explore the influence of *externally induced* electrokinetic transport. We achieve external control by embedding a macroelectrode (ME) — ∼38,000 times larger than the microelectrodes (Figure 1a, b) — that governs the (macroscopic) transport processes; see Supplementary Videos V1 and V2. Depending on the potential at the ME (with respect to its open circuit potential) and the electrolyte solution, different reactions can be fueled, and a background current is induced. In our case of a moderate KCl concentration, we roughly observe negative/positive ME currents for negative/positive ME potentials (see Figure S4). Thereby, we can expect to induce electric fields that either point toward or away from the ME surface.
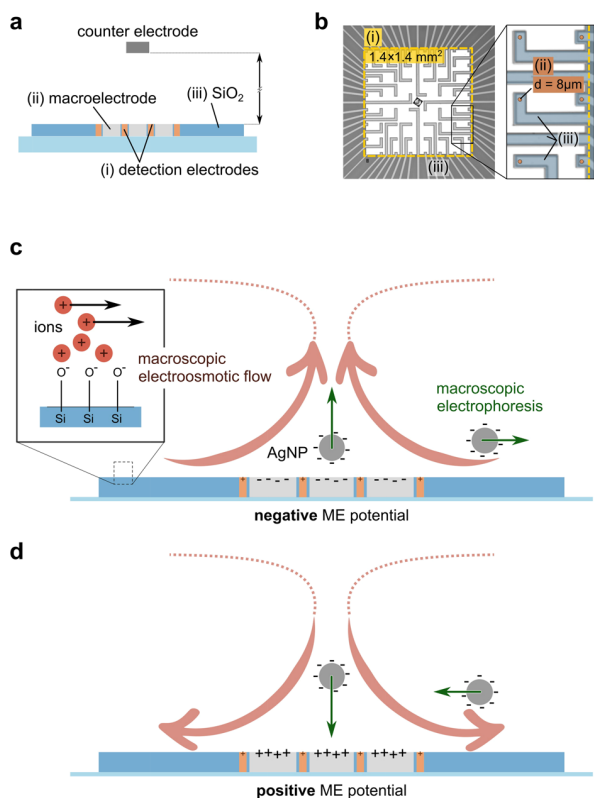
Figure 1. Macroscopic electrokinetic transport is governed by the potential at the ME. (a) Schematic and (b) top-view microscopy image of a MEA chip with a 1.4 × 1.4 mm² large ME (i, yellow) surrounding all detection electrodes. Circular detection electrodes (ii) have a diameter of 8 μm. Feedlines are covered by an insulating SiO₂-surface (iii). Effect of macroscopic electroosmosis and electrophoresis for a negative (c) and a positive (d) potential at the ME. The negative charge at the SiO₂-passivation leads to the formation of an electrical double layer. The accumulated positive charge carriers experience a force due to the electric field from the ME and generate a macroscopic electroosmotic flow. Additionally, an electric force acts on the charged particles, causing their electrophoretic attraction for a positive and their repulsion for a negative ME potential.

The electric field in solution leads to a net force on unbalanced charge densities that can drive particle motion in two different ways − via electrophoresis and/or electro-osmosis. Electrophoresis describes the movement of a charged particle due to an electric field in solution. The induced field E can be connected to the average particle velocity v_{ep} via the electrophoretic mobility μ_{ep}

$$v_{ep} = \mu_{ep} E \qquad (1)$$

The relationship between the field and the resulting particle velocity, μ_{ep}, is not trivial and challenging to predict as it critically depends on the radius of the particle r_p in relation to the thickness λ of its electrical double layer.[41] However, a qualitative picture can be gained by considering limit cases, for example, a thin electrical double layer compared to the particle size (Smoluchowski approximation). In addition to electrophoresis, the electric field also leads to electroosmotic flows, v_{eo}, by the actuation of the screening ions within the double layer next to the SiO₂-surface. Via viscous interaction, the ionic motion ultimately establishes a 3D flow field. The combination of both effects can be interpreted analogous to a swimmer within a river, where the direction of the carrying solvent flow

v_{eo} might or might not align with the direction of v_{ep}.[23] A quantitative description of the particle flux density is given by an extension of the Nernst-Planck equation, which reads

$$j = j_d + j_{ep} + j_{eo} = -D\nabla c + [v_{ep} + v_{eo}]c \qquad (2)$$

with j denoting the resulting particle flux, D the diffusion coefficient, c the particle concentration, and $v_{ep/eo}$ the particle velocities due to electrophoresis and -osmosis. Depending on the position of the particle, its charge, and the surface charge of the passivation, the potential at the ME leads to different outcomes. As shown in Figure 1c, d, both effects might point in the same or in opposite directions. In our case of negatively charged particles and a negatively charged SiO₂-insulation layer, v_{ep} and v_{eo} align in the bulk region but oppose at the chip surface.[42] Moreover, their impact varies with the strength of the electric field in solution, which in turn depends on the background reactions, the electrolyte conductivity, and the cell geometry.

To initially verify our approach of external transport control, we first studied the trajectories of dielectric microbeads (ζ-potential −9.6 ± 0.2 mV) in deionized water for high ME potentials ranging from −2 to 2 V. Our results, shown in the Supplementary Videos V1 and V2, are in line with other work at low ionic strengths[20,21] as we were able to manipulate the motion of negatively charged microbeads simply by altering the ME potential (see Figures S5 and S6).

The majority of electrochemical analyses operate at moderate electrolyte concentrations. Therefore, it is an interesting question if the previous findings are also applicable in the intermediate to the high-electrolyte regime. If so, the integration of a large ME would be an easy-to-implement approach to optimize sensor responses via micropumping. Therefore, we also studied microparticle trajectories within 25 mM KCl for high overpotentials. However, the previous effect was not retained as ME current densities on the order of 1 μA/cm² were not able to visibly govern the microparticles' trajectories. Additionally, changes in the electrical double layers at the particle (ζ-potential at 25 mM KCl −14.3 ± 1.2 mV) and the SiO₂-surface as well as promoted particle adsorption might alter the influence significantly.[42]

Manipulated AgNP Trajectories. A different, yet indirect approach to investigate the influence of externally induced electrokinetic phenomena is by means of single-impact electrochemical recordings instead of optical tracking. In the past, most research concerning this aspect has focused on blocking- or amplifying-impact experiments conducted under low ionic strength.[18,20,21] By far, less studied are electrokinetic phenomena at intermediate electrolyte concentrations, although Patel et al.[6] as well as Park et al.[19] reported significant effects in this regime. Hence, the impact method could potentially be applied to spatially sample the induced flow field.

To test our hypothesis, we conducted a highly parallelized impact experiment using 100 pM of AgNPs and 25 mM KCl because nano-impact experiments typically operate in electrolyte concentrations between 20 and 50 mM.[36,37,43] The relatively high particle concentration of 100 pM was chosen to continuously yield a high impact rate, whose temporal changes could be directly correlated with variations in the electrokinetic transport. The experiment was performed as follows: we initially applied a potential of −200 mV at the ME and injected the AgNP solution. Then, after a rest time of 60 s,
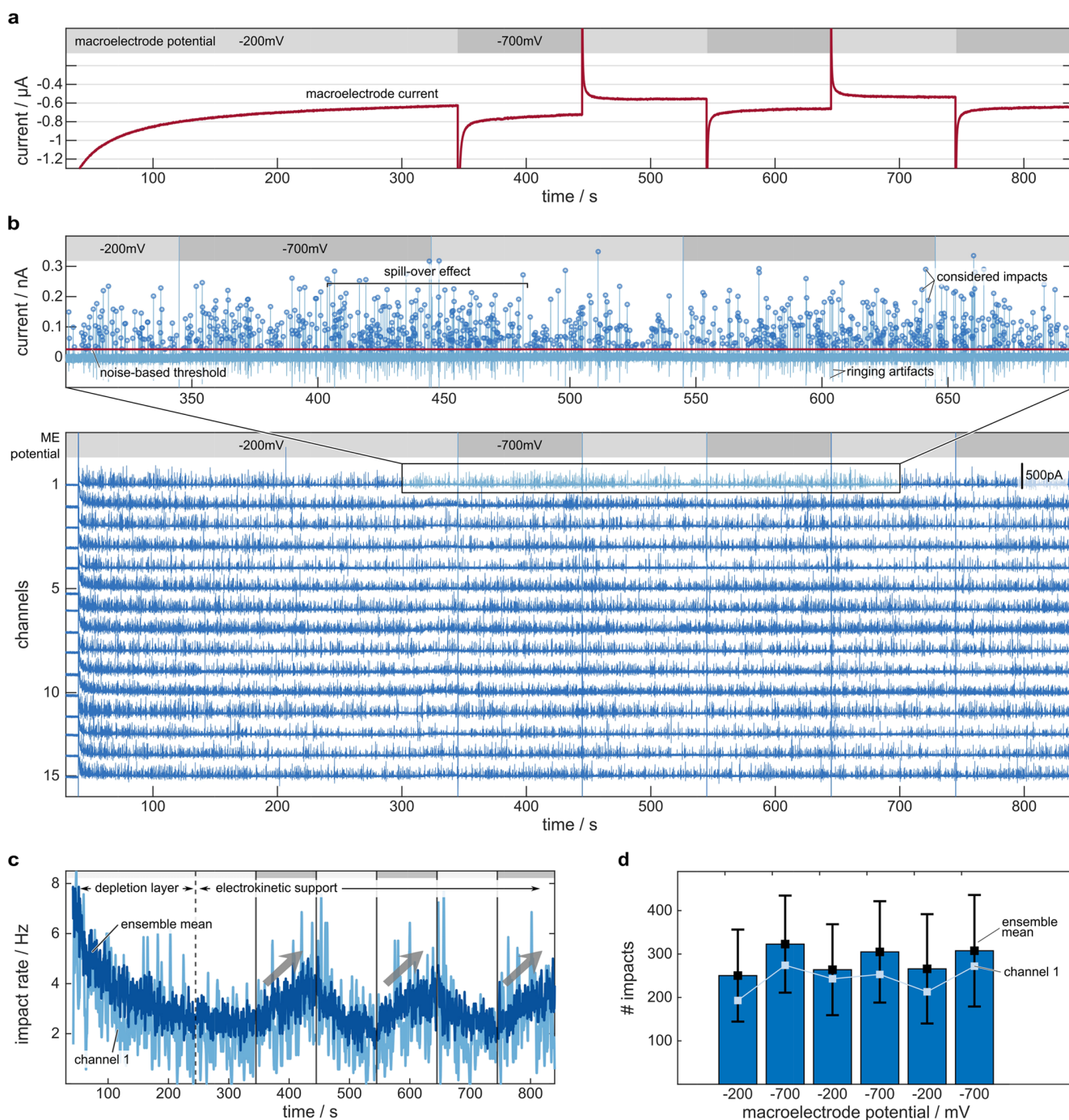
Figure 2. AgNP detection under externally induced micropumping. The potential at the ME manipulates the number of AgNP impacts on the detection electrodes. (a) Current at the ME while the ME potential is stepped between −200 and −700 mV vs Ag/AgCl. (b) Current traces from 15 detection electrodes (showing the highest number of impacts) in case of 100 pM AgNPs in 25 mM KCl. The zoom-in exemplarily depicts the channel-specific current threshold and current peaks considered for further analysis. The effect of an altered ME potential is visible, although there might be spill-over effects. It should be noted that the negative current spikes stem from amplifier-related artifacts that follow the initial charge injection. (c) Temporal evolution of the impact rate. The data are based on the electrodes shown in (b). (d) Number of impacts according to the ME potential. The graph shows the ensemble means and error bars indicate standard deviations. The analysis considers only particle impacts occurring after the initial depletion ($t > 250$ s).

the potential at the detection electrodes was stepped to an oxidation potential of 600 mV, and collisions were recorded from 62 electrodes. Concomitantly, the ME potential was altered between −200 and −700 mV every 100 s of recording; see Figure 2a. The current traces from 15 individual electrodes are depicted in Figure 2b, and further statistical data

(amplitude, duration, charge, and size distribution) are provided in Figure S7. Slightly visible in the ensemble data, but more apparent in the zoom-in for channel 1, the number of impacting particles varies in time. Initially, we observe a decreasing impact rate due to an evolving depletion layer at the vicinity of the electrodes. Afterward, we find an accumulation

of impacts for −700 mV ME potential compared to −200 mV. The effect is repeatable during the application of successive voltage steps (Figure 2c, d), and the ensemble average as well as single electrodes follow the same pattern − an increase in the impact rate for −700 mV and a decrease for −200 mV ME potential − although spill-over effects are observed in some channels' data, see, for example, Figure 2b zoom-in. In principle, there are three phenomena that could support our observations: (i) altered particle adsorption at the ME, (ii) potential-induced transport, and (iii) local changes in the electrolyte constitution affecting the oxidation kinetics.

In a previous work, we demonstrated that the adsorption of particles can be reduced via electrostatic repulsion.[35] Consequently, potential changes could modulate the adsorption of AgNPs and thereby the number of "accessible" particles during the recording. Assuming a purely diffusive transport ($D = 2.3 \times 10^{-11}$ m²/s), it would take a particle ∼4.5 s to overcome the distance between the ME and a detection electrode. Especially, at long recording times, we have to consider the evolution of a depletion layer, which is contradictory to the phenomenon shown in Figure 2c, where we do not see a diminished influence at longer times. Thus, we conclude that a purely electrostatic approach oversimplifies the situation, as the steady ME current is nonzero throughout the experiment; see Figure 2a. In fact, we most likely induce the reduction of dissolved oxygen at the platinum ME[38,39,44]

$$O_2 + 4H^+ + 4e^- \rightarrow 2H_2O$$
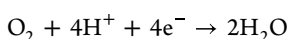
and create an electric field in solution, which potentially drives electrokinetic transport. Once, the electric field distribution is known, the electrokinetic transport could be directly predicted (for the thin-layer limit) via the Helmholtz−Smoluchowski equation,[41] which reads

$$\boldsymbol{v}_{p,\parallel} = \boldsymbol{v}_{ep} + \boldsymbol{v}_{eo} = [\mu_{ep} + \mu_{eo}]\boldsymbol{E}_\parallel = \frac{\epsilon}{\eta}(\zeta_p - \zeta_s)\boldsymbol{E}_\parallel \quad (3)$$

where $\boldsymbol{v}_{p,\parallel}$ is the particle velocity close to and in parallel to the dielectric surface, $\boldsymbol{E}_\parallel$ is the electric field parallel to the surface, η is the viscosity, ϵ is the electric permittivity in the solution, and ζ_p and ζ_s are the ζ-potentials of the particle and at the SiO₂-layer, respectively. However, estimations based on average current densities and conductivities (Ohms law) are misleading, as we expect highly heterogeneous field distributions that are established by induced chemical reactions. Furthermore, as the ME and the detection electrodes have reverse polarities − −200 mV/−700 mV and 600 mV, respectively −, the field establishes not only between the ME and the counter electrode (CE) but also strays toward the detection electrodes. Unfortunately, there is no direct experimental access to the current allocation amongst the CE and detection electrodes, which renders the calculation of the field strength based on experimental data challenging. As Kline et al. reported ionic concentration gradients to cause strong local electric fields (in the range of ∼500 V/m) during catalytic micropumping,[23,45] we assume that the field strength generated in our system is sufficient to drive local electrophoresis and -osmosis. In any case, eq 3 can still be used to estimate the relative importance of both electrokinetic effects. If we only consider particle transport to be the origin for the results in Figure 2, we have to conclude that the transport must be dominated by lateral electroosmosis because we observe an increase in impacts, even though the negatively charged particles are expected to be pushed outward by electrophoresis

(see Figure 1c). Although eq 3 is not fully applicable for a Debye length of ∼2 nm and a particle radius of 10 nm, its prediction of predominant electroosmosis ($\zeta_p = -45.7 \pm 2.2$ mV for of 25 mM KCl at pH 6, $\zeta_s \approx -60$ mV at pH 6[42]) matches well with our findings. We further performed numerical simulations in a simplified 2D-band electrode geometry that captures only major interdependencies of the chip geometry and focuses on primary effects. The results, see Figure S8, support our hypothesis of predominant electro-osmosis and an externally evoked pumping effect. Remarkably, the numerical results did not only indicate the presence of a macroscopic rotational flow field, as depicted in Figure 1c,d, but also the existence of smaller vortices induced by the SiO₂-surface around the detection electrodes.

Last, the continuous current at the ME does additionally modify the electrolyte constitution close to the detection electrodes. As H⁺ ions are consumed during the oxygen reduction reaction, we (unintentionally) manipulate the local pH-value and could thereby also alter the reaction kinetics at the detection electrodes. The depletion of H⁺ ions shifts the local pH value toward higher values and alkaline solutions were recently shown to enhance the detection rate of AgNPs.[3,46−50] A second, yet often overlooked transport phenomenon can be associated with the local Faradaic reactions because they establish a persistent concentration gradient of electrolytic ions. In our case, the local depletion of H⁺ ions at the ME and the generation of H⁺ ions at the detection electrodes (during water oxidation at the platinum surface) establishes a H⁺-gradient and could, thus, induce associated diffusiokinetic transport. In fact, Kanoufi and colleagues,[6] proposed in an experiment comparable to ours that diffusiophoresis is responsible for the propelling of particles that are close to a polarized electrode. In other research, solute concentration gradients were reported to be the origin of a plethora of fascinating phenomena, for instance, of self-propelling Janus swimmers or the levitation or separation of particles in solution, yielding diffusiokinetic velocities in the range of several 10 μm/s.[23,51−56] However, predicting the (electro-)diffusiokinetic effects is more subtle as for electrokinetic transport, especially if charged species are generated or consumed. Then, both phenomena, the electrokinetic and diffusiokinetic transport, become deeply coupled, which can lead to highly nonlinear behavior.[57−64] Therefore, it is not possible to separate both mechanisms and distinguish their isolated contributions to the particle transport. Based on our experimental findings, we hypothesize an externally induced surface-driven net transport toward the sensing area and conclude that the lateral particle supply must overcompensate electrophoretic repulsion. Then, the increase in AgNP impacts for more negative ME potentials might be attributed to the higher electric potential and the stronger H⁺-gradient tangential to the SiO₂-surface, both enhancing their convective contributions.

In terms of absolute values, however, the impact rates in Figure 2c are at all times substantially lower than expected.[65] For instance, if we assume a purely diffusive transport and a reflecting boundary, the impact rate should be ∼21 Hz according to Shoup Szabo.[66] Intuitively, one would consider even higher rates in case of additional advection. However, this reasoning is only valid for an instantaneous reaction upon collision with the microelectrode, which is only an ideal case and typically not supported by experimental data.[67,68] Moreover, particle adsorption and aggregation, as well as

electrode contamination and particle impurities play a critical role and lower the detection yield.[7,35,43]

If lateral motion primarily rules the AgNP transport, we would expect that the impact rate is dependent on the electrode position within the ME. Indeed, Figure 3 illustrates
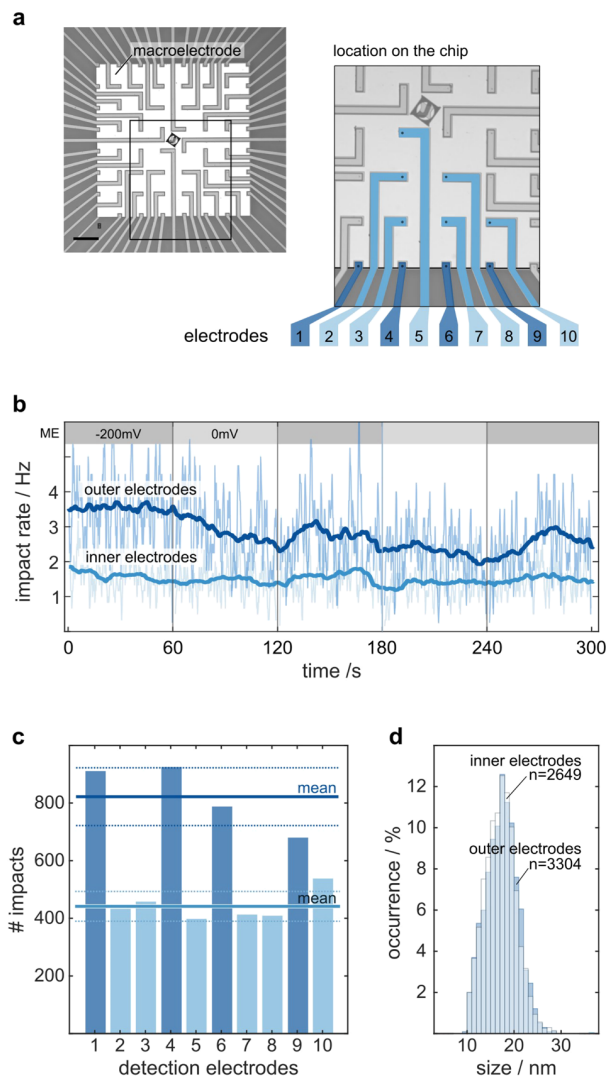

Figure 3. Position-dependent impact rates. The position of the detection electrode determines its response to different ME potentials. Lateral surface-driven flow leads to an increased detection rate at the outer electrodes. (a) Position of the detection electrodes on the chip (scale bar 250 μm). (b) Mean temporal evolution of the impact rate for the ensembles of inner and outer electrodes. (c) Number of detected peaks during the experiment. (d) Particle size distribution according to the electrode position. The distribution is calculated from all impacts at all electrodes.

such an effect. Here, we altered the ME potential (between −200 and 0 mV) and observed a significantly different response at different electrode locations; see Figure 3b, c. There are effectively two subsets of electrodes showing congruent responses. In general, outer electrodes could detect approximately twice as many AgNPs as inner ones. Moreover, a change in the ME potential is well reflected in the impact rate at outer but barely visible at the inner electrodes; see Figure 3b. To our surprise, the detected sizes also vary slightly, with the outer electrodes detecting supposedly larger particles; see

Figure 3d. A statistical analysis, see Figure S9, reveals lower amplitudes and an increased duration for impacts at the inner electrodes, which might stem from a reduced influx of chloride ions during oxidation.[37] We find further evidence for our hypothesis because more negative ME potentials also lead to smaller and slightly longer impacts (see data for −200 and 0 mV in Figure S9). A possible explanation could be the accompanying depletion of chloride ions via electrophoresis. Interestingly, Saw et al. reported similar observations — lower amplitude, extended duration of the current spike — for particle detection in water−alcohol mixtures.[69]

Influence of the Potential at the Macroelectrode. In the next experiment, we studied the influence of different ME potentials on the detection rate. Here, we chose a common potential of −200 mV at the beginning and at the end of each experiment to ensure similar conditions regarding adsorption and convection throughout the study. The temporal evolution of the impact rate (Figure 4a) and the exemplary current traces (Figure 4b) show an interesting trend. Moderate potentials between −300 and 50 mV did not significantly alter the general trend of the impact rate (within the chosen experimental time). Beyond this range, however, we observed two robust characteristics. Negative ME potentials caused a significant increase in impacts and the effect roughly scales with the current at the ME; see Figure 4c. The ME current is mainly driven by the reduction of dissolved oxygen at moderate potentials. In case of −900 mV, however, we observed a drastic increase in the ME current, as well as the impact rate, which we attributed to the onset of the hydrogen evolution reaction. A closer look at the raw data in Figure 4b illustrates also spill-over effects from one condition to the other, which we associate to inertial forces that tend to continue the previously evoked flow field. Both findings are in line with a macroscopic surface-driven convection as a major driving mechanism. Unexpectedly, more positive ME potentials also lead to increased impact rates. This is surprising because for potentials above ∼200 mV vs Ag/AgCl, the ME acts as particle sink depleting the microenvironment at the detection electrodes. The oxidation current at the ME indicates a reverse flow direction (see Figure 1d) in these cases. Hence, the convective supply and electrophoretic attraction from the bulk solution seem to (over)compensate the loss of particles due to oxidation at the ME. This hypothesis is supported by the drop in the impact rate after stepping back from a positive ME potential to −200 mV. We attribute this drop to the depletion of AgNPs in the bottom layers, which becomes apparent after reverting the flow field. The depletion for positive ME potentials is also location-dependent; see Figure S10. Again, we observed a stronger response at outer electrodes, which can be explained by the establishing flow field and a ME that competes with the inner electrodes for particle detection.

In summary, the results in Figure 4 illustrate the possibility to modulate AgNP trajectories using a macroscopic electrode. Moreover, we could clearly demonstrate the active role of background reactions driving the electrokinetic transport. Its impact, however, varies with the strength and direction of the electric field as well as the measurement time.

Effect of the Electrolyte Composition. Our results indicate strong dependence on the electrolyte composition as both the electrolyte and the ME potential govern the electric field in solution. The electrolyte does not only affect the background reactions at the ME but also the reaction kinetics
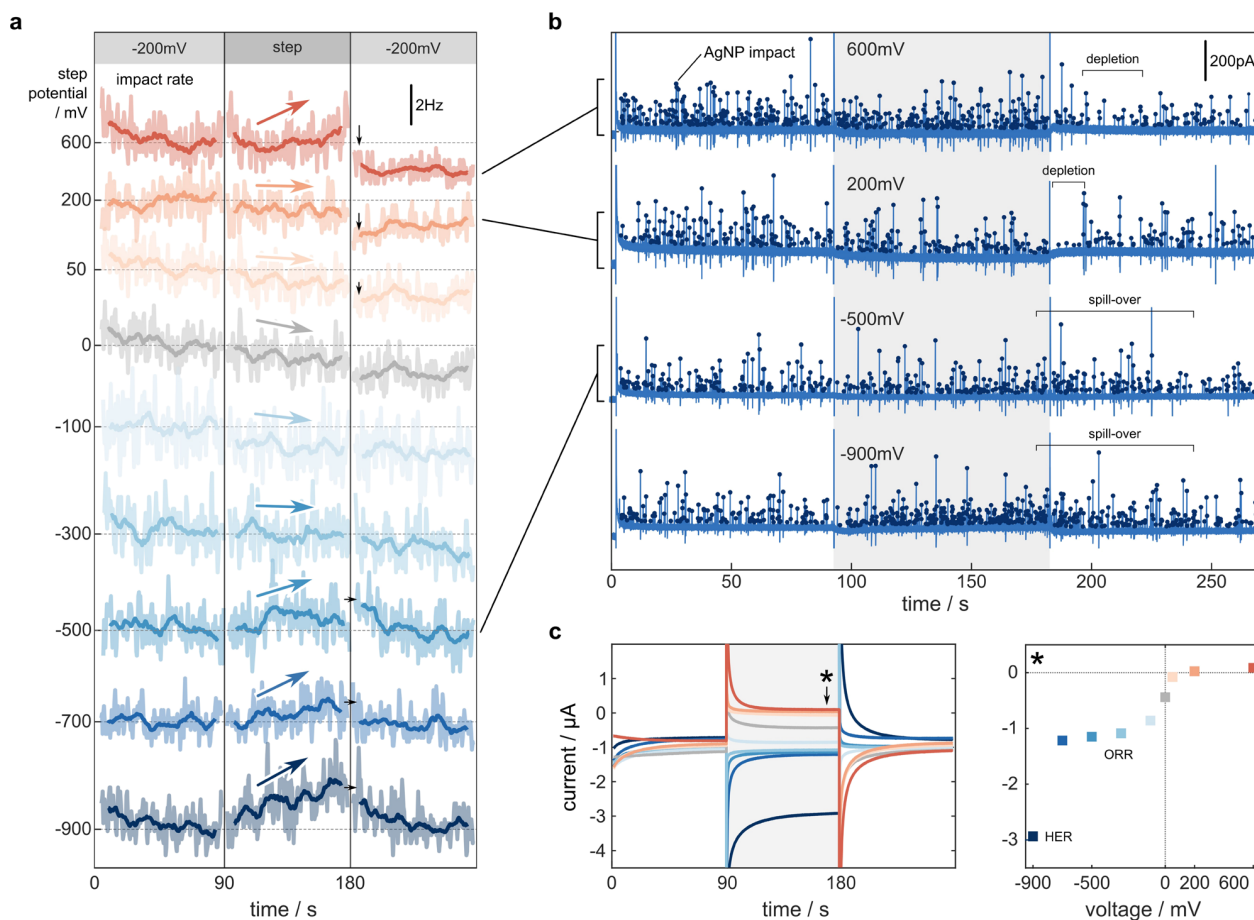
Figure 4. Influence of the potential at the ME on AgNP impacts at the detection electrodes. Background reactions at the ME determine the direction and strength of the potential and ionic gradients in solution, which govern the electro- and diffusiokinetic transport. (a) Mean temporal evolution of the impact rate for different step potentials at the ME. The data are based on a subset of 9 inner and 9 outer detection electrodes. (b) Exemplary current traces that illustrate depletion effects for positive ME potentials and spill-over effects at negative ME potentials. (c) Current at the ME for all experiments shown in (a). The oxygen reduction (ORR) determines the current for moderate negative potentials, whereas the current for −900 mV is dominated by the hydrogen evolution (HER).
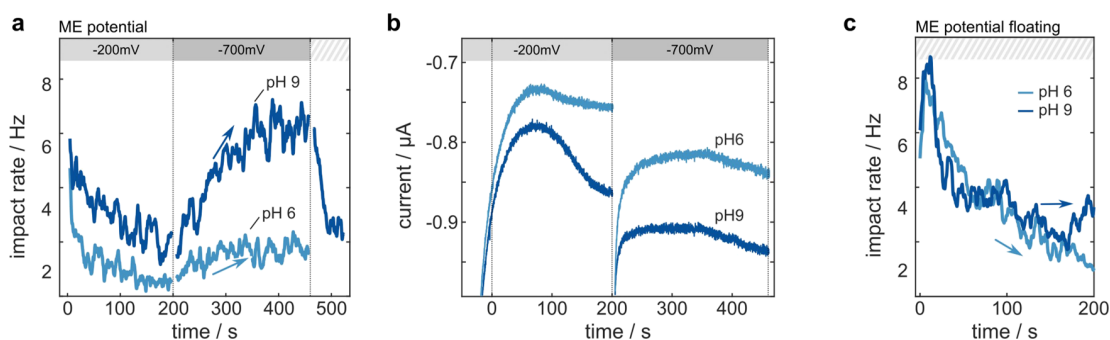
Figure 5. Effect of an alkaline electrolyte solution on the electrokinetic transport of AgNPs. There is a substantial enhancement of the impact rate at pH 9. (a) Temporal evolution of the impact rate for different pH values in case of a ME potential step from −200 to −700 mV. (b) Current at the ME reflecting the background reactions at different pH. (c) Control experiment, where the ME was not under potentiostatic control.

at the detection electrode. In fact, both the oxygen reduction reaction and the AgNP oxidation were reported to be enhanced within alkaline media, most probably due to a reduced adsorption energy and a promoted dissolution of AgCl.[3,39] Therefore, we wanted to test if a higher pH yields a more efficient transport and performed single-step experiments in 25 mM KCl at pH 6 and pH 9, as shown in Figure 5. The results are in line with our expectations and highlight the

critical role of the electrolyte composition. For instance, the impact rate at pH 9 was higher than that at pH 6 for all times. However, the drastic increase at pH 9 in case of −700 mV ME potential and its further stabilization around 6 Hz were unexpected as the particle ζ-potentials (−46 ± 2 mV for 25 mM KCl at pH 6 and −41 ± 2 mV at pH 9) as well as the ME currents were in a similar range for both pH values; see Figure 5b. Therefore, we associate the enhancement also with an

increased negative ζ-potential of the chip wall, rendering the surface-driven convection more effective.[42] The strong positive effect diminishes again after releasing the potential at the ME. This finding is supported by the control measurements shown in Figure 5c, where we recorded impacts while the ME potential was floating. The effect of pH on the impact rate is rather subtle in this case, but persisted for longer measurement times. The data indicate that the alkaline solution leads to a stabilization of the impact rate for longer times, which might be associated with a promoted dissolution of AgO_x in alkaline solutions. However, we could not observe other features attributed to AgO_x formation upon impact, like extended current tails, which Ma et al. recently reported.[3]

Our results indicate that the ME notably affects the distribution of chloride ions in solution. Further step experiments at different electrolyte concentrations (20 and 30 mM KCl, see Figure S11) confirmed this, as the outcome varied significantly for the two different chloride concentrations. Our results highlight that negative ME potentials impair the chloride flux to a point such that the initial detection rate might be significantly reduced compared to moderate potentials. In fact, other recent work highlights the crucial role of the co-reactants in impact experiments, as the reaction dynamics are very sensitive to the presence/absence of the co-species at the electrode.[70,71]

CONCLUSION AND OUTLOOK

In conclusion, we demonstrated the possibility to modulate nanoparticle trajectories via micropumping induced by a ME that controls the microenvironment around the detection electrodes. The background reactions lead to an electric field and an ionic gradient in solution that induce externally controlled convection and electro−/diffusiophoretic motion. The combined effect acting on the particle is highly position-dependent. For instance, the convective flow field establishes a vortex that points upward above the center of the ME for negative potentials. The ME potential is able to revert the flow direction and, thus, convectively supply particles either from the surrounding area close to the passivation surface − indicated by negative ME currents − or from the bulk − for positive ME currents. Interestingly, we found in both cases an increase in AgNP impacts for high potentials, although the effect was strongest for −900 mV ME potential, most likely due to the onset of the hydrogen evolution reaction. The influence of micropumping is also not uniform across the electrode ensemble. At negative potentials, we observed higher impact rates at electrodes that were located at the boundary of the ME, which indicates the surface-driven transport (e.g., electroosmosis) to be dominant. As both the potential and the electrolyte govern the pumping effect, this strategy could be appealing to optimize the mass transport by an elaborate sensor design and a careful selection of the electrolyte. Indeed, we could demonstrate that the impact rate drastically increases for experiments in alkaline solutions. However, the externally induced transport might also introduce interfering effects that thwart higher impact rates, for example, because of the depletion of co-reactants. Thus, we conclude that designing electrokinetic transport with the aim of an enhanced impact rate is challenging and requires the consideration of several interdependent processes. Here, in-depth numerical simulations might help in the design process.

Nevertheless, we provided evidence that electrokinetic transport can play an active role in impact electrochemistry

experiments, even at moderate ionic strengths. With our highly parallel recordings, we were able to investigate the phenomena under conditions typical in analytical and impact electrochemistry. Thus, the framework of a decoupled transport control and parallelized detection could be an interesting approach to study further transport phenomena as well as a promising engineering strategy for future ultrasensitive digital sensors.

ASSOCIATED CONTENT

Supporting Information

The Supporting Information is available free of charge at https://pubs.acs.org/doi/10.1021/acs.analchem.2c02017.

Details concerning the MEA chips, the cleaning routine, and the experimental setup; video recording V1 and V2 of negatively charged microparticles driven by the potential at a ME in the absence of a supporting electrolyte; cyclic voltammetry in 25 mM KCl at different pH values; statistical data including amplitude, duration and charge distributions for impact experiments shown in the manuscript; potential and velocity distributions for a simplified 2D band-electrode geometry obtained from finite-element simulations; effect of electrode location for step experiments with positive ME potentials; results for step experiments with different KCl concentrations (PDF)

Video for different ME potentials in fluorescence mode (MP4)

Zoom-in video for different ME potentials in phase-contrast mode (MP4)

AUTHOR INFORMATION

Corresponding Author

Bernhard Wolfrum − Neuroelectronics - Munich Institute of Biomedical Engineering, Department of Electrical Engineering, TUM School of Computation, Information and Technology, Technical University of Munich, Garching 85748, Germany; orcid.org/0000-0003-4438-3755; Email: bernhard.wolfrum@tum.de

Authors

Lennart J. K. Weiß − Neuroelectronics - Munich Institute of Biomedical Engineering, Department of Electrical Engineering, TUM School of Computation, Information and Technology, Technical University of Munich, Garching 85748, Germany; orcid.org/0000-0002-6943-737X

Emir Music − Neuroelectronics - Munich Institute of Biomedical Engineering, Department of Electrical Engineering, TUM School of Computation, Information and Technology, Technical University of Munich, Garching 85748, Germany; orcid.org/0000-0002-1583-7597

Philipp Rinklin − Neuroelectronics - Munich Institute of Biomedical Engineering, Department of Electrical Engineering, TUM School of Computation, Information and Technology, Technical University of Munich, Garching 85748, Germany; orcid.org/0000-0003-1063-8342

Marko Banzet − Institute of Biological Information Processing, Bioelectronics (IBI-3), Forschungszentrum Jülich, Jülich 52425, Germany

Dirk Mayer − Institute of Biological Information Processing, Bioelectronics (IBI-3), Forschungszentrum Jülich, Jülich 52425, Germany; orcid.org/0000-0003-1296-8265

Complete contact information is available at:
https://pubs.acs.org/10.1021/acs.analchem.2c02017

Author Contributions

L.J.K.W., P.R., and B.W. designed the experimental outline. M.B. fabricated the MEA devices. L.J.K.W. and E.M. performed the experiments. L.J.K.W. wrote the manuscript with support from P.R., D.M., and B.W.

■ REFERENCES

(1) Xu, W.; Zou, G.; Hou, H.; Ji, X. *Small* **2019**, *15*, No. 1804908.

(2) Brasiliense, V.; Patel, A. N.; Martinez-Marrades, A.; Shi, J.; Chen, Y.; Combellas, C.; Tessier, G.; Kanoufi, F. *J. Am. Chem. Soc.* **2016**, *138*, 3478−3483.

(3) Ma, H.; Chen, J.-F.; Wang, H.-F.; Hu, P.-J.; Ma, W.; Long, Y.-T. *Nat. Commun.* **2020**, *11*, 2307.

(4) Ustarroz, J.; Kang, M.; Bullions, E.; Unwin, P. R. *Chem. Sci.* **2017**, *8*, 1841−1853.

(5) Oja, S. M.; Robinson, D. A.; Vitti, N. J.; Edwards, M. A.; Liu, Y.; White, H. S.; Zhang, B. *J. Am. Chem. Soc.* **2017**, *139*, 708−718.

(6) Patel, A. N.; Martinez-Marrades, A.; Brasiliense, V.; Koshelev, D.; Besbes, M.; Kuszelewicz, R.; Combellas, C.; Tessier, G.; Kanoufi, F. *Nano Lett.* **2015**, *15*, 6454−6463.

(7) Sundaresan, V.; Monaghan, J. W.; Willets, K. A. *J. Phys. Chem. C* **2018**, *122*, 3138−3145.

(8) Fosdick, S. E.; Anderson, M. J.; Nettleton, E. G.; Crooks, R. M. *J. Am. Chem. Soc.* **2013**, *135*, 5994−5997.

(9) Lemineur, J.-F.; Noël, J.-M.; Courty, A.; Ausserré, D.; Combellas, C.; Kanoufi, F. *J. Am. Chem. Soc.* **2020**, *142*, 7937−7946.

(10) Hao, R.; Fan, Y.; Zhang, B. *J. Am. Chem. Soc.* **2017**, *139*, 12274−12282.

(11) Ma, C.; Wu, W.; Li, L.; Wu, S.; Zhang, J.; Chen, Z.; Zhu, J.-J. *Chem. Sci.* **2018**, *9*, 6167−6175.

(12) Peljo, P.; Manzanares, J. A.; Girault, H. H. *Chem. Sci.* **2017**, *8*, 4795−4803.

(13) Lu, S.-M.; Chen, J.-F.; Peng, Y.-Y.; Ma, W.; Ma, H.; Wang, H.-F.; Hu, P.; Long, Y.-T. *J. Am. Chem. Soc.* **2021**, *143*, 12428−12432.

(14) Ma, W.; Ma, H.; Yang, Z.-Y.; Long, Y.-T. *J. Phys. Chem. Lett.* **2018**, *9*, 1429−1433.

(15) Chung, H. J.; Lee, J.; Hwang, J.; Seol, K. H.; Kim, K. M.; Song, J.; Chang, J. *Anal. Chem.* **2020**, *92*, 12226−12234.

(16) Ma, W.; Ma, H.; Chen, J.-F.; Peng, Y.-Y.; Yang, Z.-Y.; Wang, H.-F.; Ying, Y.-L.; Tian, H.; Long, Y.-T. *Chem. Sci.* **2017**, *8*, 1854−1861.

(17) Chinappi, M.; Yamaji, M.; Kawano, R.; Cecconi, F. *ACS Nano* **2020**, *14*, 15816−15828.

(18) Boika, A.; Thorgaard, S. N.; Bard, A. J. *J. Phys. Chem. B* **2013**, *117*, 4371−4380.

(19) Park, J. H.; Boika, A.; Park, H. S.; Lee, H. C.; Bard, A. J. *J. Phys. Chem. C* **2013**, *117*, 6651−6657.

(20) Thorgaard, S. N.; Jenkins, S.; Tarach, A. R. *Anal. Chem.* **2020**, *92*, 12663−12669.

(21) Moazzenzade, T.; Yang, X.; Walterbos, L.; Huskens, J.; Renault, C.; Lemay, S. G. *J. Am. Chem. Soc.* **2020**, *142*, 17908−17912.

(22) Boika, A.; Bard, A. J. *Anal. Chem.* **2014**, *86*, 11666−11672.

(23) Kline, T. R.; Paxton, W. F.; Wang, Y.; Velegol, D.; Mallouk, T. E.; Sen, A. *J. Am. Chem. Soc.* **2005**, *127*, 17150−17151.

(24) Contento, N. M.; Bohn, P. W. *Biomicrofluidics* **2014**, *8*, No. 044120.

(25) Contento, N. M.; Bohn, P. W. *Microfluid. Nanofluid.* **2015**, *18*, 131−140.

(26) McPherson, I. J.; Brown, P.; Meloni, G. N.; Unwin, P. R. *Anal. Chem.* **2021**, *93*, 16302−16307.

(27) Fan, L.; Liu, Y.; Xiong, J.; White, H. S.; Chen, S. *ACS Nano* **2014**, *8*, 10426−10436.

(28) Kostiuchenko, Z. A.; Cui, J. Z.; Lemay, S. G. *J. Phys. Chem. C* **2020**, *124*, 2656−2663.

(29) Ma, C.; Xu, W.; Wichert, W. R. A.; Bohn, P. W. *ACS Nano* **2016**, *10*, 3658−3664.

(30) Freedman, K. J.; Otto, L. M.; Ivanov, A. P.; Barik, A.; Oh, S.-H.; Edel, J. B. *Nat. Commun.* **2016**, *7*, 10217.

(31) Jaugstetter, M.; Blanc, N.; Kratz, M.; Tschulik, K. *Chem. Soc. Rev.* **2022**, *51*, 2491−2543.

(32) Fu, K.; Han, D.; Crouch, G. M.; Kwon, S.-R.; Bohn, P. W. *Small* **2018**, *14*, No. 1703248.

(33) Branagan, S. P.; Contento, N. M.; Bohn, P. W. *J. Am. Chem. Soc.* **2012**, *134*, 8617−8624.

(34) Goines, S.; Dick, J. E. *J. Electrochem. Soc.* **2019**, *167*, No. 037505.

(35) Weiß, L. J. K.; Music, E.; Rinklin, P.; Straumann, L.; Grob, L.; Mayer, D.; Wolfrum, B. *ACS Appl. Nano Mater.* **2021**, *4*, 8314−8320.

(36) Ngamchuea, K.; Clark, R. O. D.; Sokolov, S. V.; Young, N. P.; Batchelor-McAuley, C.; Compton, R. G. *Chem. − Eur. J.* **2017**, *23*, 16085−16096.

(37) Krause, K. J.; Brings, F.; Schnitker, J.; Kätelhön, E.; Rinklin, P.; Mayer, D.; Compton, R. G.; Lemay, S. G.; Offenhäusser, A.; Wolfrum, B. *Chem. − Eur. J.* **2017**, *23*, 4638−4643.

(38) Kulkarni, A.; Siahrostami, S.; Patel, A.; Nørskov, J. K. *Chem. Rev.* **2018**, *118*, 2302−2312.

(39) Ge, X.; Sumboja, A.; Wuu, D.; An, T.; Li, B.; Goh, F. W. T.; Hor, T. S. A.; Zong, Y.; Liu, Z. *ACS Catal.* **2015**, *5*, 4643−4667.

(40) Dau, H.; Limberg, C.; Reier, T.; Risch, M.; Roggan, S.; Strasser, P. *ChemCatChem* **2010**, *2*, 724−761.

(41) Lyklema, J. Solid-Liquid Interfaces. In *Fundamentals of Interface and Colloid Science*; Elsevier, 1995; 2.

(42) Gu, Y.; Li, D. *J. Colloid Interface Sci.* **2000**, *226*, 328−339.

(43) Robinson, D. A.; Kondajji, A. M.; Castañeda, A. D.; Dasari, R.; Crooks, R. M.; Stevenson, K. J. *J. Phys. Chem. Lett.* **2016**, *7*, 2512−2517.

(44) Zhang, Y.; Robinson, D. A.; McKelvey, K.; Ren, H.; White, H. S.; Edwards, M. A. *J. Electrochem. Soc.* **2020**, *167*, 166507.

(45) Kline, T. R.; Iwata, J.; Lammert, P. E.; Mallouk, T. E.; Sen, A.; Velegol, D. *J. Phys. Chem. B* **2006**, *110*, 24513−24521.

(46) Karimi, A.; Kirk, K. A.; Andreescu, S. *ChemElectroChem* **2017**, *4*, 2801−2806.

(47) Chen, W.; Wang, H.; Tang, H.; Yang, C.; Li, Y. *Anal. Chem.* **2019**, *91*, 14188−14191.

(48) Wonner, K.; Rurainsky, C.; Tschulik, K. *Front. Chem.* **2020**, *7*, 912.

(49) Fernando, I.; Zhou, Y. *Chemosphere* **2019**, *216*, 297−305.

(50) Lemineur, J.-F.; Stockmann, T. J.; Médard, J.; Smadja, C.; Combellas, C.; Kanoufi, F. *J. Anal. Test.* **2019**, *3*, 175−188.

(51) Golestanian, R.; Liverpool, T. B.; Ajdari, A. *New J. Phys.* **2007**, *9*, 126−126.

(52) Ha, D.; Seo, S.; Lee, K.; Kim, T. *ACS Nano* **2019**, *13*, 12939−12948.

(53) Silvera Batista, C. A.; Rezvantalab, H.; Larson, R. G.; Solomon, M. J. *Langmuir* **2017**, *33*, 10861−10867.

(54) Kar, A.; Chiang, T.-Y.; Ortiz Rivera, I.; Sen, A.; Velegol, D. *ACS Nano* **2015**, *9*, 746−753.

(55) Lee, K.; Lee, J.; Ha, D.; Kim, M.; Kim, T. *Lab Chip* **2020**, *20*, 2735−2747.

(56) Feldmann, D.; Maduar, S. R.; Santer, M.; Lomadze, N.; Vinogradova, O. I.; Santer, S. *Sci. Rep.* **2016**, *6*, 36443.

(57) Yalcin, S. E.; Lee, S. Y.; Joo, S. W.; Baysal, O.; Qian, S. *J. Phys. Chem. B* **2010**, *114*, 4082−4093.

(58) Marbach, S.; Bocquet, L. *Chem. Soc. Rev.* **2019**, *48*, 3102−3144.

(59) Prieve, D. C.; Anderson, J. L.; Ebel, J. P.; Lowell, M. E. *J. Fluid Mech.* **1984**, *148*, 247−269.

(60) Tricoli, V.; Orsini, G. *J. Phys.: Condens. Matter* **2015**, *27*, No. 415102.

(61) Rica, R. A.; Bazant, M. Z. *Phys. Fluids* **2010**, *22*, 112109.

(62) Kang, K. H.; Li, D. *J. Colloid Interface Sci.* **2005**, *286*, 792−806.

(63) Keh, H. J. *Curr. Opin. Colloid Interface Sci.* **2016**, *24*, 13−22.

(64) Wu, J. H.; Keh, H. J. *Colloids Surf. A: Physicochem. Eng. Asp.* **2003**, *212*, 27−42.

(65) Sokolov, S. V.; Eloul, S.; Kätelhön, E.; Batchelor-McAuley, C.; Compton, R. G. *Phys. Chem. Chem. Phys.* **2017**, *19*, 28−43.

(66) Shoup, D.; Szabo, A. *J. Electroanal. Chem. Interfacial Electrochem.* **1982**, *140*, 237−245.

(67) Squires, T. M.; Messinger, R. J.; Manalis, S. R. *Nat. Biotechnol.* **2008**, *26*, 417−426.

(68) Defnet, P. A.; Anderson, T. J.; Zhang, B. *Curr. Opin. Electrochem.* **2020**, *22*, 129−135.

(69) Saw, E. N.; Kanokkanchana, K.; Amin, H. M. A.; Tschulik, K. *ChemElectroChem* **2022**, *9*, No. e202101435.

(70) Saw, E. N.; Blanc, N.; Kanokkanchana, K.; Tschulik, K. *Electrochim. Acta* **2018**, *282*, 317−323.

(71) Ahmadinasab, N.; Stockmann, T. J. *ChemElectroChem* **2022**, *9*, No. e202200162.

Single-Impact Electrochemistry in Paper-Based Microfluidics

L.J.K. Weiß, G. Lubins, E. Music, P. Rinklin, M. Banzet, H. Peng, K. Terkan, D. Mayer, B. Wolfrum

Synopsis

The second part of this dissertation centers on the integration of stochastic particle-based detection into classical bioassays. Two crucial aspects must be addressed: particle specificity, which will be discussed in the last part of this thesis, and the incorporation of particle detection into an assay. This study focuses on the latter aspect and aims to investigate the feasibility of conducting a typical nanoparticle detection experiment in a point-of-care setting using a lateral-flow sensor configuration. To accomplish this, we wax-patterned chromatography paper to form a fiber-based channel and attached it to a clean-room fabricated chip using polyimide tape. Nanoparticle suspensions were deposited onto the source pad of the sensor as droplets, and amperometric traces were recorded as the paper wicked and particles were transported across the electrode array. Using an on-chip reference electrode in a two-electrode setup, individual nanoparticle impacts were resolved, even at concentrations as low as pM. Furthermore, we investigated the impact of particle size on the detection rate and observed that complete oxidation events occurred most frequently with 20 nm-sized particles. Smaller 10 nm-sized particles were often masked by noise, while larger 40 nm particles underwent incomplete oxidation, in particular under flow conditions. Finally, we mimicked a typical lateral-flow rapid test by drying the nanoparticles on the source pad of the paper and subsequently releasing them with buffer solution. In summary, this work demonstrates the feasibility of conducting stochastic detection experiments using a low-cost paper-based microfluidic channel and a simplified experimental setup. The Supplementary Material to the study can be found in Appendix A.3.

Individual Contribution

conceptualization of the study, data acquisition, data processing and interpretation, data interpretation, leading role in composition and writing of the manuscript

Article

Single-Impact Electrochemistry in Paper-Based Microfluidics

Lennart J. K. Weiß, Georg Lubins, Emir Music, Philipp Rinklin, Marko Banzet, Hu Peng, Korkut Terkan, Dirk Mayer, and Bernhard Wolfrum*

Read Online

ACCESS | Metrics & More | Article Recommendations | SI Supporting Information

ABSTRACT: Microfluidic paper-based analytical devices (μPADs) have experienced an unprecedented story of success. In particular, as of today, most people have likely come into contact with one of their two most famous examples—the pregnancy or the SARS-CoV-2 antigen test. However, their sensing performance is constrained by the optical readout of nanoparticle agglomeration, which typically allows only qualitative measurements. In contrast, single-impact electrochemistry offers the possibility to quantify species concentrations beyond the pM range by resolving collisions of individual species on a microelectrode. Within this work, we investigate the integration of stochastic sensing into a μPAD design by combining a wax-patterned microchannel with a microelectrode array to detect silver nanoparticles (AgNPs) by their oxidative dissolution. In doing so, we demonstrate the possibility to resolve individual nanoparticle collisions in a reference-on-chip configuration. To simulate a lateral flow architecture, we flush previously dried AgNPs along a microchannel toward the electrode array, where we are able to record nanoparticle impacts. Consequently, single-impact electrochemistry poses a promising candidate to extend the limits of lateral flow-based sensors beyond current applications toward a fast and reliable detection of very dilute species on site.

KEYWORDS: single-impact electrochemistry, silver nanoparticles, paper-based microfluidics, μPAD, lateral flow sensor
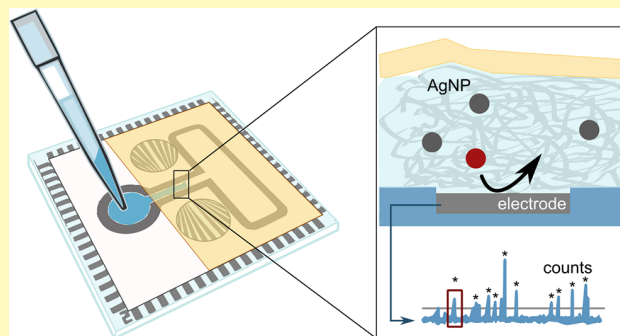
■ INTRODUCTION

In the past decade, microfluidic paper-based analytical devices (μPADs) received considerable attention as a diagnostic tool for various targets, such as environmental contaminants, pathogens, proteins, drugs, and heavy metals.[1−4] Even beyond the laboratory, μPADs were able to write an unprecedented history of success[5] as lateral flow pregnancy tests, glucose sensors, and in particular rapid tests for SARS-CoV-2 are probably familiar to all of us. Especially in resource-limited settings, μPADs offer great potential as they are portable platforms requiring only a minimal amount of analyte volume to provide an easy and quick diagnosis on site. In μPADS—unlike in active microfluidics—the sample fluid is passively driven by capillary forces and guided via hydrophobic barriers that are patterned on paper. Among other techniques, photolithography, ink-jet printing, etching, paper cutting, screen printing, laser treatment, and wax printing were employed to create wicking channels.[4,6,7] Depending on the final application, the read-out signal can be, for example, colorimetric, fluorescent, chemiluminescent, plasmonic, or electrochemical.[4,8−10] Despite their use in several point-of-care scenarios, (colorimetric) μPADs typically suffer from a relatively high limit of detection, making them insufficient for the analysis of samples with very low analyte concentrations.[11−13]

In contrast, stochastic impact electrochemistry is able to resolve individual entities by their collision on a micro-electrode.[14−17] This concept of digital sensing—the species is present (digital "1") or not present (digital "0") at the detector site—provides means to significantly reduce the limit of detection, for example, by reliably detecting entities at and beyond sub-pM concentrations.[18−20] Especially, metallic nanoparticles have been applied prominently due to their unique optical and electrochemical properties.[14,21−23]

Thus, they are increasingly employed as labels in various sensing applications.[24−28] Nanoparticle-based assays that rely on stochastic impact electrochemistry are particularly interesting as they might be the next generation of ultra-sensitive electrochemical point-of-care sensors.[29−36] Toward this goal, however, two major challenges have to be overcome: first, specificity has to be provided by functionalized nanoparticles without impeding their redox properties.[37−40] Second, a critical
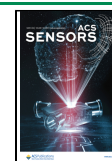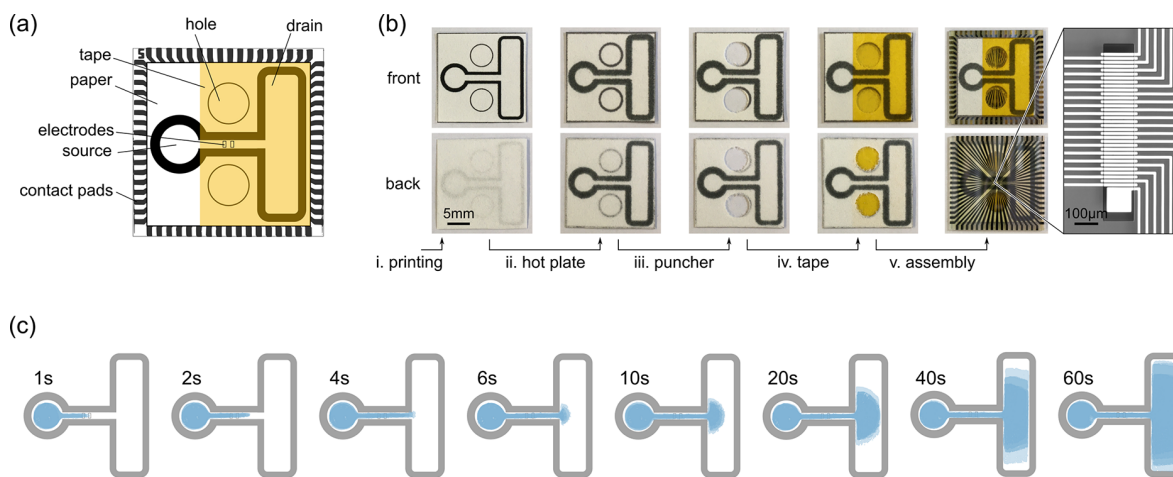
Figure 1. Electrochemical μPAD sensor. (a) Design of the μPAD-chip consisting of a cellulose paper on top of a microelectrode array. (b) μPAD-chip fabrication steps: hydrophobic barriers and alignment markers are wax-printed (i) and melted on a hot plate to generate a wax reflow (ii). The alignment and attachment between the chip and the paper is guaranteed through punched holes (iii) via adhesive tape (iv). The chip contains two sets of 31 platinum band electrodes ($125 \times 13\ \mu m^2$, see zoom-in images) and two reference electrodes ($100 \times 100\ \mu m^2$). (c) Temporal evolution of the flow within the μPAD design ($n = 5$). Initially, 10 μL of liquid were pipetted onto the source domain. A complete filling of the drain structure was reached after 81 ± 13 s.

number of detection events has to be recorded to support a reliable sensor output.[14,17,41] Here, we focus on the latter aspect and employ surface-controlled advection using paper-based microfluidics.

Within this work, we report the detection of individual silver nanoparticles (AgNPs) within a typical low-cost μPAD setting as a proof of principle. To this end, we combine a wax-patterned paper-based microchannel with a microelectrode array (MEA) chip and record amperometric traces from 62 channels in parallel. As we target point-of-care applications, all measurements are performed within a simplified electrochemical setting using a quasi-reference electrode on-chip.[42] Last, we mimic a lateral flow sensor protocol by detecting previously dried AgNPs in our μPAD. This illustrates the applicability of digital electrochemical sensing as an appealing technique for a highly sensitive quantification of very dilute species in situ.

■ MATERIALS AND METHODS

Chemicals. AgNPs in various sizes (citrate-capped, 0.02 mg/mL in aqueous solution, average diameters 10, 20, and 40 nm) as well as nitric acid (HNO$_3$, 70%) and sulfuric acid (H$_2$SO$_4$, 95.0−98.0%) were purchased from Sigma-Aldrich. Ammonium hydroxide (NH$_4$OH, 28%) was obtained from VWR Chemicals (Fontenay-sous-Bois, France), and potassium chloride (KCl) and Tween-20 were bought from Merck (Wiesbaden, Germany). Various dilutions were prepared using deionized water (conductivity 0.054 μS/cm) taken from a BerryPure purification system (Berrytec, Harthausen, Germany).

Fabrication of the Clean-Room Chips. The $1'' \times 1''$ chips were fabricated using standard clean-room techniques as reported in earlier work.[18] In summary, a stack of metal layers (20 nm Ti/200 nm Pt/5 nm Ti) was deposited onto a 500 μm-thick Borosilicate substrate (Schott Ag, Mainz, Germany) via electron beam evaporation to create the metal structures. Afterward, the feedlines were passivated with a 40 nm-thick layer of Ta$_5$O$_2$ via atomic layer deposition, followed by a stack of five alternating layers of SiO$_2$ and Si$_3$N$_4$ (O−N−O−N−O) using plasma-enhanced chemical vapor deposition. The final design comprises 62 band electrodes (length 125 μm, width 13 μm, and spacing 6 μm) and two (reference) electrodes with a size of $100 \times 100\ \mu m^2$ that were divided in two groups being 1050 μm apart. To

allow simple on-chip detection without external reference electrodes, large platinum electrodes were used as quasi-reference.

Fabrication of the μPADs. The first μPAD design, see Figure 1a, consists of a source with an inner diameter of 4.7 mm and a barrier with 800 μm thickness. The rectangular channel has a length of 8 mm and a width of 1400 μm, which is defined by a 600 μm-thick wall. The drain has an area 68 mm^2 and is also surrounded by a 600 μm-thick barrier. Furthermore, the design includes alignment markers to punch the holes that connect the paper to the chip, see Figure S1a.

A commercial wax printer (Xerox ColorQube 8900X, Xerox Corp., USA) was used to pattern the hydrophobic barriers (solid ink for ColorQube 8900) on a Cytiva Whatman Chr1 chromatography paper (pore size of 11 μm) with size 30×10 cm^2. To this end, printing was performed using the "high resolution" option to ensure a proper alignment of all four color channels (CMYK) that are used for "registration black". This option ensured a maximum amount of wax deposited onto the paper within one print job, which in turn reduces fuzzy barrier edges and fluid leakage, see Figure S2 for an exemplary print result. Subsequently, the paper stripes were heated for 30 s at 125 °C on a precision hot plate (Harry Gestigkeit, Germany) carrying a weight of 250 g on top to ensure a consistent contact and thus a homogeneous melting of the wax. After manual cutting, two holes were punched with an office puncher, and tape (Kapton, DuPont, Wilmington, DE, USA) was used to connect the paper to the chip as well as to prevent evaporation of the fluid. Last, the μPAD was bonded to the chip by gently pushing onto the tape in the cut-outs. The same process was used to fabricate the μPAD-structure for the lateral flow experiment, see also Figure S1b.

Flow Characterization. The evolution of the flow was recorded with a commercial smartphone while 10 μL of commercial ink (Pelikan 4001 royal blue, Hannover, Germany) were pipetted onto the chip. Screenshots at various time points were extracted via Camtasia, and the pictures were overlaid in Inkscape. Moreover, the videos were processed in MATLAB using a simple thresholding method to extract the wetted area and to estimate the flow rate.

AgNP Detection Experiments and Evaluation. The detection experiments were carried out with a 64-channel trans-impedance amplifier system in a two-electrode reference-on-chip configuration.[42] The system records at 10 kHz sampling rate per channel and features a bandwidth of 3.4 kHz. A $100 \times 100\ \mu m^2$-electrode was used as quasi-reference, and the potential at the working electrodes was forced to 500 mV versus open-circuit potential (OCP). The rms current noise at OCP was measured to 1.4 ± 0.2 pA for our system. In each experiment, 10 μL of freshly prepared test solution containing 25 mM
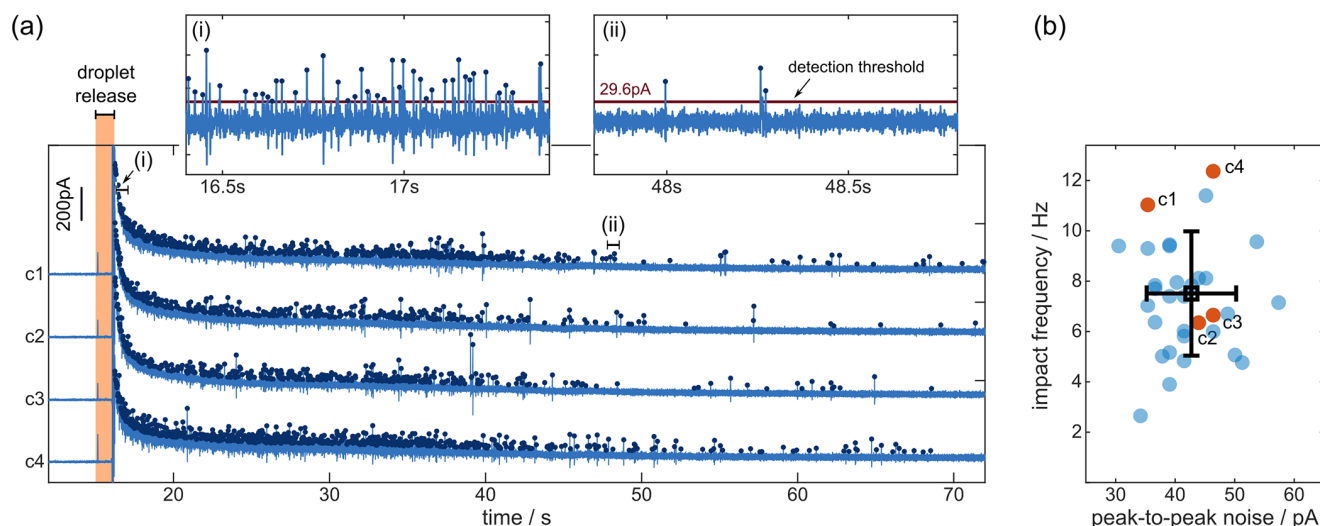
Figure 2. AgNP detection experiment in the case of a 10 μL droplet that contains 25 mM KCl and 100 pM AgNP with a 20 nm diameter. (a) Raw current traces and detected AgNP impacts (blue circles) of four different channels. The channels are displayed with an additional offset of 400 pA for clarification. The graphs in (i,ii) show zoom-in patterns at two different time points for channel c1. (b) Impact rate as a function of the peak-to-peak background noise taken from a single experiment. The channels shown in (a) are marked in red.

KCl and, for example, 20 nm-sized AgNPs were pipetted on the source. The currents were recorded for at least 60 s.

The lateral flow experiments were carried out as follows. First, a droplet of 1% Tween-20 was deposited onto the source to reduce unwanted particle aggregation. Afterward, 1 μL of 20 nm AgNP stock solution was dried on the same location. Then, the μPAD was assembled, and the potential was stepped to 500 mV versus Pt-RE, followed by the release of 12 μL of electrolyte solution (30 mM KCl and 0.1% Tween-20) onto the source area.

The raw current traces were further processed and analyzed in MATLAB, similar to earlier work.[10] In short, non-working channels were first excluded based on noise evaluation, and the current traces were de-trended to subsequently apply a channel-specific thresholding method that extracts the AgNP impacts. If not otherwise stated, all current spikes that exceed a threshold ($0.5 i_{pk2pk}$ + 7 pA, based on the channel-specific peak-to-peak current i_{pk2pk}) were considered for further investigations. Due to a mismatch of the capacitive loads and the amplifier input, initial positive current transients that stem from AgNP collisions are followed by decaying ringing artifacts, which also introduce negative current peaks. To avoid misclassification, an additional inter-peak minimum distance of 5 ms was introduced. The effect of fabrication defects is reduced by visualizing only the results of the 15 channels that show the highest number of AgNP impacts (if not otherwise stated). All statistical values given in the text are calculated as mean and standard deviations.

Chip Cleaning Procedure. Prior to the detection experiment, the chips were cleaned via incubation in NH_4OH and HNO_3 prior to cyclic voltammetry in 200 mM H_2SO_4 (potential range from −0.2 to 1.5 V, scan rate 500 mV/s, 30 cycles). All electrochemical measurements apart from the AgNP detection were performed with a VSP-300 potentiostat (BioLogic Instruments, France) using a Ag/AgCl reference electrode (Dri-Ref, Flexref from World Precision Instruments) and a coiled platinum wire as the counter electrode.

■ RESULTS AND DISCUSSION

Fabrication and Characterization of the μPAD. In our first proof of concept, we built a simple μPAD sensor by attaching a previously patterned chromatography paper to a chip that contains two groups of band electrodes, see Figure 1a. The layout (see also Figure S1a) consists of a source domain and a large drain area that are connected by a rectangular channel. As shown in Figure 1b, the fabrication includes (i) the patterning of the channel barriers via wax

printing, followed by (ii) a reflow step, where the paper is heated on a hot plate to ensure sealed barriers. As the melting ensures sealed walls and also leads to a lateral spread of wax, the final channel layout can be significantly smaller than the initial design. For instance, moderate heating for 30 s at 125 °C leads to a source radius of ~2400 μm and a microchannel with a width of 450 μm, see Figure S2. After the reflow, holes were punched (iii) and adhesive tape was used to attach the cut-out paper to the chip. Here, the structure was manually aligned such that the electrodes were covered by the center of the microchannel.

We performed an initial wetting test, see Figure 1c, to study the flow characteristics of the μPAD. After releasing a 10 μL droplet of commercial ink, we observed a fast complete wetting of the rectangular channel at ~4 s. The entire drain area, however, is only filled slowly after 81 ± 13 s, indicating different mechanisms that drive the fluid in our experiment. In general, the imbibition of the paper is governed by capillary flow along the cellulose fibers and can be modeled, for example, as a wet-out process being described by the propagation of the fluid front (Lucas−Washburn equation) and/or as a flow through porous media (Darcy's law) when the paper is fully wetted.[43] However, an accurate description of the wicking process is challenging, and fluid control was mostly achieved in a trial-and-error fashion. In our setting, we find two additional phenomena that affect the fluid motion—capillary forces at the interface between the chip and the electrolyte, as well as a pressure gradient due to the surface tension at the droplet in the source reservoir. In particular, variations in the manual droplet release and the attachment/flatness of the paper lead to large discrepancies between trials, for example, visible in the propagation differences between 20 and 60 s in Figure 1c (see also Figure S6b,c). Consequently, we expect later measurement times to be less reliable for the detection of AgNPs and restrict the evaluation window to a narrow range of ≤30 s after droplet release. Nevertheless, the wicking of the microchannel could in principle be optimized by geometrical design or surface modifications of the fibers and the chip in order to provide efficient mass transport.

Stochastic Detection of Individual AgNPs. Since the concept of stochastic electrochemistry offers great potential for ultra-sensitive point-of-care sensors, we first investigated the detection of AgNP in a simplified electrochemical setup,[42] where we used a larger electrode on the chip as quasi-reference. The OCP of a platinum electrode in 25 mM KCl was determined to be 580±4 mV versus Ag/AgCl (see Figure S3), which is well above the oxidation potential of silver in this case. However, during the measurement, the OCP of the reference electrode might drift toward the negative potentials.[44,45] Therefore, all the following detection experiments are carried out in a reference-on-chip setting, where the detection electrodes are biased to 500 mV versus Pt-RE to ensure a fast oxidation reaction throughout the entire experiment.[46,47]

Figure 2a presents the current traces of a typical detection experiment in the case of 25 mM KCl and 100 pM AgNP (diameter of 20 nm), when a 10 μL droplet was released (orange area) and the detection electrodes were kept at 500 mV versus Pt-RE. The raw data in Figure 2a clearly demonstrates that the detection of a single AgNP is possible in a conventional μPAD design (statistical data regarding the current amplitudes, durations, and charges are shown in Figure S4). At the same time, the current in a control experiment (shown in Figure S5) does not exhibit any signal distortions, rendering our approach promising for the reliable detection of very dilute (nanoparticle) species. The peak-to-peak background noise during the detection was found to be 40.4 ± 6.5 pA (rms value 7.6 ± 2.5 pA) and did not scale with the number of detected peaks. Furthermore, as we do not observe a correlation between counted impacts and current noise, see Figure 2b, we ensure that all considered peaks stem from impacting AgNPs.

Interestingly, Figure 2a reveals that all channels undergo a sharp transition at ~45 s between two detection regimes. In the beginning of the experiment, see Figure 2a(i), the collision rate is relatively high (e.g. 40 Hz), whereas it drastically drops by a factor ≥10 for later times, see Figure 2a(ii), which leads to a mean detection rate of only 6.9 Hz for an interval of 60 s.

This transition, however, can be attributed to a change in the flow characteristics (see Figure S6, where the change in wetted area per time step is estimated based on the videos from Figure 1c) and the geometrical design. Here, a continuously decreasing droplet curvature and/or an increased risk for the paper to bend upward might be possible explanations for a decreased flow rate.

To further investigate the opportunities of stochastic electrochemistry in paper-based microfluidics, we performed AgNP detection experiments at various concentrations from 100 fM to 100 pM, see Figure 3a, and analyzed the first 30 s after droplet release. For concentrations 1 pM $\leq c \leq$ 100 pM, we observe a linear relationship between the impact rate and the underlying number of particles, which is in line with our expectations. However, for very dilute suspensions, this does not hold true and only a few AgNP impacts are recorded. Interfering effects such as particle adsorption and particle velocities beyond the favorable range generally restrict the performance of a digital sensor.[48−50] Yet, their influence on the sensor output has a greater impact for lower particle concentrations. Nevertheless, the range of reliable stochastic sensing could be further extended to lower concentrations by carefully designed microchannel and sensor geometries.

The size histograms in Figure 3b reveal that we were able to correctly determine an average particle size of 20 nm for all
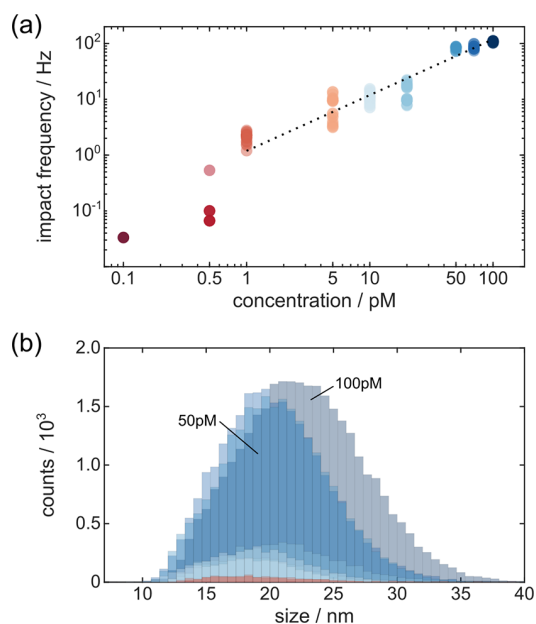
Figure 3. Calibration data for 20 nm-sized AgNPs in 25 mM KCl solution. (a) Impact rate as a function of AgNP concentration. The data is based on a 30 s evaluation window and the 10 best-performing channels. (b) Particle sizes determined by integration of the injected charge during a AgNP collision. The data is based on the same experiments as in (a).

concentrations, indicating that the particles undergo a complete oxidation at the electrodes. Furthermore, we could not observe any significant temporal changes in the mean size of detected peaks for concentrations <70 pM, leading to the conclusion that aggregation and changes at the platinum reference electrode due to particle adsorption do not play a critical role for moderate particle concentrations.[44,48,51] However, in the case of 100 pM AgNP, we observed a slight shift in the determined AgNP size (22.6 ± 4.9 nm for 100 pM compared to 20.4 ± 4.7 nm for 70 pM AgNPs), which we attribute to particle aggregation.

Toward a Digital Lateral Flow Sensor. So far, we have successfully demonstrated the integration of stochastic impact electrochemistry as a detection framework within μPAD for point-of-care applications. Apart from the challenging task of introducing specificity without sacrificing the redox properties of the nanoparticles, several interesting questions related to a sensor assay that uses metallic nanoparticles as labels remain.

The design of a lateral flow assay, for instance, typically requires a control species, which is clearly differentiable from the target species. Thus, the read-out method has to allow target multiplexing. In the context of stochastic impact electrochemistry, this could be achieved by using differently sized nanoparticles within the same recording. We studied the feasibility of such an approach and recorded nanoparticles with three different sizes—10, 20, and 40 nm. The results are provided in Figure 4, where exemplary current traces are shown in (a) and the resulting size histograms in (b). Assuming the particles to be mainly driven by free diffusion, we would expect the highest number of impacts in the case of 10 nm AgNPs. Surprisingly, this is not reflected in our data since we observe a similar impact rate for 20 and 40 nm AgNPs (29.6 ± 3.1 and 28.5 ± 2.0 Hz, see also Figure S7), whereas there is a drastically lower detection rate for 10 nm AgNPs
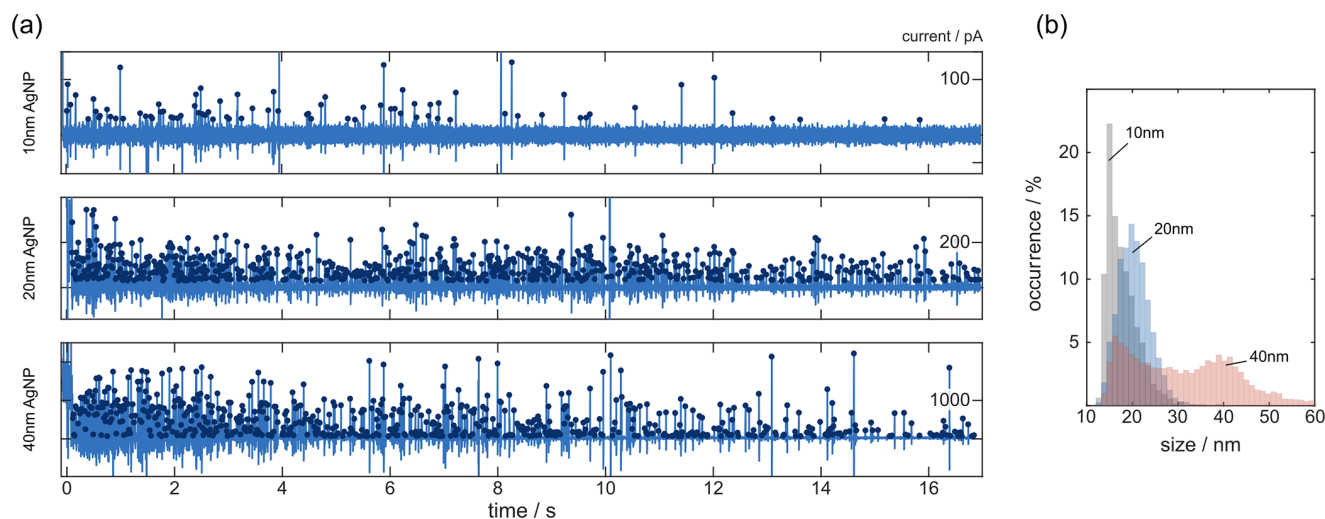
Figure 4. Effect of AgNP size. (a) Detrended current trace of a single channel within three different experiments using 50 pM AgNPs and 25 mM KCl solution. Note the different current scaling (indicated on the right *y*-axis) for better visualization. (b) Size histograms for all the three experiments based on data from 10 channels and an evaluation window of 20 s after droplet release. The *y*-axis shows the relative number of current peaks leading to a certain size compared to the total number of detected impacts.

$(10.3 \pm 1.2$ Hz). However, in the case of 10 nm AgNPs, we most likely see the effects of thresholding and current masking. This hypothesis is supported by Figure 4b, where mainly AgNP sizes above 12 nm are registered due to a conservative current threshold in the data analysis. On average, we measured a background noise of ~40 pA peak-to-peak in our experiments, stemming from a relatively large electrode area $(125 \times 13 \ \mu m^2)$. In this case, a high detection threshold greatly reduces the risk of misclassification, yet at the same time ignores small-amplitude peaks (see Figure S8).

Apart from masking that affects the detection of small-sized AgNPs, we also found an unexpectedly high impact rate for AgNPs with a diameter of 40 nm. Here, a closer look at the raw data reveals a substantial number of small-amplitude peaks exceeding the limit. These peaks convert to a second maximum in the size distribution at ~16 nm. Since neither control experiments nor recordings with smaller AgNP sizes show a similar behavior, we attribute this finding to the larger particle size. In our opinion, there are two potential reasons that could cause these small peaks. First, there could be an unexpected increase in the noise floor if 40 nm AgNPs were to change the electrode−electrolyte interface at the reference. The previously fixed threshold would then be too low and would lead to a detection of background noise. Nonetheless, larger particles— typically above 30 nm—are also known to undergo incomplete oxidation.[47,52−55] Thus, we hypothesize that partial oxidation might also play a critical role in our system for large particles. This effect is potentially increased by a low or moderate supporting electrolyte concentration,[56] a decreasing electro-active area on the electrodes,[44,57,58] and a non-negligible lateral particle velocity. Additionally, local and temporal changes of the chloride concentration due to adsorption on the cellulose might locally affect the oxidation as well.[59] Although we also identified a significant number of small peaks under static conditions (see Figure S9), the effect is more pronounced in the case of a paper-based microchannel. This supports our hypothesis of nanoparticles being flushed across the electrodes before they have the chance to become fully oxidized within a moderate electrolyte concentration.[50,56,59] However, a careful choice of the supporting electrolyte and/or modifications of

the electrode surface might lead to a more efficient detection yield.[60,61]

Hence, we conclude that target multiplexing according to different nanoparticle sizes is possible—albeit challenging. Nonetheless, several issues mentioned above could be mitigated by a careful design of the sensor structure. For instance, smaller electrodes, recordings at higher sampling rates, and tailored microfluidic channels could enable a better differentiation of individual peaks. In fact, as paper-based microfluidics enable high detection rates, nanoparticle labels with sizes >20 nm would be generally favorable since they provide a higher signal-to-noise ratio. At the same time, the correlation of one current peak per particle does not hold true for particles beyond a diameter of 30 nm. Single-impact electrochemistry, however, also promotes a different strategy for target multiplexing—one could mix different electroactive nanoparticle species and detect them on separated electrodes, as they correspond to different redox potentials.[62] In principle, this would allow a lateral flow architecture, where control and target species could be measured at different locations such that the signals do not interfere with each other.

Another interesting question in the context of lateral flow sensors relates to the incorporation of nanoparticles. Ideally, previously dried or immobilized species/nanoparticles should be carried along a channel to be then individually detected further downstream. This is particularly important since drying phenomena and/or immobilization strategies imply the risk of irreversible aggregation and adsorption.[48,63,64]

We mimicked such a scenario, depicted in Figure 5a, by drying 20 nm-sized AgNPs on the source area of a μPAD. Subsequently, we flushed the nanoparticles with an electrolyte carrier along the channel. The raw data from 13 channels is visualized in Figure 5b, whereas the control experiment is provided in Figure S10. After the droplet release, which is visible as signal distortions across all channels, individual peaks are visible in the current traces. Here, earlier current peaks, for example, the zoom-in image in Figure 5b(i), are preceded by a sharp negative transient, whereas later current peaks, see Figure 5b(ii), show the typical response associated with a AgNP impact. Interestingly, we observed negative transients
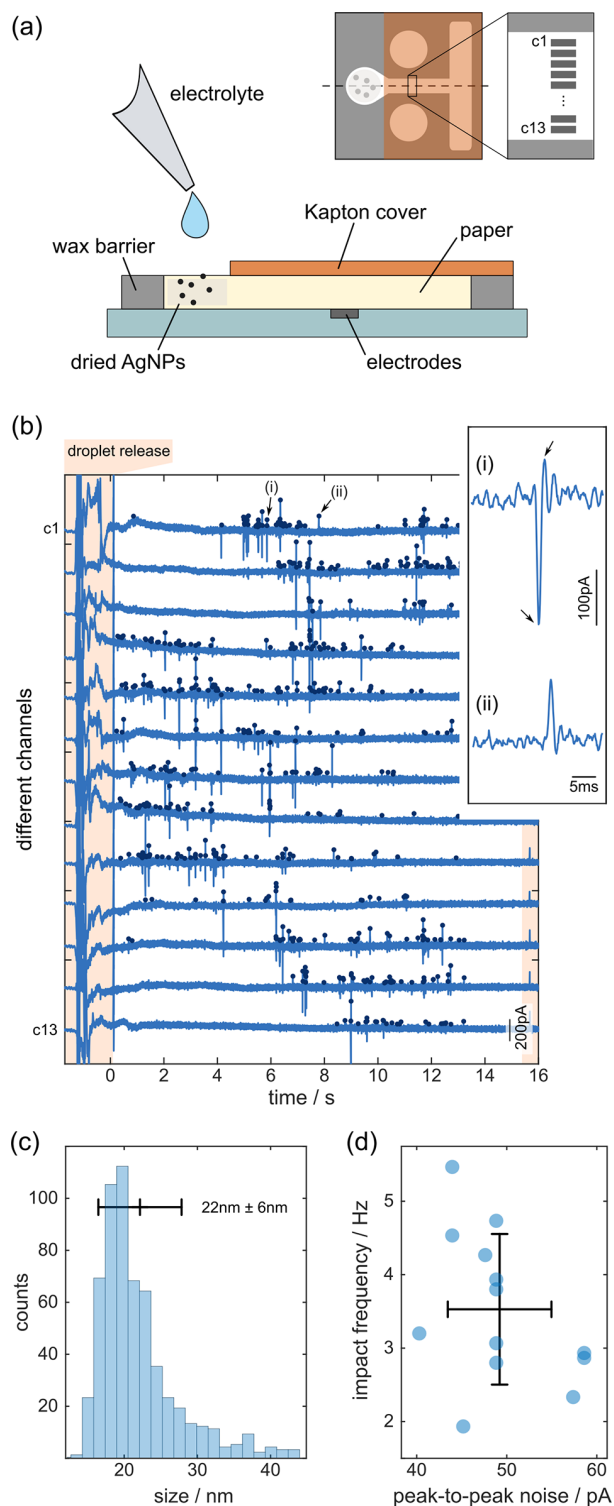
Figure 5. Digital lateral flow sensor. (a) Schematic of the sensor and top view of the μPAD design. (b) Raw data from 13 channels in the case of 1 μL 756 pM of 20 nm AgNPs and 12 μL of 30 mM KCl containing 0.1% Tween-20. The drain area is filled after ∼15 s and the experiment stopped. The order of the channels corresponds to the vertical location of the electrodes within the microchannel. (c) Particle size distribution and (d) mean impact rate over peak-to-peak current noise based on a 15 s evaluation window.

the electrolyte solution and the source pad in order to reduce aggregation and adsorption effects. Since the control experiment in Figure S10 does not indicate a strong interference of Tween-20 in the absence of particles, we attribute the negative peaks to changes at the surface of the particles. A blocking event suppressing residual currents could potentially lead to such a behavior. However, in our experiments, this is unlikely as the residual bias current is typically very small (∼20 pA). Possibly, the observed peaks are caused by capacitive effects, originating from interactions of the Tween-20-capped particles with the double layer of the detection electrode. Furthermore, drying typically leads to particle clustering, which might also play a critical role in our setup.

Remarkably, the histogram in Figure 5c is in line with the particle size of 20 nm, although particle aggregation is not completely prevented (note the longer tail of the distribution in Figure 5c compared to Figure 3b). Yet, this might also stem from a high initial concentration of 756 pM that was dried onto the source. Moreover, the raw data in Figure 5b displays an interesting pattern, where electrodes in the center show impacts at earlier times compared to channels located closer to the walls. This finding fits very well to the observed velocity distribution along a microchannel with hydrophobic barriers. In summary, our experiments demonstrate the general feasibility of a digital lateral flow sensor. However, the impact rates in the second experiment are low (∼3.5 Hz, see Figure 5d) compared to recordings, where the AgNPs were suspended in an electrolyte solution. As a sufficient amount of time is needed to release the dried particles, we believe that tailored designs could provide higher detection rates and extended measurement time as well.

CONCLUSIONS AND OUTLOOK

In summary, we combined paper microfluidics and the stochastic detection of AgNPs to investigate the requirements and challenges toward a nanoparticle-based point-of-care sensor. We demonstrated the reliable quantification of AgNPs in a μPAD sensor within a reference-on-chip configuration. Furthermore, we studied the detection of differently-sized AgNP in a μPAD. Here, we also observed interfering effects such as masking and small-amplitude peaks—probably due to incomplete oxidation—for 10 and 40 nm-AgNPs, respectively. However, a careful sensor design might be able to mitigate these shortcomings. Last, we aimed to detect previously dried AgNPs in a lateral flow setting and were able to resolve individual AgNP impacts. This is in particular interesting as the ultra-sensitive framework of stochastic impact electrochemistry could complement colorimetric assays to further extend the opportunities of low-cost sensors. Here, especially microelectrode arrays and portable detection devices could provide means toward a reliable on-site quantification of very dilute species.

ASSOCIATED CONTENT

ⓢ Supporting Information

The Supporting Information is available free of charge at https://pubs.acs.org/doi/10.1021/acssensors.1c02703.

> Sketch of the μPAD design and optical images of the channel structure; OCP of a clean platinum electrode and oxidation potential of silver in 25 mM KCl solution; statistical data and control experiments for AgNP

prior to the positive oxidation spikes only in the case of previously dried nanoparticles. Here, Tween-20 was added to

detection experiments; and characterization of the fluid motion within the µPAD (PDF)

■ AUTHOR INFORMATION

Corresponding Author

Bernhard Wolfrum − *Neuroelectronics—Munich Institute of Biomedical Engineering, Department of Electrical and Computer Engineering, Technical University of Munich, 85748 Garching, Germany;* ◉ orcid.org/0000-0003-4438-3755; Email: bernhard.wolfrum@tum.de

Authors

Lennart J. K. Weiß − *Neuroelectronics—Munich Institute of Biomedical Engineering, Department of Electrical and Computer Engineering, Technical University of Munich, 85748 Garching, Germany;* ◉ orcid.org/0000-0002-6943-737X

Georg Lubins − *Neuroelectronics—Munich Institute of Biomedical Engineering, Department of Electrical and Computer Engineering, Technical University of Munich, 85748 Garching, Germany*

Emir Music − *Neuroelectronics—Munich Institute of Biomedical Engineering, Department of Electrical and Computer Engineering, Technical University of Munich, 85748 Garching, Germany;* ◉ orcid.org/0000-0002-1583-7597

Philipp Rinklin − *Neuroelectronics—Munich Institute of Biomedical Engineering, Department of Electrical and Computer Engineering, Technical University of Munich, 85748 Garching, Germany;* ◉ orcid.org/0000-0003-1063-8342

Marko Banzet − *Institute of Biological Information Processing, Bioelectronics (IBI-3), Forschungszentrum Jülich, 52425 Jülich, Germany*

Hu Peng − *Neuroelectronics—Munich Institute of Biomedical Engineering, Department of Electrical and Computer Engineering, Technical University of Munich, 85748 Garching, Germany*

Korkut Terkan − *Neuroelectronics—Munich Institute of Biomedical Engineering, Department of Electrical and Computer Engineering, Technical University of Munich, 85748 Garching, Germany*

Dirk Mayer − *Institute of Biological Information Processing, Bioelectronics (IBI-3), Forschungszentrum Jülich, 52425 Jülich, Germany;* ◉ orcid.org/0000-0003-1296-8265

Complete contact information is available at:
https://pubs.acs.org/10.1021/acssensors.1c02703

Author Contributions

L.J.K.W. and B.W. designed the study. L.J.K.W., G.L., E.M., and H.P. carried out the experiments. M.B. fabricated the MEA chips. K.T. helped in the fabrication of the sensors. L.J.K.W. wrote the manuscript with support from G.L., P.R., D.M., and B.W. All authors provided critical feedback.

Notes

The authors declare no competing financial interest.

■ REFERENCES

(1) He, Y.; Wu, Y.; Fu, J.-Z.; Wu, W.-B. Fabrication of Paper-Based Microfluidic Analysis Devices: A Review. *RSC Adv.* **2015**, *5*, 78109−78127.

(2) Cate, D. M.; Adkins, J. A.; Mettakoonpitak, J.; Henry, C. S. Recent Developments in Paper-Based Microfluidic Devices. *Anal. Chem.* **2015**, *87*, 19−41.

(3) Yang, Y.; Noviana, E.; Nguyen, M. P.; Geiss, B. J.; Dandy, D. S.; Henry, C. S. Paper-Based Microfluidic Devices: Emerging Themes and Applications. *Anal. Chem.* **2017**, *89*, 71−91.

(4) Akyazi, T.; Basabe-Desmonts, L.; Benito-Lopez, F. Review on Microfluidic Paper-Based Analytical Devices towards Commercialisation. *Anal. Chim. Acta* **2018**, *1001*, 1−17.

(5) Nishat, S.; Jafry, A. T.; Martinez, A. W.; Awan, F. R. Paper-Based Microfluidics: Simplified Fabrication and Assay Methods. *Sens. Actuators, B* **2021**, *336*, 129681.

(6) Li, X.; Ballerini, D. R.; Shen, W. A Perspective on Paper-Based Microfluidics: Current Status and Future Trends. *Biomicrofluidics* **2012**, *6*, 011301.

(7) Ahmed, S.; Bui, M.-P. N.; Abbas, A. Paper-Based Chemical and Biological Sensors: Engineering Aspects. *Biosens. Bioelectron.* **2016**, *77*, 249−263.

(8) Glavan, A. C.; Christodouleas, D. C.; Mosadegh, B.; Yu, H. D.; Smith, B. S.; Lessing, J.; Fernández-Abedul, M. T.; Whitesides, G. M. Folding Analytical Devices for Electrochemical ELISA in Hydrophobic R^H Paper. *Anal. Chem.* **2014**, *86*, 11999−12007.

(9) Wang, Y.; Xu, H.; Luo, J.; Liu, J.; Wang, L.; Fan, Y.; Yan, S.; Yang, Y.; Cai, X. A Novel Label-Free Microfluidic Paper-Based Immunosensor for Highly Sensitive Electrochemical Detection of Carcinoembryonic Antigen. *Biosens. Bioelectron.* **2016**, *83*, 319−326.

(10) Baharfar, M.; Rahbar, M.; Tajik, M.; Liu, G. Engineering Strategies for Enhancing the Performance of Electrochemical Paper-Based Analytical Devices. *Biosens. Bioelectron.* **2020**, *167*, 112506.

(11) Liu, Y.; Zhan, L.; Qin, Z.; Sackrison, J.; Bischof, J. C. Ultrasensitive and Highly Specific Lateral Flow Assays for Point-of-Care Diagnosis. *ACS Nano* **2021**, *15*, 3593−3611.

(12) Di Nardo, F.; Chiarello, M.; Cavalera, S.; Baggiani, C.; Anfossi, L. Ten Years of Lateral Flow Immunoassay Technique Applications: Trends, Challenges and Future Perspectives. *Sensors* **2021**, *21*, 5185.

(13) Deng, Y.; Jiang, H.; Li, X.; Lv, X. Recent Advances in Sensitivity Enhancement for Lateral Flow Assay. *Microchim. Acta* **2021**, *188*, 379.

(14) Goines, S.; Dick, J. E. Review—Electrochemistry's Potential to Reach the Ultimate Sensitivity in Measurement Science. *J. Electrochem. Soc.* **2019**, *167*, 037505.

(15) Patrice, F. T.; Qiu, K.; Ying, Y.-L.; Long, Y.-T. Single Nanoparticle Electrochemistry. *Annu. Rev. Anal. Chem.* **2019**, *12*, 347−370.

(16) Dick, J. E.; Renault, C.; Bard, A. J. Observation of Single-Protein and DNA Macromolecule Collisions on Ultramicroelectrodes. *J. Am. Chem. Soc.* **2015**, *137*, 8376−8379.

(17) Sekretareva, A. Single-Entity Electrochemistry of Collision in Sensing Applications. *Sensors Actuators Rep.* **2021**, *3*, 100037.

(18) Krause, K. J.; Yakushenko, A.; Wolfrum, B. Stochastic On-Chip Detection of Subpicomolar Concentrations of Silver Nanoparticles. *Anal. Chem.* **2015**, *87*, 7321−7325.

(19) Robinson, D. A.; Yoo, J. J.; Castañeda, A. D.; Gu, B.; Dasari, R.; Crooks, R. M.; Stevenson, K. J. Increasing the Collision Rate of Particle Impact Electroanalysis with Magnetically Guided Pt-Decorated Iron Oxide Nanoparticles. *ACS Nano* **2015**, *9*, 7583−7595.

(20) Sokolov, S. V.; Bartlett, T. R.; Fair, P.; Fletcher, S.; Compton, R. G. Femtomolar Detection of Silver Nanoparticles by Flow-Enhanced Direct-Impact Voltammetry at a Microelectrode Array. *Anal. Chem.* **2016**, *88*, 8908−8912.

(21) Islam, T.; Hasan, M. M.; Awal, A.; Nurunnabi, M.; Ahammad, A. J. S. Metal Nanoparticles for Electrochemical Sensing: Progress and Challenges in the Clinical Transition of Point-of-Care Testing. *Molecules* 2020, 25, 5787.

(22) Brasiliense, V.; Patel, A. N.; Martinez-Marrades, A.; Shi, J.; Chen, Y.; Combellas, C.; Tessier, G.; Kanoufi, F. Correlated Electrochemical and Optical Detection Reveals the Chemical Reactivity of Individual Silver Nanoparticles. *J. Am. Chem. Soc.* 2016, 138, 3478−3483.

(23) Bonezzi, J.; Luitel, T.; Boika, A. Electrokinetic Manipulation of Silver and Platinum Nanoparticles and Their Stochastic Electrochemical Detection. *Anal. Chem.* 2017, 89, 8614−8619.

(24) Iglesias-Mayor, A.; Amor-Gutiérrez, O.; Costa-García, A.; de la Escosura-Muñiz, A. Nanoparticles as Emerging Labels in Electrochemical Immunosensors. *Sensors* 2019, 19, 5137.

(25) Zhang, F.; Liu, J. Label-Free Colorimetric Biosensors Based on Aptamers and Gold Nanoparticles: A Critical Review. *Anal. Sens.* 2021, 1, 30−43.

(26) Nath, N.; Chilkoti, A. Label Free Colorimetric Biosensing Using Nanoparticles. *J. Fluoresc.* 2004, 14, 377−389.

(27) Beck, F.; Horn, C.; Baeumner, A. J. Ag Nanoparticles Outperform Au Nanoparticles for the Use as Label in Electrochemical Point-of-Care Sensors. *Anal. Bioanal. Chem.* 2021, 414, 475.

(28) Oh, S.-H.; Altug, H. Performance Metrics and Enabling Technologies for Nanoplasmonic Biosensors. *Nat. Commun.* 2018, 9, 5263.

(29) Pollok, N. E.; Rabin, C.; Walgama, C. T.; Smith, L.; Richards, I.; Crooks, R. M. Electrochemical Detection of NT-ProBNP Using a Metalloimmunoassay on a Paper Electrode Platform. *ACS Sens.* 2020, 5, 853−860.

(30) Pollok, N. E.; Peng, Y.; Rabin, C.; Richards, I.; Crooks, R. M. Effect of Serum on Electrochemical Detection of Bioassays Having Ag Nanoparticle Labels. *ACS Sens.* 2021, 6, 1956.

(31) Cunningham, J. C.; Kogan, M. R.; Tsai, Y.-J.; Luo, L.; Richards, I.; Crooks, R. M. Paper-Based Sensor for Electrochemical Detection of Silver Nanoparticle Labels by Galvanic Exchange. *ACS Sens.* 2016, 1, 40−47.

(32) Cunningham, J. C.; Scida, K.; Kogan, M. R.; Wang, B.; Ellington, A. D.; Crooks, R. M. Paper Diagnostic Device for Quantitative Electrochemical Detection of Ricin at Picomolar Levels. *Lab Chip* 2015, 15, 3707−3715.

(33) Kwon, S. J.; Bard, A. J. DNA Analysis by Application of Pt Nanoparticle Electrochemical Amplification with Single Label Response. *J. Am. Chem. Soc.* 2012, 134, 10777−10779.

(34) Dick, J. E. Electrochemical Detection of Single Cancer and Healthy Cell Collisions on a Microelectrode. *Chem. Commun.* 2016, 52, 10906−10909.

(35) Karimi, A.; Hayat, A.; Andreescu, S. Biomolecular Detection at SsDNA-Conjugated Nanoparticles by Nano-Impact Electrochemistry. *Biosens. Bioelectron.* 2017, 87, 501−507.

(36) Andreescu, D.; Kirk, K. A.; Narouei, F. H.; Andreescu, S. Electroanalytic Aspects of Single-Entity Collision Methods for Bioanalytical and Environmental Applications. *Chemelectrochem* 2018, 5, 2920−2936.

(37) Krause, K. J.; Adly, N.; Yakushenko, A.; Schnitker, J.; Mayer, D.; Offenhäusser, A.; Wolfrum, B. Influence of Self-Assembled Alkanethiol Monolayers on Stochastic Amperometric On-Chip Detection of Silver Nanoparticles. *Anal. Chem.* 2016, 88, 3632−3637.

(38) Chazalviel, J.-N.; Allongue, P. On the Origin of the Efficient Nanoparticle Mediated Electron Transfer across a Self-Assembled Monolayer. *J. Am. Chem. Soc.* 2011, 133, 762−764.

(39) Barfidokht, A.; Ciampi, S.; Luais, E.; Darwish, N.; Gooding, J. J. Distance-Dependent Electron Transfer at Passivated Electrodes Decorated by Gold Nanoparticles. *Anal. Chem.* 2013, 85, 1073−1080.

(40) Bradbury, C. R.; Zhao, J.; Fermín, D. J. Distance-Independent Charge-Transfer Resistance at Gold Electrodes Modified by Thiol Monolayers and Metal Nanoparticles. *J. Phys. Chem. C* 2008, 112, 10153−10160.

(41) Weiß, L. J. K.; Rinklin, P.; Wolfrum, B. Opportunities and Challenges of Translating Direct Single Impact Electrochemistry to High-Throughput Sensing Applications. *Curr. Opin. Electrochem.* 2020, 22, 203−210.

(42) Figueiredo, P. G.; Grob, L.; Rinklin, P.; Krause, K. J.; Wolfrum, B. On-Chip Stochastic Detection of Silver Nanoparticles without a Reference Electrode. *ACS Sens.* 2018, 3, 93−98.

(43) Modha, S.; Castro, C.; Tsutsui, H. Recent Developments in Flow Modeling and Fluid Control for Paper-Based Microfluidic Biosensors. *Biosens. Bioelectron.* 2021, 178, 113026.

(44) Weiß, L. J. K.; Music, E.; Rinklin, P.; Straumann, L.; Grob, L.; Mayer, D.; Wolfrum, B. Engineering Electrostatic Repulsion of Metal Nanoparticles for Reduced Adsorption in Single-Impact Electrochemical Recordings. *ACS Appl. Nano Mater.* 2021, 4, 8314−8320.

(45) Lemineur, J.-F.; Stockmann, T. J.; Médard, J.; Smadja, C.; Combellas, C.; Kanoufi, F. Optical Nanoimpacts of Dielectric and Metallic Nanoparticles on Gold Surface by Reflectance Microscopy: Adsorption or Bouncing? *J. Anal. Test.* 2019, 3, 175−188.

(46) Saw, E. N.; Kratz, M.; Tschulik, K. Time-Resolved Impact Electrochemistry for Quantitative Measurement of Single-Nanoparticle Reaction Kinetics. *Nano Res.* 2017, 10, 3680−3689.

(47) Ma, W.; Ma, H.; Yang, Z.-Y.; Long, Y.-T. Single Ag Nanoparticle Electro-Oxidation: Potential-Dependent Current Traces and Potential-Independent Electron Transfer Kinetic. *J. Phys. Chem. Lett.* 2018, 9, 1429−1433.

(48) Robinson, D. A.; Kondajji, A. M.; Castañeda, A. D.; Dasari, R.; Crooks, R. M.; Stevenson, K. J. Addressing Colloidal Stability for Unambiguous Electroanalysis of Single Nanoparticle Impacts. *J. Phys. Chem. Lett.* 2016, 7, 2512−2517.

(49) Squires, T. M.; Messinger, R. J.; Manalis, S. R. Making It Stick: Convection, Reaction and Diffusion in Surface-Based Biosensors. *Nat. Biotechnol.* 2008, 26, 417−426.

(50) Alligrant, T. M.; Anderson, M. J.; Dasari, R.; Stevenson, K. J.; Crooks, R. M. Single Nanoparticle Collisions at Microfluidic Microband Electrodes: The Effect of Electrode Material and Mass Transfer. 2014, 8. 13462. DOI: 10.1021/la503628h

(51) Lemineur, J.-F.; Noël, J.-M.; Courty, A.; Ausserré, D.; Combellas, C.; Kanoufi, F. In Situ Optical Monitoring of the Electrochemical Conversion of Dielectric Nanoparticles: From Multistep Charge Injection to Nanoparticle Motion. *J. Am. Chem. Soc.* 2020, 142, 7937−7946.

(52) Robinson, D. A.; Liu, Y.; Edwards, M. A.; Vitti, N. J.; Oja, S. M.; Zhang, B.; White, H. S. Collision Dynamics during the Electrooxidation of Individual Silver Nanoparticles. *J. Am. Chem. Soc.* 2017, 139, 16923−16931.

(53) Oja, S. M.; Robinson, D. A.; Vitti, N. J.; Edwards, M. A.; Liu, Y.; White, H. S.; Zhang, B. Observation of Multipeak Collision Behavior during the Electro-Oxidation of Single Ag Nanoparticles. *J. Am. Chem. Soc.* 2017, 139, 708−718.

(54) Ustarroz, J.; Kang, M.; Bullions, E.; Unwin, P. R. Impact and Oxidation of Single Silver Nanoparticles at Electrode Surfaces: One Shot versus Multiple Events. *Chem. Sci.* 2017, 8, 1841−1853.

(55) Ma, W.; Ma, H.; Chen, J.-F.; Peng, Y.-Y.; Yang, Z.-Y.; Wang, H.-F.; Ying, Y.-L.; Tian, H.; Long, Y.-T. Tracking Motion Trajectories of Individual Nanoparticles Using Time-Resolved Current Traces. *Chem. Sci.* 2017, 8, 1854−1861.

(56) Ngamchuea, K.; Clark, R. O. D.; Sokolov, S. V.; Young, N. P.; Batchelor-McAuley, C.; Compton, R. G. Single Oxidative Collision Events of Silver Nanoparticles: Understanding the Rate-Determining Chemistry. *Chem. - Eur. J.* 2017, 23, 16085−16096.

(57) Kätelhön, E.; Cheng, W.; Batchelor-McAuley, C.; Tschulik, K.; Compton, R. G. Nanoparticle-Impact Experiments Are Highly Sensitive to the Presence of Adsorbed Species on Electrode Surfaces. *Chemelectrochem* 2014, 1, 1057−1062.

(58) Batchelor-McAuley, C.; Ellison, J.; Tschulik, K.; Hurst, P. L.; Compton, R. G.; Compton, R. In Situ Nanoparticle Sizing with Zeptomole Sensitivity. *Analyst* 2015, 140, 5048−5054.

(59) Krause, K. J.; Brings, F.; Schnitker, J.; Kätelhön, E.; Rinklin, P.; Mayer, D.; Compton, R. G.; Lemay, S. G.; Offenhäusser, A.; Wolfrum,

B. The Influence of Supporting Ions on the Electrochemical Detection of Individual Silver Nanoparticles: Understanding the Shape and Frequency of Current Transients in Nano-Impacts. *Chem.—Eur. J.* **2017**, *23*, 4638−4643.

(60) Ma, H.; Chen, J.-F.; Wang, H.-F.; Hu, P.-J.; Ma, W.; Long, Y.-T. Exploring Dynamic Interactions of Single Nanoparticles at Interfaces for Surface-Confined Electrochemical Behavior and Size Measurement. *Nat. Commun.* **2020**, *11*, 2307.

(61) Defnet, P. A.; Zhang, B. Collision, Adhesion, and Oxidation of Single Ag Nanoparticles on a Polysulfide-Modified Microelectrode. *J. Am. Chem. Soc.* **2021**, *143*, 16154−16162.

(62) Cheng, W.; Compton, R. G. Electrochemical Detection of Nanoparticles by 'Nano-Impact' Methods. *Trac. Trends Anal. Chem.* **2014**, *58*, 79−89.

(63) Shrestha, S.; Wang, B.; Dutta, P. Nanoparticle Processing: Understanding and Controlling Aggregation. *Adv. Colloid Interface Sci.* **2020**, *279*, 102162.

(64) Park, K. Prevention of Nanoparticle Aggregation during Freeze-Drying. *J. Controlled Release* **2017**, *248*, 153.

📖 **Recommended by ACS**

Single-Entity Electrochemistry for Digital Biosensing at Ultralow Concentrations

Serge G. Lemay and Taghi Moazzenzade
JUNE 24, 2021
ANALYTICAL CHEMISTRY
READ ☑

Parallel Field-Effect Nanosensors Detect Trace Biomarkers Rapidly at Physiological High-Ionic-Strength Conditions

Benjamin Barnes, YuHuang Wang, *et al.*
JUNE 14, 2022
ACS SENSORS
READ ☑

Real-Time Monitoring of Biomolecules: Dynamic Response Limits of Affinity-Based Sensors

Rafiq M. Lubken, Menno W. J. Prins, *et al.*
JANUARY 03, 2022
ACS SENSORS
READ ☑

Numerical Modeling for Sensitive and Rapid Molecular Detection by Membrane-Based Immunosensors

Hiroto Okuyama, Takeo Yamaguchi, *et al.*
MAY 06, 2021
ANALYTICAL CHEMISTRY
READ ☑

Get More Suggestions >

Prototype Digital Lateral Flow Sensor Using Impact Electrochemistry in a Competitive Binding Assay

L.J.K. Weiß, P. Rinklin, B. Thakur, E. Music, H. Url, I. Kopic, D. Hoven, M. Banzet, T. von Trotha, D. Mayer, B. Wolfrum

Synopsis

Whereas commercial citrate-capped nanoparticles have been used in the previous study, this work can be seen as follow-up, as it implements particle specificity to design a prototype bioassay. Specifically, we demonstrate in this work the potential of impact electrochemistry to be integrated into common assay schemes to detect small molecules at low concentrations by using the biotin/streptavidin model system as an example. In our sensor, biotin-functionalized nanoparticles compete with free biotin species for streptavidin binding sites and any unbound nanoparticles are monitored further downstream. To facilitate this approach, the nanoparticles require a well-designed corona that enables specific binding to the target species while maintaining redoxactivity and colloid stability. In order to accomplish this task, we employed a mixed self-assembled monolayer consisting of protruding, specific ligands and short 'spacer' alkanethiolate molecules, which enabled concurrent binding and detection. We applied a pH-assisted ligand exchange method to modify the nanoparticles with biotin and confirmed successful modification via UV/Vis spectra, dynamic light scattering, and zeta-potential measurements. We further verified the colloid stability of the nanoparticles in various buffers and tested their ability to bind specifically to streptavidin with SPR sensorgrams. We also conducted experiments to study the redoxactivity of the particles revealing that sufficiently high oxidation potentials are required for complete oxidation. Finally, we integrated the nanoparticles into a lateral-flow architecture and designed a proof-of-concept sensor. It consists of a fiber-based membrane that was laser patterned and attached to a clean-room fabricated MEA chip. A capture area was created via streptavidin-coated latex microbeads located upstream to the sensing area. We performed complementary colorimetric and impact measurements and were able to monitor free biotin at nM to pM concentrations. In summary, this work pioneers digital sensing under typical point-of-care constraints, showcasing its immense potential for the future on-site detection of extremely dilute species. The Supplementary Material to the study is provided in Appendix A.4.

Individual Contribution

conceptualization of the study, data acquisition, data processing and analysis, data interpretation, leading role in composition and writing of the manuscript

Prototype Digital Lateral Flow Sensor Using Impact Electrochemistry in a Competitive Binding Assay

Lennart J. K. Weiß, Philipp Rinklin, Bhawana Thakur, Emir Music, Heike Url, Inola Kopic, Darius Hoven, Marko Banzet, Tassilo von Trotha, Dirk Mayer, and Bernhard Wolfrum*

Read Online

ACCESS | Metrics & More | Article Recommendations | SI Supporting Information

ABSTRACT: This work demonstrates a lateral flow assay concept on the basis of stochastic-impact electrochemistry. To this end, we first elucidate requirements to employ silver nanoparticles as redox-active labels. Then, we present a prototype that utilizes nanoimpacts from biotinylated silver nanoparticles as readouts to detect free biotin in solution based on competitive binding. The detection is performed in a membrane-based microfluidic system, where free biotin and biotinylated particles compete for streptavidin immobilized on embedded latex beads. Excess nanoparticles are then registered downstream at an array of detection electrodes. In this way, we establish a proof of concept that serves as a blueprint for future "digital" lateral flow sensors.
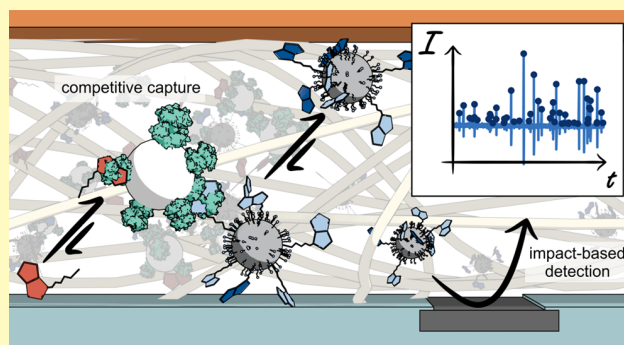
R ecent advances in nanotechnology render (bio)sensing on the brink of a new era.[1−3] In particular, stochastic-impact electrochemistry enables species to be detected at and beyond pM-concentrations.[4,5] Here, individual nano-entities in solution can be traced by a characteristic $i-t$-signal when they collide with an electrode of μm scale. This method facilitates a new concept of "digital" sensing, which determines the presence of a species by an unambiguously identifiable perturbation ("1") compared to the background signal in its absence ("0"). Since every single entity colliding on the microelectrode causes a current transient, the concentration of the species can be inferred by simply counting the number of observed spikes in a given time frame.

Digital sensors come with several interesting properties that are fundamentally different from common (optical) techniques in environmental and biosensing applications. Most prominently, they feature a limit of detection at the theoretical constraint of a single entity while the statistical certainty increases with time. This allows, for instance, the reliable detection of ultralow concentrations by employing extended measurement durations. Further statistical validity can be gained via parallel recordings from microelectrode arrays.[6] Therefore, impact-based sensing is an appealing approach to detect dilute species in future point-of-care settings. In the past decade, metallic and, particularly, silver nanoparticles (AgNPs) have been the subject of extended studies.[7] By exploiting their redox activity, these nanoparticles can be oxidized at an appropriately biased electrode, leading to a distinct positive current spike.

In general, (metal) nanoparticles received great attention across many research fields due to their special physicochemical properties, which render them a useful tool in various (bio)applications. A key aspect in this context is particle specificity, which is typically implemented by surface modifications that enable selective targeting. Especially in immunosensing, functionalized nanoparticles can act as labels for biorecognition processes, similar to optical tags and enzymes that drive catalytic reactions.[8−11] For instance, the widely used lateral flow sensor relies on the colorimetric readout of agglomerating gold nanoparticles that are captured within a sandwich assay. In quantitative methods, nanoparticles have mostly been used as carriers to amplify the (optical) signal or to yield electrochemical information based on ensemble characteristics.[11−14] Whereas optical methods mostly rely on (enzyme- or dye-conjugated) gold nanoparticles, electrochemical readouts often use silver and platinum nanoparticles due to their useful redox properties.[15−19] Especially, the catalytic behavior of platinum and the electrooxidation of silver are exploited to design sensor responses.[20,21]
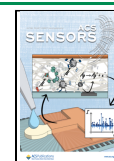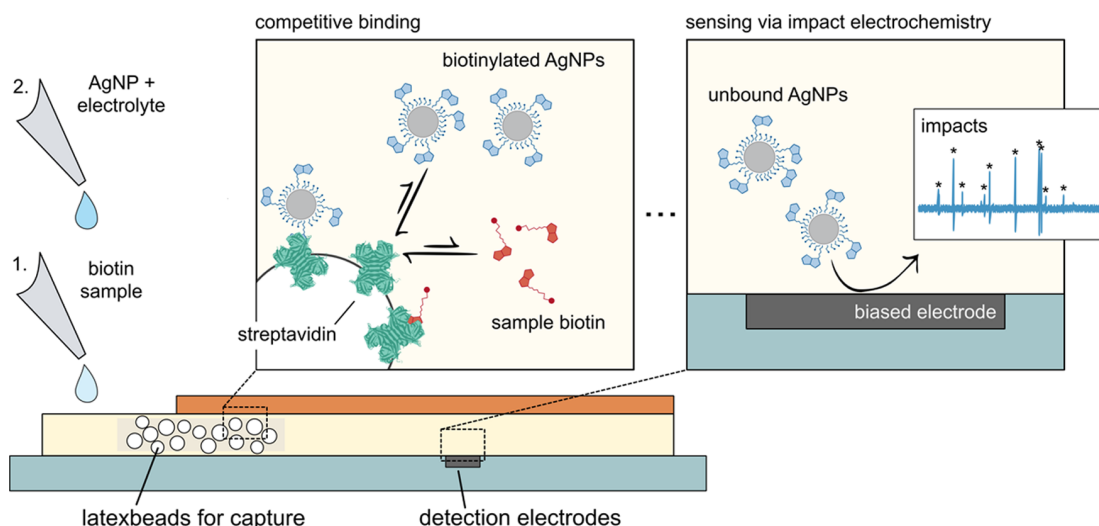
Figure 1. A digital lateral flow sensor based on competitive binding and stochastic-impact electrochemistry. The biotinylated particles compete with free biotin for streptavidin capture sites. Excess nanoparticles are detected further downstream by their electrooxidative impacts at biased microelectrodes.

In contrast to mean-field techniques, impact-based sensing could raise immunoassays to a new level of sensitivity. As the majority of biorecognition couples (e.g., antibodies or aptamers) can be combined with thiol-based particle conjugation, the detection method is essentially interchangeable. This allows translating already existing optical and electrochemical assays into digital ones. Although there have been recent attempts to design impact-based biosensors,[22−28] the integration of stochastic sensing into existing schemes is still challenging. Particularly, the selection of buffers and the coating of the particles become critical, as various criteria, e.g., specific binding and detection, have to be guaranteed at the same time. Up until now, the presence of the analyte species is oftentimes monitored by either turning on or off the digital signal due to changes in the particles' corona—e.g., via DNA strand replacement or species adsorption/aggregation.[21,29,30]

We, however, imagine particles—being all-time redox-active until detection—that could be specifically bound to the target analyte/aptamer/antibody, thus, integrated into competitive and sandwich assay workflows.

In this study, we propose a sensor concept that utilizes impacts of electroactive, specifically coated silver nanoparticles as readout within a lateral flow configuration. We integrate stochastic sensing into a competitive binding assay for the well-known couple of biotin/streptavidin (see Figure 1). We selected this model, since the interaction of biotin/streptavidin is rapid, strong, and stable ($K_d < 10^{-14}$ M) over a wide range of pH values, temperatures, buffers, and detergents, which allows us to apply favorable conditions for the detection.[31−33] As we aim for a framework that could potentially be used in future point-of-care settings, our sensor prototype (shown in Figure 2) employs a membrane-based microfluidic system with a simplified electrochemical setup. We recorded impacts from 62 electrodes in parallel and were able to yield results within 5 min.

■ MATERIALS AND METHODS

Chemicals. AgNPs (40 nm diameter, citrate-capped, 0.02 mg/mL in aqueous solution), sulfuric acid (H$_2$SO$_4$, 95.0−98.0%), 3-mercaptopropionic acid (MPA), 11-mercaptoundecanoic acid (MUA), N-(3-dimethylaminopropyl)-N'-ethylcarbodiimide hydro-
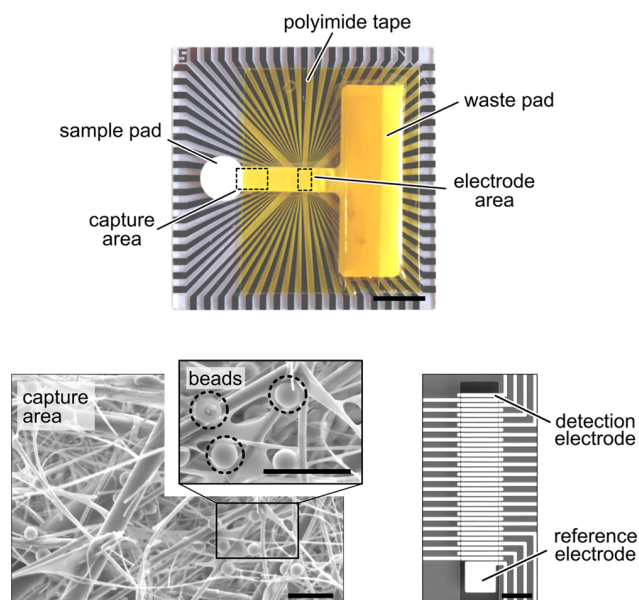
Figure 2. Sensor structure. The digital sensor consists of a 64-electrode chip and a membrane-based microfluidic support (scale bar 0.5 cm). The close-ups show the capture area consisting of streptavidin-coated 3 μm-sized latex beads (scale bar 10 μm, scanning electron microscopy) and the electrode array (scale bar 100 μm, optical image).

chloride (EDC), N-hydroxysulfosuccinimide sodium salt (s-NHS), 2-(N-morpholino)ethanesulfonic acid (MES), ethanolamine, modified phosphate-buffered saline (PBS) solution, and ethanol were purchased from Sigma-Aldrich (St. Louis). Potassium chloride (KCl), potassium hydroxide (KOH), sodium hydroxide (NaOH), and Tween 20 were bought from Merck (Wiesbaden, Germany). EZ-Link pentylamine-biotin, biotinylated peroxidase, streptavidin, and carboxylated latex beads (4% w/v, 3 μm diameter) were purchased from Thermo Fisher Scientific (Waltham). Thiolated PEG-biotin (HS-C11-(EG)3-biotin) was obtained from ProChimia Surfaces (Gdynia, Poland). TMB substrate solution was bought from Mercodia (Uppsala, Sweden). All dilutions were prepared via deionized water (conductivity 0.054 μS/cm) from a Berry Pure purification system

(Berrytec, Harthausen, Germany). The pH was adjusted using either 100 mM HCl or 100 mM NaOH solution.

EDC/NHS Chemistry for Biotin Complex and Streptavidin-Coated Latex Beads. The biotin ligand was prepared using common EDC/NHS coupling chemistry. To ensure a negative surface charge in case of incomplete coupling, 3-mercaptopropionic acid (MPA) and pentylamine-biotin were selected to form the ligand complex. For coupling, 100 μL of 1 mM pentylamine-biotin, 100 μL of 100 μM MPA, and 25 μL of 2 mg/mL EDC in 50 mM MES pH 5 and 25 μL of 3 mg/mL s-NHS in 50 mM MES pH 5 were shaken for 15 min at 35 °C. Afterward, 10 μL of 1 M ethanolamine was added to deactivate unreacted esters. Consequently, the final concentration of the biotin complex is ~39 μM, assuming a 100% coupling yield.

The streptavidin-coated latex beads were prepared similarly to the above procedure, using 400 μL of 4% w/v carboxylated latex beads with a diameter of 3 μm, 100 μL of 2 mg/mL EDC in 50 mM MES pH 5, 100 μL of 3 mg/mL s-NHS in 50 mM MES pH 5, 200 μL of 1 μM streptavidin, 200 μL of 1% Tween 20, and 50 μL of 1 M ethanolamine. The final suspension was centrifuged for four times at 10,000×g for 5 min to remove the excess streptavidin.

pH-Assisted Functionalization of AgNPs. The particle functionalization was done via pH-assisted ligand exchange similar to the protocol of Zhang et al.[34] First, 600 μL of commercially available citrate-capped AgNPs were mixed with 4 μL of ligand solution. For the preparation of carboxylated particles, 100 μM MPA was used, whereas biotinylated particles were prepared using the complex solution described above, which contains ~39 μM of thiolated-biotin ligands. Then, 2 μL of 500 mM sodium citrate at pH 3 was added and vigorously mixed. After 15 min of incubation, 6 μL of 500 mM HEPES was inserted to adjust the pH back to neutral values. Afterward, 2 μL of 100 μM MPA was added, and the suspension was left overnight at 4 °C. Finally, 10 μL of 1% Tween 20 and 900 μL of deionized water were added prior to particle washing. The purification was done via repeated (4×) centrifugation at 6,100×g for 15 min. The final biotin particle concentration was estimated to be ~65 pM, based on the comparison of UV/Vis spectra with the commercially available citrate-capped AgNPs (~94 pM). The biotinylated AgNPs were further concentrated by another centrifugation step, leading to a stock concentration of ~260 pM.

Fabrication of the Lateral Flow Sensors. The sensor prototype comprises a glass fiber-based microfluidic support attached to a cleanroom-fabricated microelectrode chip (see Figure 2). The fabrication of the chips is described in earlier work.[35] A chip contains 64 platinum electrodes that are passivated by a stack of 40 nm Ta_2O_5 and 5 alternating SiO_2 and Si_3N_4 layers, with SiO_2 being the top layer. It consists of 62 band electrodes with 13 μm width and 125 μm length, which are divided into two arrays on the chip. Each electrode set contains a platinum quasi-reference electrode with an area of 100 × 100 μm².

The microchannel is fabricated via laser-cutting of a Fusion 5 membrane (Whatman, Cytiva). The membrane is 370 μm thick, features wicking velocities of ~1 mm/s, and has a hydrophilic surface that does not need additional blocking. The channel boundaries were created with a Keyence 3-axis laser marker MD-U1000C (wavelength 355 nm) using five boundary lines being 10 μm apart, which are illuminated 150 times with 2.5 W at 40 kHz pulse frequency and a scan velocity of 1 m/s. The channel design includes a sample pad with a radius of 5.5 mm, a 6 mm wide and 25 mm long channel, and a rectangular waste area of 48 × 15 mm². The sensor prototype was prepared by adding 8 μL of streptavidin-coated beads (3 μm diameter, suspension ~4% w/v) onto the capture area before the microchannel membrane was manually fixed onto the chip using 120 μm thick polyimide tape (Kapton tape, DuPont, Wilmington).

Single-Impact Experiments and Evaluation. Prior to the experiments, the chips were electrochemically activated via cyclic voltammetry in 200 mM H_2SO_4 (potential range from −0.2 to 1.5 V vs Ag/AgCl, scan rate 500 mV/s, 30 cycles) using a VSP-300 potentiostat (BioLogic Instruments, France) in a three-electrode configuration with an Ag/AgCl Dri-Ref reference electrode from World Precision Instruments and a coiled platinum wire as a

counter electrode, respectively. The detection experiments were performed with a custom 64-channel amplifier system (10 kHz sampling frequency per channel, 3.4 kHz bandwidth) in a 2-electrode configuration. The large 100 × 100 μm²-electrodes were used as quasi-reference on-chip, which leads to a simplified detection setup and enables the multiple usage of a single chip. All lateral flow experiments were conducted in the following way: If not otherwise stated, the electrodes were first forced to a high overpotential of 1.2 V versus the open circuit potential (OCP) of the platinum quasi-reference. Then, 2 μL of biotin analyte was added, and the microchannel was subsequently flushed with 30 μL of the electrolyte solution containing 35 mM KCl, 50 mM KOH, and 30 pM of biotinylated 40 nm-AgNPs. In the case of carboxylated AgNPs, the final concentration in the detection solution was 8 pM.

The data was processed and analyzed in MATLAB as described earlier.[36] The algorithm includes the detrending of the current traces, the evaluation of the channel quality based on the background noise, and the application of a current threshold to extract the current peaks associated with AgNP impacts. All lateral flow experiments were evaluated based on a conservative fixed threshold of 50 pA to avoid misclassification of noise, whereas channel-specific thresholds ($0.5 i_{pk2pk}$ +25 pA, where i_{pk2pk} is the peak-to-peak current for the respective potential in the absence of particle impacts) were used to extract the current peaks at different oxidation potentials. Amplifier-related ringing artifacts that follow the initial charge injection—visible as negative current peaks—are excluded by considering a minimum inter-peak distance of 15 ms. To account for fabrication defects among the chips, the results are typically based on a subset of electrodes, which detected the highest number of peaks. For the calibration curve, the subset from all working electrodes was determined via the 2σ-interval of all impact rates. After the removal of the outlier, the displayed statistical measures were calculated as ensemble means and standard deviations and transferred to a logarithmic scale. Thus, the error bars visualize the log(mean) and the relative errors, calculated via 1/ln(10) std/mean for each concentration.

The current peaks are further analyzed regarding their amplitude and duration to extract the delivered charge during impact and the associated particle size. The charge is obtained from integration of all sample points that exceed the noise level during a collision event. Assuming a spherical shape, the charge per impact can be converted into a particle diameter d_p via

$$d_p = 2 \cdot \sqrt[3]{\frac{3 M_{Ag} Q}{4\pi z F \rho_{Ag}}}$$

where M_{Ag} is the molar mass of Ag, Q is the delivered charge, z is the valency of Ag, F is Faraday's constant, and ρ_{Ag} is the mass density of Ag. Consequently, estimated diameters that are substantially lower than the known particle size indicate either incomplete or prolonged and, thereby, masked oxidation events.

Surface Plasmon Resonance Experiments. The surface plasmon resonance (SPR) experiments were performed with a 2-channel system (SR7500DC from Reichert, Depew) using a 100 μL sample loop. The SPR chips were fabricated in-house and featured a thin Ti layer, followed by a 45−50-nm thick Au layer on top of borosilicate glass (0.3 mm thick, AF32eco from Schott, Germany). Before usage, the chips were cleaned in O_2-plasma (0.6−0.8 mbar at 80 W, Diener Femto, Diener electronic, Germany) for 30 min and subsequently functionalized with a heterogeneous biotin self-assembled monolayer. To this end, the chips were immersed in 6:1 MUA/HS-PEG-Biotin solution (14 μM HS-PEG-Biotin, in ethanolic solution) overnight and stored in ethanol until usage.

To evaluate the interaction of biotinylated and carboxylated AgNPs with streptavidin and biotin surfaces, only one channel was flushed with streptavidin to bind with heterogeneous biotin-SAM, whereas the reference channel was decoupled during the streptavidin step. The measurements were carried out in 10 mM MES at pH 4.5 as a running buffer at a flow rate of 10 μL/min during the immobilization of streptavidin (200 nM in 10 mM MES at pH 4.5) and all elution steps.
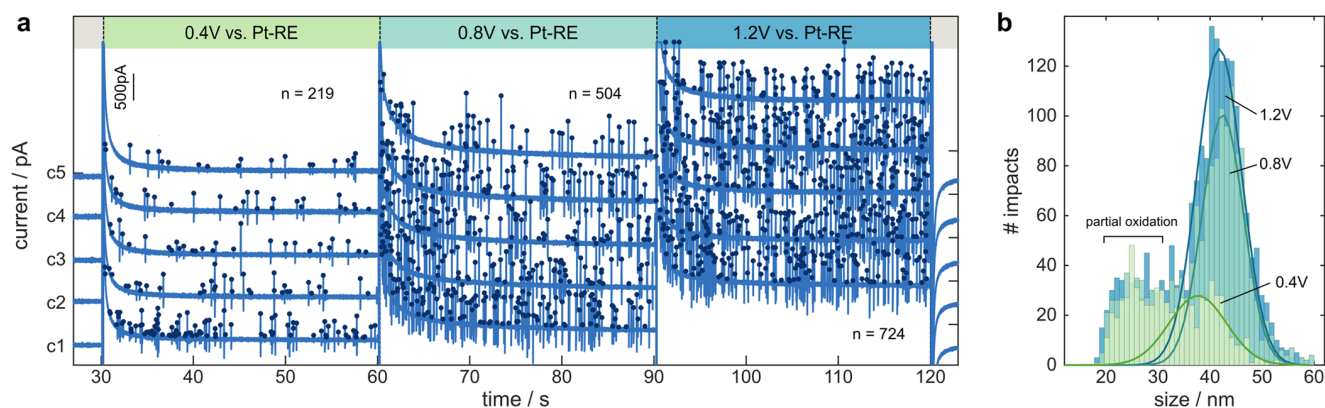
Figure 3. Electrooxidation of biotinylated AgNPs. The AgNPs remain redox-active after ligand exchange and high overpotentials lead to a greater detection yield. (a) Current recordings within a 35 mM KCl, 50 mM KOH solution containing ~20 pM biotin-AgNPs. The potential was stepped from −0.4 V to different oxidation potentials of 0.4, 0.8, and 1.2 V vs Pt-RE, respectively. All current peaks considered for further analysis are highlighted by blue dots. Note that negative current spikes follow the initial charge injections and are amplifier-related artifacts. (b) Particle size distribution for different potentials obtained from 10 channels.

For the association and dissociation of AgNPs, the flow rate was decreased to 5 μL/min. Since solutions containing chloride ions caused particle adsorption in the tubes, the elution steps were performed with 10 mM NaOH. Additionally, 1% Tween 20 was flushed over the chip prior to the AgNP capture, which helped to block the tube walls and flow cell surfaces and reduced interfering phenomena. The carboxylated and biotinylated AgNPs were diluted to ~30 pM using 10 mM MES at pH 4.

Colorimetric Experiments Using Horseradish Peroxidase. Complementary information for the competitive binding assay was obtained from colorimetric experiments using the 3,3′,5,5′-tetramethylbenzidine (TMB) substrate solution and horseradish peroxidase-tagged (HRP) biotin. To this end, small strips of the Fusion 5 membrane (3 mm wide and 10 cm long) were used to locally embed 8 μL of 4% w/v streptavidin-coated or carboxylated latex beads, as well as 10 μL of modified AgNPs. Then, 2 μL of 100 nM biotin-HRP were released to be flushed over the capture area using 100 μL of 1:10-diluted modified PBS solution. Afterward, 5 μL of the TMB substrate solution was added to the capture area, and the color change was imaged after 10 min using a conventional photo camera.

Other Optical Measurements. UV/Vis spectra were recorded in polystyrol cuvettes with a Analytik Jena Specord 200 (Jenoptik, Jena, Germany). The ζ-potentials were determined using a Zetasizer Nano ZS (Malvern Panalytical, Malvern, U.K.) and disposable folded capillary cells. The hydrodynamic diameters of the functionalized particles were also assessed with the Zetasizer Nano ZS within a polystyrol semi-micro cuvette. The scanning electron microscopy was performed with a JEOL JSM-6060LV (JEOL, Japan) at 10 kV acceleration voltage.

■ RESULTS AND DISCUSSION

Coated Nanoparticles as Labels. To utilize AgNPs as labels for biosensing, several requirements regarding the particle corona have to be fulfilled: (i) the particle should exhibit only target-specific binding while (ii) its shell must not impede redox activity, and (iii) it should ensure colloid stability.

The detectability of a coated particle's impact is mainly a matter of ligand length and density, as the particle surface has to reach the tunneling distance of the electrode to become oxidized.[37] Therefore, the challenge of designing specific yet detectable particles is reciprocal to studies that target electrode functionalization. Self-assembled monolayers (SAM) on detection electrodes are known to play a critical role in impact experiments,[38] where a long (C16) chain length was found to

inhibit particle oxidation completely.[37,39] Keeping this in mind, we aimed for a heterogeneous particle functionalization using a short "spacer" ligand (mercaptoproprionic acid) and a longer ligand that provides specificity (mercaptoproprionic acid and pentylamine-biotin, chain length ~C13). This mixed corona is expected to both maintain redox activity as well as improve specific binding by reducing steric hindrance. In addition, the short carboxylic spacer leads to increased colloid stability. Furthermore, the actual size of the particle is also a critical parameter for impact electrochemistry, since large particles with diameters ≥30 nm were shown to undergo incomplete oxidation.[40−42] In this case, the relationship of one peak per particle no longer holds true, and multiple collisions with small current amplitudes can occur. However, as we use large electrodes with a size of $125 \times 13 \ \mu m^2$, we also face an increased noise level during recording. Based on previous investigations,[35] we selected 40 nm particles, since they yield sufficiently high current amplitudes compared to the background noise of the electrodes. This choice increases the signal-to-noise ratio, yet it comes at the cost of reduced diffusive transport and an increased likelihood of incomplete oxidation upon collision.

To obtain biotinylated and carboxylated (control) particles, we modified commercial citrate-capped particles via pH-assisted ligand exchange.[34] The modification was monitored by recording UV/Vis spectra (see Figure S1a). The biotinylation led to a small red shift (~2 nm) of the localized surface plasmon resonance (LSPR) peak, which is typically attributed to a successful thiol bond formation.[43,44] This result was further confirmed by changes in the hydrodynamic diameters and ζ-potentials after the functionalization of the particles (see Figure S1b,c).

After a successful ligand exchange, we investigated the stability of the suspensions. In general, the particles have to be stable not only during modification at low ionic strength but also within the electrolyte later used for impact-detection, as aggregation and adsorption impede a reliable calibration. Typically, AgNPs are detected in KCl solutions, although other electrolytes are also possible.[45,46] Since alkaline solutions yield higher impact rates,[47] we chose a detection environment of 35 mM KCl and 50 mM KOH and studied the colloid stability therein (see Figure S2a,b). Both suspensions were stable, and

we measured a ζ-potential of -35 mV in the case of biotin-AgNPs.

Since colloid stability is guaranteed for the plain detection solution, we are left to investigate the functionality of the particles regarding their (i) redox behavior and their (ii) binding characteristics. Figure 3a visualizes the electrooxidation of ~20 pM biotin-AgNPs for different potentials. The associated size distribution is given in Figure 3b (see Figure S3 for further statistical evaluation). Figure 3 clearly demonstrates that redox activity is preserved, although substantial overpotentials are required to detect a sufficient amount of particles. This could be attributed to the larger particle corona, which requires a high potential to extend the tunneling distance and modulate the reaction kinetics.[37,48−50] Apart from the likeliness of charge transfer, the electrode potential can also affect the particles' trajectories in solution. Here, strong background reactions—indicated by different current baselines—might also fuel additional convective transport for high potentials, leading to more impacts.[51−53] Interestingly, the electrode potential alters not only the absolute number of impacts but also the ratio between partial and complete oxidation events significantly (see Figure 3c). Therefore, we applied 1.2 V vs Pt-RE in all following experiments, as it yields the highest number of fully oxidized impacts across the tested potential range. Typically, higher potentials lead to a greater yield of impacts, as they extend the tunneling distance and increase the electrokinetic mass transport toward the electrodes, but they eventually lead also to a simultaneous shrinkage of the electroactive area over time due to platinum oxidation and reactions with interfering species.[36]

Lastly, the coated nanoparticles have to specifically bind to the capture molecule—in our case, streptavidin. We investigated the binding characteristics of biotinylated and carboxylated particles using surface plasmon resonance (SPR), and the results are provided in Figure 4. As the binding of biotin/streptavidin is efficient over a large range of experimental conditions and electrolytes containing chloride ions were subject to particle adsorption in the tubes of the SPR

device, we conducted the measurements in acidic 10 mM MES buffer.[32,33] Here, we studied the interactions of both particle types with previously immobilized streptavidin (blue) and with a biotin self-assembled monolayer (orange). Both conditions can be seen as extreme cases—full capture and absence of the target—and the results in Figure 4 reveal that biotinylated AgNPs specifically bind to streptavidin, whereas there is negligible nonspecific adsorption for carboxylic particles. Both particle types do not interact with the biotin surface.

Digital Competitive Lateral Flow Assay. As we demonstrated the particles (i) to be redox-active, (ii) to bind specifically, and (iii) to be stable in solution, we now aim for a prototype digital lateral flow sensor. Our sensor is supposed to detect free biotin in solution based on a competitive binding assay (see Figure 1). In this case, the free sample biotin competes with biotinylated AgNPs for streptavidin binding sites. We implemented the assay in a lateral flow membrane[35] and created a capture area using streptavidin-coated latex beads (see Figure 2) that is located upstream to the detection electrodes. By flushing the analyte prior to the nanoparticle solution, we were able to monitor free biotin by the detected excess nanoparticles, which are not able to bind to the already occupied streptavidin binding sites. Figure 5 shows exemplary current traces for the digital sensor (blank experiment in Figure S4 and statistical data in Figure S5). The control conditions for nonspecific beads or particles in Figure 5a,b) verify that aggregation and adsorption do not critically interfere. The data in Figure 5c shows the detection of particles in the absence of free biotin, and Figure 5d visualizes the sensor response for 10 nM of free biotin. The comparison of Figure 5c,d clearly demonstrates that biotin-sensing based on a competitive assay in conjunction with impact electrochemistry is possible, as impacts are present/absent in the presence/absence of free biotin.

Common to all signal traces is the transition (see Figure S4) from a fast transport to a slow transport/diffusive regime, which can be attributed to the flow within the membrane geometry.[35] As particle capture is not instantaneous—although very fast for biotin/streptavidin—we generally observe an initial flushing-over effect with many impacts at early times, followed by a slow transport detection regime. In both regimes, we observe a substantial amount of small-amplitude peaks, which can be related to partial oxidation events. In line with our previous work,[35] we find the partial oxidation (see size distribution in Figure S5) to be enhanced during convective flow compared to static conditions (represented in Figure 3b). As a consequence, several small-peak oxidations might stem from the same particle colliding multiple times at the electrode/s. To recover a true 1:1 counting, one could use smaller particles and electrodes to avert multi-collisions while sustaining a high signal-to-noise ratio. Yet, smaller electrodes also lead to decreased impact rates by shrinking the overall electrode area. Moreover, the sampling frequency of the recording device and its bandwidth dictate the temporal resolution of the signal.[54,55] Here, a comprehensive investigation of the noise, the absolute number of detected collisions, and their distribution among the electrode ensemble for different electrode sizes and arrangements along the channel could lead to improved responses.

Complementary to our digital lateral flow sensor, we optically determined the capture of HRP-tagged biotin via streptavidin after previous incubation with biotinylated AgNPs (see Figures 6 and S6). The blue color indicates immobilized
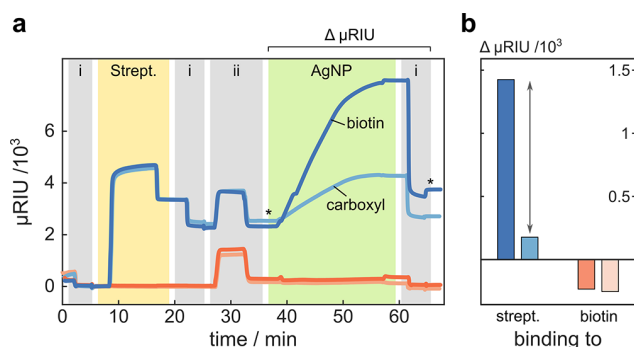

Figure 4. Specificity of AgNP labels. The biotinylated particles bind specifically to streptavidin, whereas particles with a carboxylic coating show only minor unspecific adsorption. Both particle types do not interact with a biotin surface. (a) 2-channel SPR sensograms for the subsequent immobilization of streptavidin onto a biotin layer followed by the capture of biotinylated (dark colors) or carboxylated AgNPs (light colors). The control channel (orange) shows the particle interaction with the biotin-SAM. (b) Difference in binding to streptavidin for biotinylated and carboxylated AgNPs. The data is evaluated at times marked * in panel (a). Elution with NaOH (i) and blocking with Tween 20 (ii) were performed to reduce nonspecific adsorption.
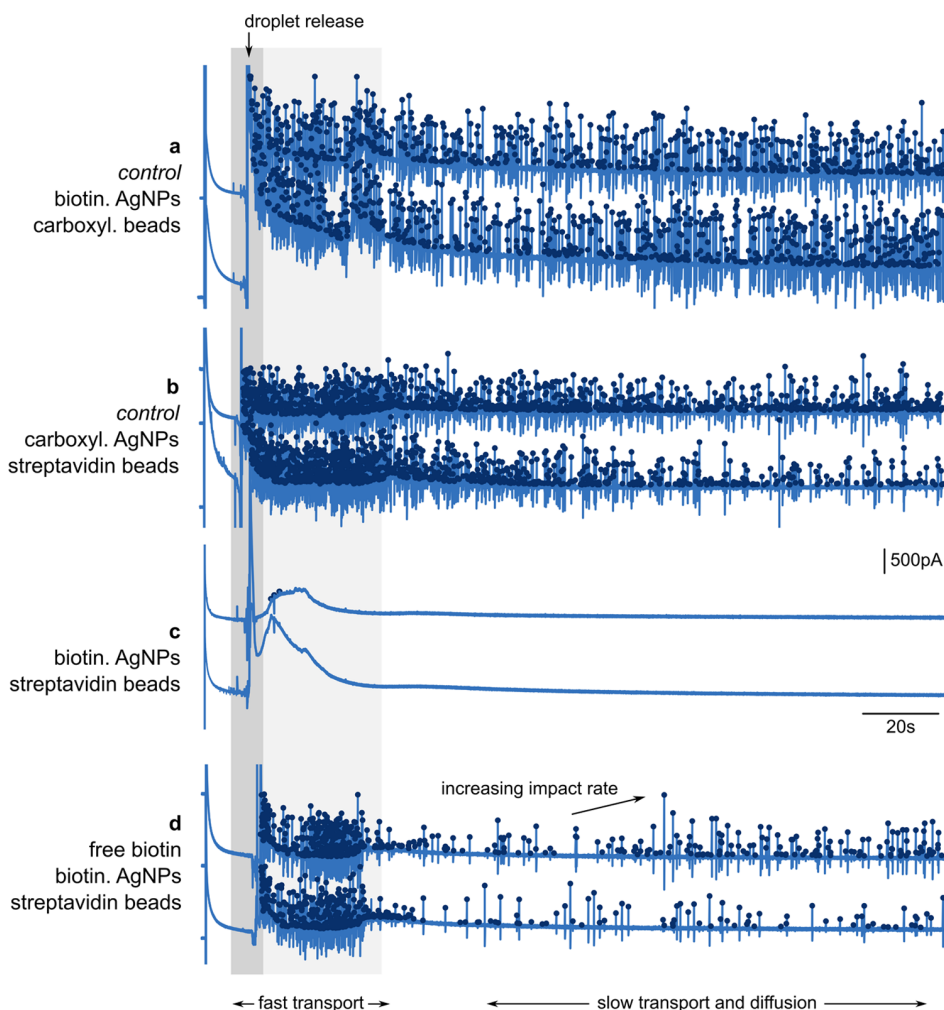
Figure 5. Exemplary recordings of the impact-based sensor in competitive mode. The detection electrodes monitor impacts from excess nanoparticle labels that were not previously captured by functionalized latex beads further upstream. The capture area is either formed by carboxylated (a) or streptavidin-coated beads (b−d). In the case of (d), 2 μL of 10 nM biotin sample solution is released prior to the flushing of the detection solution that contained the nanoparticle labels. All experiments were carried out in 30 μL of 35 mM KCl, 50 mM KOH electrolyte, and with electrodes biased to 1.2 V vs Pt-RE.
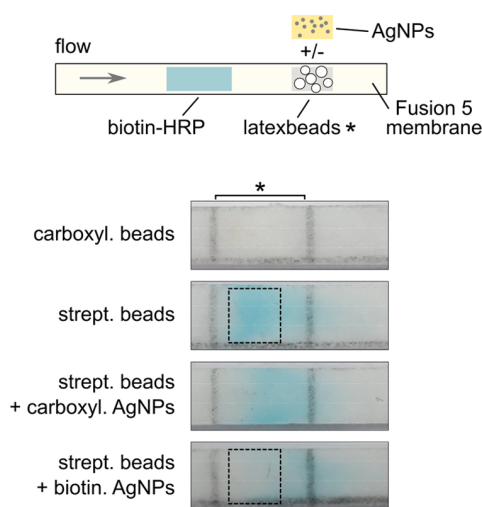
Figure 6. Concept and results of complementary optical tests using biotin-HRP. The modified AgNPs were used to occupy streptavidin binding sites prior to the flushing and capturing of biotin-HRP.

biotin-HRP. The optical results are in line with our previous findings, as we observe a signal inhibition in the presence of biotin particles, whereas the absence of particles leads to a strong blue color change.

To further demonstrate our concept, we monitored free biotin from 10 pM to 100 nM concentrations (see Figure 7). The temporal evolution of the mean impact rate (across the electrode ensemble) in Figure 7a reveals that both transport regimes could, in principle, be used for biotin quantification, although the design guidelines might differ for an optimized detection within one or the other. Consequently, we computed the mean impact rate across the entire acquisition time to obtain the calibration curve in Figure 7b. In this logarithmic plot, each electrode is visualized as a blue dot, and the error graph indicates the mean responses and relative errors. The large errors arise from interfering effects, which most likely stem from differences in the fluid flow, a varying distribution of latex beads within the membrane, and manual handling. Here, a longer microfluidic channel and a different attachment method might improve consistency. During assay establishment, we aimed to strongly reduce the impact rate for the control condition (no free biotin is present). As a
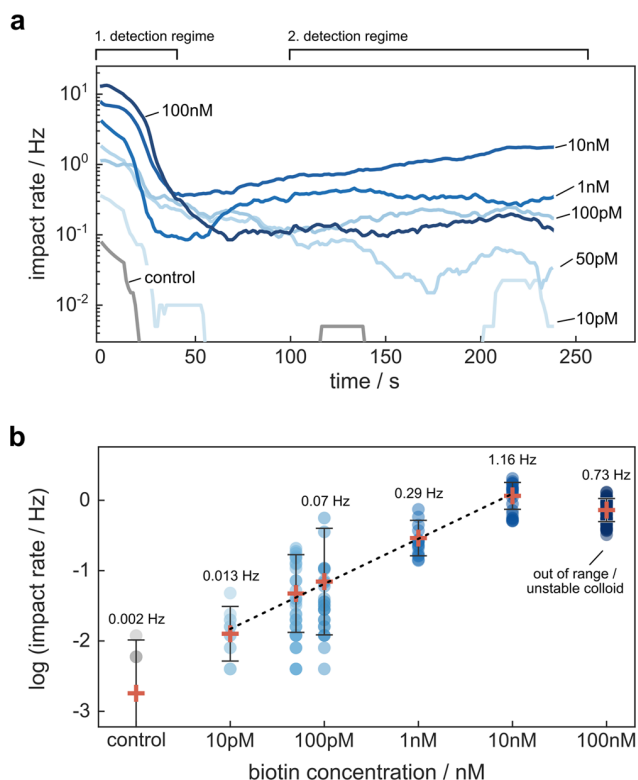
Figure 7. Calibration curve of the digital lateral flow sensor. (a) Temporal evolution of the mean impact rate based on a subset of channels. (b) Calibration plot obtained from 250 s of recording. Individual channels are represented as blue dots, whereas ensemble characteristics are shown as mean and relative error. In all experiments, 2 μL of the analyte was added prior to 30 μL of electrolyte solution containing 30 pM biotinylated AgNPs.

consequence, the range of possible impacts drastically decreases for low concentrations, and we could not reliably differentiate biotin concentrations below 10 pM.

Nonetheless, it is possible to tailor the digital response for a specific concentration range, since the amount of streptavidin and biotinylated particles determine the limit of detection and the sensitivity for a fixed measurement time (see Figure S7). Therefore, we believe that a careful sensor design can push the limits of detection beyond the proof of principle reported here. Another way to achieve lower detection limits is to extend the recording time. The reliable quantification of higher analyte concentrations (see Figures 7b and S8) might be challenging as adsorption and aggregation caused by drying effects can diminish the sensor response in our competitive assay. Furthermore, the 100 nM of biotin is most likely also "out of range," as the maximum number of detectable events is mainly determined by the concentration of biotinylated particles (30 pM). The amount of particles theoretically defines the number of possible impacts, yet the signal is further reduced by particle losses due to advection and interfering adsorption, which might be altered by manual handling or even the analyte concentration itself. Nevertheless, the comparison with a conventional colorimetric approach (in Figure 6) reveals the inherent advances of a digital sensor that relies on impact counting instead of amplitude differences.

Yet, to be fully applicable in future point-of-care settings, the sensor chips should be ready for immediate usage—without preliminary "cleaning" steps. Electrodes are regularly activated

(e.g., in sulfuric acid) prior to their usage to remove oxide layers and increase their performance.[56,57] Especially in impact experiments, the metal-oxide formation due to air exposure can become a critical factor.[36,58] Contrarily, inert conditions during storage (e.g., nitrogen atmosphere or vacuum) could stabilize the electrode condition. We tested the stability of activation during storage in a vacuum chamber for 80 h by performing subsequent impact experiments. The results in Figure S9 reveal that the detection of impacts is still possible—although incomplete oxidation events seem to dominate for the conservation method tested here. Nonetheless, we believe that advanced activation and conservation methods might circumvent this problem so that digital sensing could be performed under point-of-care constraints in the future.

In this work, we successfully detected redox-active particle labels that can be used within a bioassay concept. The performance of such a digital sensor is affected by various factors that should be assessed and taken into account during response optimization. First of all, our findings highlight the crucial role of the particle corona. It should be stable under a variety of electrolyte conditions, such that adsorption and aggregation are less interfering. Moreover, within a competitive assay, the binding affinities of the analyte and the analyte-coated particles are of interest. In our case, it is expected that the biotin being bound to the particle faces less degrees of freedom during capturing than the free molecule. Besides steric hindrance, which could be mitigated by long-chain linkers and/or sparse coverage, the biotinylated nanoparticle also experiences a drastically lower diffusion coefficient than the free biotin. This aspect might be negligible for the couple of biotin/streptavidin due to their strong interaction but becomes increasingly relevant for targets with lower affinity constants. Apart from biorecognition, a suitable (heterogeneous) particle corona is further needed to guarantee efficient detection downstream. In the competitive assay, both mechanisms are also influenced by convective transport because it determines the time available for capture and charge transfer before being swept away.[59] Therefore, the design of the fluidic support, as well as the location of the electrodes, their (electroactive) size, and number, are critical parameters. In an ideal scenario, digital sensing follows a 1:1-relationship between the analyte and the detected particle label.

■ CONCLUSIONS AND OUTLOOK

In conclusion, we demonstrated the integration of impact electrochemistry into an existing assay approach and were able to detect different concentrations of free biotin. Therefore, our study could serve as the groundwork for future sensors that target small analytes, e.g., neurotransmitters or organophosphates, at low concentrations. Especially in these cases, the competitive mode might be favorable, although it comes with its own challenges. Additionally, the application of nanoparticle labels could also be extended to other well-established assays. For instance, nanoparticles could be also conjugated with specific aptamers or Fab fragments—qualifying them as electroactive labels for sandwich assays.

However, the detection of other "real" targets might be far more challenging, since the interaction of our model biotin/streptavidin is mostly insensitive to external factors such as pH, ionic strength, and temperature. This is typically not the case for other specific biorecognition targets. To obtain reliable responses with our approach, several aspects should be

considered during sensor design. First, the selection of electrolytes and the design of the particle labels are of major importance, as colloid stability, specific binding, and redox activity have to be ensured (at the same time). Second, the electrode size, the fluid support, and the bandwidth and sampling rate of the recording device essentially determine whether single-particle collisions can be detected and resolved well.

Within our work, we reported a novel framework that could translate qualitative lateral flow sensors into digital ones by detecting the impacts of nanoparticle labels. We believe that impact electrochemistry is an appealing strategy for next-generation point-of-care sensing as it provides means to detect molecules of interest at low concentrations.

■ ASSOCIATED CONTENT

Supporting Information

The Supporting Information is available free of charge at https://pubs.acs.org/doi/10.1021/acssensors.2c00728.

> Particle functionalization; amplitude, duration, and charge distribution for AgNP impacts; noise evaluation during lateral flow experiment; sensor responses for different streptavidin bead amounts; additional data for the optical experiment; additional data for sensor response in the case of 100 nM biotin; impact experiment after chip storage in vacuum chamber (PDF)

■ AUTHOR INFORMATION

Corresponding Author

Bernhard Wolfrum − *Neuroelectronics - Munich Institute of Biomedical Engineering, Department of Electrical and Computer Engineering, Technical University of Munich, 85748 Garching, Germany;* ⓘ orcid.org/0000-0003-4438-3755; Email: bernhard.wolfrum@tum.de

Authors

Lennart J. K. Weiß − *Neuroelectronics - Munich Institute of Biomedical Engineering, Department of Electrical and Computer Engineering, Technical University of Munich, 85748 Garching, Germany;* ⓘ orcid.org/0000-0002-6943-737X

Philipp Rinklin − *Neuroelectronics - Munich Institute of Biomedical Engineering, Department of Electrical and Computer Engineering, Technical University of Munich, 85748 Garching, Germany;* ⓘ orcid.org/0000-0003-1063-8342

Bhawana Thakur − *Neuroelectronics - Munich Institute of Biomedical Engineering, Department of Electrical and Computer Engineering, Technical University of Munich, 85748 Garching, Germany;* ⓘ orcid.org/0000-0001-9444-4291

Emir Music − *Neuroelectronics - Munich Institute of Biomedical Engineering, Department of Electrical and Computer Engineering, Technical University of Munich, 85748 Garching, Germany;* ⓘ orcid.org/0000-0002-1583-7597

Heike Url − *Neuroelectronics - Munich Institute of Biomedical Engineering, Department of Electrical and Computer Engineering, Technical University of Munich, 85748 Garching, Germany;* ⓘ orcid.org/0000-0002-8738-6529

Inola Kopic − *Neuroelectronics - Munich Institute of Biomedical Engineering, Department of Electrical and Computer Engineering, Technical University of Munich, 85748 Garching, Germany;* ⓘ orcid.org/0000-0002-4147-462X

Darius Hoven − *Neuroelectronics - Munich Institute of Biomedical Engineering, Department of Electrical and Computer Engineering, Technical University of Munich, 85748 Garching, Germany;* ⓘ orcid.org/0000-0003-3814-2699

Marko Banzet − *Institute of Biological Information Processing, Bioelectronics (IBI-3), Forschungszentrum Jülich, 52425 Jülich, Germany*

Tassilo von Trotha − *Neuroelectronics - Munich Institute of Biomedical Engineering, Department of Electrical and Computer Engineering, Technical University of Munich, 85748 Garching, Germany;* ⓘ orcid.org/0000-0003-0549-7119

Dirk Mayer − *Institute of Biological Information Processing, Bioelectronics (IBI-3), Forschungszentrum Jülich, 52425 Jülich, Germany;* ⓘ orcid.org/0000-0003-1296-8265

Complete contact information is available at:
https://pubs.acs.org/10.1021/acssensors.2c00728

Author Contributions

L.J.K.W., P.R., and B.W. designed the study. L.J.K.W., E.M., B.T., T.v.T., and H.U. prepared and performed the experiments. L.J.K.W., M.B., D.H., and I.K. developed and fabricated the sensor structures. L.J.K.W. wrote the manuscript with support from B.T., P.R., D.M., and B.W. All authors provided critical feedback.

Notes

The authors declare no competing financial interest.

■ ACKNOWLEDGMENTS

■ REFERENCES

(1) Goines, S.; Dick, J. E. Review—Electrochemistry's Potential to Reach the Ultimate Sensitivity in Measurement Science. *J. Electrochem. Soc.* **2019**, *167*, No. 037505.

(2) Sekretareva, A. Single-Entity Electrochemistry of Collision in Sensing Applications. *Sens. Actuators Rep.* **2021**, *3*, No. 100037.

(3) Lemay, S. G.; Moazzenzade, T. Single-Entity Electrochemistry for Digital Biosensing at Ultralow Concentrations. *Anal. Chem.* **2021**, *93*, 9023−9031.

(4) Dick, J. E.; Renault, C.; Bard, A. J. Observation of Single-Protein and DNA Macromolecule Collisions on Ultramicroelectrodes. *J. Am. Chem. Soc.* **2015**, *137*, 8376−8379.

(5) Yoo, J. J.; Anderson, M. J.; Alligrant, T. M.; Crooks, R. M. Electrochemical Detection of Insulating Beads at Subattomolar

Concentration via Magnetic Enrichment in a Microfluidic Device. *Anal. Chem.* **2014**, *86*, 4302−4307.

(6) Krause, K. J.; Yakushenko, A.; Wolfrum, B. Stochastic On-Chip Detection of Subpicomolar Concentrations of Silver Nanoparticles. *Anal. Chem.* **2015**, *87*, 7321−7325.

(7) Sokolov, S. V.; Eloul, S.; Kätelhön, E.; Batchelor-McAuley, C.; Compton, R. G. Electrode−Particle Impacts: A Users Guide. *Phys. Chem. Chem. Phys.* **2017**, *19*, 28−43.

(8) Chumbimuni-Torres, K. Y.; Dai, Z.; Rubinova, N.; Xiang, Y.; Pretsch, E.; Wang, J.; Bakker, E. Potentiometric Biosensing of Proteins with Ultrasensitive Ion-Selective Microelectrodes and Nanoparticle Labels. *J. Am. Chem. Soc.* **2006**, *128*, 13676−13677.

(9) Wongkaew, N.; Simsek, M.; Griesche, C.; Baeumner, A. J. Functional Nanomaterials and Nanostructures Enhancing Electrochemical Biosensors and Lab-on-a-Chip Performances: Recent Progress, Applications, and Future Perspective. *Chem. Rev.* **2019**, *119*, 120−194.

(10) Zha, Y.; Lu, S.; Hu, P.; Ren, H.; Liu, Z.; Gao, W.; Zhao, C.; Li, Y.; Zhou, Y. Dual-Modal Immunosensor with Functionalized Gold Nanoparticles for Ultrasensitive Detection of Chloroacetamide Herbicides. *ACS Appl. Mater. Interfaces* **2021**, *13*, 6091.

(11) Iglesias-Mayor, A.; Amor-Gutiérrez, O.; Costa-García, A.; de la Escosura-Muñiz, A. Nanoparticles as Emerging Labels in Electrochemical Immunosensors. *Sensors* **2019**, *19*, 5137.

(12) Liu, Y.; Zhan, L.; Qin, Z.; Sackrison, J.; Bischof, J. C. Ultrasensitive and Highly Specific Lateral Flow Assays for Point-of-Care Diagnosis. *ACS Nano* **2021**, *15*, 3593−3611.

(13) Lee, K.-S.; El-Sayed, M. A. Gold and Silver Nanoparticles in Sensing and Imaging: Sensitivity of Plasmon Response to Size, Shape, and Metal Composition. *J. Phys. Chem. B* **2006**, *110*, 19220−19225.

(14) Anfossi, L.; Di Nardo, F.; Russo, A.; Cavalera, S.; Giovannoli, C.; Spano, G.; Baumgartner, S.; Lauter, K.; Baggiani, C. Silver and Gold Nanoparticles as Multi-Chromatic Lateral Flow Assay Probes for the Detection of Food Allergens. *Anal. Bioanal. Chem.* **2019**, *411*, 1905−1913.

(15) Dasari, R.; Robinson, D. A.; Stevenson, K. J. Ultrasensitive Electroanalytical Tool for Detecting, Sizing, and Evaluating the Catalytic Activity of Platinum Nanoparticles. *J. Am. Chem. Soc.* **2013**, *135*, 570−573.

(16) Kleijn, S. E. F.; Lai, S. C. S.; Koper, M. T. M.; Unwin, P. R. Electrochemistry of Nanoparticles. *Angew. Chem., Int. Ed.* **2014**, *53*, 3558−3586.

(17) Li, X.; Scida, K.; Crooks, R. M. Detection of Hepatitis B Virus DNA with a Paper Electrochemical Sensor. *Anal. Chem.* **2015**, *87*, 9009−9015.

(18) Li, H.; Sun, Z.; Zhong, W.; Hao, N.; Xu, D.; Chen, H.-Y. Ultrasensitive Electrochemical Detection For DNA Arrays Based on Silver Nanoparticle Aggregates. *Anal. Chem.* **2010**, *82*, 5477−5483.

(19) Zahran, M.; Khalifa, Z.; Zahran, M. A.-H.; Azzem, M. A. Recent Advances in Silver Nanoparticle-Based Electrochemical Sensors for Determining Organic Pollutants in Water: A Review. *Mater. Adv.* **2021**, *2*, 7350−7365.

(20) Pollok, N. E.; Rabin, C.; Walgama, C. T.; Smith, L.; Richards, I.; Crooks, R. M. Electrochemical Detection of NT-ProBNP Using a Metalloimmunoassay on a Paper Electrode Platform. *ACS Sens.* **2020**, *5*, 853−860.

(21) Kwon, S. J.; Bard, A. J. DNA Analysis by Application of Pt Nanoparticle Electrochemical Amplification with Single Label Response. *J. Am. Chem. Soc.* **2012**, *134*, 10777−10779.

(22) Dick, J. E. Electrochemical Detection of Single Cancer and Healthy Cell Collisions on a Microelectrode. *Chem. Commun.* **2016**, *52*, 10906−10909.

(23) Couto, R. A. S.; Chen, L.; Kuss, S.; Compton, R. G. Detection of Escherichia Coli Bacteria by Impact Electrochemistry. *Analyst* **2018**, *143*, 4840−4843.

(24) Andreescu, D.; Kirk, K. A.; Narouei, F. H.; Andreescu, S. Electroanalytic Aspects of Single-Entity Collision Methods for Bioanalytical and Environmental Applications. *ChemElectroChem* **2018**, *5*, 2920−2936.

(25) Pandey, P.; Bhattarai, N.; Su, L.; Wang, X.; Leng, F.; Gerstman, B.; Chapagain, P. P.; He, J. Detecting Individual Proteins and Their Surface Charge Variations in Solution by the Potentiometric Nanoimpact Method. *ACS Sens.* **2022**, *7*, 555−563.

(26) Bai, Y.-Y.; Yang, Y.-J.; Wu, Z.; Yang, X.-Y.; Lin, M.; Pang, D.-W.; Zhang, Z.-L. Size-Resolved Single Entity Collision Biosensing for Dual Quantification of MicroRNAs in a Single Run. *ACS Appl. Mater. Interfaces* **2021**, *13*, 22254−22261.

(27) Karimi, A.; Andreescu, S.; Andreescu, D. Single-Particle Investigation of Environmental Redox Processes of Arsenic on Cerium Oxide Nanoparticles by Collision Electrochemistry. *ACS Appl. Mater. Interfaces* **2019**, *11*, 24725−24734.

(28) Sepunaru, L.; Plowman, B. J.; Sokolov, S. V.; Young, N. P.; Compton, R. G. Rapid Electrochemical Detection of Single Influenza Viruses Tagged with Silver Nanoparticles. *Chem. Sci.* **2016**, *7*, 3892−3899.

(29) Zhang, J.-H.; Zhou, Y.-G. Nano-Impact Electrochemistry: Analysis of Single Bioentities. *TrAC, Trends Anal. Chem.* **2020**, *123*, No. 115768.

(30) Kirk, K. A.; Vasilescu, A.; Andreescu, D.; Senarathna, D.; Mondal, S.; Andreescu, S. Collision-Based Electrochemical Detection of Lysozyme Aggregation. *Anal. Chem.* **2021**, *93*, 2026−2037.

(31) Stayton, P. S.; Freitag, S.; Klumb, L. A.; Chilkoti, A.; Chu, V.; Penzotti, J. E.; To, R.; Hyre, D.; Le Trong, I.; Lybrand, T. P.; Stenkamp, R. E. Streptavidin−Biotin Binding Energetics. *Biomolecular Engineering* **1999**, *16*, 39−44.

(32) Wilchek, M.; Bayer, E. A. The Avidin-Biotin Complex in Bioanalytical Applications. *Anal. Biochem.* **1988**, *171*, 1−32.

(33) Savage, M. D. *Avidin-Biotin Chemistry*; Pierce Chemical Co., 1992.

(34) Zhang, X.; Servos, M. R.; Liu, J. Fast PH-Assisted Functionalization of Silver Nanoparticles with Monothiolated DNA. *Chem. Commun.* **2012**, *48*, 10114−10116.

(35) Weiß, L. J. K.; Lubins, G.; Music, E.; Rinklin, P.; Banzet, M.; Peng, H.; Terkan, K.; Mayer, D.; Wolfrum, B. Single-Impact Electrochemistry in Paper-Based Microfluidics. *ACS Sens.* **2022**, *7*, 884.

(36) Weiß, L. J. K.; Music, E.; Rinklin, P.; Straumann, L.; Grob, L.; Mayer, D.; Wolfrum, B. Engineering Electrostatic Repulsion of Metal Nanoparticles for Reduced Adsorption in Single-Impact Electrochemical Recordings. *ACS Appl. Nano Mater.* **2021**, *4*, 8314−8320.

(37) Lu, S.-M.; Chen, J.-F.; Peng, Y.-Y.; Ma, W.; Ma, H.; Wang, H.-F.; Hu, P.; Long, Y.-T. Understanding the Dynamic Potential Distribution at the Electrode Interface by Stochastic Collision Electrochemistry. *J. Am. Chem. Soc.* **2021**, *143*, 12428.

(38) Krause, K. J.; Adly, N.; Yakushenko, A.; Schnitker, J.; Mayer, D.; Offenhäusser, A.; Wolfrum, B. Influence of Self-Assembled Alkanethiol Monolayers on Stochastic Amperometric On-Chip Detection of Silver Nanoparticles. *Anal. Chem.* **2016**, *88*, 3632−3637.

(39) Xiao, X.; Pan, S.; Jang, J. S.; Fan, F.-R. F.; Bard, A. J. Single Nanoparticle Electrocatalysis: Effect of Monolayers on Particle and Electrode on Electron Transfer. *J. Phys. Chem. C* **2009**, *113*, 14978−14982.

(40) Oja, S. M.; Robinson, D. A.; Vitti, N. J.; Edwards, M. A.; Liu, Y.; White, H. S.; Zhang, B. Observation of Multipeak Collision Behavior during the Electro-Oxidation of Single Ag Nanoparticles. *J. Am. Chem. Soc.* **2017**, *139*, 708−718.

(41) Ustarroz, J.; Kang, M.; Bullions, E.; Unwin, P. R. Impact and Oxidation of Single Silver Nanoparticles at Electrode Surfaces: One Shot versus Multiple Events. *Chem. Sci.* **2017**, *8*, 1841−1853.

(42) Robinson, D. A.; Liu, Y.; Edwards, M. A.; Vitti, N. J.; Oja, S. M.; Zhang, B.; White, H. S. Collision Dynamics during the Electrooxidation of Individual Silver Nanoparticles. *J. Am. Chem. Soc.* **2017**, *139*, 16923−16931.

(43) Ghosh, S. K.; Nath, S.; Kundu, S.; Esumi, K.; Pal, T. Solvent and Ligand Effects on the Localized Surface Plasmon Resonance (LSPR) of Gold Colloids. *J. Phys. Chem. B* **2004**, *108*, 13963−13971.

(44) Szekrényes, D. P.; Kovács, D.; Zolnai, Z.; Deák, A. Chemical Interface Damping as an Indicator for Hexadecyltrimethylammonium

Bromide Replacement by Short-Chain Thiols on Gold Nanorods. *J. Phys. Chem. C* **2020**, *124*, 19736−19742.

(45) Krause, K. J.; Brings, F.; Schnitker, J.; Kätelhön, E.; Rinklin, P.; Mayer, D.; Compton, R. G.; Lemay, S. G.; Offenhäusser, A.; Wolfrum, B. The Influence of Supporting Ions on the Electrochemical Detection of Individual Silver Nanoparticles: Understanding the Shape and Frequency of Current Transients in Nano-Impacts. *Chem.-Eur. J.* **2017**, *23*, 4638−4643.

(46) Ngamchuea, K.; Clark, R. O. D.; Sokolov, S. V.; Young, N. P.; Batchelor-McAuley, C.; Compton, R. G. Single Oxidative Collision Events of Silver Nanoparticles: Understanding the Rate-Determining Chemistry. *Chem.-Eur. J.* **2017**, *23*, 16085−16096.

(47) Ma, H.; Chen, J.-F.; Wang, H.-F.; Hu, P.-J.; Ma, W.; Long, Y.-T. Exploring Dynamic Interactions of Single Nanoparticles at Interfaces for Surface-Confined Electrochemical Behavior and Size Measurement. *Nat. Commun.* **2020**, *11*, No. 2307.

(48) Ma, W.; Ma, H.; Yang, Z.-Y.; Long, Y.-T. Single Ag Nanoparticle Electro-Oxidation: Potential-Dependent Current Traces and Potential-Independent Electron Transfer Kinetic. *J. Phys. Chem. Lett.* **2018**, *9*, 1429−1433.

(49) Saw, E. N.; Kratz, M.; Tschulik, K. Time-Resolved Impact Electrochemistry for Quantitative Measurement of Single-Nanoparticle Reaction Kinetics. *Nano Res.* **2017**, *10*, 3680−3689.

(50) Tanner, E. E. L.; Sokolov, S. V.; Young, N. P.; Compton, R. G. DNA Capping Agent Control of Electron Transfer from Silver Nanoparticles. *Phys. Chem. Chem. Phys.* **2017**, *19*, 9733−9738.

(51) Patel, A. N.; Martinez-Marrades, A.; Brasiliense, V.; Koshelev, D.; Besbes, M.; Kuszelewicz, R.; Combellas, C.; Tessier, G.; Kanoufi, F. Deciphering the Elementary Steps of Transport-Reaction Processes at Individual Ag Nanoparticles by 3D Superlocalization Microscopy. *Nano Lett.* **2015**, *15*, 6454−6463.

(52) Thorgaard, S. N.; Jenkins, S.; Tarach, A. R. Influence of Electroosmotic Flow on Stochastic Collisions at Ultramicroelectrodes. *Anal. Chem.* **2020**, *92*, 12663−12669.

(53) Park, J. H.; Boika, A.; Park, H. S.; Lee, H. C.; Bard, A. J. Single Collision Events of Conductive Nanoparticles Driven by Migration. *J. Phys. Chem. C* **2013**, *117*, 6651−6657.

(54) Kanokkanchana, K.; Saw, E. N.; Tschulik, K. Nano Impact Electrochemistry: Effects of Electronic Filtering on Peak Height, Duration and Area. *ChemElectroChem* **2018**, *5*, 3000−3005.

(55) Ma, H.; Zhong, C. B.; Ying, Y.-L.; Long, Y.-T. Seeing Is Not Believing: Filtering Effects on Random Nature in Electrochemical Measurements of Single-Entity Collision. *ACS Meas. Au* **2022**, DOI: 10.1021/acsmeasuresciau.2c00004.

(56) Gilroy, D.; Conway, B. E. Surface Oxidation and Reduction of Platinum Electrodes: Coverage, Kinetic and Hysteresis Studies. *Can. J. Chem.* **1968**, *46*, 875−890.

(57) Jacobse, L.; Raaijman, S. J.; Koper, M. T. M. The Reactivity of Platinum Microelectrodes. *Phys. Chem. Chem. Phys.* **2016**, *18*, 28451−28457.

(58) Kätelhön, E.; Cheng, W.; Batchelor-McAuley, C.; Tschulik, K.; Compton, R. G. Nanoparticle-Impact Experiments Are Highly Sensitive to the Presence of Adsorbed Species on Electrode Surfaces. *ChemElectroChem* **2014**, *1*, 1057−1062.

(59) Squires, T. M.; Messinger, R. J.; Manalis, S. R. Making It Stick: Convection, Reaction and Diffusion in Surface-Based Biosensors. *Nat. Biotechnol.* **2008**, *26*, 417−426.

▢ Recommended by ACS

5. Conclusion and Outlook

The focal point of the research presented herein was to explore the potential of stochastic impact electrochemistry as a tool for (bio)sensing applications. The research was divided into two parts: the design and implementation of engineering solutions to enhance the detection yield in chip-based experiments and the development of a stochastic biosensor using nanoparticle collisions as readout. To conduct multiple consecutive experiments on the same sensing chip, establishing a reliable cleaning routine was prerequisite for all subsequent experimental achievements.

The particle collision rate represents a pivotal parameter in impact-based sensing applications and in first approximation it can be estimated by continuum mass transfer laws. A summary of salient aspects to tailor the mass transfer of particles has been presented in a review article. The first experimental study focused on particle adsorption at insulating walls and proposed to utilize a second macroscopic electrode to induce electrostatic repulsion in the surrounding area of the detection electrode. Two subsequent experimental studies focused on different implementations of forced advection, namely electrokinetic transport and capillary flow, and characterized their effects on the particle yield in detail. Another joint project, which remains ongoing, involves the particle supply via classical microfluidics and demonstrates the advantageous effects of passive mixing by embedding herringbone structures. Alternatively, the trade-off associated with surface-embedded sensors may be also circumvented by means of advanced electrode geometries. In collaborative work presented in Appendix B.1 we demonstrated that nanoparticles can be detected from micro-ring electrodes located at the tip of three-dimensional pillars, which offer improved diffusional fields compared to surface-embedded electrodes.

The second aspect of this research pertains to the translation of stochastic impact electrochemistry by utilizing the principle of counting discrete events as a readout mechanism for future biosensors. Successful translation must take into account aspects of cost-efficient fabrication approaches and measurement procedures. While the bioassay development presented here exclusively relied on clean-room fabricated chips, future commercial applications would require a scalable high-throughput fabrication at low cost. In a collaborative work, shown in Appendix B.2, we developed a fabrication process for low-cost microelectrode arrays via screen printing and laser patterning. Furthermore, we demonstrated that particle detection can also be performed on site with a portable detection device. The study on nanoparticle detection in paper-based microfluidics highlights the potential utility of on-site detection in point-of-care settings, where colorimetric lateral flow sensors are widely employed nowadays.

The final part of the thesis focuses on the challenge of introducing specificity in nano-impact studies. Here, we developed a robust protocol to modify the nanoparticle shell and applied it to create biotinylated nanoparticles, where a mixed self-assembled monolayer on the particle ensured its specific binding and redoxactivity simultaneously. This preliminary work for the model system biotin/streptavidin gave rise to several ongoing collaborative projects. First, the discovered difficulties in maintaining colloidal stability and redoxactivity have been a starting point for a follow-up project. In the joint work, we investigate en detail the effect of the particle corona

on its redoxactivity for various unspecific coatings, where alkanethiolate molecules of different chain lengths and chemical moieties are utilized to create homogeneous monolayers with different characteristics. This ongoing study promises general insights for the future design of functional particle coronas. Moreover, the prototype assay for biotin/streptavidin demonstrated the general feasibility of digital biosensing using silver nanoparticles. A recent collaborative project tries to implement such competitive assay strategies for other small-molecule targets, such as dopamine and glyphosate. Moreover, nanoparticle labels could also be used in a general sandwich assay configuration. Other ongoing work investigates the performance of aptamer-coated silver nanoparticle labels in order to replace commonly-used secondary antibodies that are used for colorimetric readouts.

The nascent utilization of (particle-based) stochastic electrochemistry holds great promise for future scientific and technological advances. With the ability to employ compact detection setups and detect a wide range of analytes via stochastic impacts, this technique is poised to evolve and mature over the next several years and decades. The present work has already shown early proof of concepts revealing the immense opportunities of this approach. This exciting progress has the potential to revolutionize the field of sensing by opening up new avenues for detecting and quantifying a wide range of substances with unparalleled precision and accuracy.

References

1. Zhou, H., Park, J. H., Fan, F.-R. F. & Bard, A. J. Observation of Single Metal Nanoparticle Collisions by Open Circuit (Mixed) Potential Changes at an Ultramicroelectrode. *J. Am. Chem. Soc.* **134,** 13212–13215 (2012).

2. Roehrich, B., Liu, E. Z., Silverstein, R. & Sepunaru, L. Detection and Characterization of Single Particles by Electrochemical Impedance Spectroscopy. *J. Phys. Chem. Lett.* **12,** 9748–9753 (2021).

3. Percival, S. J. & Zhang, B. Fast-Scan Cyclic Voltammetry Allows Determination of Electron-Transfer Kinetic Constants in Single Nanoparticle Collision. *J. Phys. Chem. C* **120,** 20536–20546 (2016).

4. Goines, S. & Dick, J. E. Review—Electrochemistry's Potential to Reach the Ultimate Sensitivity in Measurement Science. *J. Electrochem. Soc.* **167,** 037505 (2019).

5. Patrice, F. T., Qiu, K., Ying, Y.-L. & Long, Y.-T. Single Nanoparticle Electrochemistry. *Annual Review of Analytical Chemistry* **12,** 347–370 (2019).

6. Einstein, A. Über die von der molekularkinetischen Theorie der Wärme geforderte Bewegung von in ruhenden Flüssigkeiten suspendierten Teilchen. *Annalen der Physik* **322,** 549–560 (1905).

7. von Smoluchowski, M. Zur kinetischen Theorie der Brownschen Molekularbewegung und der Suspensionen. *Annalen der Physik* **21,** 756–780 (1906).

8. Eloul, S., Kätelhön, E., Batchelor-McAuley, C., Tschulik, K. & Compton, R. G. Diffusional impacts of nanoparticles on microdisc and microwire electrodes: The limit of detection and first passage statistics. *Journal of Electroanalytical Chemistry* **755,** 136–142 (2015).

9. Jung Kwon, S. *et al.* Stochastic Electrochemistry with Electrocatalytic Nanoparticles at Inert Ultramicroelectrodes—Theory and Experiments. *Physical Chemistry Chemical Physics* **13,** 5394–5402 (2011).

10. Krause, K. J., Yakushenko, A. & Wolfrum, B. Stochastic On-Chip Detection of Subpicomolar Concentrations of Silver Nanoparticles. *Anal. Chem.* **87,** 7321–7325 (2015).

11. Kätelhön, E., Krause, K. J., Singh, P. S., Lemay, S. G. & Wolfrum, B. Noise Characteristics of Nanoscaled Redox-Cycling Sensors: Investigations Based on Random Walks. *J. Am. Chem. Soc.* **135,** 8874–8881 (2013).

12. Lin, C.-H., Ye, J.-J. & Huang, X.-J. Understanding the Ensemble Electrochemistry of Random-Walk Nanoparticles: Improved Reaction Efficiency and Mechanistic Insights. *Chemical Engineering Journal* **418,** 129393 (2021).

13. Robinson, D. A. *et al.* Collision Dynamics during the Electrooxidation of Individual Silver Nanoparticles. *Journal of the American Chemical Society* (2017).

14. Eloul, S., Kätelhön, E., Batchelor-McAuley, C., Tschulik, K. & Compton, R. G. Diffusional Nanoimpacts: The Stochastic Limit. *J. Phys. Chem. C* **119,** 14400–14410 (2015).

15. Cottrell, F. G. Der Reststrom bei galvanischer Polarisation, betrachtet als ein Diffusionsproblem. *Z. Phys. Chem.* **42,** 385 (1903).

16. Shoup, D. & Szabo, A. Chronoamperometric current at finite disk electrodes. *J. Electroanal. Chem.* **140,** 237–245 (1982).

17. Saito, Y. A theoretical study on the diffusion current at the stationary electrodes of circular and narrow band types. English. *Review of Polarography* **15,** 177–187 (1968).

18. Britz, D., Poulsen, K. & Strutwolf, J. Reference values of the diffusion-limited chronoamperometric current at a microband electrode. *Electrochimica acta* **51,** 333–339 (2005).

19. Eloul, S., Kätelhön, E., Batchelor-McAuley, C., Tschulik, K. & Compton, R. G. Diffusional Impacts of Nanoparticles on Microdisc and Microwire Electrodes: The Limit of Detection and First Passage Statistics. *Journal of Electroanalytical Chemistry* **755,** 136–142 (2015).

20. Lemay, S. G., Renault, C. & Dick, J. E. Particle Mass Transport in Impact Electrochemistry. *Current Opinion in Electrochemistry,* 101265 (2023).

21. Eloul, S. & Compton, R. G. Shielding of a Microdisc Electrode Surrounded by an Adsorbing Surface. *ChemElectroChem* **1,** 917–924 (2014).

22. Langmuir, I. The Evaporation, Condensation and Reflection of Molecules and the Mechanism of Adsorption. *Phys. Rev.* **8,** 149–176 (2 1916).

23. Brunauer, S., Emmett, P. H. & Teller, E. Adsorption of Gases in Multimolecular Layers. *Journal of the American Chemical Society* **60,** 309–319 (1938).

24. Bevan, M. A. & Prieve, D. C. Hindered diffusion of colloidal particles very near to a wall: Revisited. *The Journal of Chemical Physics* **113,** 1228–1236 (2000).

25. Goldman, A., Cox, R. & Brenner, H. Slow viscous motion of a sphere parallel to a plane wall - II Couette flow. *Chemical Engineering Science* **22,** 653–660 (1967).

26. Kihm, K. D., Banerjee, A., Choi, C. K. & Takagi, T. Near-Wall Hindered Brownian Diffusion of Nanoparticles Examined by Three-Dimensional Ratiometric Total Internal Reflection Fluorescence Microscopy (3-D R-TIRFM). *Exp Fluids* **37,** 811–824 (2004).

27. Eloul, S., Kätelhön, E. & Compton, R. G. When Does Near-Wall Hindered Diffusion Influence Mass Transport towards Targets? *Phys. Chem. Chem. Phys.* **18,** 26539–26549 (2016).

28. Choi, C., Margraves, C. & Kihm, K. Examination of near-wall hindered Brownian diffusion of nanoparticles: Experimental comparison to theories by Brenner (1961) and Goldman et al.(1967). *Physics of Fluids* **19,** 103305 (2007).

29. Kätelhön, E., Sokolov, S. V. & Compton, R. G. Near-wall hindered diffusion: Implications for surface-based sensors. *Sensors and Actuators B: Chemical* **234,** 420–425 (2016).

30. Lyklema, J. in *Fundamentals of Interface and Colloid Science* (Elsevier, 1995).

31. von Smoluchowski, M. Contribution à La Théorie de l'endosmose Électrique et de Quelques Phénomènès Corrélatifs. *Bull. Int. Acad. Sci. Cracovie* **8,** 182 (1903).

32. Moazzenzade, T., Huskens, J. & G. Lemay, S. Stochastic Electrochemistry at Ultralow Concentrations: The Case for Digital Sensors. *Analyst* **145,** 750–758 (2020).

33. Boika, A. & Bard, A. J. Time of First Arrival in Electrochemical Collision Experiments as a Measure of Ultralow Concentrations of Analytes in Solution. *Anal. Chem.,* 6 (2015).

34. Boika, A. & Bard, A. J. Electrophoretic Migration and Particle Collisions in Scanning Electrochemical Microscopy. *Anal. Chem.* **86,** 11666–11672 (2014).

35. Boika, A., Thorgaard, S. N. & Bard, A. J. Monitoring the Electrophoretic Migration and Adsorption of Single Insulating Nanoparticles at Ultramicroelectrodes. *J. Phys. Chem. B,* 10 (2013).

36. Park, J. H., Boika, A., Park, H. S., Lee, H. C. & Bard, A. J. Single collision events of conductive nanoparticles driven by migration. *The Journal of Physical Chemistry C* **117,** 6651–6657 (2013).

37. Fosdick, S. E., Anderson, M. J., Nettleton, E. G. & Crooks, R. M. Correlated Electrochemical and Optical Tracking of Discrete Collision Events. *J. Am. Chem. Soc.* **135,** 5994–5997 (2013).

38. Moazzenzade, T. *et al.* Self-Induced Convection at Microelectrodes via Electroosmosis and Its Influence on Impact Electrochemistry. *J. Am. Chem. Soc.* **142,** 17908–17912 (2020).

39. Thorgaard, S. N., Jenkins, S. & Tarach, A. R. Influence of Electroosmotic Flow on Stochastic Collisions at Ultramicroelectrodes. *Anal. Chem.* **92,** 12663–12669 (2020).

40. Patel, A. N. *et al.* Deciphering the Elementary Steps of Transport-Reaction Processes at Individual Ag Nanoparticles by 3D Superlocalization Microscopy. *Nano Lett.* **15,** 6454–6463 (2015).

41. Bonezzi, J., Luitel, T. & Boika, A. Electrokinetic Manipulation of Silver and Platinum Nanoparticles and Their Stochastic Electrochemical Detection. *Anal. Chem.* **89,** 8614–8619 (2017).

42. Shim, S. Diffusiophoresis, Diffusioosmosis, and Microfluidics: Surface-Flow-Driven Phenomena in the Presence of Flow. *Chem. Rev.* **122,** 6986–7009 (2022).

43. Velegol, D., Garg, A., Guha, R., Kar, A. & Kumar, M. Origins of Concentration Gradients for Diffusiophoresis. *Soft Matter* **12,** 4686–4703 (2016).

44. Keh, H. J. Diffusiophoresis of Charged Particles and Diffusioosmosis of Electrolyte Solutions. *Current Opinion in Colloid & Interface Science* **24,** 13–22 (2016).

45. Keh, H. J. & Ma, H. C. Diffusioosmosis of Electrolyte Solutions along a Charged Plane Wall. *Langmuir* **21,** 5461–5467 (2005).

46. Rica, R. A. & Bazant, M. Z. Electrodiffusiophoresis: Particle Motion in Electrolytes under Direct Current. *Physics of Fluids* **22,** 112109 (2010).

47. Bazant, M. Z., Kilic, M. S., Storey, B. D. & Ajdari, A. Towards an Understanding of Induced-Charge Electrokinetics at Large Applied Voltages in Concentrated Solutions. *Advances in Colloid and Interface Science* **152,** 48–88 (2009).

48. Tricoli, V. & Orsini, G. Electrodiffusiophoresis of a Large-Zeta-Potential Particle in Weak Fields. *J. Phys.: Condens. Matter* **27,** 415102 (2015).

49. Alligrant, T. M., Anderson, M. J., Dasari, R., Stevenson, K. J. & Crooks, R. M. Single Nanoparticle Collisions at Microfluidic Microband Electrodes: The Effect of Electrode Material and Mass Transfer, 8 (2014).

50. Olanrewaju, A., Beaugrand, M., Yafia, M. & Juncker, D. Capillary Microfluidics in Microchannels: From Microfluidic Networks to Capillaric Circuits. *Lab on a Chip* **18,** 2323–2347 (2018).

51. Gong, M. M. & Sinton, D. Turning the Page: Advancing Paper-Based Microfluidics for Broad Diagnostic Application. *Chem. Rev.* **117,** 8447–8480 (2017).

52. Kirby, B. J. *Micro- and nanoscale fluid mechanics: transport in microfluidic devices* 1st (Cambride University Press, USA, 2010).

53. Squires, T. M., Messinger, R. J. & Manalis, S. R. Making It Stick: Convection, Reaction and Diffusion in Surface-Based Biosensors. *Nat Biotechnol* **26,** 417–426 (2008).

54. Amatore, C., Pebay, C., Sella, C. & Thouin, L. Mass Transport at Microband Electrodes: Transient, Quasi-Steady-State, and Convective Regimes. *ChemPhysChem* **13,** 1562–1568 (2012).

55. Bird, R. B., Stewart, W. E. & Lightfoot, E. N. *Transport Phenomena* 2nd (John Wiley & Sons, Inc., 2006).

56. Beek, W., Muttzall, K. & van Heuven, J. *Transport Phenomena* 2000.

57. Stroock, A. D. *et al.* Chaotic Mixer for Microchannels. *Science* **295,** 647–651 (2002).

58. Kirtland, J. D., McGraw, G. J. & Stroock, A. D. Mass Transfer to Reactive Boundaries from Steady Three-Dimensional Flows in Microchannels. *Physics of Fluids* **18,** 073602 (2006).

59. Wu, J. Understanding the Electric Double-Layer Structure, Capacitance, and Charging Dynamics. *Chem. Rev.* **122,** 10821–10859 (2022).

60. Debye, P. & Hückel, E. Zur Theorie der Elektrolyte. I. Gefrierpunktserniedrigung und verwandte Erscheinungen. *Physikalische Zeitschrift* **9,** 185 (1923).

61. *CRC Handbook of Chemistry and Physics* Ninety-seventh (ed Haynes, W. M.) (CRC Press).

62. Mie, G. Beiträge Zur Optik Trüber Medien, Speziell Kolloidaler Metallösungen. *Annalen der Physik* **330,** 377–445 (1908).

63. Drude, P. Zur Elektronentheorie Der Metalle. *Annalen der Physik* **306,** 566613 (1900).

64. Sannomiya, T. & Vörös, J. Single Plasmonic Nanoparticles for Biosensing. *Trends in Biotechnology* **29,** 343–351 (2011).

65. Dileseigres, A. S., Prado, Y. & Pluchery, O. How to Use Localized Surface Plasmon for Monitoring the Adsorption of Thiol Molecules on Gold Nanoparticles? *Nanomaterials* **12,** 292 (2022).

66. Ghosh, S. K., Nath, S., Kundu, S., Esumi, K. & Pal, T. Solvent and Ligand Effects on the Localized Surface Plasmon Resonance (LSPR) of Gold Colloids. *J. Phys. Chem. B* **108,** 13963–13971 (2004).

67. Amendola, V., Bakr, O. M. & Stellacci, F. A Study of the Surface Plasmon Resonance of Silver Nanoparticles by the Discrete Dipole Approximation Method: Effect of Shape, Size, Structure, and Assembly. *Plasmonics* **5,** 85–97 (2010).

68. Mayer, K. M. & Hafner, J. H. Localized Surface Plasmon Resonance Sensors. *Chem. Rev.* **111,** 3828–3857 (2011).

69. Amendola, V., Pilot, R., Frasconi, M., Maragò, O. M. & Iatì, M. A. Surface Plasmon Resonance in Gold Nanoparticles: A Review. *J. Phys.: Condens. Matter* **29,** 203002 (2017).

70. Bayram, S. S., Lindfors, K. & Blum, A. S. Tunable Longitudinal Modes in Extended Silver Nanoparticle Assemblies. *Beilstein J. Nanotechnol.* **7,** 1219–1228 (2016).

71. Chuntonov, L. & Haran, G. Trimeric Plasmonic Molecules: The Role of Symmetry. *Nano Lett.* **11,** 2440–2445 (2011).

72. Loiseau, A. *et al.* Silver-Based Plasmonic Nanoparticles for and Their Use in Biosensing. *Biosensors* **9,** 78 (2019).

73. Micka, K. Depolarisation Der Quecksilbertropfelektrode Durch Suspensionen Unlöslicher Stoffe I. Allgemeine Beobachtungen. *Collect. Czech. Chem. Commun.* **21,** 647–651 (1956).

74. Jones, I. F. & Kaye, R. C. Polarography of Carbon Suspensions. *Journal of Electroanalytical Chemistry and Interfacial Electrochemistry* **20,** 213–221 (1969).

75. Holland, A. & Feinerman, A. An Improved Electrolytic Grain-Size Anlyzer. *J. Applied Photographic Engineering* **8,** 165 (1982).

76. Quinn, B. M., van't Hof, P. G. & Lemay, S. G. Time-Resolved Electrochemical Detection of Discrete Adsorption Events. *Journal of the American Chemical Society* **126.** PMID: 15237976, 8360–8361 (2004).

77. Zhou, Y.-G., Rees, N. V. & Compton, R. G. The Electrochemical Detection and Characterization of Silver Nanoparticles in Aqueous Solution. *Angewandte Chemie* **50,** 4219–4221 (2011).

78. Defnet, P. A. & Zhang, B. Collision, Adhesion, and Oxidation of Single Ag Nanoparticles on a Polysulfide-Modified Microelectrode. *J. Am. Chem. Soc.* **143,** 16154–16162 (2021).

79. Krause, K. J. *et al.* The Influence of Supporting Ions on the Electrochemical Detection of Individual Silver Nanoparticles: Understanding the Shape and Frequency of Current Transients in Nano-impacts. *Chemistry–A European Journal* **23,** 4638–4643 (2017).

80. Ngamchuea, K. *et al.* Single Oxidative Collision Events of Silver Nanoparticles: Understanding the Rate-Determining Chemistry. *Chemistry–A European Journal* **23,** 16085–16096 (2017).

81. Sokolov, S. V., Tschulik, K., Batchelor-McAuley, C., Jurkschat, K. & Compton, R. G. Reversible or Not? Distinguishing Agglomeration and Aggregation at the Nanoscale. *Analytical Chemistry* **87,** 10033–10039 (2015).

82. Oja, S. M. *et al.* Observation of Multipeak Collision Behavior during the Electro-Oxidation of Single Ag Nanoparticles. *J. Am. Chem. Soc* **139,** 708–718 (2017).

83. Ustarroz, J., Kang, M., Bullions, E. & R. Unwin, P. Impact and Oxidation of Single Silver Nanoparticles at Electrode Surfaces: One Shot versus Multiple Events. *Chemical Science* **8,** 1841–1853 (2017).

84. Wonner, K., Rurainsky, C. & Tschulik, K. Operando Studies of the Electrochemical Dissolution of Silver Nanoparticles in Nitrate Solutions Observed With Hyperspectral Dark-Field Microscopy. *Front. Chem.* **7** (2020).

85. Saw, E. N., Kratz, M. & Tschulik, K. Time-Resolved Impact Electrochemistry for Quantitative Measurement of Single-Nanoparticle Reaction Kinetics. *Nano Res.* **10,** 3680–3689 (2017).

86. Lemineur, J.-F. *et al.* In Situ Optical Monitoring of the Electrochemical Conversion of Dielectric Nanoparticles: From Multistep Charge Injection to Nanoparticle Motion. *J. Am. Chem. Soc.* **142,** 7937–7946 (2020).

87. Brasiliense, V. *et al.* Correlated Electrochemical and Optical Detection Reveals the Chemical Reactivity of Individual Silver Nanoparticles. *J. Am. Chem. Soc.* **138,** 3478–3483 (2016).

88. Wonner, K., Evers, M. V. & Tschulik, K. Simultaneous Opto- and Spectro-Electrochemistry: Reactions of Individual Nanoparticles Uncovered by Dark-Field Microscopy. *J. Am. Chem. Soc.* **140,** 12658–12661 (2018).

89. Krause, K. J. *et al.* The Influence of Supporting Ions on the Electrochemical Detection of Individual Silver Nanoparticles: Understanding the Shape and Frequency of Current Transients in Nano-impacts. *Chem. Eur. J.* **23,** 4638–4643 (2017).

90. Kanokkanchana, K., Saw, E. N. & Tschulik, K. Nano Impact Electrochemistry: Effects of Electronic Filtering on Peak Height, Duration and Area. *ChemElectroChem* **5,** 3000–3005 (2018).

91. Ma, H., Zhong, C. B., Ying, Y.-L. & Long, Y.-T. Seeing Is Not Believing: Filtering Effects on Random Nature in Electrochemical Measurements of Single-Entity Collision. *ACS Meas. Au* (2022).

92. Robinson, D. A., Edwards, M. A., Ren, H. & White, H. S. Effects of Instrumental Filters on Electrochemical Measurement of Single-Nanoparticle Collision Dynamics. *ChemElectroChem* **5,** 3059–3067 (2018).

93. Defnet, P. A., Anderson, T. J. & Zhang, B. Stochastic Collision Electrochemistry of Single Silver Nanoparticles. *Current Opinion in Electrochemistry* **22,** 129–135 (2020).

94. Ma, H. *et al.* Exploring Dynamic Interactions of Single Nanoparticles at Interfaces for Surface-Confined Electrochemical Behavior and Size Measurement. *Nat Commun* **11,** 2307 (2020).

95. Lu, S.-M. *et al.* Understanding the Dynamic Potential Distribution at the Electrode Interface by Stochastic Collision Electrochemistry. *J. Am. Chem. Soc.* (2021).

96. Ma, W., Ma, H., Yang, Z.-Y. & Long, Y.-T. Single Ag Nanoparticle Electro-oxidation: Potential-Dependent Current Traces and Potential-Independent Electron Transfer Kinetic. *J. Phys. Chem. Lett.* **9,** 1429–1433 (2018).

97. Sundaresan, V., Monaghan, J. W. & Willets, K. A. Visualizing the Effect of Partial Oxide Formation on Single Silver Nanoparticle Electrodissolution. *J. Phys. Chem. C* **122,** 3138–3145 (2018).

98. Dery, L., Dery, S., Gross, E. & Mandler, D. Influence of Charged Self-Assembled Monolayers on Single Nanoparticle Collision. *Anal. Chem.* (2023).

99. Krause, K. J. *et al.* Influence of Self-Assembled Alkanethiol Monolayers on Stochastic Amperometric On-Chip Detection of Silver Nanoparticles. *Anal. Chem.* **88,** 3632–3637 (2016).

100. Kanokkanchana, K. & Tschulik, K. Electronic Circuit Simulations as a Tool to Understand Distorted Signals in Single-Entity Electrochemistry. *J. Phys. Chem. Lett.* **13,** 10120–10125 (2022).

101. Saw, E. N., Blanc, N., Kanokkanchana, K. & Tschulik, K. Time-Resolved Impact Electrochemistry - A New Method to Determine Diffusion Coefficients of Ions in Solution. *Electrochimica Acta* **282,** 317–323 (2018).

102. Saw, E. N., Kanokkanchana, K., Amin, H. M. A. & Tschulik, K. Unravelling Anion Solvation in Water-Alcohol Mixtures by Single Entity Electrochemistry. *ChemElectroChem* **9,** e202101435 (2022).

103. Hao, R., Fan, Y. & Zhang, B. Imaging Dynamic Collision and Oxidation of Single Silver Nanoparticles at the Electrode/Solution Interface. *J. Am. Chem. Soc.* **139,** 12274–12282 (2017).

104. Batchelor-McAuley, C. *et al.* In Situ Nanoparticle Sizing with Zeptomole Sensitivity. *Analyst* **140,** 5048–5054 (2015).

105. Axson, J. L. *et al.* Rapid Kinetics of Size and pH-Dependent Dissolution and Aggregation of Silver Nanoparticles in Simulated Gastric Fluid. *J. Phys. Chem. C* **119,** 20632–20641 (2015).

106. Robinson, D. A. *et al.* Addressing Colloidal Stability for Unambiguous Electroanalysis of Single Nanoparticle Impacts. *The journal of physical chemistry letters* (2016).

107. Huynh, K. A. & Chen, K. L. Aggregation Kinetics of Citrate and Polyvinylpyrrolidone Coated Silver Nanoparticles in Monovalent and Divalent Electrolyte Solutions. *Environ. Sci. Technol.* **45,** 5564–5571 (2011).

108. Shrestha, S., Wang, B. & Dutta, P. Nanoparticle Processing: Understanding and Controlling Aggregation. *Advances in Colloid and Interface Science* **279,** 102162 (2020).

109. Lemay, S. G. & Moazzenzade, T. Single-Entity Electrochemistry for Digital Biosensing at Ultralow Concentrations. *Anal. Chem.* **93,** 9023–9031 (2021).

110. Sekretareva, A. Single-Entity Electrochemistry of Collision in Sensing Applications. *Sensors and Actuators Reports* **3,** 100037 (2021).

111. Peng, Y.-Y., Qian, R.-C., Hafez, M. E. & Long, Y.-T. Stochastic Collision Nanoelectrochemistry: A Review of Recent Developments. *ChemElectroChem* **4,** 977–985 (2017).

112. Kim, B.-K., Kim, J. & Bard, A. J. Electrochemistry of a Single Attoliter Emulsion Droplet in Collisions. *J. Am. Chem. Soc.* **137,** 2343–2349 (2015).

113. Lebègue, E., Anderson, C. M., Dick, J. E., Webb, L. J. & Bard, A. J. Electrochemical Detection of Single Phospholipid Vesicle Collisions at a Pt Ultramicroelectrode. *Langmuir* **31,** 11734–11739 (2015).

114. Hoang, N. T. T. *et al.* Observing Phase Transition of a Temperature-Responsive Polymer Using Electrochemical Collisions on an Ultramicroelectrode. *Anal. Chem.* **90,** 7261–7266 (2018).

115. Lee, J. *et al.* Stochastic Electrochemical Cytometry of Human Platelets via a Particle Collision Approach. *ACS Sens.* **4,** 3248–3256 (2019).

116. Dick, J. E. Electrochemical Detection of Single Cancer and Healthy Cell Collisions on a Microelectrode. *Chem. Commun.* **52,** 10906–10909 (2016).

117. Chen, Y., Wang, D., Liu, Y., Gao, G. & Zhi, J. Redox Activity of Single Bacteria Revealed by Electrochemical Collision Technique. *Biosensors and Bioelectronics* **176,** 112914 (2021).

118. Ronspees, A. T. & Thorgaard, S. N. Blocking Electrochemical Collisions of Single E. Coli and B. Subtilis Bacteria at Ultramicroelectrodes Elucidated Using Simultaneous Fluorescence Microscopy. *Electrochimica Acta* **278,** 412–420 (2018).

119. Luy, J., Ameline, D., Thobie-Gautier, C., Boujtita, M. & Lebègue, E. Detection of Bacterial Rhamnolipid Toxin by Redox Liposome Single Impact Electrochemistry. *Angewandte Chemie International Edition* **61,** e202111416 (2022).

120. Dick, J. E., Hilterbrand, A. T., Boika, A., Upton, J. W. & Bard, A. Electrochemical Detection of a Single Cytomegalovirus at an Ultramicroelectrode and Its Antibody Anchoring. *Proceedings of the National Academy of Sciences* (2015).

121. Pandey, P. *et al.* Detecting Individual Proteins and Their Surface Charge Variations in Solution by the Potentiometric Nanoimpact Method. *ACS Sens.* **7,** 555–563 (2022).

122. Andreescu, S. & Vasilescu, A. Advances in Electrochemical Detection for Probing Protein Aggregation. *Current Opinion in Electrochemistry,* 100820 (2021).

123. Dick, J. E., Renault, C. & Bard, A. J. Observation of Single-Protein and DNA Macromolecule Collisions on Ultramicroelectrodes. *J. Am. Chem. Soc.* **137,** 8376–8379 (2015).

124. Pensa, E., Bogawat, Y., Simmel, F. C. & Santiago, I. Single DNA Origami Detection by Nanoimpact Electrochemistry. *ChemElectroChem* **9,** e202101696 (2022).

125. Shen, X., Liu, R. & Wang, D. Nanoconfined Electrochemical Collision and Catalysis of Single Enzyme inside Carbon Nanopipettes. *Anal. Chem.* **94,** 8110–8114 (2022).

126. Kätelhön, E., Sepunaru, L., Karyakin, A. A. & Compton, R. G. Can Nanoimpacts Detect Single-Enzyme Activity? Theoretical Considerations and an Experimental Study of Catalase Impacts. *ACS Catal.* **6,** 8313–8320 (2016).

127. Sekretaryova, A. N., Vagin, M. Y., Turner, A. P. F. & Eriksson, M. Electrocatalytic Currents from Single Enzyme Molecules. *J. Am. Chem. Soc.* **138,** 2504–2507 (2016).

128. Lin, C., Sepunaru, L., Kätelhön, E. & Compton, R. G. Electrochemistry of Single Enzymes: Fluctuations of Catalase Activities. *J. Phys. Chem. Lett.* **9,** 2814–2817 (2018).

129. Vannoy, K. J., Ryabykh, A., Chapoval, A. I. & Dick, J. E. Single Enzyme Electroanalysis. *Analyst* **146,** 3413–3421 (2021).

130. Couto, R. A. S., Chen, L., Kuss, S. & Compton, R. G. Detection of Escherichia Coli Bacteria by Impact Electrochemistry. *Analyst* **143,** 4840–4843 (2018).

131. Sepunaru, L., Plowman, B. J., Sokolov, S. V., Young, N. P. & Compton, R. G. Rapid Electrochemical Detection of Single Influenza Viruses Tagged with Silver Nanoparticles. *Chem. Sci.* **7,** 3892–3899 (2016).

132. Qiu, X., Tang, H., Dong, J., Wang, C. & Li, Y. Stochastic Collision Electrochemistry from Single Pt Nanoparticles: Electrocatalytic Amplification and MicroRNA Sensing. *Anal. Chem.* **94,** 8202–8208 (2022).

133. Bai, Y.-Y. *et al.* One-to-Many Single Entity Electrochemistry Biosensing for Ultrasensitive Detection of microRNA. *Anal. Chem.* **92,** 853–858 (2020).

134. Castañeda, A. D., Brenes, N. J., Kondajji, A. & Crooks, R. M. Detection of microRNA by Electrocatalytic Amplification: A General Approach for Single-Particle Biosensing. *J. Am. Chem. Soc.* **139,** 7657–7664 (2017).

135. Bai, Y.-Y. *et al.* Size-Resolved Single Entity Collision Biosensing for Dual Quantification of MicroRNAs in a Single Run. *ACS Appl. Mater. Interfaces* **13,** 22254–22261 (2021).

136. Karimi, A., Hayat, A. & Andreescu, S. Biomolecular Detection at ssDNA-conjugated Nanoparticles by Nano-Impact Electrochemistry. *Biosensors and Bioelectronics* **87,** 501–507 (2017).

137. Khan, R., Andreescu, D., Hassan, M. H., Ye, J. & Andreescu, S. Nanoelectrochemistry Reveals Selective Interactions of Perfluoroalkyl Substances (PFASs) with Silver Nanoparticles. *Angewandte Chemie International Edition* **61,** e202209164 (2022).

138. Karimi, A., Andreescu, S. & Andreescu, D. Single-Particle Investigation of Environmental Redox Processes of Arsenic on Cerium Oxide Nanoparticles by Collision Electrochemistry. *ACS Appl. Mater. Interfaces* **11,** 24725–24734 (2019).

139. Li, J. *et al.* Clinically Applicable Homogeneous Assay for Serological Diagnosis of Alpha-Fetoprotein by Impact Electrochemistry. *ACS Sens.* **7,** 3216–3222 (2022).

140. Yang, Y.-J. *et al.* Single-Nanoparticle Collision Electrochemistry Biosensor Based on an Electrocatalytic Strategy for Highly Sensitive and Specific Detection of H7N9 Avian Influenza Virus. *Anal. Chem.* **94,** 8392–8398 (2022).

141. Narouei, F. H., Andreescu, D. & Andreescu, S. Rapid Characterization of Arsenic Adsorption on Single Magnetite Nanoparticles by Collisions at Microelectrodes. *Environ. Sci.: Nano* **7,** 1999–2009 (2020).

142. Yang, J. *et al.* Magnetic Rolling Circle Amplification-Assisted Single-Particle Collision Immunosensor for Ultrasensitive Detection of Cardiac Troponin I. *Anal. Chem.* **94,** 12514–12522 (2022).

A. Supplementary Material to the Contributions Included

A.1 Engineering Electrostatic Repulsion of Metal Nanoparticles for Reduced Adsorption in Single-Impact Electrochemical Recordings

Engineering Electrostatic Repulsion of Metal Nanoparticles for Reduced Adsorption in Single-Impact Electrochemical Recordings

Lennart J. K. Weiß[†], Emir Music[†], Philipp Rinklin[†], Lea Straumann[†], Leroy Grob[†], Dirk Mayer[‡], Bernhard Wolfrum[*,†]

[†] Neuroelectronics, Munich School of Bioengineering, Department of Electrical and Computer Engineering, Technical University of Munich, 85748 Garching, Germany

[‡] Institute of Biological Information Processing, Bioelectronics (IBI-3), Forschungszentrum Jülich, 52425 Jülich, Germany

[*] Corresponding Author: Bernhard Wolfrum, bernhard.wolfrum@tum.de

I. Open Circuit Potential of a Floating Shield Electrode

We measured the open circuit potentials (OCP) of the floating Pt shield electrode against Ag/AgCl before and after the insertion of AgNPs as shown in Fig. S1. First, the OCP of the floating shield electrode in 25 mM KCl was recorded for 180 s. Then, the OCP after insertion of AgNPs was measured for 300 s. We found the OCP to be 209 ± 4 mV (mean, standard deviation) in a pure electrolyte solution. After the insertion of AgNPs, we observe a drastic change of ~120 mV within the time of a typical experiment. Finally after 10 min, the OCP was measured again for 300 s and reached a constant value of -154 ± 3 mV.
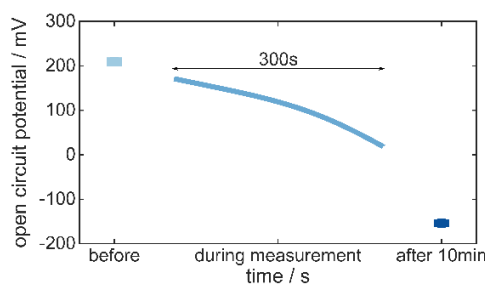
Figure S1 OCP of a floating Pt shield electrode during a detection experiment with 43 pM of 20 nm-AgNP in 25 mM KCl solution. Error bars (before, after 10 min) indicate standard deviations.

II. Anodic Stripping Voltammetry of a Shield Electrode

We investigated the electrodeposition of Ag^+ ions on the shield electrode being held at -200 mV vs Ag/AgCl during an anodic stripping voltammetry experiment. To this end, we exchanged the electrolyte after the experiment and applied a linear sweep from 0 mV to 800 mV vs Ag/AgCl with a scan rate of 100 mV/s after an initial phase with 5 s at -200 mV and 2 s at 0 mV. We compared the results to a clean chip, see Fig. S2, and did not find a significant difference indicating the presence of Ag^+ ions. This can probably be explained by the limited mass transport of oxidized species towards the shield electrode within the time scale of our experiment.
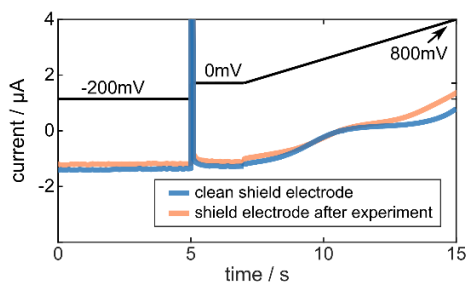
Figure S2 Anodic stripping voltammetry of a shield electrode directly after the detection experiment (red) compared to a cleaned shield electrode (blue). The potential was first held at -200 mV and after 2 s at 0 mV swept to 800 mV vs Ag/AgCl with a scan rate of 100mV/s.

III. Statistical Information on Amplitudes, Durations and Charge of AgNP Impacts for Different Passivation Conditions

Fig. S3 provides statistical information about the amplitudes, the durations and the charge of all considered peaks that have been used in Fig. 2d, e, and f for further analysis.
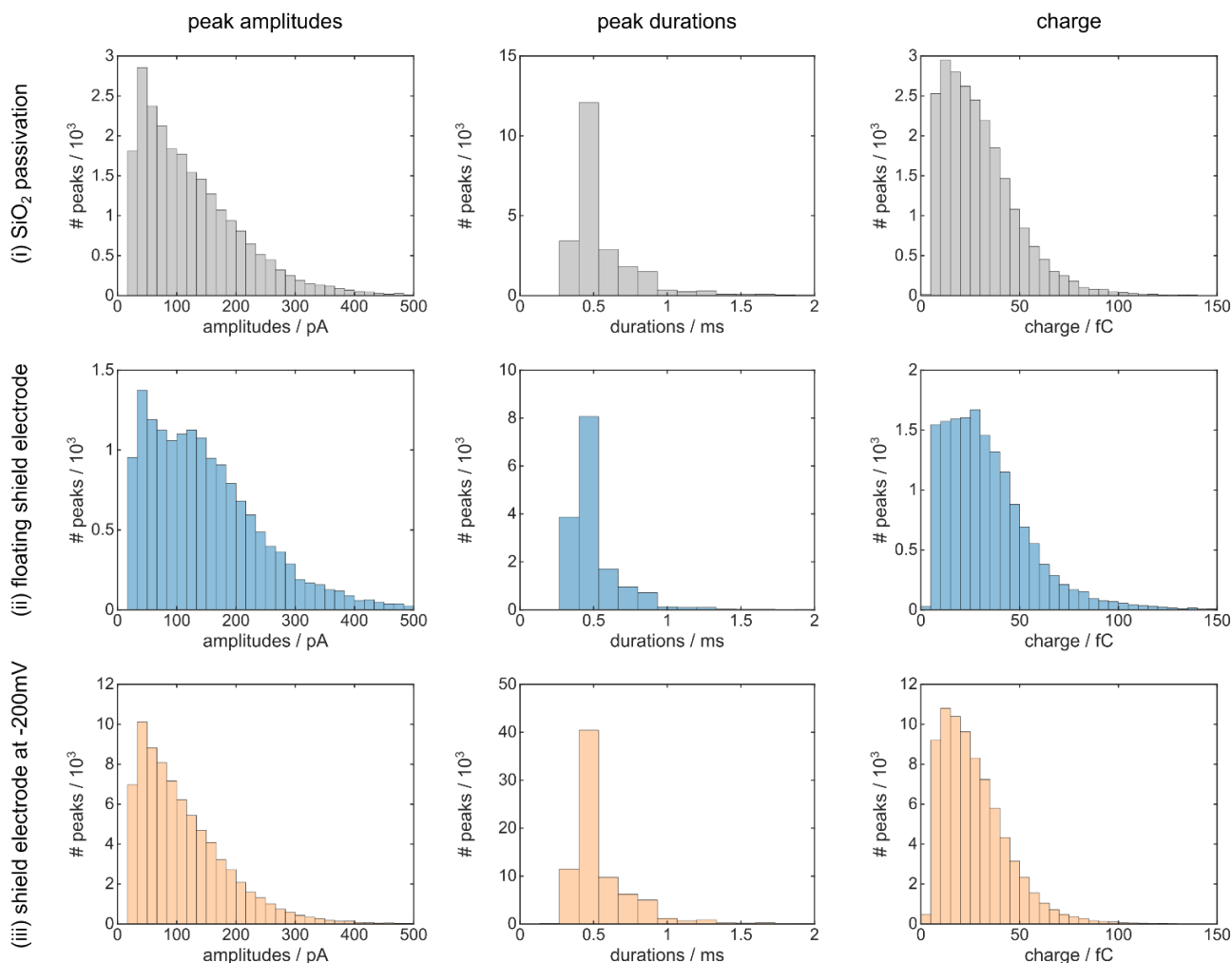
Figure S3 Statistical information on amplitudes, durations and charge of all considered current peaks for the experimental conditions of (i) a SiO₂-passivated chip, (ii) a floating shield electrode and (iii) a shield electrode held at -200 mV vs Ag/AgCl.

IV. Significance Test for Size Distributions

The AgNP sizes measured with a standard-MEA chip (i), a floating shield-MEA chip (ii) and a negatively-biased shield-MEA chip (iii) are 17.5 ± 3.6 nm ($n = 26,799$), 18.2 ± 4.3 nm ($n = 20,479$) and 17.0 ± 3.6 nm ($n = 104,712$), respectively. By performing Welch t-tests, we find significant differences in the scores for all pairwise comparisons, (i) and (ii) $t(401,230) = -18.36$, $p < 10^{-75}$; (i) and (iii) $t(408,910) = 14.52$, $p < 10^{-50}$; (ii) and (iii) $t(395,390) = 32.87$, $p < 10^{-232}$. Hence, there is evidence that differently charged passivation surfaces are slightly size-discriminant.

V. Particle-size Dependent Diffusive Mass Transfer

The mass transport of AgNPs towards the detection electrodes is particle-size depended. Fig. S3 exemplarily shows the theoretical limits for the collision rate at a single microelectrode calculated from Eqn. 3 and 4 for AgNPs with a diameter of 10 nm, 15 nm, and 20 nm, respectively. The effect of an altered passivation is drastically increasing for smaller particles, as depicted in Fig. S4. For instance, the mean collision rate (within the experimental time of 180 s) increases approximately by a factor of 19 from 0.48 Hz to 9.3 Hz for 20 nm-AgNPs, whereas we find a 27-fold enhancement from 0.7 Hz to 18.3 Hz for 10 nm-sized AgNPs.
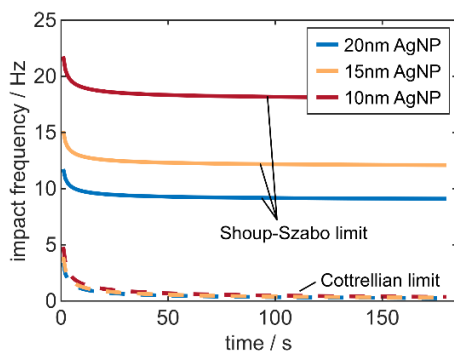
Figure S4 Theoretical impact frequencies at a single microelectrode with a radius of 4 μm for a fully adsorbing boundary (dashed, Cottrellian limit, Eqn. 4) and a reflecting boundary (solid, Shoup-Szabo limit, Eqn. 3) for differently-sized AgNPs.

VI. Silver Chloride Residues

We observe differences in the electrochemical cleaning during the recycling procedure consisting of subsequent immersions in HNO_3, NH_4OH, KOH and H_2SO_4. Fig. S5a and b show the typical responses for all platinum electrodes short-circuited within the electrochemical cleaning in 100 mM KOH and 200 mM H_2SO_4, respectively. Additionally, the experimental data for detection experiments of chips being contaminated with AgCl residues is visualized. Fig. 5c depicts the number of detected AgNPs (measured at 62 electrodes) for successive experiments. Interestingly, there is a significant decrease if the cleaning in ammonium hydroxide (NH_4OH) is left out, suggesting that the electrode area might by covered with AgCl, thus, leading to a smaller electroactive surface. This finding is similar to the observed behavior from Compton and co-workers, when they reported differences between recordings cycles with and without mechanical cleaning in between.[1]
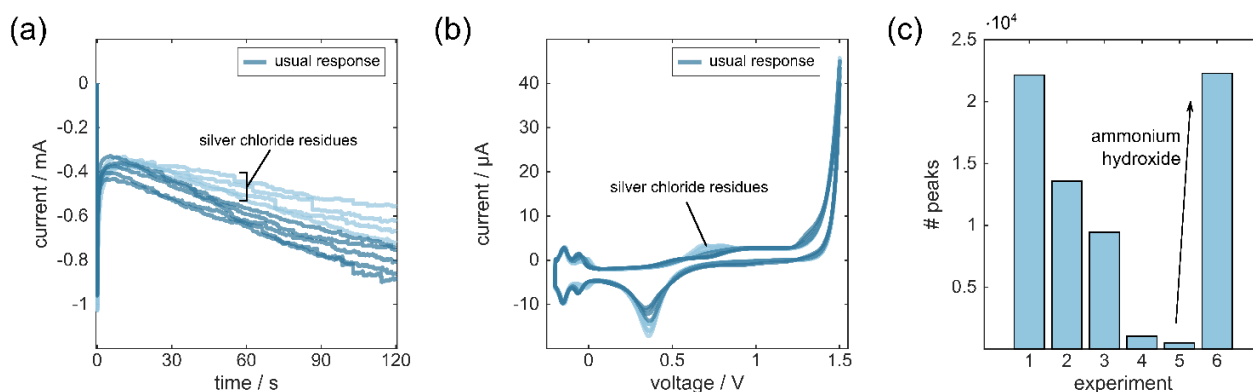
Figure S5 (a) Chronoamperometry in 100 mM KOH of all electrodes short-circuited. (b) Cyclic voltammetry in 200 mM H_2SO_4. (c) Number of detected peaks for subsequent detection experiments without removing silver chloride residues in between with ammonium hydroxide. The immersion in ammonium hydroxide leads to a sensor performance as before.

VII. Aggregation of Silver Nanoparticles in KCl Solution

UVvis spectra (Specord 210, analytic Jena, Jena, Germany) and DLS measurements (Zetasizer Nano ZS, Malvern Analytics, Worcestershire, UK) were obtained in order to investigate changes within the AgNP ensemble in different electrolyte solutions. To this end, macro-cuvettes (PMMA, Carl Roth, Karlsruhe, Germany) were filled with 1 mL electrolyte, the AgNPs were subsequently inserted and mixed twice. The recordings started between 3 and 5 s after the insertion of AgNPs.

To investigate the effect of aggregation, we recorded within 5 min successive UV spectra from a solution containing 50 pM AgNP (20 nm diameter) and 20 mM KCl. Additionally, we investigated the temporal change in the hydrodynamic radius, obtained from DLS measurements, at different KCl concentrations. As shown in Fig. S6a and b, we see a slight decrease in the absorbance during a UVvis experiment indicating minor changes in the AgNP ensemble within the experimental timeframe. This finding is complemented by the DLS results in Fig. S6c, which show a significant increase in the hydrodynamic radius for KCl concentrations above 25 mM.
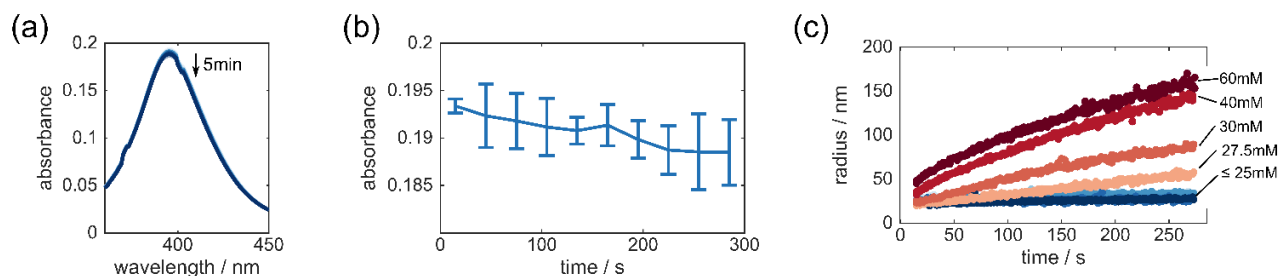
Figure S6 (a) UVvis spectra for 50 pM AgNP in 20 mM KCl solution during 5 min of recording. (b) Absorbance at the peak ($\lambda = 395$ nm) in (a). The sample was measured every 30 s after AgNP insertion for 5 min. Error bars indicate standard deviations across 3 trials. (c) Temporal change in the hydrodynamic radius obtained from DLS measurements in case of 500 pM AgNP with 20 nm size for various KCl concentrations.

VIII. References

(1)   Batchelor-McAuley, C.; Ellison, J.; Tschulik, K.; L. Hurst, P.; Boldt, R.; G. Compton, R. In Situ Nanoparticle Sizing with Zeptomole Sensitivity. *Analyst* **2015**, *140* (15), 5048–5054. https://doi.org/10.1039/C5AN00474H.

A.2 On-Chip Electrokinetic Micropumping for Nanoparticle Impact Electrochemistry

On-Chip Electrokinetic Micropumping for Nanoparticle Impact Electrochemistry

Lennart J. K. Weiß[†], Emir Music[†], Philipp Rinklin[†], Marko Banzet[‡], Dirk Mayer[‡], Bernhard Wolfrum[*,†]

[†] Neuroelectronics - Munich Institute of Biomedical Engineering, Department of Electrical Engineering, TUM School of Computation, Information and Technology, Technical University of Munich, Boltzmannstrasse 11, 85748 Garching, Germany

[‡] Institute of Biological Information Processing, Bioelectronics (IBI-3), Forschungszentrum Jülich, 52425 Jülich, Germany

[*] Corresponding Author: Bernhard Wolfrum, bernhard.wolfrum@tum.de

Table of Content

I. Experimental Details

Chemicals

Silver nanoparticles (0.02 mg/mL in aqueous solution, average size 20 nm), nitric acid (HNO$_3$, 70%), sulfuric acid (H$_2$SO$_4$, 95-98%), potassium chloride (KCl) and potassium hydroxide (KOH, ≥85%) were purchased from Merck, Germany. Ammonium hydroxide (NH$_4$OH, 28%) was obtained from VWR Chemicals, France. Dilutions were prepared using deionized water from a BerryPURE purification system (Berrytec, Germany).

Chip Fabrication

The microelectrode arrays (MEAs) were fabricated using clean-room technology as described in earlier work.[1] In short, the metal structures were deposited as a stack of 10 nm Ti / 100 nm Pt / 5 nm Ti onto a borosilicate wafer using electron beam evaporation and were patterned using optical lithography. Then, the structures were passivated by an alternating stack of 200 nm-thick SiO$_2$ (O) and 100 nm-thick Si$_4$N$_3$ (N) layers (5 layers with order O-N-O-N-O) via plasma-enhanced vapor deposition. Finally, reactive ion etching was applied to create 62 detection electrodes with a diameter of 8 μm and a pitch of 200 μm. The macroscopic electrode (ME) has dimensions of 1.4×1.4 mm^2 and surrounds all detection electrodes. Lastly, glass rings with 17 mm diameter were glued onto the chips and served as fluid reservoirs.

Chip Cleaning Routine

Prior to each experiment, the MEA chips were cleaned in a four-step routine. First, an electrochemical reduction step (chronoamperometry, -2.5 V vs Ag/AgCl for 3 min) in 28 % NH$_4$OH was performed to support the dissolution of any previously deposited AgCl and AgO$_x$. Then, the chips were immersed in concentrated HNO$_3$ to account for contamination by Ag residues. Lastly, the electrodes were activated via electrochemical reduction in 100 mM KOH (chronoamperometry, -1.5 V vs Ag/AgCl for 3 min) followed by cyclic voltammetry in 200 mM H$_2$SO$_4$ (potential range -0.2 V to 1.5 V vs Ag/AgCl, scan rate 200 mV/s, 10 cycles). All electrodes were short-circuited during the electrochemical cleaning procedure. The entire cleaning process was performed with a VSP-300 potentiostat (BioLogic Instruments, France) in a three-electrode setup using a Ag/AgCl reference electrode (3 M NaCl, RE-6 from BASi, West Lafayette) and a coiled Pt-wire counter electrode, respectively. All potentials stated in the manuscript refer to the Ag/AgCl reference potential.

Optical Investigation of Microbead Trajectories

The trajectories of the microbeads (4 μm diameter, rhodamine B-marked, melamin resin, from Sigma-Aldrich, Germany) were imaged with a fluorescence microscope (Leica DM 2700 M and Las X software, Leica, Wetzlar, Germany) using a 10x immersion objective (HC APO L 10x/0.30 W U-V-I). The potential at the ME electrode was controlled by a PalmSens4 potentiostat (PalmSens BV, The Netherlands). The microbead trajectories and the current evolution were simultaneously recorded using a desktop recording program (Bandicam, Bandicam Company, US). The solution contained 4 μl of 1:10-diluted microbeads and 1 ml deionized water (BerryPURE purification system, Berrytec, Germany). The conductivity of the solution was 0.14 mS/cm and the ζ-potential of the particles was -9.6 ± 0.2 mV (electrophoretic mobility - 6.8 m^2/Vs). The videos were cut and post-processed via Camtasia Studio 2020 (TechSmith, US) and Inkscape.

II. Microelectrode Array Chips
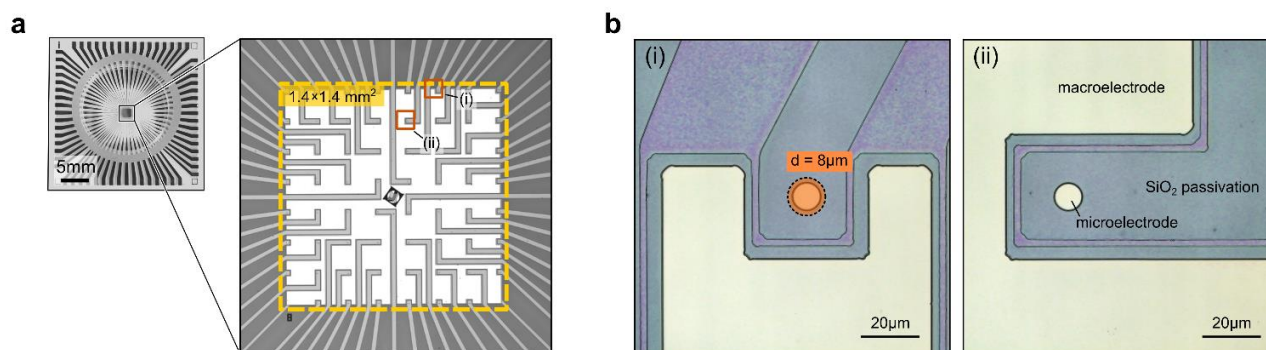
Figure S1 Layout of the microelectrode array chips. (a) Optical images of the chip and the electrode array. The macroscopic electrode (yellow, 1.4×1.4 mm^2) surrounds all 62 detection electrodes that are arranged in an 8×8 array. (b) Zoomed images of different microelectrodes with a diameter of 8 μm. The macroelectrode and microelectrode structures were fabricated in the same layer. A small gap later covered by the passivation layer separates the metal structures.

III. Chemical Cleaning Routine

The status of the electrode surface is a key parameter to obtain consistent detection results. Therefore, we typically perform a cyclic voltammetry in H_2SO_4 solution to activate the metal surfaces and asses their cleanliness. The presence / absence of redox peaks and their amplitude values, see Fig. S2, can be used to evaluate the electroactive surface and judge the usability of the chips by comparison with a benchmark curve (black). We use this strategy to ensure a consistent performance across different experiments. Since electrode polishing is not feasible for our MEA chips, we apply (electro-)chemical cleaning methods after the impact experiment. Our routine involves the electrochemical reduction in NH_4OH and KOH to remove AgCl and AgO_x residues that stem from previous experiments. Moreover, the chips are incubated in HNO_3 to dissolve residual silver prior to the activation. In case of a substantial deviation from the activation to an unused clean chip (see colored graphs for examples), the full cleaning routine is repeated.
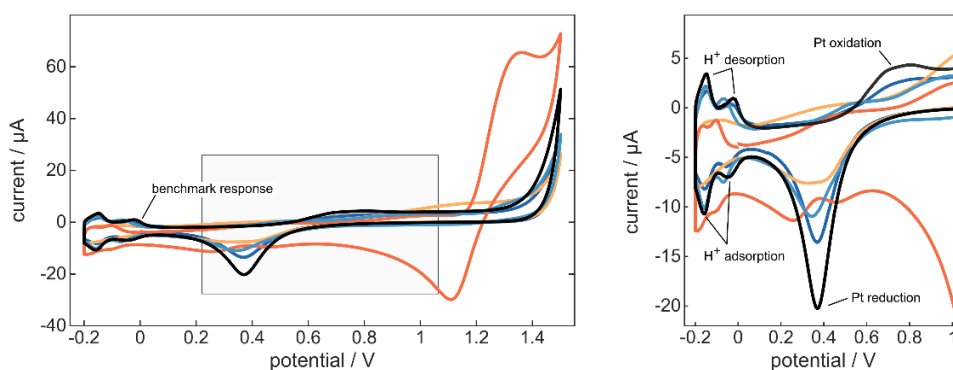
Figure S2 Cyclic voltammograms of short-circuited electrodes in 200mM H_2SO_4. The graph shows the 10th cycle at a scan rate of 200 mV/s. The black curve represents the benchmark response obtained from a clean chip. All other responses show various electrode contaminations clearly visible as deviations (in amplitude and shift of the redox peaks) from the benchmark response. The cleaning routine was performed until the chip response reached the benchmark.

IV. Experimental Setup for Impact Experiments
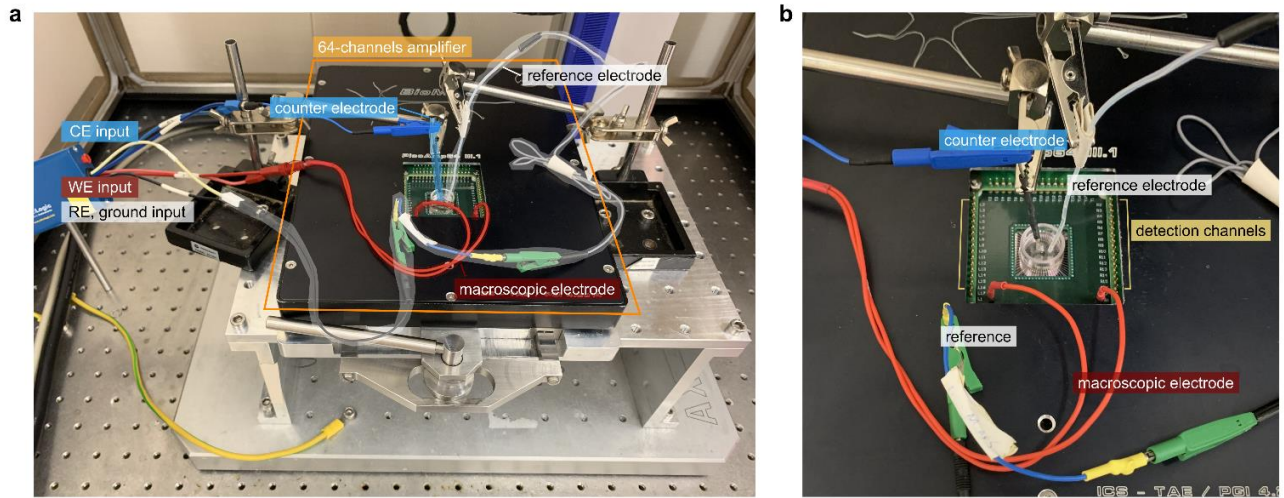
Figure S3 Experimental setup for the impact Experiments. (a) Assembly of the devices within a shielded environment. The 64-channel amplifier system is mounted on a grounded metal table sitting in a Faraday cage. The amplifier system (orange) is operated in a two-electrode configuration. The macroscopic electrode is externally controlled in a three-electrode setup, indicated by the common Ag/AgCl reference electrode (white, ground), the coiled Pt-wire as counter electrode (blue) and the connections to the break-out pins of the amplifier circuit board. (b) Zoomed view of the setup. The detection electrodes on the chip are connected to individual amplifiers (yellow) and the break-out pins link to the macroscopic electrode (red). The potential at the detection electrodes, as well as the potential of the macroscopic electrode is set with respect to the shared Ag/AgCl reference electrode.

V. Background Reactions in 25 mM KCl
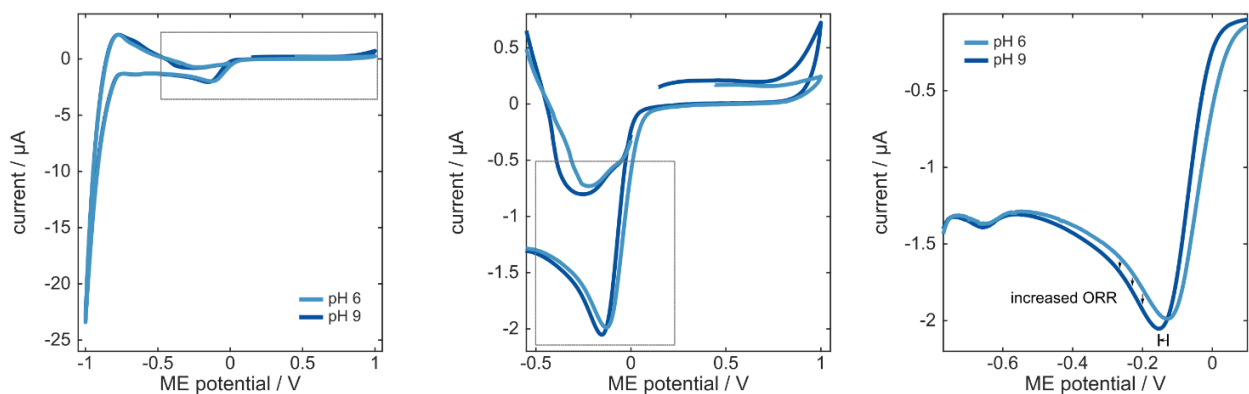
Figure S4 Cyclic voltammograms for 25 mM KCl at pH 6 and pH 9 for a ME potential between -1V to 1V vs Ag/AgCl and a scan rate of 5 mV/s. The shift in pH value leads to an increased cathodic current for potentials between -600 mV and -200 mV.

VI. Trajectories of Insulated Microbeads Under External Transport Control
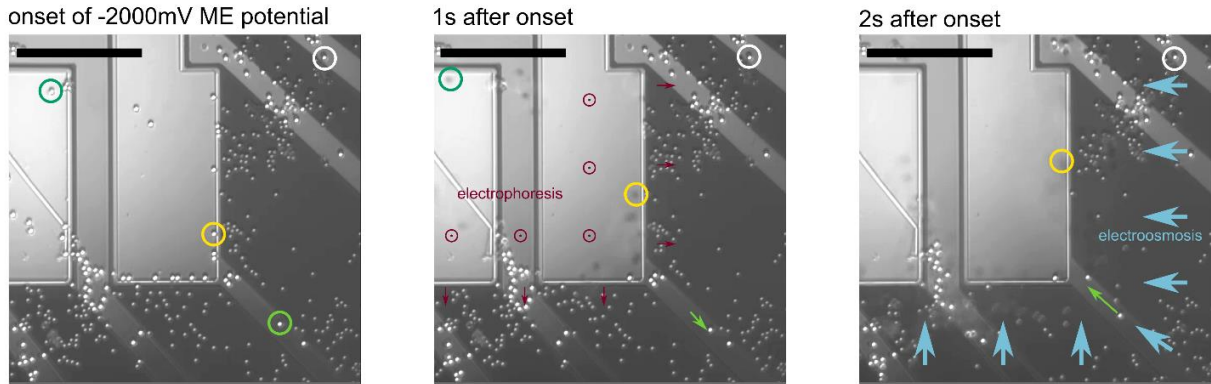
Figure S5 Exemplary video frames (starting from 1 min 34 s in video V2) in case of -2 V ME potential and deionized water. The circles at the beginning indicate four different 4 μm-sized microparticles. The potential change towards a negative potential leads to an upward motion (dark green and yellow circles) of particles located above the ME electrode. The fast motion of particles that surround the ME is governed by the relaxation of the electrical double layer and electrophoretic effects (light green). After an initial phase, a flow field establishes due to electroosmosis. The direction of the solvent is counteracting the electrophoretic effects on negatively charged particles.

We were able to manipulate the motion of negatively charged microbeads simply by manipulating the ME potential, as indicated in Fig. S5 and Fig. S6 as well as video V1 and V2. For instance, a high negative ME potential repelled the microbeads directly above the ME and pushed them out of the focal plane, whereas a high positive potential attracted them. The trajectories of the microbeads that initially surrounded the ME, showed a more complex behavior since the development of electrophoresis and –osmosis supposedly act at different timescales, see V2 and Fig. S2. Shortly after the potential steps, ion redistribution governs the particle motion (e.g. particles are pushed outwards at negative potentials), whereas the macroscopic electroosmotic velocity field dominates at longer times (particles are carried towards the ME).
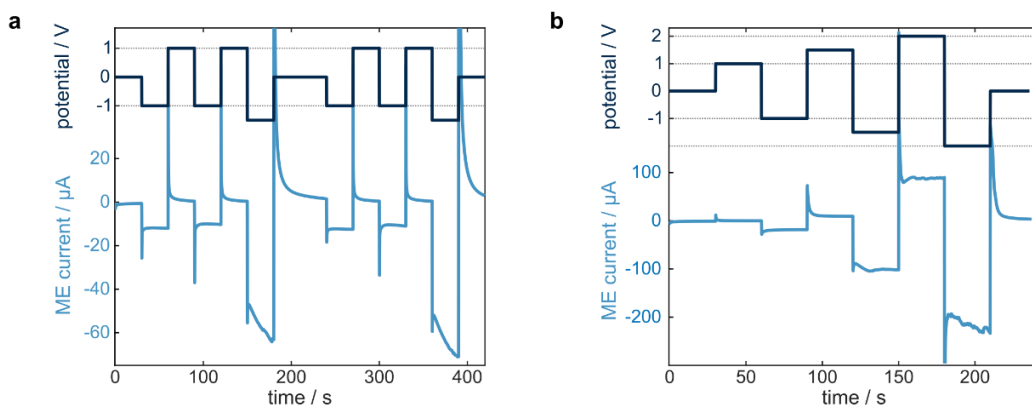
Figure S6 Current and potential at the ME in contact with deionized water during the recordings shown in (a) video V1 and (b) video V2.

VII. Statistical Data for 100 pM AgNP in 25 mM KCl Solution with Stepped ME Potential

a amplitude distribution with labels 89.6 ± 50.6 nm and 88.6 ± 50 nm; ME potential legend: −200mV, −700mV

b duration distribution with labels 0.71 ± 0.32 ms and 0.7 ± 0.31 ms

c charge distribution with labels 30 ± 15.7 fC and 29.5 ± 15.5 fC

d size distribution with labels 17.8 ± 3 nm and 17.7 ± 3 nm
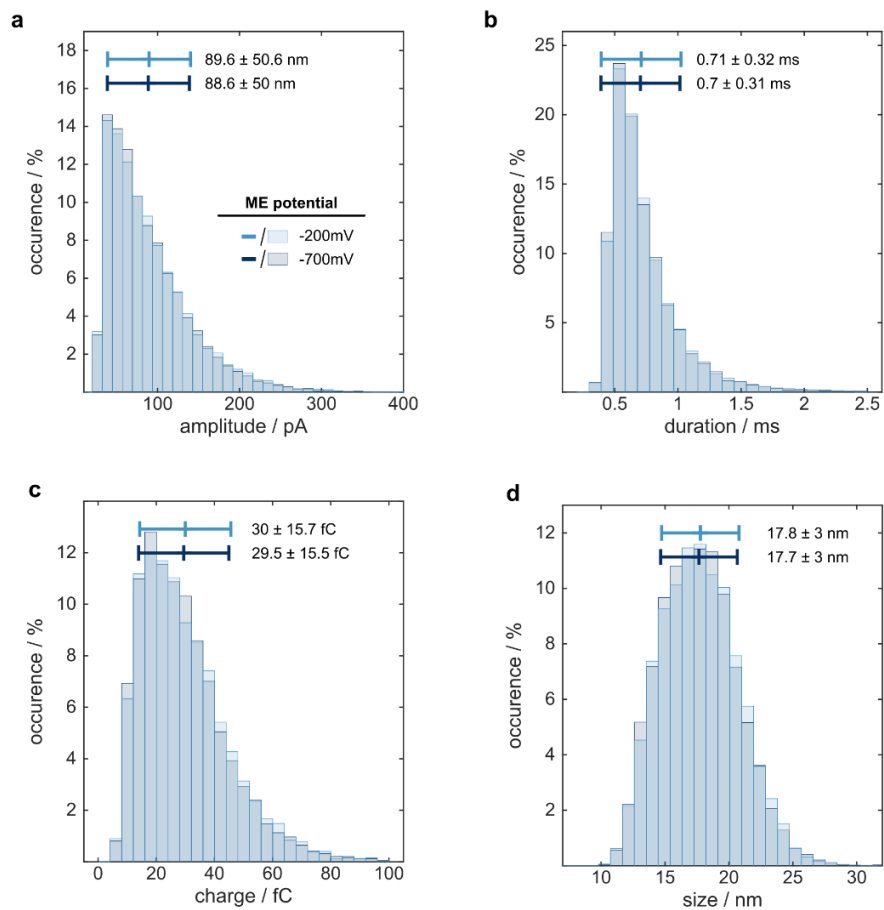
Figure S7 Statistical data for AgNP detection shown in Figure 2 in the manuscript including (a) amplitude, (b) duration, (c) charge and (d) size distributions for measurement times between 250 s and 850 s. Error bars indicate mean and standard deviations.

VIII. Potential and Velocity Distributions in a Simplified Geometry

The finite-element simulation of a simplified 2D band electrode-geometry was performed with Comsol Multiphysics 5.4 using the Laminar Flow and the Electric Currents modules. The simulation further includes only primary effects of the biased electrodes on the electrolyte and neglects specific reactions, as well as, the redistribution of ions. Thus, the absolute values of the resulting fields are overestimated. Furthermore, in contrast to the experimental conditions, the simulation represents a simplified geometry with four infinitely extended band electrodes as well as an infinitely extended counter electrode, see Figure S8a. Nevertheless, the influence of a macroscopic electrode that surrounds the detection electrodes is captured in the model. The settings are given in Table S1 and the results are depicted in Figure S8b.

The velocity distribution and the streamlines indicate that apart from the expected macroscopic transport also smaller vortices around the detection electrode might drive particle transport.

Table S1. Comsol simulation parameter for the Laminar Flow and the Electric Currents module that were used in the study.

settings at/for …	electric currents module	laminar flow module
A – detection electrodes	electric potential $V = 600\,\text{mV}$	no-slip
B – macroscopic electrode	electric potential $V = \{-900, -700, 600\}\,\text{mV}$	no-slip
C – insulating SiO_2 surface	electric insulation	electroosmotic velocity, input from electric field (ec/cucn1) $\zeta_s = -50\,\text{mV},^2\,\epsilon_r = 80$
D – electrical ground	ground, $V = 0$	open boundary, normal stress $f_0 = 0$
E - liquid	floating potential floating potential group	open boundary, normal stress $f_0 = 0$
electrolyte domain	current conservation, $\sigma = 3.5\,\text{mS/cm}$ isotropic $\epsilon_r = 80$	density and viscosity of water
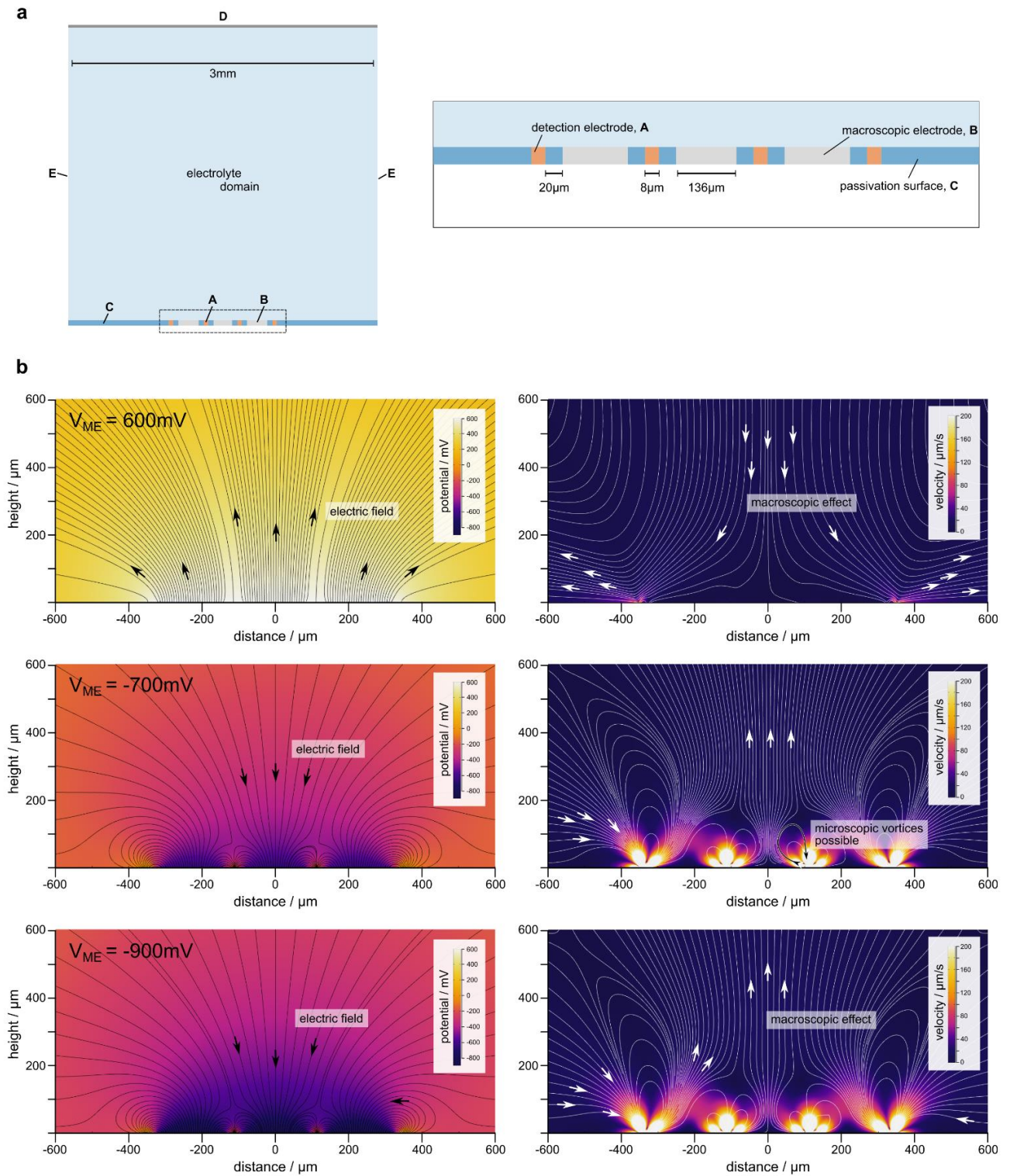
Figure S8 Numerical simulation result of a simplified 2D-geometry, including a set of detection electrodes and a macroscopic electrode. (a) Schematic of the simulated geometry with settings (for A to E) provided in Tab S1. (b) Potential and velocity distribution for macroelectrode potentials of 600 mV, -700mV and -900 mV, respectively. The potential plot includes the field lines of the electric field, whereas the velocity plot depicts streamlines. The direction of the velocity distribution (see white arrow) indicates small micro vortices that are introduced by the passivation layer between detection and macroscopic electrode biased to different potentials.

IX. Statistical Data of AgNP Impacts for Detection Electrodes Located at Different Positions
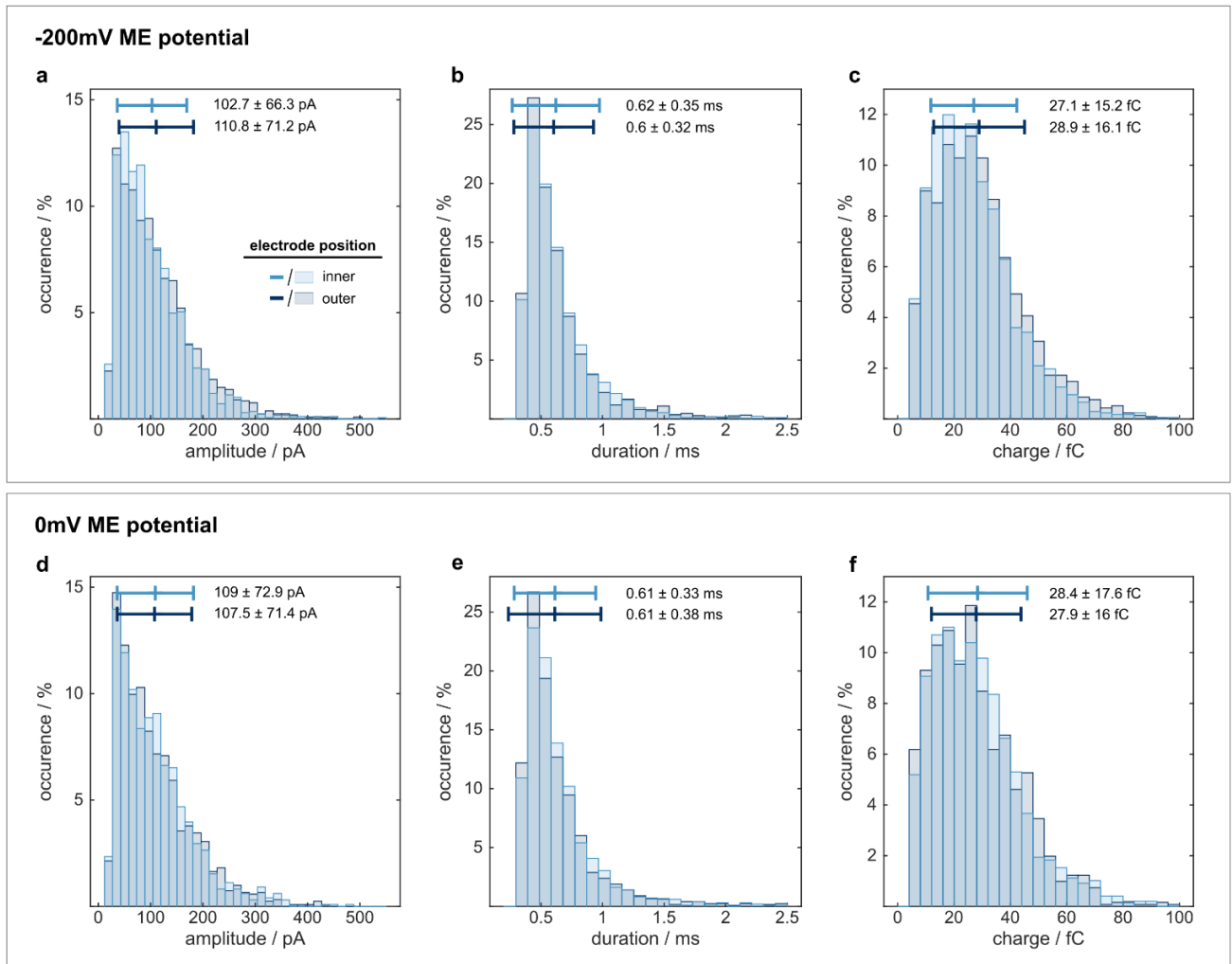
Figure S9 Additional data to Figure 3 in the manuscript. (a,d) Amplitude, (b,e) duration and (c,f) charge distributions for all considered impacts recorded at different ME potentials.

X. Effect of Electrode Location on Impact Rate for Positive ME Potentials
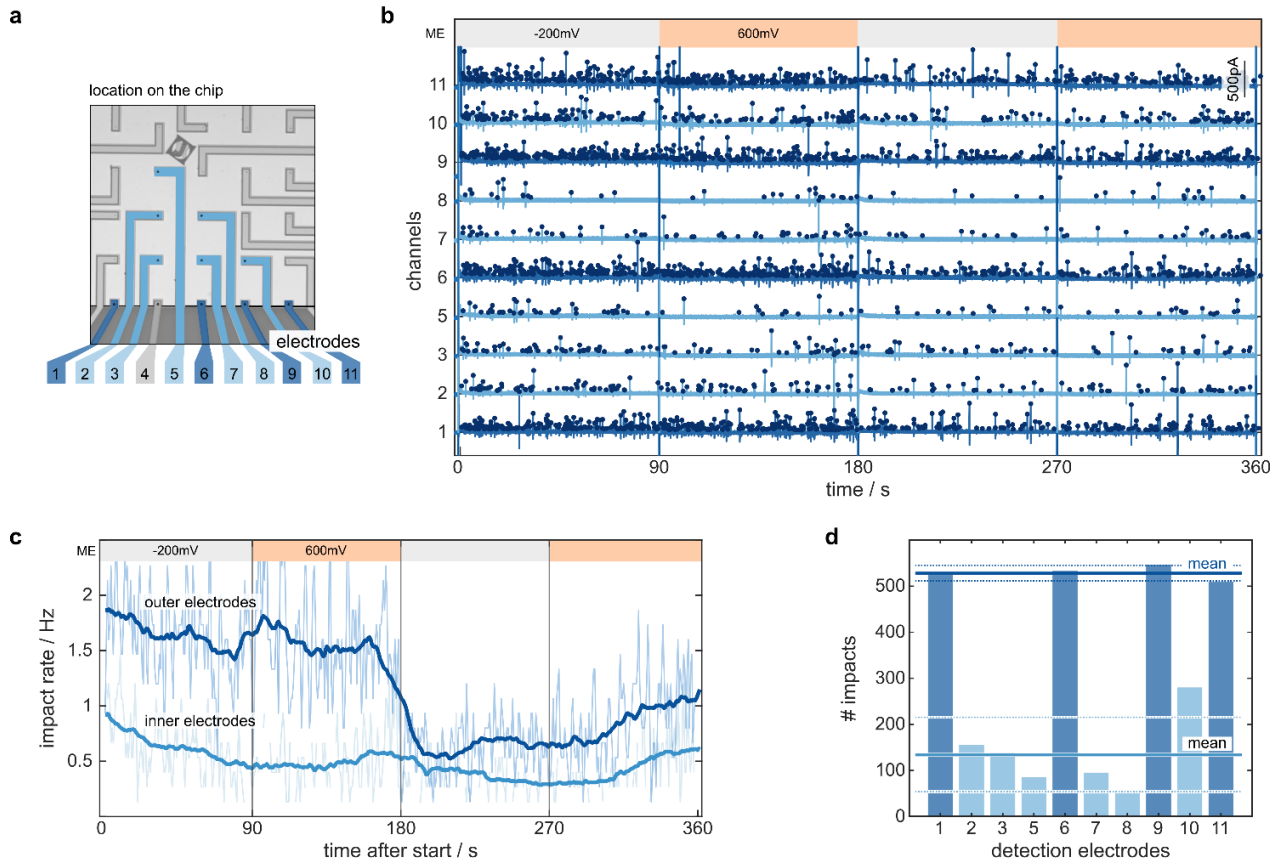
Figure S10 Effect of electrode location on the chip for positive potentials at the macroelectrode. (a) Schematic of the channels on the microelectrode array. Note, channel 4 is discarded for the analysis as its peak-to-peak noise exceeds the channels quality criteria. (b) Raw current traces of 10 electrodes during an experiment with alternating potentials every 90s. The data is collected from the same subset of channels as in Fig. 3 for the experiment shown in Fig. 4 (for 600 mV, shown in red in the main text). The channels are displayed with an offset of 500 pA for clarity and considered impacts are marked as blue dots. (c) Temporal evolution of the mean impact rate for outer and inner electrodes based on the raw traces shown in (b). (d) Mean impact rate across the entire experiment. Solid and dashed lines indicate the ensemble mean and standard deviations for inner (light blue) and outer channels (dark blue).

XI. Effect of Anion Distribution and Initial Adsorption
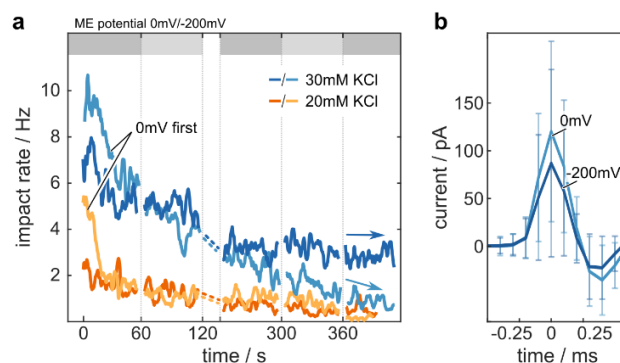
Figure S11 Effect of ME potential and electrolyte concentration on the AgNP impact rate. The ME potential does also affect the chloride concentration, which can lead to a decreased impact rate and smaller amplitudes. (a) Temporal evolution of the impact rate in case of 20 mM and 30 mM KCl each containing 100 pM of 20nm-AgNPs. The ME potential was altered between 0 mV and -200 mV. Light colors indicate a ME potential of 0 mV first, whereas dark colors represent -200 mV at the start. (b) Average current transients during AgNP impact for a potential of 0 mV and -200 mV in case of 30 mM KCl. The first 30s of recordings are considered for the evaluation. Note, the negative overshoot at 0.25 ms is stemming from an amplifier-related artifact.

The critical role of the anion concentration is visualized in Fig. S11, where the order of the subsequent ME potential steps – 0mV and -200mV – was altered for two different electrolyte concentrations. In case of 20 mM KCl, the impact rate is significantly lower compared to 30 mM KCl – regardless of the potential order. Remarkably, the negative initial ME potential leads to a substantially reduced rate at early measurement times. Here, the values for 0 mV ME potential clearly outperform the rates for -200 mV in case of both electrolyte concentrations. If we consider only mass transport effects that are evoked by a moderate oxygen reduction, we would assume exactly the opposite. A smaller ME current in case of 0 mV indicates a weaker electric field, thus, a reduced particle supply due to surface-driven convection. However, the electric field and the H^+ gradient do not exclusively alter the nanoparticles' trajectories, but also act on the chloride ions in solution. Since the ME potential is stepped prior to the detection, it is most likely that an initial depletion of chloride ions causes the remarkable difference. The shortage of chloride ions is additionally reflected in the shape of the AgNP impacts, where we found slightly smaller amplitudes, see Fig. S11b. This effect might be again associated with an impaired chloride influx. Lastly, Fig. S11a reveals another phenomenon that becomes more apparent for extended measurement times. The initial variation in impact rate between the two potential conditions diminishes after ~35 s, as the impact rate for 0 mV drastically drops. This trend was found to be persistent and even stronger for longer times. We attribute this phenomenon to a loss of particles prior to detection, since particles that approached the ME surface might be irreversibly adsorbed for a reduced electrostatic repulsion.

XII. References

(1)   Weiß, L. J. K.; Music, E.; Rinklin, P.; Straumann, L.; Grob, L.; Mayer, D.; Wolfrum, B. Engineering Electrostatic Repulsion of Metal Nanoparticles for Reduced Adsorption in Single-Impact Electrochemical Recordings. *ACS Appl. Nano Mater.* **2021**, *4* (8), 8314–8320. https://doi.org/10.1021/acsanm.1c01507.
(2)   Gu, Y.; Li, D. The ζ-Potential of Glass Surface in Contact with Aqueous Solutions. *J. Colloid Interface Sci.* **2000**, *226* (2), 328–339. https://doi.org/10.1006/jcis.2000.6827.

A.3   Single-Impact Electrochemistry in Paper-Based Microfluidics

Single-Impact Electrochemistry in Paper-Based Microfluidics

Lennart J. K. Weiß[†], Georg Lubins[†], Emir Music[†], Philipp Rinklin[†], Marko Banzet[‡], Hu Peng[†], Korkut Terkan[†], Dirk Mayer[‡], Bernhard Wolfrum[†,*]

[†] Neuroelectronics - Munich Institute of Biomedical Engineering, Department of Electrical and Computer Engineering, Technical University of Munich, Boltzmannstrasse 11, 85748 Garching, Germany

[‡] Institute of Biological Information Processing, Bioelectronics (IBI-3), Forschungszentrum Jülich, 52425 Jülich, Germany

[*] Corresponding Author: Bernhard Wolfrum, bernhard.wolfrum@tum.de

I. Design and Optical Images of the µPAD
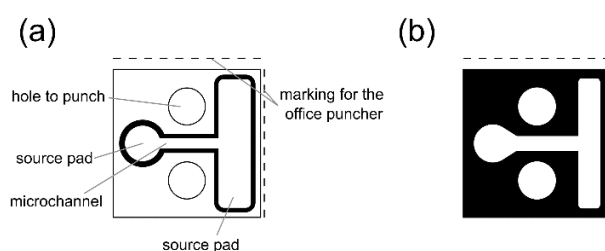
Figure S1: µPAD Designs (a) for the detection experiments, where the AgNP are suspended in the electrolyte solution and (b) for the lateral flow experiments, where AgNPs were previously dried onto the source pad. The layouts, shown in their actual size, fit the dimensions of the microelectrode chip.
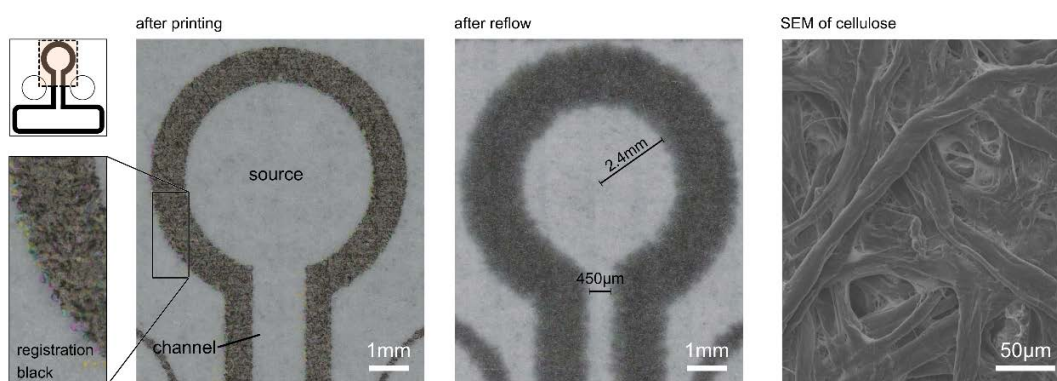
Figure S2: Optical images of the µPAD structure from Fig. S1a before and after the reflow step, as well as, a scanning electron microscopy (SEM) image of the chromatography paper used in the study.

II. Electrochemistry Using a Reference-On-Chip Setup
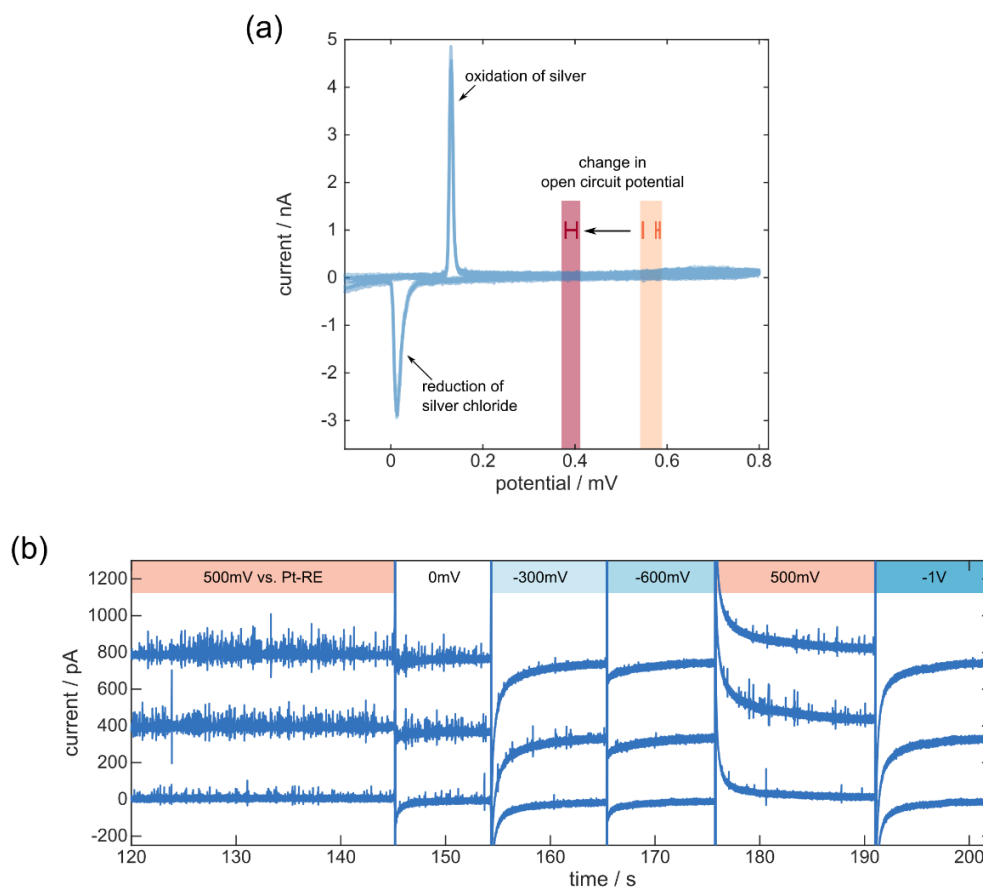
Figure S3: (a) Open circuit potential of a clean platinum electrode in 25 mM KCl solution before (orange, the errorbars show mean ± std of two measurements) and after (red) a detection experiment. Furthermore, the blue graphs show cyclic voltammograms of two individual microelectrodes being exposed to 25 mM KCl and 100 pM of 20nm-AgNPs. (b) Raw current traces for three channels in 25 mM KCl containing 100 pM of 20 nm-AgNPs. During the experiment, the potential at the detection electrodes was altered between values where AgNP oxidation occurs (-300 mV to 500 mV vs Pt-RE) and potentials where the oxidation is not promoted (e.g. -600 mV and -1 V vs. Pt-RE). The traces are shifted vertically with an offset of 400 pA for clarity.

III. Additional Data for Experiments Using a Paper-Based Microfluidic Channel
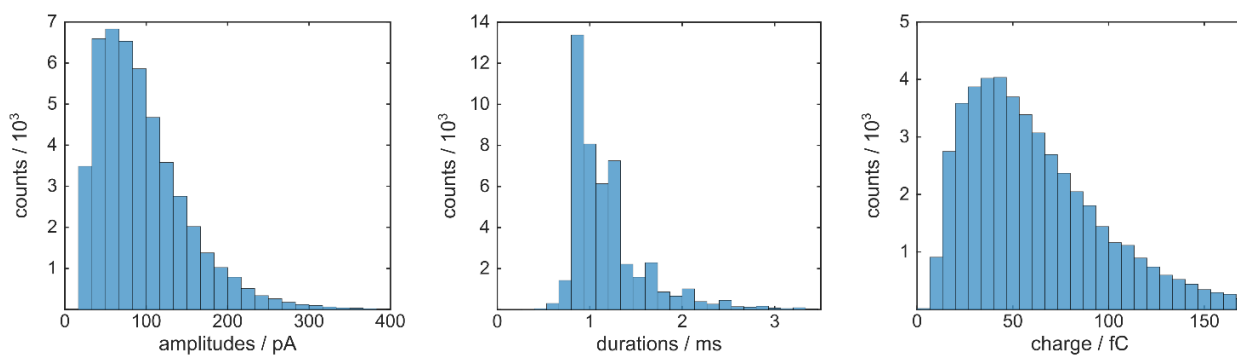
Figure S4: Statistical results of all considered impacts for 100 pM of 20nm-AgNPs in 25mM KCl. The data from 15 channels is based on 30 s of evaluation and corresponds to the raw data presented in Fig. 2 in the manuscript.
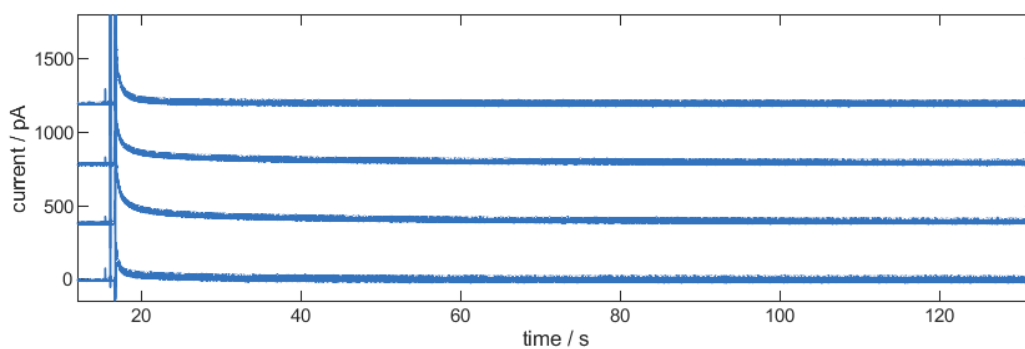
Figure S5: Raw data of a control experiment. Here, a 12μl droplet that contains 25mM KCl solution is released on a μPAD. The graph shows the same channels as Fig. 2 in the manuscript. Individual channels are displayed with an offset of 400pA for better visualization. The peak-to-peak noise level is calculated to 44.9±3.8 pA.
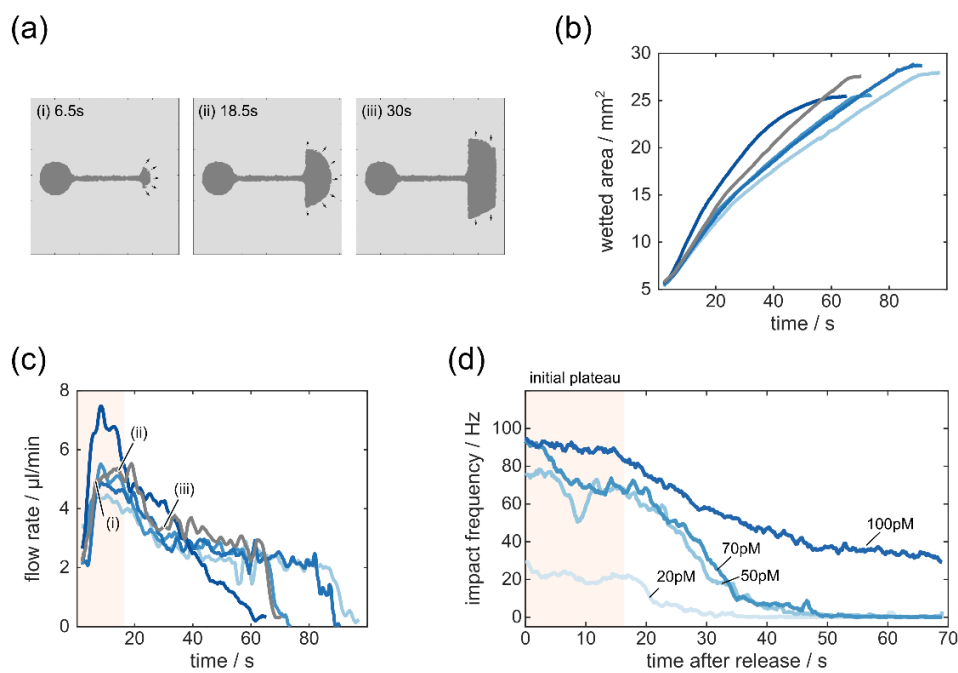
Figure S6: Flow characterization in the μPAD. (a) Exemplary images of the flow that were image-processed via thresholding. The analysis is based on the video recordings related to Fig. 1c in the manuscript. (b) Wicking of the paper depicted as temporal change in the wetted area. (c) Temporal evolution of the flow rate based on the data shown in (b) and a constant paper height of 180 μm. (d) Temporal change in the impact rate for four different detection experiments from Fig. 3 in the manuscript. The initial plateau in the impact rate matches well with the flow characteristics shown in (b) and (c). Here, higher flow rates are in line with higher detection rates. Moreover, similar detection rates for different particle concentrations might suggest a heterogeneous particle distribution within the droplet/solution.

IV. Additional Data for Experiments with Nanoparticles of Different Sizes
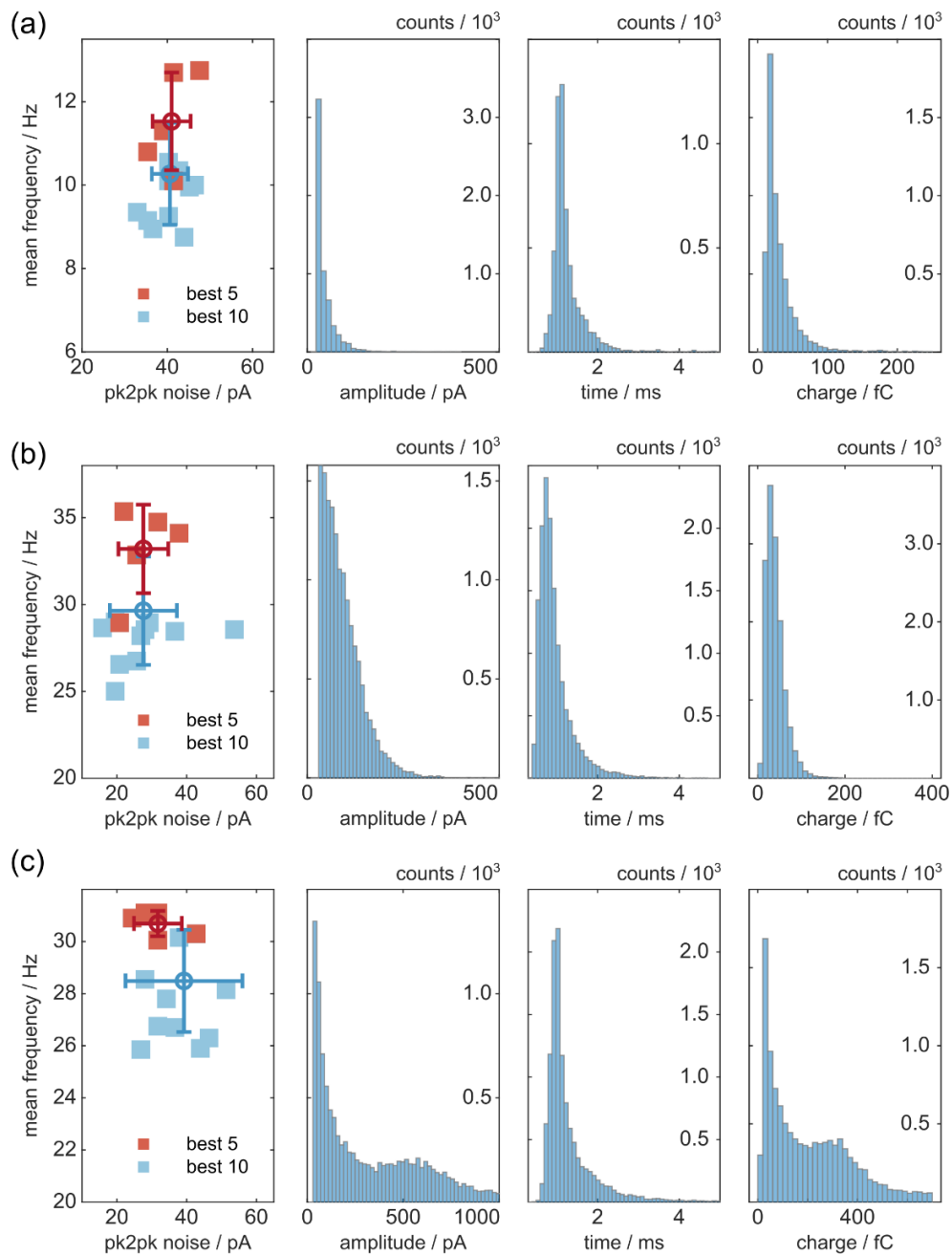
Figure S7: Statistical data of detection experiments in 25 mM KCl for 50 pM AgNP with (a) a diameter of 10 nm, (b) 20 nm, and (c) 40 nm. The graphs present the mean impact rate based on a 20 s evaluation window, as well as the amplitude, duration and charge distribution of all considered impacts.
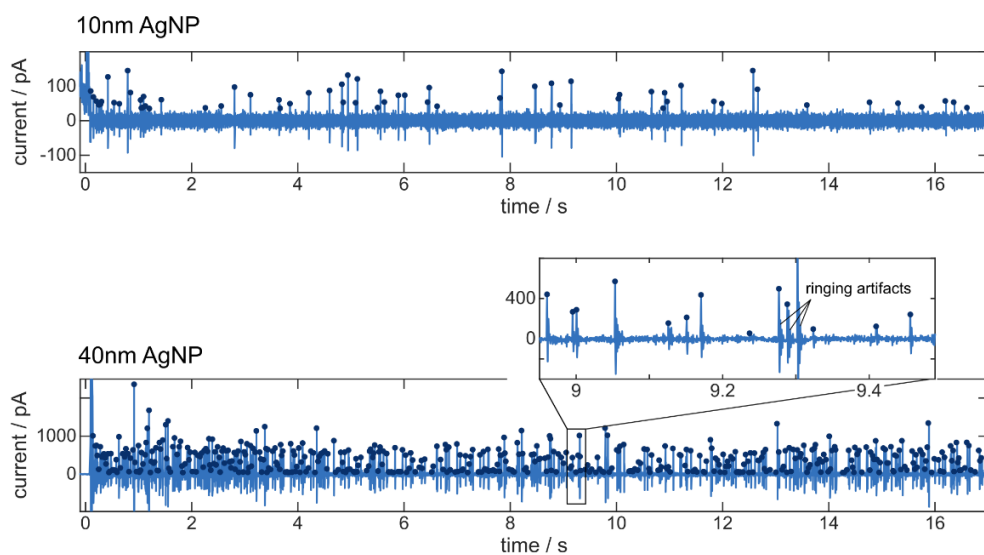
Figure S8: AgNP detection for 50 pM of 10 nm- and 40 nm-AgNPs in 12 µl 25 mM KCl electrolyte solution. The solution was directly pipetted onto a clean chip. Note the different current scalings.
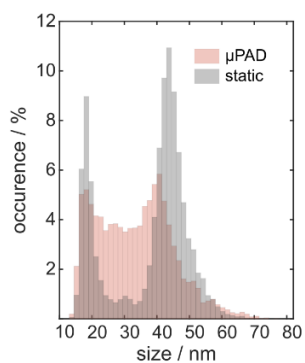
Figure S9: Histograms for 25 mM KCl containing 50pM AgNPs with average diameter of 40 nm in case of a static experiment (gray), where a droplet was directly released onto the electrode array and a detection experiment that uses a paper-based microchannel (red).

V. Additional Data for Lateral Flow Experiments
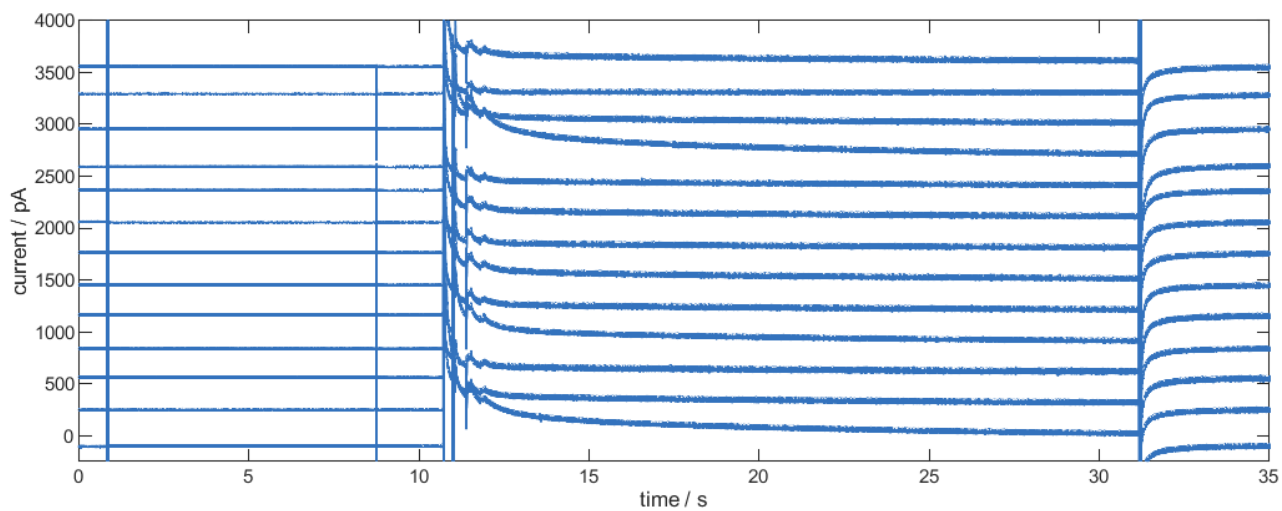
Figure S10: Control measurement for the lateral flow experiment. The 12μl-droplet contained 30 mM KCl and 0.1% Tween20. The potential at the electrodes was held at 500 mV vs. Pt-RE while a droplet was released (~11 s in the graph). The channels are displayed with a current offset of 300pA for clarity.

A.4 Prototype Digital Lateral Flow Sensor Using Impact Electrochemistry in a Competitive Binding Assay

Prototype Digital Lateral Flow Sensor Using Impact Electrochemistry in a Competitive Binding Assay

Lennart J. K. Weiß[†], Philipp Rinklin[‡], Bhawana Thakur[‡], Emir Music[†], Heike Url[†], Inola Kopic[‡], Darius Hoven[†], Marko Banzet[‡], Tassilo von Trotha[‡], Dirk Mayer[‡], Bernhard Wolfrum[†,*]

[†] Neuroelectronics - Munich Institute of Biomedical Engineering, Department of Electrical and Computer Engineering, Technical University of Munich, Boltzmannstrasse 11, 85748 Garching, Germany

[‡] Institute of Biological Information Processing, Bioelectronics (IBI-3), Forschungszentrum Jülich, 52425 Jülich, Germany

[*] Corresponding Author: Bernhard Wolfrum, bernhard.wolfrum@tum.de

I. Biotinylated Nanoparticles

The pH-assisted ligand exchange was monitored by UV/Vis recordings of the colloid at various process steps. Fig. S1a visualizes the final spectrum of biotinylated and carboxylated AgNPs in comparison to commercial citrate-capped particles. The successful modification was verified by a red-shift of the resonance frequency for biotinylated particles (from 413 nm to 415 nm) and a narrowing of the spectrum for carboxylated particles. The exchange of the ligand is further confirmed by changes of the hydrodynamic particle diameter and the ζ-potential of the different suspensions, see Fig. S1 b and c.
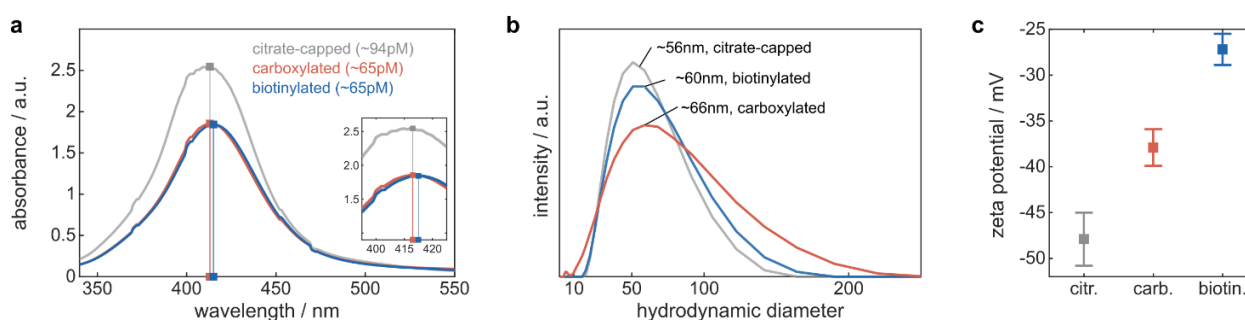
Figure S1 Nanoparticle characterization. (a) UV/Vis spectra of biotinylated and carboxylated AgNPs after pH-assisted ligand exchange of commercial citrate-capped 40 nm-AgNPs. (b) Hydrodynamic diameters and (c) ζ-potentials within 3.5 mM KCl, 5 mM KOH solution of the final suspensions.

After functionalization, the colloid stability of the AgNPs was probed via successive UV/Vis recordings after suspending 100 μl of ~65 pM biotin-AgNPs in 900 μl electrolyte solution, see Fig. S2a and b. The colloid was found to be stable under the conditions used for detection (in 35 mM KCl, 50 mM KOH) and coupling during SPR experiments (10 mM MES at pH 4). After minor initial changes, the spectrum showed no further significant deviations within the evaluation time of 15 min / 5 min. ζ-potentials of -34.7±0.9 mV for biotinylated particles in 35 mM KCl, 50 mM KOH and -20.4±2.6 mV in 10 mM MES (pH 4) further indicate a stable colloid for both conditions used.
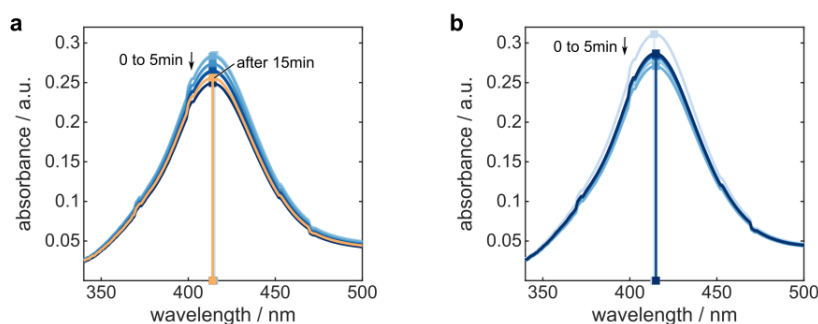
Figure S2 Colloid stability of biotinylated AgNPs in (b) detection solution containing 35 mM KCl and 50 mM KOH, and (c) in 10 mM MES (pH 4) coupling solution.

II. Statistical Data of Single-Impact Experiment at Different Oxidation Potentials
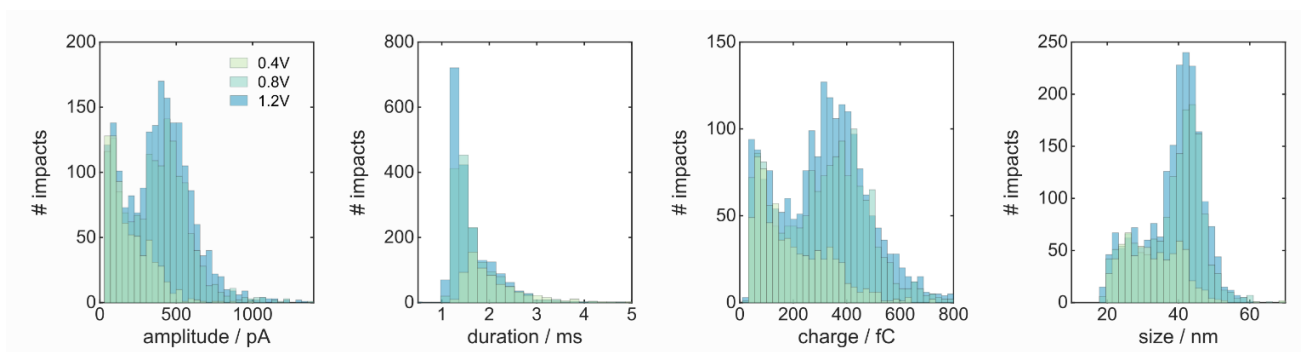
Figure S3 Amplitude, duration, charge, and size distributions for the redox activity experiment based on recordings of 10 channels.

III. Current Noise in Lateral Flow Sensor Experiments

Fig. S4 depicts the current traces of three individual electrodes forced to 1.2 V vs. Pt-RE for a lateral flow experiment in the absence of nanoparticles and streptavidin beads. The temporal evolution at all three electrodes follows a common trend, where the bias current within the first 50 s after the release of 30 μl 35 mM KCl, 50 mM KOH solution is significantly higher than at later measurement times. This finding is in line with observations of the evolving flow through the Fusion 5 membrane, where the initial fast wicking occurs within the first 50 s. As the microchannel has a limited size due to the geometrical constraints of the chip, the wicking of the membrane structure is not only governed by capillary flow within the membrane, but also greatly influenced by the droplet at the source (that generates a pressure gradient) and by interfering flow along the gap between the membrane and tape and/or the chip surface.

Since colliding particles are registered by current peaks that exceed a pre-set threshold, the recordings in Fig. S4 are evaluated to determine the current noise floor, see Tab. S1. Based on the data in Table S1, a fixed current threshold of 50 pA was set for all lateral flow experiments in order to avoid misclassification.
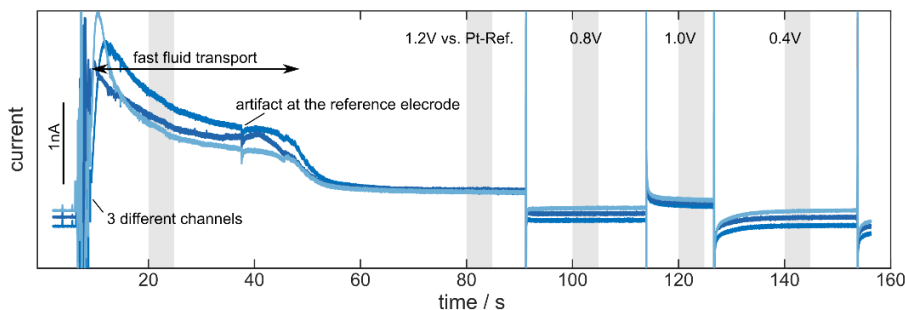
Figure S4 Flushing of the membrane with 30 μl of 35 mM KCl, 50 mM KOH solution in the absence of nanoparticles and latex beads. The potential at the detection electrodes was initially held at 1.2 V vs Pt-RE and later altered. The current noise is evaluated at the indicated (gray) times and provided in Table S1.

Table S1 RMS and peak-to-peak current noise after detrending for different oxidation potentials measured versus Pt-RE.

oxidation potential	RMS current	peak-to-peak current
1.2 V (20 s – 25 s)	10.2 ± 0.9 pA	89.7 ± 3.6 pA
1.2 V (80 s – 85 s)	7.1 ± 0.8 pA	57.0 ± 9.9 pA
1.0 V	6.4 ± 0.5 pA	51.8 ± 3.8 pA
0.8 V	5.9 ± 0.6 pA	50.5 ± 4.5 pA
0.4 V	5.7 ± 0.9 pA	46.6 ± 7.4 pA

IV. Statistical Data of Lateral Flow Experiments

a, *control*, botin. AgNPs, carboxyl. beads
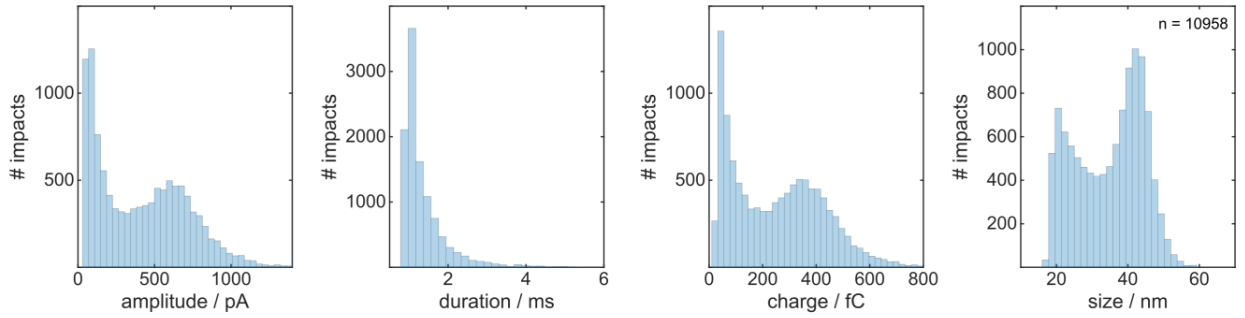
b, *control*, carboxyl. AgNPs, streptavidin beads
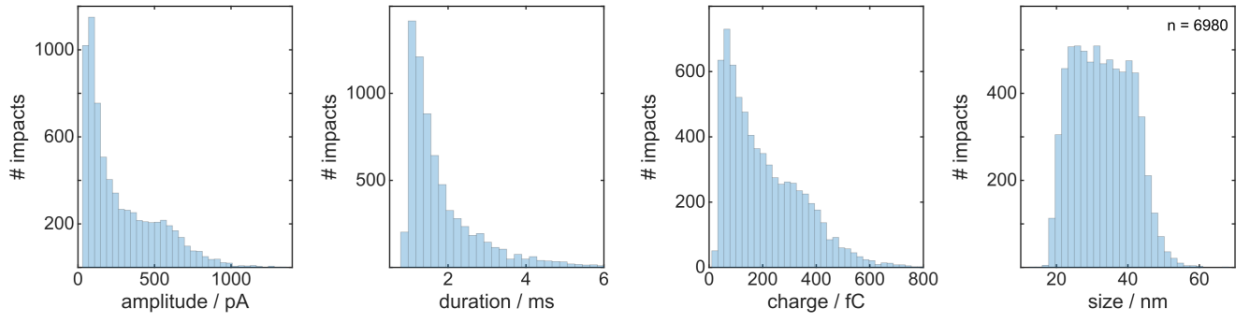
c, biotin. AgNPs, streptavidin beads
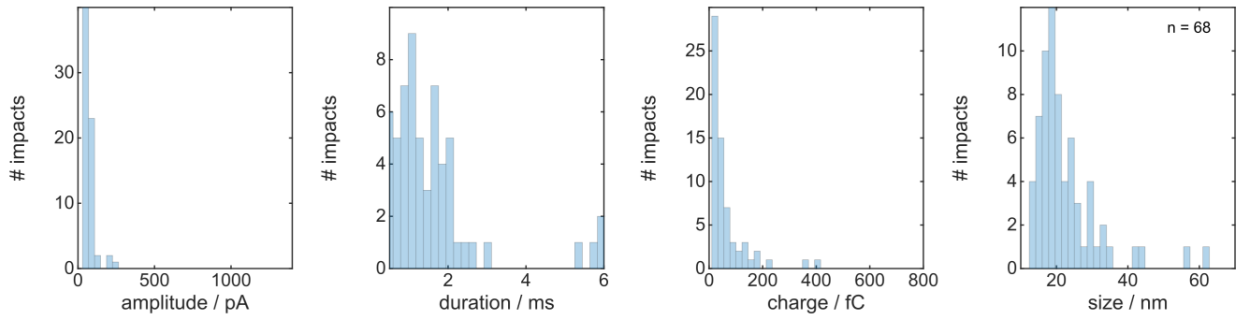
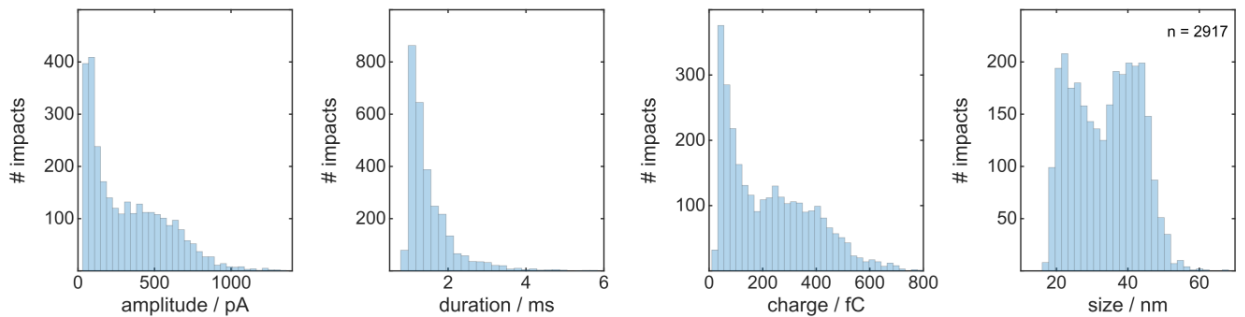**d**, free biotin, biotin. AgNPs, streptavidin beads

Figure S5 Statistical data for the single-impact experiments shown in Fig. 5 in the manuscript. Amplitude, duration, charge, and size distributions for all considered impacts. The data is based on 10 channels and 185 s of recording. (a) Impacts of biotinylated AgNPs previously flushed over carboxylated latex beads. (b) Impact of carboxylated AgNPs previously flushed over streptavidin-coated latex beads. (c) Impacts of biotinylated AgNPs previously flushed over streptavidin-coated latex beads. (d) Impacts of biotinylated AgNPs previously flushed over streptavidin-coated latex beads if additional free biotin is present.

V. Colorimetric Experiments Using biotin-tagged HRP and TMB Substrate
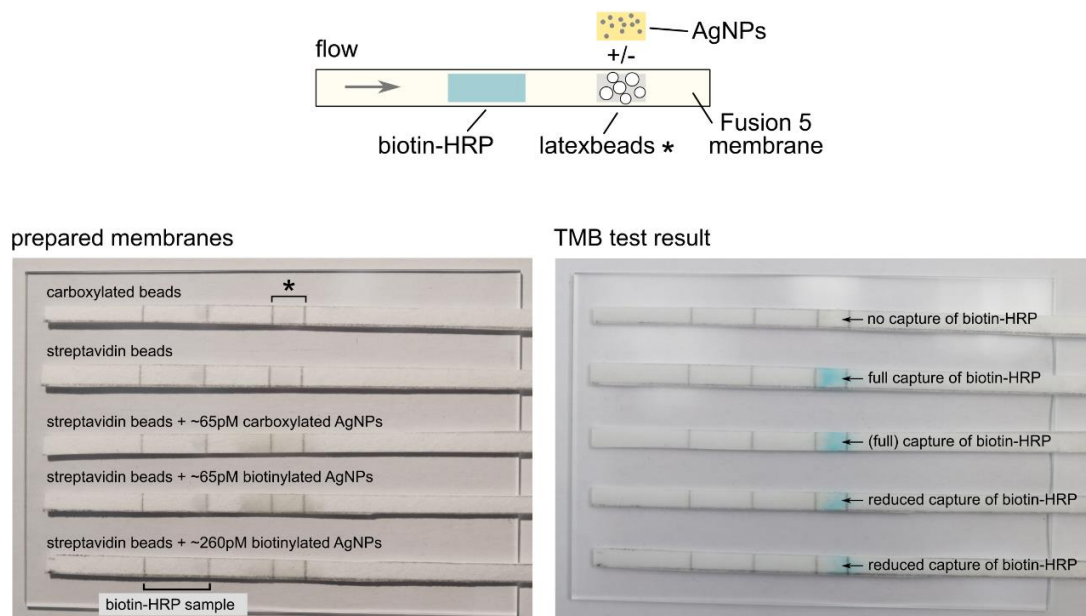
Figure S6 Colorimetric experiment using biotin-tagged HRP to evaluate the occupation of streptavidin binding sites by modified AgNPs, which were pipetted onto the capture area prior to the flushing of 2 µl of 100 nM biotin-HRP. Afterwards, the capture of biotin-HRP was visualized by releasing 5 µl of TMB substrate solution, which leads to a blue color development. The reduced intensity in case of biotinylated AgNPs indicates binding of nanoparticles to streptavidin.

VI. Impacts for Different Streptavidin-Latex Bead Volumes
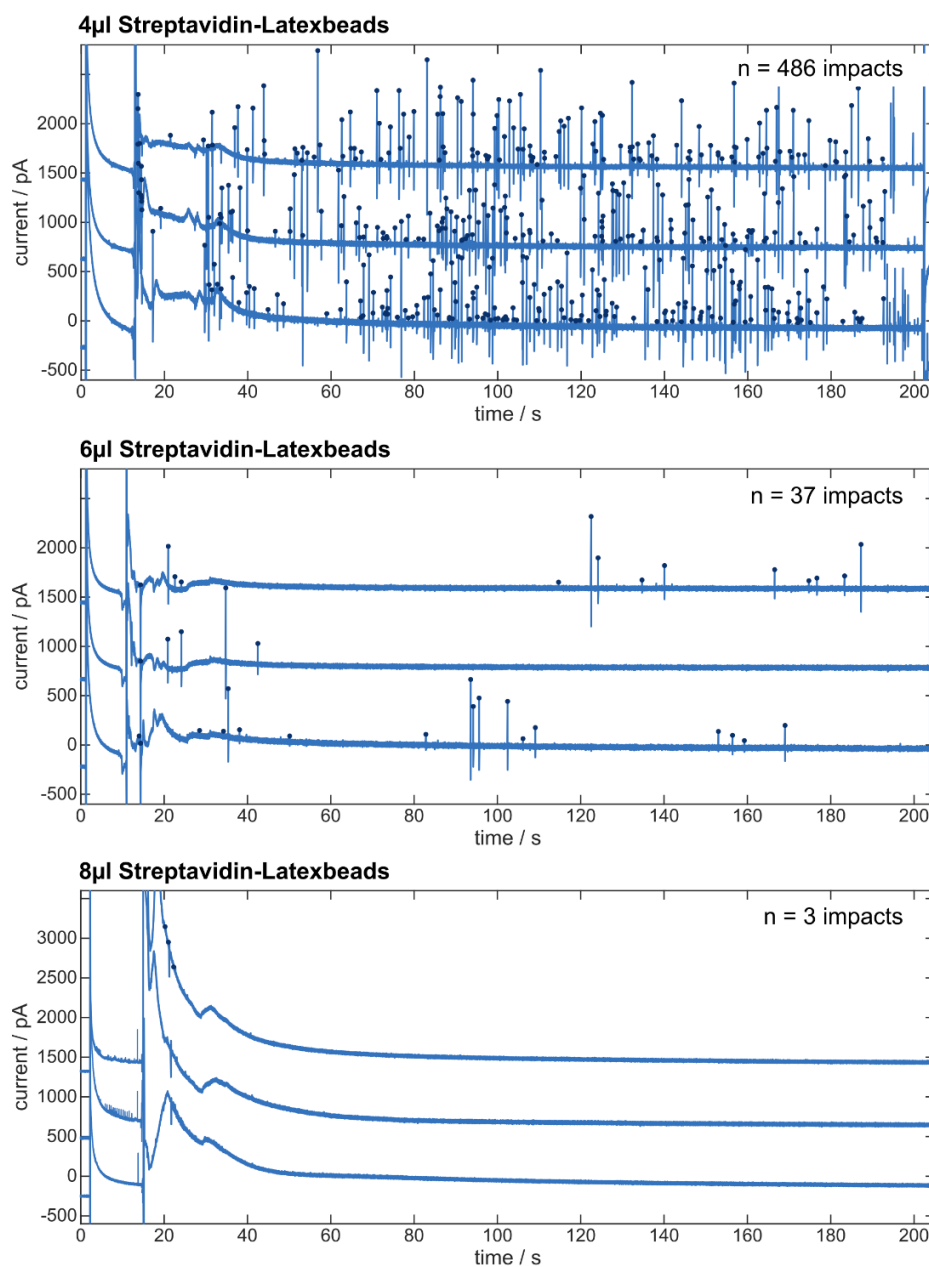
Figure S7 Impact experiments using 30 µl of 35 mM KCl, 50 mM KOH solution that contains 30 pM of biotinylated AgNPs. Free biotin is not present. Prior to the detection, different volumes of 4 % w/v streptavidin-coated latex beads were dried onto the capture area. The electrodes were biased to 1.2 V vs Pt-RE and the currents are displayed with an offset of 800 pA for clarity. Depending on the amount of released streptavidin, the number of impacts that can be expected during fast transport is modulated. A careful selection of latex bead and particle amounts could optimize the sensor responses and tailor the detection for specific measurement times. Moreover, the streptavidin concentration and the size of the latex beads can be manipulated to yield different capture efficiencies during the flushing of the membrane.

VII. Additional Data for Different Biotin Concentrations
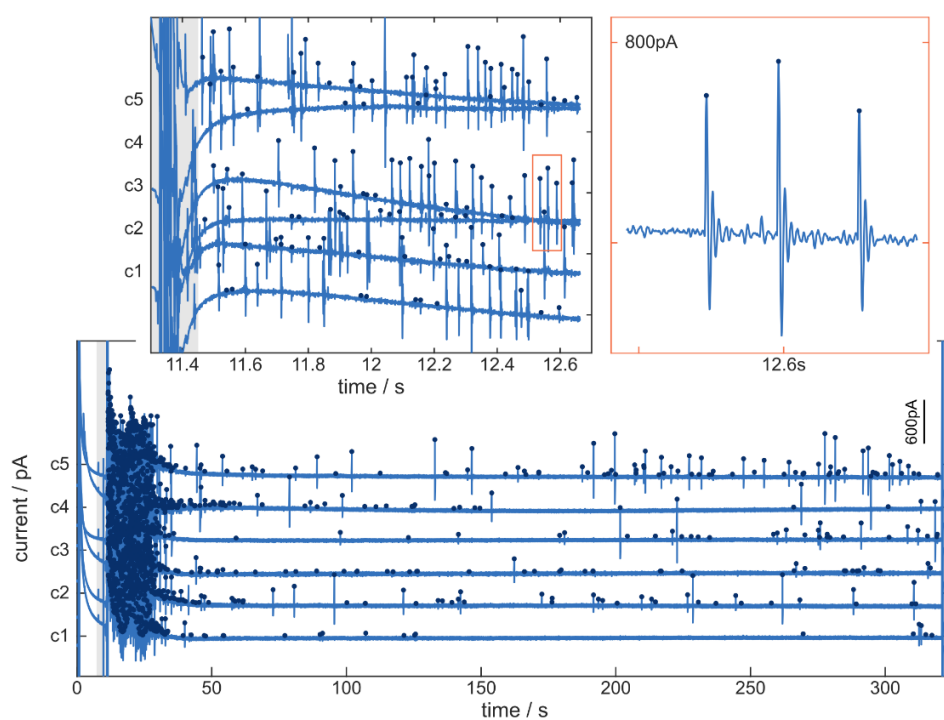
Figure S8 Lateral flow experiment for 100 nM biotin. After an initial flush of particles over the capture area, the detection rate drastically decreases most likely due to a depletion and/or aggregation effects. The lateral flow membrane contained 8 µl of ~4 % w/v streptavidin-functionalized latex beads with 3 µm diameter. Prior to 30 µl of detection solution containing 30 pM biotinylated AgNPs in 35 mM KCl, 50 mM KOH, 2 µl of 100 nM biotin were released on the source pad. The electrodes were biased to 1.2 V vs Pt-RE for the entire experiment. Note the amplifier-related ringing artifacts (zoom in the orange box) after initial charge injection upon AgNP collision.

VIII. Impact Recordings after Chip-Storage in a Vacuum Chamber

The stability of the electrode array activation was tested by storing a chip in vacuum. The chips were rinsed with deionized water and isopropanol after activation and before storage in a vacuum chamber for 80 hours (pressure below -0.08 MPa, temperature ~23°C). To see if the electrode activation is preserved under these storage conditions, we recorded impacts (~14 pM biotinylated AgNPs) in 35 mM KCl, 50 mM KOH solution afterwards, see Fig. S9. The open circuit potential of the electrodes was ~53mV. We were able to detect particle impacts after storage, see Fig. S9a. However, the inspection of the peaks (see Fig. S9b to d) reveals that most collisions lead only to partial oxidations, which may indicate a deterioration of the electrode surface.
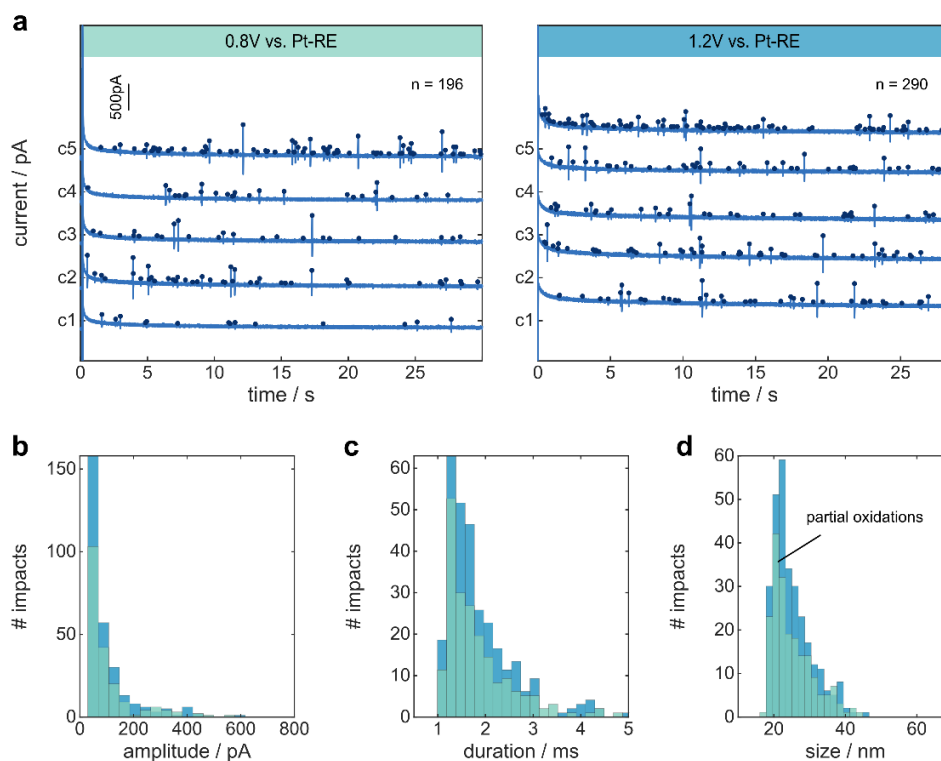
Figure S9 Impact experiment after storage in vacuum. (a) Current traces for ~14 pM biotinylated AgNPs (40nm diameter) in 35 mM KCl, 50 mM KOH and oxidation potentials of 0.8V and 1.2V, respectively. The chip was activated and then stored in a vacuum chamber for 80 h prior to the experiment. All considered impacts are visualized as blue dots. The channels are displayed with an offset of 1 nA for clarity. (b) Amplitude distribution from all considered impacts in (a). (c) Duration distribution. (d) Associated particle size distribution.

B. Further Published First-Author Contributions

B.1 Inkjet-printed 3D Micro-Ring-Electrode Arrays for Amperometric Nanoparticle Detection

H. Peng*, L. Grob*, **L.J.K. Weiß***, L. Hiendlmeier, E. Music, I. Kopic, T. Teshima,
P. Rinklin, B. Wolfrum

Abstract

Chip-based impact electrochemistry can provide means to measure nanoparticles in solution by sensing their stochastic collisions on appropriately-polarized microelectrodes. However, a planar microelectrode array design still restricts the particle detection to the chip surface and does not allow detection in 3D environments. In this work, we report a fast fabrication process for 3D microelectrode arrays by combining ink-jet printing with laser-patterning. To this end, we printed 3D pillars from polyacrylate ink as a scaffold. Then, the metal structures are manufactured via sputtering and laser-ablation. Finally, the chip is passivated with a parylene-C layer and the electrode tips are created via laser-ablation in a vertical alignment. As a proof of principle, we employ our 3D micro-ring-electrode arrays for single impact recordings from silver nanoparticles.

Individual Contribution

supporting role in the design of the study, data collection, data processing and analysis, data interpretation, supporting role in composition and writing of the manuscript

Check for updates

Inkjet-printed 3D micro-ring-electrode arrays for amperometric nanoparticle detection†

Hu Peng, [‡a] Leroy Grob,[‡a] Lennart Jakob Konstantin Weiß, [‡a]
Lukas Hiendlmeier,[a] Emir Music,[a] Inola Kopic,[a] Tetsuhiko F. Teshima, [a,b]
Philipp Rinklin[a] and Bernhard Wolfrum*[a]

Chip-based impact electrochemistry can provide means to measure nanoparticles in solution by sensing their stochastic collisions on appropriately-polarized microelectrodes. However, a planar microelectrode array design still restricts the particle detection to the chip surface and does not allow detection in 3D environments. In this work, we report a fast fabrication process for 3D microelectrode arrays by combining ink-jet printing with laser-patterning. To this end, we printed 3D pillars from polyacrylate ink as a scaffold. Then, the metal structures are manufactured *via* sputtering and laser-ablation. Finally, the chip is passivated with a parylene-C layer and the electrode tips are created *via* laser-ablation in a vertical alignment. As a proof of principle, we employ our 3D micro-ring-electrode arrays for single impact recordings from silver nanoparticles.

1. Introduction

Silver nanoparticles (AgNPs) play a significant role in consumer and industrial products.[1,2] Particularly, due to their antimicrobial property and relatively low cost,[3] they have been extensively used, *e.g.* in food containers,[4] cosmetics,[5] textiles,[6] laundry detergents,[7] biocide sprays,[8] paints,[9] and medical devices.[10] As a result, AgNPs are released into aquatic ecosystems either directly or *via* formation of secondary incidental nanoparticles.[11] Once AgNPs are present in the environment, their fate becomes unclear.[12] Typically, AgNPs release Ag^+ ions, which are known to interfere with living organisms and may lead to toxic effects.[13] Therefore, techniques for monitoring the presence of AgNPs in aquatic systems are urgently required to assess long-term effects on the environment. However, a fast and reliable on-site detection method for AgNPs is still missing.

Standard approaches for quantifying and characterizing nanoparticles typically rely on optical techniques or electron microscopy. Transmission electron microscopy (TEM) and scanning electron microscopy (SEM) are reliable techniques to analyze nanoparticle size. Yet they are both *ex situ* methods and are thus not suitable for screening large sample numbers in an efficient manner.[14] Optical methods, such as dynamic light scattering (DLS), are mainly applicable for rather monodisperse and clear suspensions.[15] Furthermore, tracing nanoparticles smaller than 25 nm can be challenging using this approach.[16]

As an alternative, single-impact electrochemistry can provide means to measure nanoparticles reliably at high-throughput *in situ*.[17] In this approach, nanoparticles are detected in solution by sensing their stochastic collisions on appropriately-polarized microelectrodes.[18] For redox active particles, such as AgNPs, characteristic current spikes can be generated during collision with the electrode due to the oxidation of the particles.[19] Typically, such experiments are performed using low-noise amperometric recordings with a single probe microelectrode.[20] However, a single electrode recording inherently limits the number of collision events that can be monitored within a given experimental time frame. To scale up the number of detected collision events, on-chip detection methods have been implemented using individually addressable microelectrode arrays.[17] This way, the impact rate of nanoparticles is increased without compromising noise levels in amperometric recordings due to an increased electrode–electrolyte interface. Nonetheless, standard planar microelectrode arrays only record collision events in the proximity of the chip surface. Thus, such measurements were shown to be highly affected by particle adsorption at the insulating surface near the detection electrodes.[21,22] This can lead to a dramatic decrease in the nanoparticle impact rate, as adsorbed AgNPs are ultimately lost for detection. Here, special surface coatings

a Neuroelectronics, Munich Institute of Biomedical Engineering, Department of Electrical Engineering, TUM School of Computation, Information and Technology, Technical University of Munich, Hans-Piloty-Str. 1, Garching, 85748, Germany. E-mail: bernhard.wolfrum@tum.de
b Medical & Health Informatics Laboratories NTT Research Incorporated 940 Stewart Dr, Sunnyvale, CA 94085, USA
†Electronic supplementary information (ESI) available. See DOI: https://doi.org/10.1039/d2nr05640b
‡These authors contributed equally

or externally-controlled electrostatic repulsion were proposed to mitigate this effect with partial success.[23] Nevertheless, a planar electrode array design still restricts the particle detection to the chip surface and, in contrast to single-probe devices, does not allow detection in 3D environments, *e.g.* the center of a microfluidic channel. The present work addresses this challenge and introduces arrays of 3D electrodes as detection sites that directly access the bulk solution reducing the influence of large-scale interfacial effects on AgNP detection.[24] Since 3D 'tip' electrodes are accessible from almost all directions, they are expected to provide more efficient mass transport in 3D environments compared to their planar counterparts.

Typically, MEAs are fabricated *via* cleanroom fabrication, which allows the production of well-defined microelectrodes for low-noise recordings.[25,26] However, implementing 3D features using these conventional fabrication approaches can be costly and time-consuming due to more complex etching and/or deposition workflows. As an alternative, additive manufacturing techniques have emerged as a promising candidate for rapid prototyping of 3D electrode array devices.[27–29] In particular, inkjet printing increasingly gains attention due to the advantage of directly printing materials in a maskless process.[30] While inkjet printing has mainly been used for prototype fabrication, approaches for upscaling the throughput for inkjet printing have been suggested.[31] In a previous study, we have demonstrated the application of inkjet-printed 3D electrode arrays for extracellular recordings of action potentials from HL-1 cells.[32] To this end, we used conductive and dielectric inks as feedlines and insulation, respectively, with the entirety of the 3D electrodes protruding from the passivation. However, such an approach is detrimental for low-noise amperometric recordings since the current noise scales with the exposed electrode area. In particular, nanoimpact recordings are affected by this as they usually involve the detection of current spikes in the pA to nA regime. Thus, current spikes associated with individual AgNP collisions become indistinguishable from the background noise for such fully exposed 3D microelectrodes.

In this report, we present an alternative process for the fast fabrication of electrode arrays with insulating 3D structures by combining ink-jet printing with laser-patterning technology. To this end, we first print 3D pillar scaffolds using a polyacrylate (PA) ink before we deposit and structure platinum electrodes and parylene insulation. Ultimately, we create a ring electrode at the tip of each pillar *via* vertical cutting using laser-ablation. The exposed area of this ring electrode is comparable to that of a planar electrode with 7 μm in diameter. As a proof of principle, we record with our 3D electrode arrays stochastic impacts of 20 nm-sized AgNPs.

2. Experiments

2.1 Chemicals

Citrate stabilized AgNPs with a diameter of 20 nm (stock concentration 756 pM), potassium chloride (KCl), modified phos-

phate buffered saline (PBS), as well as, potassium ferricyanide were purchased from Sigma-Aldrich (St. Louis, Mo). Unless otherwise stated, dilutions from the AgNP dispersion were prepared using ultra-pure water (conductivity 5.5 μS m⁻¹) taken from a Berry Pure purification system (Berrytec, Harthausen, Germany) to reach final concentrations of 10, 50, 100, and 500 pM in KCl solution.

2.2 Fabrication of 3D micro-ring-electrode arrays

24.1×24.1 mm^2 glass slides were cleaned *via* ultrasonication for 10 min (Bransonic ultra-sonic cleaner 5510E-MTH, Branson ultrasonic, Danbury, CT, USA) in acetone, isopropanol, and deionized water. The procedure was repeated twice and afterwards the samples were blow-dried by pressurized air. PA pillar arrays were inkjet-printed on the clean glass slides with an inkjet printer (CeraPrinter F-series, Ceradrop, Limoges, France). To decrease printing time, droplets were deposited subsequently at the individual pillar locations in a row-by-row printing method. Prior to printing, ultraviolet (UV)-curable polyacrylate ink (PA-1210-004, JNC corporation, Japan) was equilibrated to room temperature, 4 μL of the ink was filtered with a 0.22 μm polyethersulfone (PES) filter, and filled into a 10 pL cartridge (DMC-11610, Fujifilm Dimatix, Santa Clara, CA, USA). A unipolar voltage pulse of 40 V with a rise, dwell, and falling time of 3, 12, and 1 μs, respectively, was applied to the nozzle plate to eject individual ink droplets. The nozzle temperature was set to 50 °C, and the substrate temperature was held at 55 °C. After each layer the samples were cured with an inbuilt UV lamp at maximum power. A metal layer (10 nm titanium, 150 nm platinum) was then sputtered (BAL-TEC MED 020, BAL-TEC AG, Balzers, Liechtenstein) onto the chip to make all structures conductive. A laser-patterning system (MD-U1000C, Keyence, Osaka, Japan) was used to generate microelectrode arrays by selectively ablating the metal film in between individual electrode structures. Subsequently, parylene (PPS Parylene 3000, Plasma Parylene System GmbH, Rosenheim, Germany) was deposited to passivate the entire chip while masking the contact area with Kapton tape. Finally, the ring electrodes were exposed *via* laser-ablation of the pillar tip (800 mm s⁻¹ scan speed, 350 Hz pulse frequency, 100 repetitions).

2.3 Structural characterization of 3D micro-ring-electrode arrays

The printed pillars were imaged with a 3D laser scanning confocal microscope (Vk-X250, Keyence, Osaka, Japan) to acquire the dimensions of the pillars and assess the growth rate depending on the applied droplet number. All measurements were run at a z-pitch of 80 nm on a vibration-dampened table (Vision IsoStation, Newport, USA) to eliminate mechanical interference.

Scanning electron microscopy (JSM-6060 LV, JOEL, Japan) was used to image the micropillar electrodes. To this end, the MEAs were fixed onto a specimen holder and taped with conductive carbon cement and paste (LEit-C-Plast, Neubauer Chemikalien, Germany, and N 650 Planocarbon, Plano GmbH,

Germany, respectively). In order to prevent charging artifacts, a thin layer of gold (~5 nm) was sputtered onto the sample using a high vacuum coating system (BAL-TEC MED 020, BAL-TEC AG, Balzers, Liechtenstein) before loading the sample into the chamber.

2.4   Electrochemical characterization

Cyclic voltammetry (CV; −0.6 to 0.4 V *vs.* Ag/AgCl at a scan speed of 10 mV s^{-1}) and electrochemical impedance spectroscopy (EIS; 200 mV offset *vs.* open circuit potential, 10 mV amplitude, 1 Hz to 100 kHz scan range) were carried out with a VSP-300 potentiostat (Biologic Science Instruments, Seyssinet-Pariset, France). We used a three-electrode configuration with an Ag/AgCl reference electrode (Dri-Ref, Flexref from World Precision Instruments) and a coiled platinum wire as counter electrode. The characterization experiments were conducted in different concentration of potassium ferricyanide in PBS. Prior to the detection of AgNPs, the 3D MEA was activated in 200 mM H$_2$SO$_4$ using cyclic voltammetry (scan rate 500 mV s^{-1}, −0.2 to 1.5 V *vs.* Ag/AgCl, 20 cycles), see ESI Fig. 1.†

2.5   Nanoparticle detection

The detection was performed with a 64-channel amplifier system (10 kHz sampling rate per channel, 3.4 kHz bandwidth) in a two-electrode setup using a Ag/AgCl reference electrode. Before applying the oxidation potential, the AgNP dispersion was mixed with a KCl solution (25 mM final concentration) and left for 30 s. Afterwards, the ring electrodes were stepped to an oxidation potential of 800 mV *vs.* Ag/AgCl and current traces were recorded for 200 s. The raw data was processed using MATLAB as described previously.[33] First, all current traces were evaluated regarding their noise characteristics and non-working and noisy channels have been excluded. Then, the current

spikes were extracted by a thresholding method and all peaks exceeding 30 pA are considered as AgNP impacts for further analysis. The data shown is based on a subset of channels, yielding the highest number of impacts. In between the experiments, the chip was cleaned and activated in H$_2$SO$_4$ again.

3.   Results and discussion

Our approach combines inkjet-printing and laser-patterning technology to generate 3D ring electrode arrays for low-noise amperometric recordings. A schematic of the fabrication procedure of 3D MEAs is shown in Fig. 1. In a first step, 64 (8 × 8) PA pillars were directly inkjet-printed onto the glass slides (Subpanel 1 of Fig. 1a). An adhesion layer of titanium followed by the main conductive layer of platinum was subsequently deposited onto the sample using a sputtering process to coat the entire surface of the sample including the printed 3D pillar structures with metal. As a next step, laser-patterning was used to define the feedlines and electrodes (Subpanel 2 of Fig. 1a). A chemically inert conformal layer of parylene-C was deposited *via* chemical vapor deposition to passivate the sample (Subpanel 3 of Fig. 1a). To expose a defined ring electrode only at the tip of the pillar we used a laser-ablation process. Typically, dry etching techniques such as reactive ion etching, would be commonly used to remove parylene-C in the desired electrode areas. Yet, these techniques usually require the application of a mask for selectivity. Once the 3D structure is fabricated, however, it becomes challenging to pattern a mask such that an electrode opening is generated only at the tip of the pillar structure. To solve this problem, our approach uses a vertical chip arrangement that allows positioning and exposing
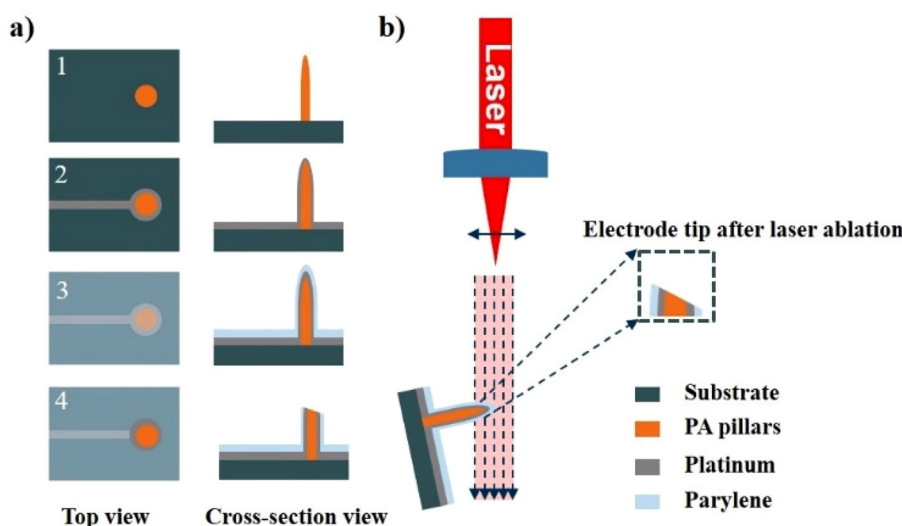

Fig. 1 Schematic of the fabrication process for the 3D electrode arrays including laser ablation. (a) Schematic of the fabrication process for the 3D electrode arrays. In a first step, PA pillars are printed on a glass substrate (1). Subsequently, a platinum layer is vapor deposited and laser patterned to generate individual electrodes and feedlines (2). The structures are insulated using parylene deposition (3) and the tip is exposed *via* laser ablation at an angle (4). (b) Schematic for the laser ablation process of the tip.
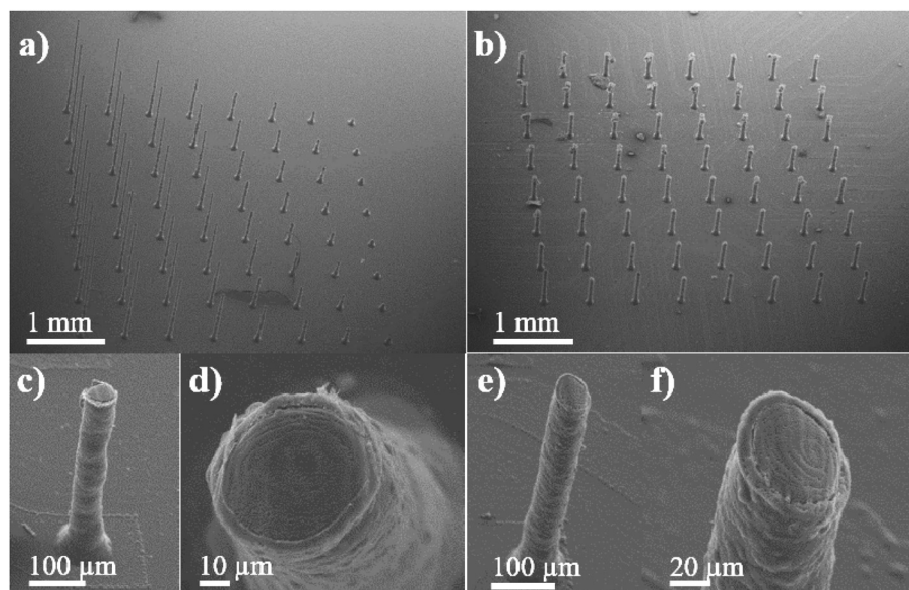
Fig. 2 SEM images of inkjet-printed PA pillars. (a) PA pillars printed using different amounts of ink droplets per pillar. From the right to the left column, the pillars were printed from 100 (lowest) to 800 (highest) droplets, in increments of 100 droplets per pillar. (b) PA pillars printed using 400 droplets after laser-ablation of the tip. (c)–(f) Show close-up images of an individual tip after applying perpendicular (c and d) and angled (e and f) laser-ablation.

the tip of the pillar perpendicular or at inclined angles to the beam path of a laser-ablation system (Fig. 1b).

Fig. 2 shows SEM images of printed 3D microelectrode structures that were produced with varying droplet numbers ranging from 100 droplets to 800 droplets. As expected the height of the pillars is directly affected by the applied droplet number (Fig. 2a) and we were able to reliably produce electrodes with aspect ratios of up to 20 (*i.e.* heights in the range of 1 mm, diameter ~50 μm). Fig. 2b shows an array of insulated 3D electrodes after laser-ablation of the tip surface. All 3D electrodes were cut at the same height and we can see that the pillars remain structurally intact. Fig. 2c and d show close-up images of individual 3D electrodes and their tips. The ablated tips exhibited a rather smooth surface and we did not observe major redeposition artifacts. In our study we focused on blunt tips that were cut under an angle of 90°, which is sufficient for performing experiments in liquid environment. However, sharp tips generated by ablating the tip at different angles can also be reliably processed (see Fig. 2e and f). This is of particular interest in applications if the electrodes are required to penetrate into soft matter samples such as organoids or tissue slices.[34,35]

To characterize the fabrication process of the 3D electrodes we printed arrays with electrodes of different height by changing the applied droplet number using a single nozzle (see Fig. 3a). Interestingly, the height of the pillars was not directly proportional to the droplet number but exhibits a minor non-linearity. For pillars between 100 and 300 droplets the growth rate was approximately constant at 1.47 ± 0.04 μm per droplet. However, for higher droplet numbers, the growth rate was significantly larger (*e.g.* 2.95 ± 0.21 μm per droplet between 600

and 800 droplets). Potentially, the change in growth rate could be caused by a difference in temperature. As the sample is heated *via* the substrate holder (55 °C) to facilitate stable printing conditions, we obtain a temperature gradient from the pillar tip to the substrate surface. The resulting lower temperature at the pillar tip and corresponding decrease in ink viscosity as well as increase in surface tension could result in reduced spreading of the impacting droplets, which would explain an increasing growth rate (Fig. 3b). In accordance, we see a slight decrease in the pillar width with increasing droplet number (Fig. 3c). Using our process parameters, the 3D electrode's full width at half maximum was in the range of 50 μm including the parylene passivation layer. After laser-ablation a metal ring coating the PA core of the 3D structure is exposed. Assuming a smooth ablation process, the geometrical area A of the resulting ring electrode can be calculated:

$$A = \pi(2rt + t^2)$$

where r is the radius of the PA core (~38 μm) and t is the thickness of the metal layer (~160 nm). The area we obtain in this way is $A \approx 38$ μm^2, which is comparable to a planar disk electrode, 7 μm in diameter. Concerning the exposed area, our 3D ring electrodes are thus comparable to planar electrodes from previous studies that have been used for nanoparticle impact experiments. After exposing the pillars' tip *via* laser-ablation, we performed CV and EIS measurements to characterize the electrochemical interface. The CV, seen in Fig. 4a, was recorded in PBS with different potassium ferricyanide concentrations over a potential window ranging from - 0.6 to 0.4 V *vs.* Ag/AgCl at a scan speed of 10 mV s^{-1}. We can estimate the
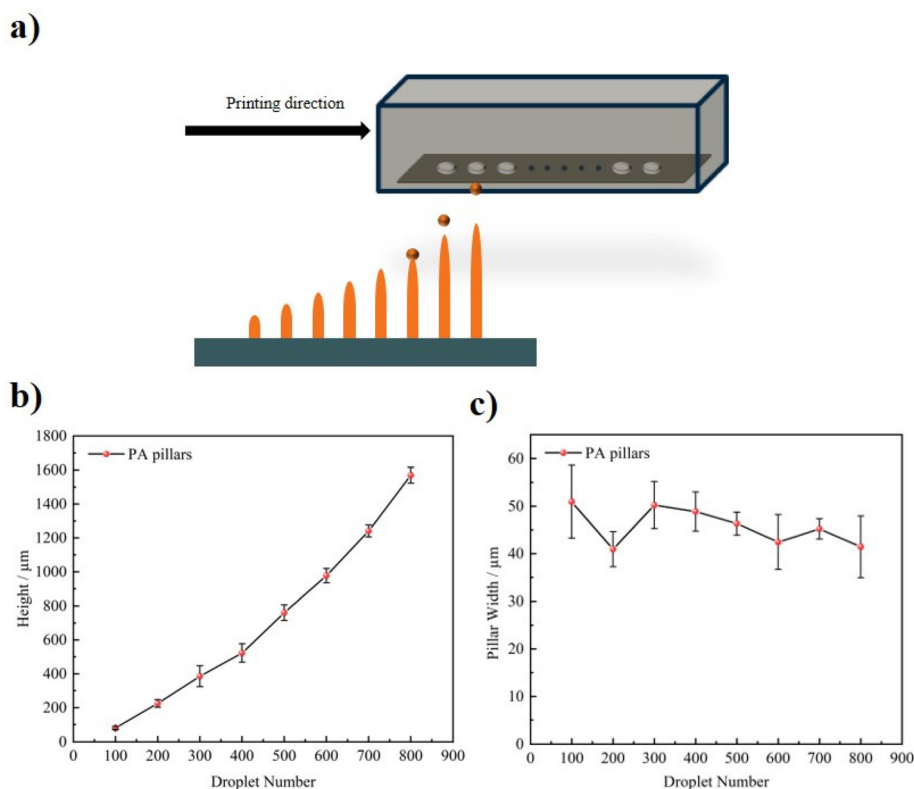
Fig. 3 Characterization of the fabrication process of pillars. (a) Inkjet-printing PA pillars in different height on a blank glass substrate. (b and c) Pillar analysis for a fixed working distance of ≈1.5 mm. (b) Absolute height of the micropillars, and (c) pillar width at half height. Error bars indicate the standard deviation ($n = 4$).

expected steady-state diffusion-limited current to a ring electrode using the equation.[36]

$$I_{\mathrm{l}} = nFDC \frac{2\pi^2 r}{\ln\left(\dfrac{32r}{t}\right)}, \, t << r$$

Where I_{l} is the diffusion limited current, n is the number of electrons, F is the Faraday constant (9.65×10^4 C mol^{-1}), D is

the diffusion coefficient of ferricyanide (7.32×10^{-10} m^2 s^{-1}), C is the concentration, t is the width of the ring, and r is the ring radius. Although, in our geometry, we expect additional flux contributions from below the pillar tip, the estimated diffusion-limited current for a 10 mM solution (~63 nA) is in a similar range as our observed values (see Fig. 4a). The measured current might also be affected by additional convection or migration effects. EIS was carried out to further characterize the
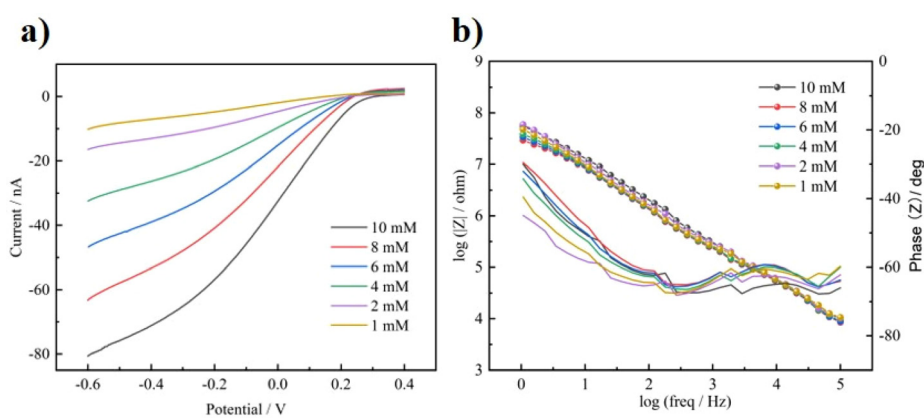
Fig. 4 Electrochemical characterization of a 3D microring-electrode within different concentrations of potassium ferricyanide in PBS. (a) exemplary CV curves in potassium ferricyanide solution within different concentrations from 1 mM to 10 mM (potential from −0.6 V to 0.4 V *vs*. Ag/AgCl, 10 mV s^{-1}, graph shows 3rd scan). (b) EIS of the corresponding exemplary electrode. The EIS was conducted at a frequency ranging from 1 Hz to 100 kHz with a 10 mV amplitude.

electrode–electrolyte interface of the 3D MEAs (Fig. 4b). The impedance can be fitted using a modified Randel's circuit with a constant phase element (exponent $n \sim 0.72$) indicating a deviation from purely capacitive behavior. Specifically, at 1 kHz the impedance magnitude is around 0.35 MΩ.

To test the suitability of the fabricated 3D MEAs for nanoparticle detection, we recorded stochastic impacts of AgNPs. Fig. 5a shows three exemplary current traces that were recorded for a suspension of 10 pM AgNPs in 25 mM KCl. Here, the presence of current spikes reveals the successful detection of AgNPs. To assess the performance of the fabricated electrodes, we further analyzed the current spikes and estimated the particle size based on the delivered charge per impact. All impacts exceeding a threshold of 30 pA (indicated as blue dots in Fig. 5a) are considered as AgNP collisions in the further evaluation. Integrating each of the current spikes yields a charge distribution, which can be transferred to a size distribution assuming a spherical geometry and using:

$$d_{\mathrm{p}} = 2 \cdot \sqrt[3]{\frac{3\,M_{\mathrm{Ag}}Q}{4\pi z F p_{\mathrm{Ag}}}}$$

where d_{p} is the particle diameter, M_{Ag} is the molar mass of Ag, Q is the charge, z the valency of Ag, F is the Faraday constant and p_{Ag} the mass density of Ag. The corresponding size distribution to Fig. 5a is given in Fig. 5b, leading to an estimated particle size of 16.8 nm ± 3.9 nm ($n = 539$). This value is

slightly lower than the expected size of 20 nm. A possible reason for this might be that particles do not completely oxidize upon collision with the electrodes although such a behavior would rather be expected for particles larger than 40 nm.[37] Incomplete oxidation can result from insufficient anion fluxes,[38] high adsorption energies at the electrode surface,[39] a contaminated electroactive area[40] or a reduced reaction yield due to additional particle motion.[41] However, we obtain larger particle sizes in case of higher particle concentrations after exposing the chip to successive measurements and cleaning cycles, e.g. 20.4 nm ± 2.3 nm for 100 pM AgNP ($n = 5050$). Possibly, the initially underestimated particle size is caused by contaminated electrodes due to the laser-ablation process.

Additional experiments and H_2SO_4-activation/cleaning cycles could lead to a removal of the metal–oxide/debris isles caused by the laser-ablation. Nevertheless, colloid instability could also lead to increased sizes for higher particle concentrations, as the likelihood of (irreversible) particle collisions within the bulk increases. However, colloid stability for 25 mM KCl supporting is typically preserved on the time scale of our experiments.[40]

We observe a rather large variance between different electrodes, which we mainly assign to differences in the fabrication process. Similar deviations across the electrode ensemble are also reported for other MEA chips,[41,42] as slight fabrication differences and the resulting flow fields affect the impact rates. Moreover, the cleaning/activation process is not compar-
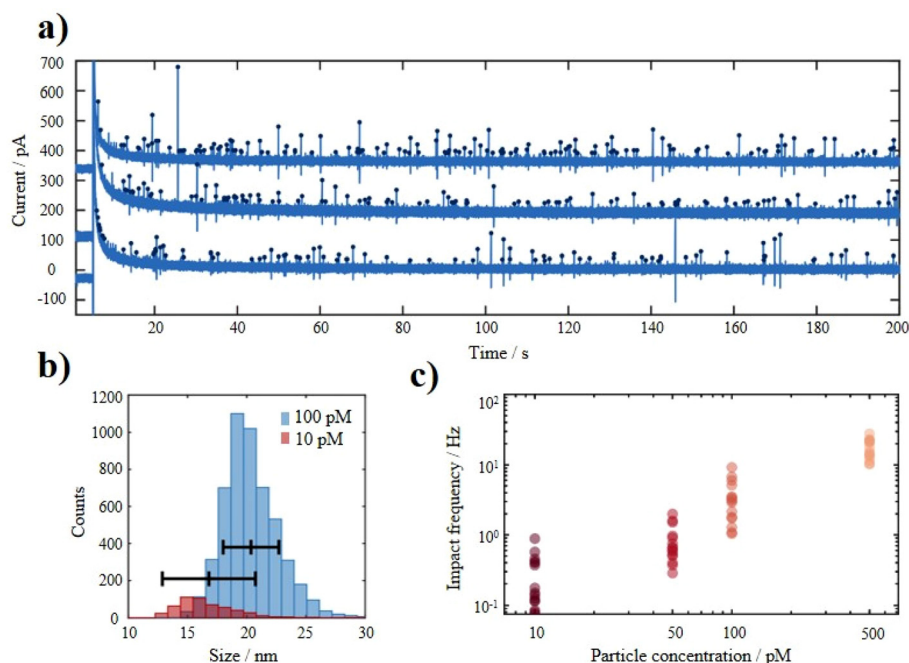

Fig. 5 AgNP detection experiment. (a) Raw current traces and detected AgNPs impacts of three different channels for 10 pM AgNP in 25 mM KCl and an oxidation potential of 800 mV vs. Ag/AgCl. The traces are offset by 200 pA for clarity. (b) Size distribution of individually detected particles during successive measurements and cleaning cycles. The particle sizes are calculated by integration of the current traces caused by AgNPs collision. The errorbar depicts the mean particle size and standard deviation based on the electrochemical data. (c) Impact frequency per electrode in dependence of the particle concentration measured within 25 mM KCl solution. The dots represent the impact frequencies of individual electrodes within a 200s window.

able to standard electrochemical probes where intensive mechanical polishing is possible. Overall, the results indicate the possibility to use 3D laser-ablated MEAs for stochastic impact electrochemistry or detection of redox active analytes.

In the context of manufacturing 3D MEAs capable of electrochemical detection, our method offers several advantages over conventional clean-room processes. The use of inkjet printing in the fabrication of the 3D structure makes defining different electrode heights relatively straightforward compared to classical approaches. Furthermore, at least for small batch fabrication, the use of laser-ablation in defining the feedlines and exposing the electrode tips is substantially faster than traditional microfabrication. Patterning an entire chip only takes a few minutes overall. Thus, the presented method allows tuning geometric parameters of 3D electrode arrays in a rapid prototyping approach.

4. Conclusions

We presented a simple process for the fabrication of 3D microelectrode arrays by inkjet printing in combination with laser-patterning. Inkjet-printed 3D structures were insulated using parylene-C and electrode tips were exposed *via* laser-ablation in a perpendicular alignment. The resulting ring electrodes were characterized using CV and EIS confirming applicability for electrochemical recordings. As a proof of principle, we demonstrated the electrochemical detection of AgNPs concentrations from 10 pM to 500 pM using 3D microelectrode arrays. We believe that this concept can be applied for electrochemical detection of analytes in various 3D environments.

Conflicts of interest

The authors declare that they have no known competing financial interests or personal relationships that could have appeared to influence the work reported in this paper.

Acknowledgements

References

1 M. E. Vance, T. Kuiken, E. P. Vejerano, S. P. McGinnis, M. F. Hochella, D. Rejeski and M. S. Hull, *Beilstein J. Nanotechnol.*, 2015, **6**, 1769–1780.

2 B. Nowack, H. F. Krug and M. Height, *Environ. Sci. Technol.*, 2011, **45**, 1177–1183.

3 J. Y. Maillard and P. Hartemann, *Crit. Rev. Microbiol.*, 2013, **39**, 373–383.

4 M. Carbone, D. T. Donia, G. Sabbatella and R. Antiochia, *J. King Saud Univ., Sci.*, 2016, **28**, 273–279.

5 S. Gajbhiye and S. Sakharwade, *J. Cosmet., Dermatol. Sci. Appl.*, 2016, **06**, 48–53.

6 E. Lombi, E. Donner, K. G. Scheckel, R. Sekine, C. Lorenz, N. Von Goetz and B. Nowack, *Chemosphere*, 2014, **111**, 352–358.

7 J. Hedberg, S. Skoglund, M. E. Karlsson, S. Wold, I. O. Wallinder and Y. Hedberg, *Environ. Sci. Technol.*, 2014, **48**, 7314–7322.

8 D. Musino, J. Devcic, C. Lelong, S. Luche, C. Rivard, B. Dalzon, G. Landrot, T. Rabilloud and I. Capron, *Nanomaterials*, 2021, **11**, 20.

9 A. Kumar, P. K. Vemula, P. M. Ajayan and G. John, *Nat. Mater.*, 2008, **7**, 236–241.

10 X. Chen and H. J. Schluesener, *Toxicol. Lett.*, 2008, **176**, 1–12.

11 A. J. Bone, B. P. Colman, A. P. Gondikas, K. M. Newton, K. H. Harrold, R. M. Cory, J. M. Unrine, S. J. Klaine, C. W. Matson and R. T. Di Giulio, *Environ. Sci. Technol.*, 2012, **46**, 6925–6933.

12 P. G. Figueiredo, L. Grob, P. Rinklin, K. J. Krause and B. Wolfrum, *ACS Sens.*, 2018, **3**, 93–98.

13 M. M. Ghobashy, M. Abd Elkodous, S. H. Shabaka, S. A. Younis, D. M. Alshangiti, M. Madani, S. A. Al-Gahtany, W. F. Elkhatib, A. M. Noreddin, N. Nady and G. S. El-Sayyad, *Nanotechnol. Rev.*, 2021, **10**, 954–977.

14 X. F. Zhang, Z. G. Liu, W. Shen and S. Gurunathan, *Int. J. Mol. Sci.*, 2016, **17**, 34.

15 W. Anderson, D. Kozak, V. A. Coleman, A. K. Jamting and M. Trau, *J. Colloid Interface Sci.*, 2013, **405**, 322–330.

16 C. A. Little, C. Batchelor-McAuley, N. P. Young and R. G. Compton, *Nanoscale*, 2018, **10**, 15943–15947.

17 K. J. Krause, A. Yakushenko and B. Wofrum, *Anal. Chem.*, 2015, **87**, 7321–7325.

18 S. V. Sokolov, S. Eloul, E. Katelhon, C. Batchelor-McAuley and R. G. Compton, *Phys. Chem. Chem. Phys.*, 2017, **19**, 28–43.

19 X. Y. Xiao and A. J. Bard, *J. Am. Chem. Soc.*, 2007, **129**, 9610.

20 J. Ellison, C. Batchelor-McAuley, K. Tschulik and R. G. Compton, *Sens. Actuators, B*, 2014, **200**, 47–52.

21 W. Gan, B. L. Xu and H. L. Dai, *Angew. Chem., Int. Ed.*, 2011, **50**, 6622–6625.

22 S. Eloul, E. Katelhon and R. G. Compton, *Phys. Chem. Chem. Phys.*, 2016, **18**, 26539–26549.

23 S. Eloul and R. G. Compton, *ChemElectroChem*, 2014, **1**, 917–924.

24 L. J. K. Weiss, P. Rinklin and B. Wolfrum, *Curr. Opin. Electrochem.*, 2020, **22**, 203–210.

25 Y. G. Zhou, N. V. Rees and R. G. Compton, *Angew. Chem., Int. Ed.*, 2011, **50**, 4219–4221.

26 K. Ito, K. Y. Inoue, T. Ito-Sasaki, K. Ino and H. Shiku, *ACS Appl. Nano Mater.*, 2021, **4**, 12393–12400.

27 S. Zips, L. Grob, P. Rinklin, K. Terkan, N. Y. Adly, L. J. K. Weiss, D. Mayer and B. Wolfrum, *ACS Appl. Mater. Interfaces*, 2019, **11**, 32778–32786.

28 M. R. Khosravani and T. Reinicke, *Sens. Actuators, A*, 2020, **305**, 17.

29 L. Grob, H. Yamamoto, S. Zips, P. Rinklin, A. Hirano-Iwata and B. Wolfrum, *Adv. Mater. Technol.*, 2020, **5**, 10.

30 D. Martín-Yerga, *Biosensors*, 2019, **9**, 47.

31 K. Y. Mitra, E. Sowade, C. Martinez-Domingo, E. Ramon, J. Carrabina, F. L. GornesD and R. R. Baumann, Thessaloniki, GREECE, 2014.

32 L. Grob, P. Rinklin, S. Zips, D. Mayer, S. Weidlich, K. Terkan, L. J. K. Weiss, N. Adly, A. Offenhausser and B. Wolfrum, *Sensors*, 2021, **21**, 3981.

33 L. J. K. Weiss, G. Lubins, E. Music, P. Rinklin, M. Banzet, H. Peng, K. Terkan, D. Mayer and B. Wolfrum, *ACS Sens.*, 2022, **7**, 884–892.

34 K. Tasnim and J. Liu, *J. Mol. Biol.*, 2021, 167165.

35 P. Wijdenes, K. Haider, C. Gavrilovici, B. Gunning, M. Wolff, T. Lijnse, R. Armstrong, G. Teskey, J. Rho and C. Dalton, *Sci. Rep.*, 2021, **11**, 1–13.

36 T. Moazzenzade, T. Walstra, X. J. Yang, J. Huskens and S. G. Lemay, *Anal. Chem.*, 2022, **94**, 10168–10174.

37 N. B. Li, M. S. Du, Y. Meng, H. D. Xue, F. H. Cao, H. Y. Hsu and F. Liu, *Sens. Actuators, B*, 2021, **349**, 8.

38 K. J. Krause, F. Brings, J. Schnitker, E. Katelhon, P. Rinklin, D. Mayer, R. G. Compton, S. G. Lemay, A. Offenhausser and B. Wolfrum, *Chem. – Eur. J.*, 2017, **23**, 4638–4643.

39 H. Ma, J. F. Chen, H. F. Wang, P. J. Hu, W. Ma and Y. T. Long, *Nat. Commun.*, 2020, **11**, 2307.

40 L. J. K. Weiss, E. Music, P. Rinklin, L. Straumann, L. Grob, D. Mayer and B. Wolfrum, *ACS Appl. Nano Mater.*, 2021, **4**, 8314–8320.

41 L. J. K. Weiss, P. Rinklin, B. Thakur, E. Music, H. Url, I. Kopic, D. Hoven, M. Banzet, T. von Trotha, D. Mayer and B. Wolfrum, *ACS Sens.*, 2022, **7**, 1967–1976.

42 L. J. K. Weiss, E. Music, P. Rinklin, M. Banzet, D. Mayer and B. Wolfrum, *Anal. Chem.*, 2022, **94**, 11600–11609.

B.2 Low-cost, On-site, Nanoimpact Detection of Silver Nanoparticles via Laser-ablated Screen-printed Microelectrodes

L. Grob*, **L.J.K. Weiß***, E. Music, I. Schwertfeger, G. Al Boustani, J. Feuerbach, M. Nikić,
L. Hiendlmeier, P. Rinklin, B. Wolfrum

Abstract

With the ever-growing presence of silver nanoparticles in consumer products, there is a need for cost-effective and on-site monitoring of their influence on our environment. Herein, we report the use of screen-printed and laser-ablated microelectrode arrays (SPMEAs) for the electrochemical detection of 20 nm-sized silver nanoparticles (AgNPs) via collision electrochemistry. The electrodes' morphology is optically analyzed and their electrochemical properties later characterized using cyclic voltammetry and impedance spectroscopy. The SPMEAs were calibrated using a AgNP concentration range of 1 to 100 pM, resulting in a linear dependency of $22\,\mathrm{mHz}\,\mathrm{pM}^{-1}$ for the impact frequency. Finally, to demonstrate the possibility of future on-site applications, an in-house built portable nanoparticle detection (POND) device was used to measure Faradaic AgNP impacts on a SPMEA, in a solution contaminated with urea.

Individual Contribution

conceptualization of the study, data analysis, data interpretation, composition and writing of the manuscript

Low-Cost, On-Site, Nano-Impact Detection of Silver Nanoparticles via Laser-Ablated Screen-Printed Microelectrodes

*Leroy Grob, Lennart J. K. Weiß, Emir Music, Ilja Schwertfeger, George Al Boustani,
Julian Feuerbach, Marta Nikić, Lukas Hiendlmeier, Philipp Rinklin,
and Bernhard Wolfrum**

With the ever-growing presence of silver nanoparticles in consumer products, there is a need for cost-effective and on-site monitoring of their influence on our environment. Herein, we report the use of screen-printed and laser-ablated microelectrode arrays (SPMEAs) for the electrochemical detection of 20 nm-sized silver nanoparticles (AgNPs) via collision electrochemistry. The electrodes' morphology is optically analyzed and their electrochemical properties later characterized using cyclic voltammetry and impedance spectroscopy. The SPMEAs were calibrated using a AgNP concentration range of 1 to 100 pM, resulting in a linear dependency of 22 mHz pM^{-1} for the impact frequency. Finally, to demonstrate the possibility of future on-site applications, an in-house built portable nanoparticle detection (POND) device was used to measure Faradaic AgNP impacts on a SPMEA, in a solution contaminated with urea.

1. Introduction

Nanoparticles have been increasingly used over the past decades,[1–4] without a clear understanding of their impact on the environment.[5,6] In particular, there has been a preferential interest in silver nanoparticles (AgNPs) due to their antimicrobial properties.[7] For instance, AgNPs have been used in coatings or within fluids on a number of consumer products.[3,8–10] However, once these consumer products are in use, it becomes

challenging to know the AgNPs individual fate due to their small size and complex chemical interactions in different environments.[7] The increased interest in AgNPs has also in part been due to their size-dependent cytotoxic behavior.[11,12] In particular, small AgNPs (i.e. 10 nm) have shown to induce a "Trojan-horse" type mechanism in cells, potentially leading to cellular degradation.[13–16] There is therefore a need to monitor the presence of AgNPs in our environment,[17,18] and our ecosystems.[19]

In order to better understand the impact of AgNPs on the environment, trace analysis of potentially contaminated samples is required. For determining the nanoparticles' size, techniques such as electron microscopy (EM), atomic force microscopy, and dynamic light scattering have commonly been used.[6,7] In addition to the size of particles, their concentration is also a critical parameter. This is more commonly investigated using element-selective detection techniques such as inductively coupled plasma mass spectroscopy (ICP-MS), ICP-optical emission spectroscopy (ICP-OES), or Raman spectroscopy.[20,21] Besides their specific pros and cons, all these techniques lack the possibility of rapid on-site detection. Furthermore, typically they require samples to be transported to centralized lab facilities. This can in turn lead to sample fouling and greatly increase administrative tasks. In order to save time and resources, mobile (pre-)screening techniques would greatly aid in collecting appropriate samples before more in-depth analysis is undertaken. In this regard, electrochemical sensors in combination with a mobile electronic system have shown to be good prescreening platforms for detecting environmental contaminants such as heavy metals.[22–27] In fact, the AgNP themselves are known to interfere with their environment and could be the most straightforward sensing target for detecting redox active contaminants.[28–32]

To date, there are several methods by which various nanoparticle species can be detected electrochemically.[33] In the case of AgNPs, they can be directly detected by using the Faradaic nano-impact approach.[34–36] Faradaic nano-impacts involve an electron transfer upon collision of a single nanoparticle at an appropriately biased microelectrode. By applying an oxidation potential, AgNPs can react with halides.[37] In turn, an electron

L. Grob, L. J. K. Weiß, E. Music, G. Al Boustani, J. Feuerbach, M. Nikić,
L. Hiendlmeier, P. Rinklin, B. Wolfrum
Neuroelectronics – Munich Institute of Biomedical Engineering
Department of Electrical Engineering
TUM School of Computation
Information and Technology
Technical University of Munich
Hans-Piloty-Str. 1, 85748 Garching, Germany
E-mail: bernhard.wolfrum@tum.de
I. Schwertfeger
Hoffmann + Krippner GmbH
Siemensstrasse 1 74722, Buchen, Germany

transfer occurs and is monitored by an electronic amplifier as a current spike. From the resulting current–time traces, two pieces of information can be gathered: By integrating over the current spike, the charge can be calculated, which in turn relates to the size of the AgNP. In addition, the frequency of current spikes relates to the underlying concentration of AgNPs in the solution. Typically, single-impact recordings are carried out in experimentally controlled media.[37,38] Yet, recent work demonstrated that it is also possible to measure in sea, bottled or tap water.[39–41] Moreover, impact electrochemistry is able to quantify samples containing unknown concentrations of (differently-sized) AgNPs.[42,43] Such measurements are typically performed in a standard three-electrode setup.[33] Due to the small currents at play during individual impacts, however, this can be further simplified to a two-electrode setup.[44,45] Moreover, with the possibility of designing small and simple potentiostats,[46–51] developed using sensitive integrated-chips, nano-impact electrochemistry could become a promising technique for on-site quantification.

Traditionally, a single glassy carbon electrode is used for detection.[38] However, in order to improve statistical validity, parallel recordings from microelectrode arrays (MEAs) can be implemented.[37,44,45,52] MEAs are typically fabricated using classical clean-room lithography methods. This established technique allows well-defined electrode openings (e.g. in the low micrometer range) with inert metals such as platinum.[53] However, for environmental monitoring, cost-effective sensors are preferred mainly due to the volume of tests that need to be conducted. In addition, disposable or single-use sensors are desired for their easy-to-use, reliable, and fast response times.[54] To this end, screen-printing is a promising additive manufacturing process capable to go roll-to-roll whilst limiting the amount of wasted material.[55,56] For example, heavy metal ions such as arsenic, cadmium, lead, and mercury have been detected via screen-printed electrodes (SPEs) for environmental monitoring.[22–26] Generally, SPEs tend to be quite large, ranging from a few mm to as low as 100 μm in diameter.[57–60] Due to their large size and porosity (i.e. carbon, Pt, or Au), SPEs have quite low impedances in electrolyte media. For amperometric measurements this increases the current noise and ultimately obscures single nanoparticle impacts. This issue can be circumvented by limiting the electrode-electrolyte area by only pipetting a microliter sample onto the SPEs.[61] However, this is impractical for the end user and a more favorable approach would be to fabricate electrodes of smaller size via laser ablation.[62–65]

In this work, we investigate the use of screen-printed, laser-patterned microelectrode arrays (SPMEAs) for the electrochemical detection of AgNPs. In addition, we demonstrate the applicability of these sensors using an in-house built, portable nanoparticle detection (POND) device for detecting AgNPs contaminated with urea. Our method presents itself as a cost-effective platform for on-site monitoring of AgNPs via direct nano-impact electrochemistry.

2. Screen-Printed MEAs

In order to detect nanoparticles for future on-site applications, screen-printed microelectrode arrays (SPMEAs) were
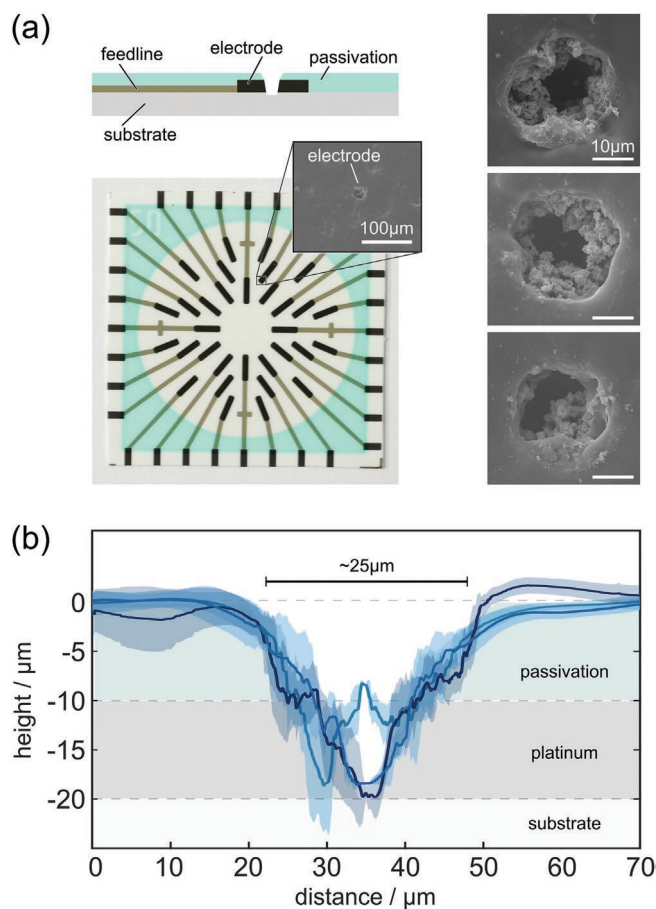

Figure 1. SPMEA for nano-impact electrochemistry. a) Schematic, optical, and SEM images of a laser-patterned screen-printed MEA (size 24.15 × 24.15 mm). b) Average cross-sectional profiles of the three electrodes displayed in (a). The mean and standard deviation were calculated using six cross-sectional profiles 30° apart from each other.

fabricated via screen-printing and subsequent laser pattering, see **Figure 1**. In principle, three different electrode geometries – a disk electrode,[64] a recessed electrode,[65] and a ring electrode[62,63] – are possible with the laser ablation technique. The electrode radius r and the depth of ablation is primarily determined by the laser's pulse energy, pulse width, wavelength, focal area, and the number of pulses. In addition, the passivation's absorption characteristics and layer height will also influence the electrodes' final geometry. Therefore, to yield electrode geometries with only little dependence on the laser process, we tuned the parameter toward full penetration of the Pt layer. We obtained SPMEAs with 32 individually addressable electrodes which are hollow and ≈12.5 μm in radius (view Figure 1a,b). In this case, the electrode size is mainly governed by the screen-printed layer height and electrode impedances suitable for single-impact electrochemical experiments can be achieved.

Nevertheless, after the laser patterning, it is important to clean the SPMEAs of process residues in order to expose active electrode sites.[66,67] These residues could be for example leftover binder components or potential oxide layers that arose due to laser ablation. Platinum oxide layers can be electrochemically reduced by using strong alkaline solutions such as KOH.[68]

**ADVANCED
SCIENCE NEWS**

www.advancedsciencenews.com

**ADVANCED
MATERIALS
TECHNOLOGIES**

www.advmattechnol.de

However, in the case of screen-printed microelectrodes, we observed larger capacitive currents once they were activated in 100 mM KOH (see Supporting Information), most likely due to over etching and critical removal of the passivation layer.[69] This ultimately leads to a large electrode-electrolyte interface and consequent masking of the individual single nanoparticle impacts by the increased noise. In contrast, we observed a gradual but continuous activation for cyclic voltammetry cleaning in 0.2 M sulfuric acid (see **Figure 2**a). After 100 cycles, it was possible to see the characteristic oxidation and reduction of Pt in sulfuric acid as shown similarly in the literature.[70,71]

(a)

(b)

(c)
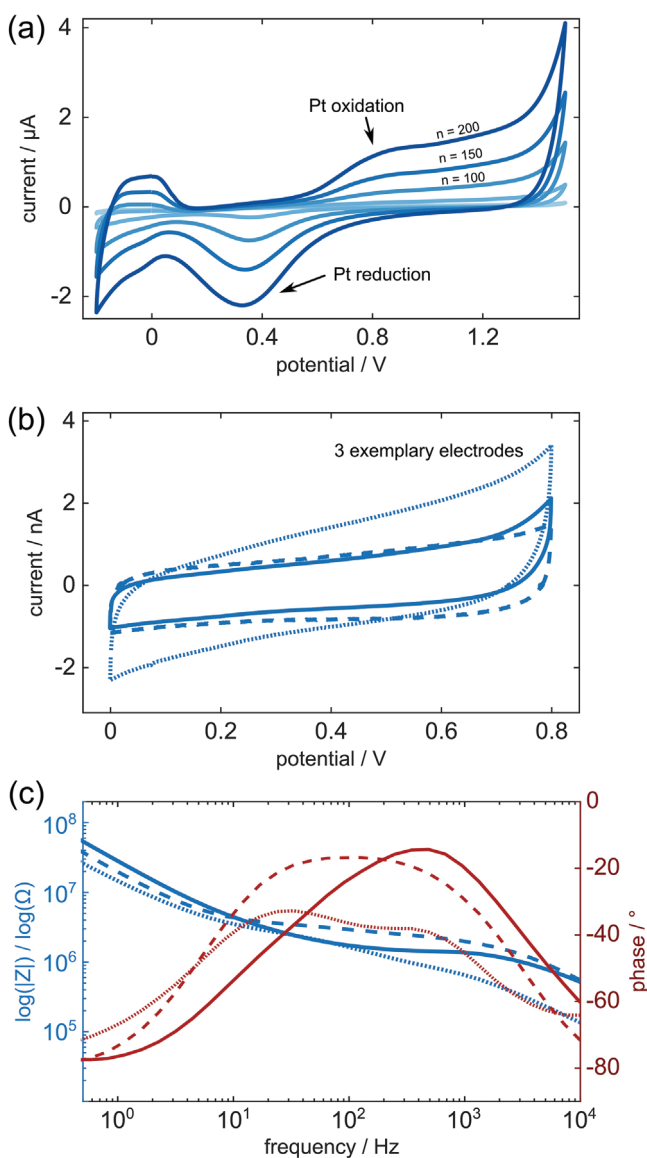
Figure 2. Electrochemical Characterization. a) Activation in 200 mM H_2SO_4 solution. All electrodes were short-circuited during the activation (potential range −0.2 to 1.5 V, 500 mV s^{-1} scan rate, 200 cycles). The graph shows every 50th cycle. b) Cyclic voltammetry (0 to 800 mV, 100 mV s^{-1} scan rate, 2nd cycle) of individual electrodes (solid, dashed, and dotted) and c) impedance spectroscopy (at 0.18 ± 0.01 V) in PBS solution containing 1 mM ferri/ferrocyanide.

Once the SPMEA was activated, we rinsed the chips with deionized water and individually characterized representative electrodes with a redox-active tracer (1 mM ferri/ferrocyanide in phosphate-buffered saline). Exemplary cyclovoltammograms are shown in Figure 2b, displaying a clear capacitive nature. We associate this capacitive behavior primarily to the electrodes' porous composite material which is known to form distributed contact impedances.[72] This is also confirmed by the impedance spectroscopy data shown in Figure 2c which displays a combination of RC elements (view plateau visible at ≈100 Hz). Inter-electrode variations are most likely explained by slight variations in the manufacturing process.

3. Nano-Impact Electrochemistry

After activation of the SPMEAs, we performed nano-impact experiments using 20 nm-sized citrate-capped AgNPs. Exemplary raw current traces are shown in **Figure 3** for 200 pM AgNPs in 25 mM KCl solution. The electrodes were biased to 800 mV vs. Ag/AgCl to ensure a maximum yield and the particles were inserted at ≈45 s. The data shows a clear difference between a solution containing pure electrolyte ($t < 45$ s) and the AgNP-spiked solution ($t > 50$ s). In fact, the current peaks associated with collision events exceed the RMS noise floor of 7.7 ± 2.3 pA noticeably. We further applied a channel-specific threshold to extract the AgNP impacts that are considered in the subsequent analysis (visualized as blue dots) and measured an impact rate of 4 ± 1 Hz (200 pM AgNPs in 25 mM KCl). This value is in the same range as values reported for clean-room fabricated MEAs.[45,52] Hence, we conclude that the oxide layer at the electrode was successfully removed during the activation step. Thus, we expect SPMEAs to be suitable for quantitative AgNP detection.

To test this, we conducted nano-impact experiments with various particle concentrations in the pM-range and obtained an approximately linear relationship of 22 mHz pM^{-1} between the impact rate and the underlying concentration, see **Figure 4**. Moreover, we were able to detect AgNP impacts at low concentrations of 1 pM.

3.1. Towards On-Site Nanoparticle-Detection Using A Portable Device

We believe that nano-impact electrochemistry is a promising candidate to bridge the gap from the laboratory towards a highly sensitive yet cost-effective sensing technique for on-site applications.[73–75] To date, there are no commercially available portable multichannel amperometric systems dedicated for detecting AgNPs via impact electrochemistry. Therefore, we developed a portable nanoparticle detection (POND) device (see **Figure 5**a) that can be used for contamination sensing in-field. Our prototype can be connected to a notebook and directly used for pA-measurements. It supports parallel recordings from 8 channels, each at 20 kHz sampling rate (additional information can be found in the supplementary), and shielded from unwanted noise.
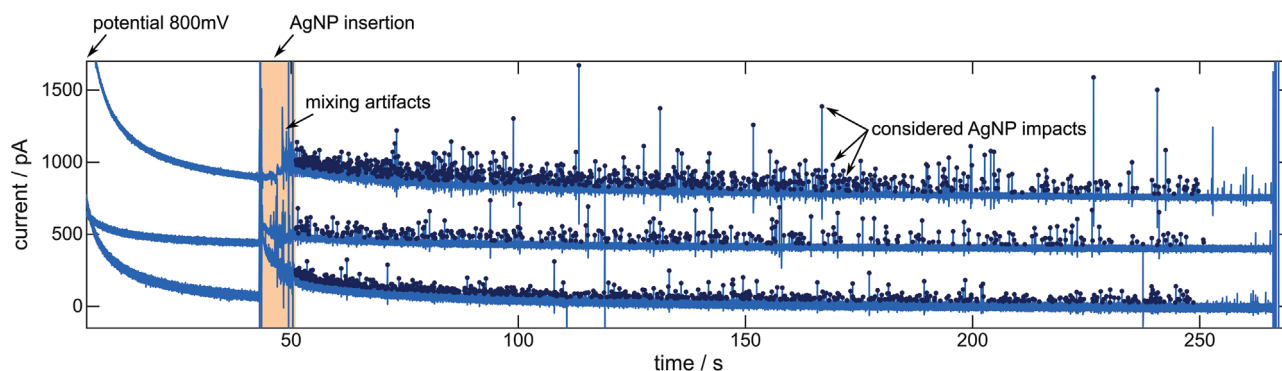
Figure 3. Single-impact experiment using 30 mM KCl solution containing 200 pM AgNP with 20 nm diameter. Current traces of three electrodes biased to 800 mV vs Ag/AgCl throughout the experiment. The particles were added and mixed (orange shading). Blue dots mark current peaks that are considered as AgNP impacts. Traces are shifted by 500 pA relative to one another for visual clarity.

To test the POND device in a simulated on-site environment, preliminary experiments were done in controlled media as similarly described (data not shown). Thereafter, we performed an initial proof-of-concept and detected AgNP in urea-spiked electrolyte solution using the 8-channel POND system. Since urea is typically present in natural (waste) water, we were interested in investigating their effect on our detection method. This study is to the best of our knowledge, the first attempt where a portable device was used to record nano-impacts on a low-cost MEA chip on-site. An exemplary current trace of a single electrode is provided in Figure 5b. The background noise in Figure 5b ($\approx$13 pA) can be attributed to weakly-shielded electronic circuits, as the cover of the device was left open during the measurement (to be able to insert the urea). Nevertheless, the current peaks upon collisions are clearly distinguishable from background noise – even after polluting the solution with urea.

Even in this non-ideal situation, we were generally able to differentiate particle impacts from noise by simple thresholding and obtained estimated particles sizes (19.0 $\pm$ 2.4 nm and 19.3 $\pm$ 2.9 nm with and without urea pollution) that are similar to the expected value of 20 nm.

The data in Figure 5b also indicates that moderate amounts of urea do not critically interfere with the detection, since the number of current spikes is not drastically reduced after pollution. In fact, we observed a minor change from 1.0 Hz before pollution to 0.86 Hz afterward for the data in Figure 5. Moreover, the difference in impact rate might be also explained by dilution effects as well as differences in the diffusive mass transport, as there is typically a strong initial decrease after the potential application.

4. Conclusion

We demonstrated the use of screen-printed, laser-patterned microelectrode arrays (SPMEAs) for detecting 20 nm diameter silver nanoparticles (AgNPs) via nano-impact electrochemistry. By simple laser ablation through the electrode material, electrodes were formed allowing pA current transients to be measured after cleaning. With our 64-channel lab-based amplifier system, we were able to obtain a linear relationship between the impact frequency and the AgNP concentration (22 mHz pM^{-1}, R^2 = 97.6 %). This allows future unknown concentrations of AgNPs to be identified using our SPMEAs. In order to go towards more real-world measurements, an on-site portable nanoparticle detection (POND) device was built. Its capability under on-site constraints was exemplarily demonstrated during a pollution-experiment, where we recorded impacts with our low-cost platform. Faradaic nano-impacts were detected, before and after the addition of urea, with marginal changes to their measured size. We also believe a similar setup could be of use in directly detecting other metals such as Ni or Cu nanoparticles. [42,76,77] However, careful consideration to the electrode's material, electrolyte composition, and applied potential is required. In summary, we believe this simple and cost-effective SPMEA coupled with a POND-like device would allow more rapid on-site monitoring of potentially contaminated AgNP environments.

Figure 4. Impact frequency as a function of AgNP concentration. All experiments used an oxidation potential of 800 mV vs Ag/AgCl and were taken in 30 mM KCl solution. The data is based on the first 200 s after mixing. The dashed linear fit has a value of 22 mHz pM^{-1}. The impact frequencies of individual electrode channels are represented as circular dots. The error bars indicate standard deviation.

5. Experimental Section

Chemicals: Silver nanoparticles (mean size 20 nm, 0.02 mg mL^{-1} in aqueous solution), sulfuric acid (H$_2$SO$_4$, 95%–98%), urea, potassium chloride (KCl), potassium ferricyanide, potassium ferrocyanide, and

**ADVANCED
SCIENCE NEWS**

www.advancedsciencenews.com

**ADVANCED
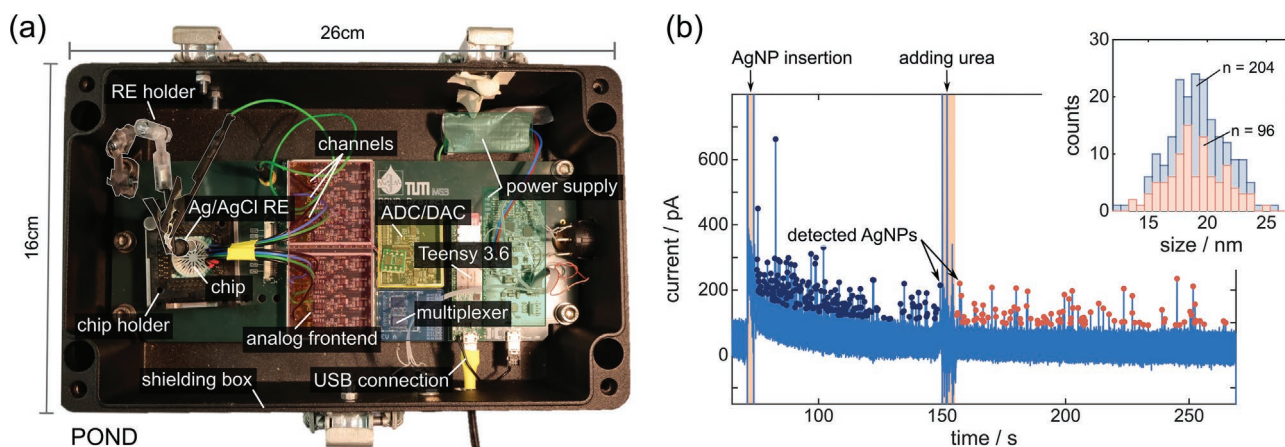MATERIALS
TECHNOLOGIES**

www.advmattechnol.de

Figure 5. On-site AgNP detection using the in-house built portable nanoparticle detection (POND) device for a waste-water mimicking experiment. a) Schematic of the POND device that is able to record simultaneously from 8 channels at a sampling rate 20 kHz. b) Raw data of a single electrode for 223 pM AgNP in 30 mM KCl. After 150 s, the solution was polluted with 10 µM urea simulating a typical contaminant in waste water.

modified phosphate-buffered saline (PBS) solution were purchased from Merck, Germany. All dilutions were prepared using deionized water from a BerryPURE purification system (Berrytec GmbH, Germany).

Screen-Printed Microelectrode Arrays: The screen-printed microelectrode arrays (SPMEAs) were fabricated on commercial polyester substrates (Melinex 339, Dupont Teijin Films, Wilton, UK) using a semi-automatic screen-printer (EKRA X5, Scanditron, Spånga, Sweden). The screen characteristics regarding mesh count and emulsion thickness were selected in accordance with the specifications of the ink manufacturers.

The fabrication of the SPMEAs consists of six individual layers printed subsequently with a drying step after each print. The feedlines were printed using a silver-based ink (Smart Screen F (S-CS21303), GenesInk, Rousset, France) and covered with carbon ink (Loctite EDAG 423 SS, Henkel, California, USA) at the contact areas. Platinum ink (BQ-321, DuPont, Bristol, UK) was used at the electrode site. In order to cover the printed features, a transparent dielectric ink (Luxprint 7165, DuPont, Bristol, UK) was printed twice to minimize the risk of pinholes. Finally, an encapsulation ink (Loctite EDAG 452SS Henkel, California, USA) was printed as an additional flow stop boundary. Solvent-based inks were dried using a conveyor belt oven set to 120 °C with a speed of 4 m min^{-1}. The overall heat-treatment procedure lasts for about 2 min. The UV-ink was cured with a dose of ≈0.7 J cm^{-2}.

A three-axis UV laser marker (MD-U1000C, Keyence, Osaka, Japan) was used to cut a 20 µm hole through the passivation layer, exposing the conductive Pt layer. A two-step laser procedure was used. For the first laser step, the system was set to 10 kW, with a filling interval of 4 µm, and only repeated once. The second laser setting was repeated 100 times as a polishing step, with the laser set to 0.2 kW and a filling interval of 2 µm. Both used a shutter frequency of 400 kHz, writing at a speed of 1 m s^{-1}.

Glass rings were glued onto the SPMEAs and served as fluid reservoirs. They had a height and inner diameter of 10 mm and 17 mm, respectively.

Electrochemical Experiments: The electrochemical activation and the electrode characterization were performed with a VSP-300 potentiostat (Bio-Logic Science Instruments, Seyssinet-Pariset, France) in a three-electrode configuration with a flexible Ag/AgCl reference (Dri-Ref, Flexref from World Precision Instruments, Sarasota, USA) and a coiled platinum wire counter electrode. To initially clean and activate the electrode surface, a cyclic voltammetry (CV) step from −0.2 to 1.5 V with a scan rate of 500 mV s^{-1} and 200 cycles was performed in 200 mM H_2SO_4. Prior to the detection experiments, the chips were additionally cleaned by thoroughly rinsing with deionized water and applying another short electrochemical activation: CV in H_2SO_4 with 20 cycles.

The characterization of the individual electrodes was performed in modified PBS solution that contained 1 mM ferricyanide and 1 mM ferrocyanide as redox couple. Here, a CV (potential range from 0 to 0.8 V, 50 mV s^{-1} scan rate, 2nd cycle evaluated) and a subsequent impedance spectroscopy (PEIS, frequency range 0.5 Hz to 10 kHz, applied potential 0.18 ± 0.01 V) was carried out for each electrode. In total, 20 electrodes from 2 chips were analyzed.

The silver nanoparticle calibration measurements were performed in a shielded and vibration-dampened environment, using a two-electrode setup. An inhouse-built transimpedance amplifier system that is able to record 64 channels in parallel at 10 kHz was used (3.4 kHz bandwith) to obtain the calibration curve.[44,45,78] In these experiments a Ag/AgCl from BaSi (RE-4, 3 M NaCl gel electrode) served as reference. All measurements used 30 mM of KCl solution with a total volume of 700 µL. The AgNPs were directly added from stock solution after biasing the electrodes to the oxidation potential of 800 mV vs Ag/AgCl. Then, the solution was mixed by pipetting 500 µL volume in and out three times (within ≈5 to 10 s) and AgNP impacts were recorded. The total analysis time was 200 s.

The contamination experiment was carried out in an in-house built portable nanoparticle detection (POND) device that features 8 channels in a two-electrode configuration (further information see Supporting Information). In this experiment, Faradaic nano-impacts from 200 pM AgNP in 30 mM KCl were recorded after direct pipetting and mixing. After an initial recording phase, the solution was contaminated by adding 100 µL of 1 mM urea while the potential was kept at 800 mV vs Ag/AgCl.

Scanning Electron Microscopy: The screen-printed microelectrode array (SPMEA) was sputtered with ≈10 nm of Au (5 Pa, 40 s, 40 mA) using a high-vacuum coating system (BAL-TEC Med 020, LabMakelaar Benelux BV, The Netherlands). Copper tape and conductive double sided carbon-tab was used to fix the SPMEA to the holder to prevent charge accumulation. All scanning electron images were taken using a scanning electron microscope (JSM-6060LV, JEOL, Tokyo, Japan) at an acceleration voltage of 15 kV, a magnification of 100× or 2500×, and a substrate tilt of 0°.

Optical Profilometry: Already sputtered screen-printed microelectrodes were measured using a 3D laser scanning confocal microscope (VK-X250, Keyence, Osaka, Japan) in combination with a 150× objective (150×/0.95 CF Plan Apo OFN25, Nikon, Japan). A high and low laser intensity (double-scan feature) was used on each individual microelectrode in order to evaluate its morphology. The neutral density filter of the microscope was automatically calibrated (auto gain function) after setting the lower and upper limits of the scan. A z-pitch of 80 nm was used for each measurement, that was carried out

on a vibration-dampened table (Vision IsoStation, Newport Corporation, California, USA) to reduce external interferences.

Data Processing: The data was processed via a custom algorithm in Matlab, similar to previous work.[52] First, channels that show noisy as well as unresponsive electrodes were excluded. Then all raw traces were de-trended to account for low-frequency relaxation of the background current. The AgNP impacts were identified via current thresholding. Here, a channel-specific threshold was set (0.5 i_{pk2pk} + 5 pA) by considering the individual peak-to-peak background noise (i_{pk2pk}). Depending on the capacitive load of each electrode, amplifier related ringing-artifacts can be observed after the initial charge injection caused by an impacting AgNP. These artifacts were excluded by setting a minimum inter-peak distance of 10 ms. The results shown above are based on recordings from $n \geq 6$ electrodes per concentration, acquired from two different chips.

Profilometric data was evaluated using MultiFileAnalyzer software (Keyence, Osaka, Japan). Background subtraction was manually set around the electrode opening using a 2D polynomial of order one in x and y. Within the software, six individual profiles were taken at 30° intervals (see Supporting Information). These profiles were later averaged in Matlab displaying the mean and standard deviation.

Supporting Information

Supporting Information is available from the Wiley Online Library or from the author.

Acknowledgements

Conflict of Interest

The authors declare no conflict of interest.

Data Availability Statement

The data that support the findings of this study are available from the corresponding author upon reasonable request.

Keywords

[1] K. Schmid, M. Riediker, *Environ. Sci. Technol.* **2008**, *42*, 2253.
[2] R. Kessler, *Environ. Health Perspect.* **2011**, *119*, A120.
[3] M. E. Vance, T. Kuiken, E. P. Vejerano, S. P. McGinnis, M. F. Hochella, D. Rejeski, M. S. Hull, *Beilstein J. Nanotechnol.* **2015**, *6*, 1769.
[4] S. F. Hansen, L. R. Heggelund, P. R. Besora, A. Mackevica, A. Boldrin, A. Baun, *Environ Sci: Nano* **2016**, *3*, 169.
[5] N. Savage, M. S. Diallo, *J Nanopart Res* **2005**, *7*, 331.
[6] B. C. Englert, *J Environ Monit* **2007**, *9*, 1154.
[7] E. McGillicuddy, I. Murray, S. Kavanagh, L. Morrison, A. Fogarty, M. Cormican, P. Dockery, M. Prendergast, N. Rowan, D. Morris, *Sci. Total Environ.* **2017**, *575*, 231.
[8] M. Rai, A. Yadav, A. Gade, *Biotechnol. Adv.* **2009**, *27*, 76.
[9] B. Nowack, H. F. Krug, M. Height, *Environ. Sci. Technol.* **2011**, *45*, 1177.
[10] C. A. Dos Santos, M. M. Seckler, A. P. Ingle, I. Gupta, S. Galdiero, M. Galdiero, A. Gade, M. Rai, *J. Pharm. Sci.* **2014**, *103*, 1931.
[11] V. De Matteis, M. A. Malvindi, A. Galeone, V. Brunetti, E. De Luca, S. Kote, P. Kshirsagar, S. Sabella, G. Bardi, P. P. Pompa, *Nanomedicine* **2015**, *11*, 731.
[12] R. de Lima, A. B. Seabra, N. Durán, *J. Appl. Toxicol.* **2012**, *32*, 867.
[13] P. V. AshaRani, G. Low Kah Mun, M. P. Hande, S. Valiyaveettil, *ACS Nano* **2009**, *3*, 279.
[14] T.-H. Kim, M. Kim, H.-S. Park, U. S. Shin, M.-S. Gong, H.-W. Kim, *J. Biomed. Mater. Res.* **2012**, *100A*, 1033.
[15] A. R. Gliga, S. Skoglund, I. Odnevall Wallinder, B. Fadeel, H. L. Karlsson, *Part. Fibre Toxicol.* **2014**, *11*, 11.
[16] L. R. R. Souza, V. S. da Silva, L. P. Franchi, T. A. J. de Souza, in *Cellular and Molecular Toxicology of Nanoparticles* (Eds.: Q. Saquib, M. Faisal, A. A. Al-Khedhairy, A. A. Alatar), Springer International Publishing, Cham **2018**, pp. 251–262.
[17] L. Degenkolb, F. Leuther, S. Lüderwald, A. Philippe, G. Metreveli, S. Amininejad, H.-J. Vogel, M. Kaupenjohann, S. Klitzke, *Sci. Total Environ.* **2020**, *699*, 134387.
[18] J.-L. Wang, E. Alasonati, M. Tharaud, A. Gelabert, P. Fisicaro, M. F. Benedetti, *Water Res.* **2020**, *176*, 115722.
[19] J. Fabrega, S. N. Luoma, C. R. Tyler, T. S. Galloway, J. R. Lead, *Environ Int* **2011**, *37*, 517.
[20] E. M. Heithmar, *Screening Methods for Metal-Containing Nanoparticles in Water*, U.S. Environmental Protection Agency, Washington, DC **2011**.
[21] J. Liu, S. Yu, Y. Yin, J. Chao, *Trends Analyt Chem* **2012**, *33*, 95.
[22] G. Hanrahan, D. G. Patil, J. Wang, *J Environ Monit* **2004**, *6*, 657.
[23] M. Li, Y.-T. Li, D.-W. Li, Y.-T. Long, *Anal. Chim. Acta* **2012**, *734*, 31.
[24] A. Hayat, J. L. Marty, *Sensors* **2014**, *14*, 10432.
[25] J. Barton, M. B. G. García, D. H. Santos, P. Fanjul-Bolado, A. Ribotti, M. McCaul, D. Diamond, P. Magni, *Microchim. Acta* **2016**, *183*, 503.
[26] M. Li, D.-W. Li, G. Xiu, Y.-T. Long, *Curr. Opin. Electrochem.* **2017**, *3*, 137.
[27] E. Bernalte, S. Arévalo, J. Pérez-Taborda, J. Wenk, P. Estrela, A. Avila, M. Di Lorenzo, *Sens. Actuators, B* **2020**, *307*, 127620.
[28] M. C. Stensberg, Q. Wei, E. S. McLamore, D. M. Porterfield, A. Wei, M. S. Sepúlveda, *Nanomedicine* **2011**, *6*, 879.
[29] Z. Ferdous, A. Nemmar, *Int. J. Mol. Sci.* **2020**, *21*, 2375.
[30] S. Garcia-Segura, X. Qu, P. J. J. Alvarez, B. P. Chaplin, W. Chen, J. C. Crittenden, Y. Feng, G. Gao, Z. He, C.-H. Hou, X. Hu, G. Jiang, J.-H. Kim, J. Li, Q. Li, J. Ma, J. Ma, A. B. Nienhauser, J. Niu, B. Pan, X. Quan, F. Ronzani, D. Villagran, T. D. Waite, W. S. Walker, C. Wang, M. S. Wong, P. Westerhoff, *Environ. Sci.: Nano* **2020**, *7*, 2178.
[31] A. Sekretareva, *Sens Actuators Rep* **2021**, *3*, 100037.
[32] K. E. Fink, B. J. Polzin, J. T. Vaughey, J. J. Major, A. R. Dunlop, S. E. Trask, G. T. Jeka, J. S. Spangenberger, M. A. Keyser, *J. Power Sources* **2022**, *518*, 230760.

**ADVANCED
SCIENCE NEWS**

www.advancedsciencenews.com

**ADVANCED
MATERIALS
TECHNOLOGIES**

www.advmattechnol.de

[33] S. V. Sokolov, S. Eloul, E. Kätelhön, C. Batchelor-McAuley, R. G. Compton, *Phys. Chem. Chem. Phys.* **2017**, *19*, 28.

[34] Y.-Y. Peng, R.-C. Qian, M. E. Hafez, Y.-T. Long, *ChemElectroChem* **2017**, *4*, 977.

[35] F. T. Patrice, K. Qiu, Y.-L. Ying, Y.-T. Long, *Annu. Rev. Anal. Chem.* **2019**, *12*, 347.

[36] P. A. Defnet, T. J. Anderson, B. Zhang, *Curr. Opin. Electrochem.* **2020**, *22*, 129.

[37] K. J. Krause, F. Brings, J. Schnitker, E. Kätelhön, P. Rinklin, D. Mayer, R. G. Compton, S. G. Lemay, A. Offenhäusser, B. Wolfrum, *Chemistry* **2017**, *23*, 4638.

[38] Y.-G. Zhou, N. V. Rees, R. G. Compton, *Angew. Chem., Int. Ed.* **2011**, *50*, 4219.

[39] E. J. E. Stuart, N. V. Rees, J. T. Cullen, R. G. Compton, *Nanoscale* **2013**, *5*, 174.

[40] E. J. E. Stuart, K. Tschulik, D. Omanović, J. T. Cullen, K. Jurkschat, A. Crossley, R. G. Compton, *Nanotechnology* **2013**, *24*, 444002.

[41] X. Li, C. Batchelor-McAuley, R. G. Compton, *ACS Sens.* **2019**, *4*, 464.

[42] E. J. E. Stuart, Y.-G. Zhou, N. V. Rees, R. G. Compton, *RSC Adv.* **2012**, *2*, 6879.

[43] P. Bélteky, A. Rónavári, N. Igaz, B. Szerencsés, I. Y. Tóth, I. Pfeiffer, M. Kiricsi, Z. Kónya, *Int J Nanomedicine* **2019**, *14*, 667.

[44] K. J. Krause, A. Yakushenko, B. Wolfrum, *Anal. Chem.* **2015**, *87*, 7321.

[45] P. G. Figueiredo, L. Grob, P. Rinklin, K. J. Krause, B. Wolfrum, *ACS Sens.* **2018**, *3*, 93.

[46] J. L. Delaney, E. H. Doeven, A. J. Harsant, C. F. Hogan, *Anal. Chim. Acta* **2013**, *790*, 56.

[47] M. D. Steinberg, P. Kassal, I. Kereković, I. M. Steinberg, *Talanta* **2015**, *143*, 178.

[48] E. H. Doeven, G. J. Barbante, A. J. Harsant, P. S. Donnelly, T. U. Connell, C. F. Hogan, P. S. Francis, *Sens. Actuators, B* **2015**, *216*, 608.

[49] A. Ainla, M. P. S. Mousavi, M.-N. Tsaloglou, J. Redston, J. G. Bell, M. T. Fernández-Abedul, G. M. Whitesides, *Anal. Chem.* **2018**, *90*, 6240.

[50] A. W. Colburn, K. J. Levey, D. O'Hare, J. V. Macpherson, *Phys. Chem. Chem. Phys.* **2021**, *23*, 8100.

[51] R. B. Clark, M. W. Glasscott, M. D. Verber, J. C. DeMartino, A. Netchaev, J. D. Ray, E. W. Brown, E. Alberts, P. U. A. I. Fernando, L. C. Moores, J. E. Dick, *Anal. Chem.* **2021**, *93*, 7381.

[52] L. J. K. Weiß, E. Music, P. Rinklin, L. Straumann, L. Grob, D. Mayer, B. Wolfrum, *ACS Appl. Nano Mater.* **2021**, *4*, 8314.

[53] L. R. Grob, *Printed 3D Electrodes for Sensing and Bioelectronics*, Technische Universität, München **2021**.

[54] C. Dincer, R. Bruch, E. Costa-Rama, M. T. Fernández-Abedul, A. Merkoçi, A. Manz, G. A. Urban, F. Güder, *Adv. Mater.* **2019**, *31*, 1806739.

[55] R. Søndergaard, M. Hösel, D. Angmo, T. T. Larsen-Olsen, F. C. Krebs, *Mater. Today* **2012**, *15*, 36.

[56] L. Hakola, E. Jansson, R. Futsch, T. Happonen, V. Thenot, G. Depres, A. Rougier, M. Smolander, *Int J Adv Manuf Technol* **2021**, *117*, 2921.

[57] S. Laschi, I. Palchetti, G. Marrazza, M. Mascini, *J. Electroanal. Chem.* **2006**, *593*, 211.

[58] R. O. Kadara, N. Jenkinson, C. E. Banks, *Electrochem. Commun.* **2009**, *11*, 1377.

[59] R. O. Kadara, N. Jenkinson, C. E. Banks, *Sens. Actuators, B* **2009**, *142*, 342.

[60] F. Tan, J. P. Metters, C. E. Banks, *Sens. Actuators, B* **2013**, *181*, 454.

[61] M. Z. M. Nasir, M. Pumera, *Phys. Chem. Chem. Phys.* **2016**, *18*, 28183.

[62] J. C. Ball, J. K. Lumpp, S. Daunert, L. G. Bachas, *Electroanalysis* **2000**, *12*, 685.

[63] J. C. Ball, D. L. Scott, J. K. Lumpp, S. Daunert, J. Wang, L. G. Bachas, *Anal. Chem.* **2000**, *72*, 497.

[64] C. Cugnet, O. Zaouak, A. René, C. Pécheyran, M. Potin-Gautier, L. Authier, *Sens. Actuators, B* **2009**, *143*, 158.

[65] S. Liébana, L. J. Jones, G. A. Drago, R. W. Pittson, D. Liu, W. Perrie, J. P. Hart, *Sens. Actuators, B* **2016**, *231*, 384.

[66] J. P. Metters, R. O. Kadara, C. E. Banks, *Analyst* **2011**, *136*, 1067.

[67] H. Wan, Q. Sun, H. Li, F. Sun, N. Hu, P. Wang, *Sens. Actuators, B* **2015**, *209*, 336.

[68] S.-M. Park, S. Ho, S. Aruliah, M. F. Weber, C. A. Ward, R. D. Venter, S. Srinivasan, *J. Electrochem. Soc.* **1986**, *133*, 1641.

[69] J. Lee, D. W. M. Arrigan, D. S. Silvester, *Sens Biosensing Res* **2016**, *9*, 38.

[70] Y. Sugawara, T. Okayasu, A. P. Yadav, A. Nishikata, T. Tsuru, *J. Electrochem. Soc.* **2012**, *159*, F779.

[71] L. Jacobse, S. J. Raaijman, M. T. M. Koper, *Phys. Chem. Chem. Phys.* **2016**, *18*, 28451.

[72] S. Zips, L. Grob, P. Rinklin, K. Terkan, N. Y. Adly, L. J. K. Weiß, D. Mayer, B. Wolfrum, *ACS Appl. Mater. Interfaces* **2019**, *11*, 32778.

[73] L. M. Furtado, M. Bundschuh, C. D. Metcalfe, *Bull. Environ. Contam. Toxicol.* **2016**, *97*, 449.

[74] A. Syafiuddin, S. Salmiati, T. Hadibarata, A. B. H. Kueh, M. R. Salim, M. A. A. Zaini, *Sci. Rep.* **2018**, *8*, 986.

[75] M. Millour, J.-P. Gagné, C. Doiron, I. Marcotte, A. A. Arnold, É. Pelletier, *Colloids Surf. A* **2021**, *623*, 126767.

[76] Y.-G. Zhou, B. Haddou, N. V. Rees, R. G. Compton, *Phys. Chem. Chem. Phys.* **2012**, *14*, 14354.

[77] B. Haddou, N. V. Rees, R. G. Compton, *Phys. Chem. Chem. Phys.* **2012**, *14*, 13612.

[78] A. Yakushenko, E. Kätelhön, B. Wolfrum, *Anal. Chem.* **2013**, *85*, 5483.

© 2023 The Authors. Advanced Materials Technologies published by Wiley-VCH GmbH

B.3 Influence of Auditory Cues on the Neuronal Response to Naturalistic Visual Stimuli in a Virtual Reality Setting

G. Al Boustani*, **L.J.K. Weiß***, H. Li, S.M. Meyer, L. Hiendlmeier, P. Rinklin, B. Menze, W. Hemmert, B. Wolfrum

Abstract

Virtual reality environments offer great opportunities to study the performance of brain-computer interfaces (BCIs) in real-world contexts. As real-world stimuli are typically multimodal, their neuronal integration elicits complex response patterns. To investigate the effect of additional auditory cues on the processing of visual information, we used virtual reality to mimic safety-related events in an industrial environment while we concomitantly recorded electroencephalography (EEG) signals. We simulated a box traveling on a conveyor belt system where two types of stimuli – an exploding and a burning box – interrupt regular operation. The recordings from 16 subjects were divided into two subsets, a visual-only and an audio-visual experiment. In the visual-only experiment, the response patterns for both stimuli elicited a similar pattern – a visual evoked potential (VEP) followed by an event-related potential (ERP) over the occipital-parietal lobe. Moreover, we found the perceived severity of the event to be reflected in the signal amplitude. Interestingly, the additional auditory cues had a twofold effect on the previous findings: The P1 component was significantly suppressed in the case of the exploding box stimulus, whereas the N2c showed an enhancement for the burning box stimulus. This result highlights the impact of multisensory integration on the performance of realistic BCI applications. Indeed, we observed alterations in the offline classification accuracy for a detection task based on a mixed feature extraction (variance, power spectral density, and discrete wavelet transform) and a support vector machine classifier. In the case of the explosion, the accuracy slightly decreased by $-1.64\,\%$p. in an audio-visual experiment compared to the visual-only. Contrarily, the classification accuracy for the burning box increased by $5.58\,\%$p. when additional auditory cues were present. Hence, we conclude, that especially in challenging detection tasks, it is favorable to consider the potential of multisensory integration when BCIs are supposed to operate under (multimodal) real-world conditions.

Individual Contribution

conceptualization of the study, data analysis, data interpretation, composition and writing of the manuscript

Influence of Auditory Cues on the Neuronal Response to Naturalistic Visual Stimuli in a Virtual Reality Setting

George Al Boustani[1†], Lennart Jakob Konstantin Weiß[1†], Hongwei Li[2,3], Svea Marie Meyer[1], Lukas Hiendlmeier[1], Philipp Rinklin[1], Bjoern Menze[2,3], Werner Hemmert[4] and Bernhard Wolfrum[1*]

[1] Neuroelectronics – Munich Institute of Biomedical Engineering, Department of Electrical and Computer Engineering, Technical University of Munich, Munich, Germany, [2] Department of Quantitative Biomedicine, University of Zurich, Zurich, Switzerland, [3] Department of Informatics, Technical University of Munich, Munich, Germany, [4] Bio-Inspired Information Processing – Munich Institute of Biomedical Engineering, Department of Electrical and Computer Engineering, Technical University of Munich, Munich, Germany

Virtual reality environments offer great opportunities to study the performance of brain-computer interfaces (BCIs) in real-world contexts. As real-world stimuli are typically multimodal, their neuronal integration elicits complex response patterns. To investigate the effect of additional auditory cues on the processing of visual information, we used virtual reality to mimic safety-related events in an industrial environment while we concomitantly recorded electroencephalography (EEG) signals. We simulated a box traveling on a conveyor belt system where two types of stimuli – an exploding and a burning box – interrupt regular operation. The recordings from 16 subjects were divided into two subsets, a visual-only and an audio-visual experiment. In the visual-only experiment, the response patterns for both stimuli elicited a similar pattern – a visual evoked potential (VEP) followed by an event-related potential (ERP) over the occipital-parietal lobe. Moreover, we found the perceived severity of the event to be reflected in the signal amplitude. Interestingly, the additional auditory cues had a twofold effect on the previous findings: The P1 component was significantly suppressed in the case of the exploding box stimulus, whereas the N2c showed an enhancement for the burning box stimulus. This result highlights the impact of multisensory integration on the performance of realistic BCI applications. Indeed, we observed alterations in the offline classification accuracy for a detection task based on a mixed feature extraction (variance, power spectral density, and discrete wavelet transform) and a support vector machine classifier. In the case of the explosion, the accuracy slightly decreased by −1.64% p. in an audio-visual experiment compared to the visual-only. Contrarily, the classification accuracy for the burning box increased by 5.58% p. when additional auditory cues were present. Hence, we conclude, that especially in challenging detection tasks, it is favorable to consider the potential of multisensory integration when BCIs are supposed to operate under (multimodal) real-world conditions.

Keywords: brain computer interface, event-related potential (ERP), combinational audio-visual stimulus, visual evoked potential (VEP), virtual reality, support vector machine (SVM)

INTRODUCTION

Neuroscientists aim to understand the human brain by deciphering neuronal signals due to different tasks and stimuli (Adrian and Yamagiwa, 1935; Gross, 1999; Finger, 2001; Strotzer, 2009). Although there are other techniques, most research up to date is based on non-invasive electroencephalography (EEG) recordings, where the electrical activity across the scalp is monitored using distributed electrode arrays (Adrian and Yamagiwa, 1935; Homan et al., 1987; Cincotti et al., 2008; Nicolas-Alonso and Gomez-Gil, 2012). In the past, extensive research focused on unraveling basic neuronal patterns in response to different isolated conditions (Adrian and Yamagiwa, 1935; Penfield and Evans, 1935; Davis et al., 1939; Davis, 1939; Hill, 1958). Thus, an extensive collection of experimental paradigms that evoke specific responses – e.g., event-related potentials (ERPs), steady-state visually evoked potentials (SSVEPs), and motor imaginary related activity, among others – has been established (Ritter et al., 1979; Lines et al., 1984; Alho et al., 1994; Creel, 1995; Comerchero and Polich, 1999; Stige et al., 2007; Sur and Sinha, 2009). Nowadays, applied neuroscientists and engineers use these stimuli–response relations to design brain-computer interfaces (BCIs) that can automatically read out and analyze signals for a specific task. For instance, the P300-speller, a brain-controlled wheelchair, and a brain-controlled prosthetic arm are common BCI applications in the medical context (Rebsamen et al., 2010; Belitski et al., 2011; Nicolas-Alonso and Gomez-Gil, 2012; Abdulkader et al., 2015; Bright et al., 2016). Furthermore, recent technological improvements enable EEG recordings not only under "clean" laboratory conditions but also in natural environments via portable EEG devices. Hence, there is considerable interest in translating BCI applications into more complex real-world settings (Zander and Kothe, 2011). However, in such scenarios, the performance of BCIs and their discriminatory power are drastically affected by interfering signals and physiological artifacts (Fatourechi et al., 2007; Zander et al., 2010; Minguillon et al., 2017). Here, a combined read-out of multiple cues and/or measurement modalities – a so-called hybrid BCI (hBCI) – addresses this issue by providing an enlarged dataset for classification (Allison et al., 2010; Pfurtscheller et al., 2010; Leeb et al., 2011; Amiri et al., 2013; Yin et al., 2015; Hong and Khan, 2017). For instance, ERPs were combined with motor or mental tasks to design multiple-cue hBCIs (Hong and Khan, 2017). Additionally, parallel recordings from EEG and electrooculography (EOG) or functional near-infrared spectroscopy (fNIRS) were reported to improve performance (Amiri et al., 2013; Hong and Khan, 2017). Consequently, hBCIs offer great potential in various fields, e.g., in diagnostics, rehabilitation, machine control, entertainment, and safety (Allison et al., 2010; Blankertz et al., 2010; Brumberg et al., 2010; Nicolas-Alonso and Gomez-Gil, 2012; Hong and Khan, 2017). Another promising area of application is in the context of industry 4.0, where the aim is to operate factories most efficiently by fusing data streams and monitoring all relevant processes digitally (Douibi et al., 2021).

However, the affiliated classification tasks will be very challenging in most real-world cases depending on the paradigm and the interfering background signals. Although novel machine learning approaches help to find common patterns, they rely on massive amounts of input data. Here, virtual reality technology (VR) can help to gather consistent training data by simulating natural environments (Holper et al., 2010; Kober and Neuper, 2012; Lotte et al., 2012; Tauscher et al., 2019; Vourvopoulos et al., 2019; Marucci et al., 2021). It has been shown that VR enhances the feeling of presence and provides a real-world experience that keeps the subject more engaged (Kober and Neuper, 2012; Marucci et al., 2021). So far, most EEG-VR studies focused on 3D visual cues, disregarding the effect of simultaneous visual and acoustic stimuli in realistic situations. Previous studies on multimodal audio-visual cues, (Marucci et al., 2021) revealed that the simultaneous neuronal processing of vision and sound is strongly dependent on the exact experiment, determined by the nature, strength, and synchronicity of the stimulus.

This work aims to reveal the effect of additional auditory cues on visually-evoked ERPs within a complex naturalistic scene. To this end, we created an industrial VR environment and designed two visual stimuli that are different in the degree of event severity and stimulus strength. In our experiment, the subject's vision is a conveyor belt-based industrial warehouse, where packages are carried along a unilateral path during regular operation. However, as we target safety applications, in some instances, the regular operation is interrupted by either an exploding or an igniting/burning box.

Since both naturalistic stimuli are visually complex, we first investigate the neuronal response to such visual stimuli and study the effect of perceived severity. Then, we compare our previous findings (visual-only) to a set of experiments, where additional auditory cues match the subject's vision (audio-visual). Lastly, we apply three basic feature extraction methods – variance-, power-spectral-density- and discrete-wavelet-transform-based – to evaluate the effect of additional auditory cues on the classification performance by using a support vector machine (SVM) classifier. Throughout the study, we focused on hardware (24-channel portable EEG) and processing methods suitable for real-world applications.

MATERIALS AND METHODS

Participants

Eighteen subjects (7 females, 11 males) with a mean age of 26 ± 3.4 years participated in this study. Nine subjects were recorded in a visual-only experiment, and nine participated in an audio-visual experiment. To avoid interferences and adaptation, each participant took part only in one of the two experiments. All subjects had normal or corrected to normal vision, normal hearing, no history of neurological diseases, and no previous experience with BCIs or/and EEG recordings. Subjects that exhibited a skin-to-electrode impedance above 10 kOhm across the parietal-occiptal lobe electrodes were not considered for further analysis. The study was approved by the Ethics Commission of the Technical University of Munich.

Experimental Setup

The experiments were conducted in a quiet room with a mean sound pressure level (SPL) of 32.1 ± 2.1 dBA (measured with a precision sound analyzer Nor140, Norsonic-Tippkemper GmbH). All subjects were seated comfortably in an idle state in front of a keyboard, see **Figure 1A**. The visual scene and stimuli were designed with Blender v2.81 (The Blender Foundation) and Unity 2018 (Unity Software Inc.) and displayed via an HTC Cosmos virtual reality headset (90 FPS). In the case of an audio-visual experiment, the subjects were facing an active loudspeaker (8020C, GENELEC) placed at a distance of 1 m in front of the subject, as shown in **Figure 1A**.

All experiments were recorded using a portable 24-channel EEG system (SMARTING, mbraintrain, Serbia) with a sampling frequency of 250 Hz. The EEG was equipped with passive Ag/AgCl electrodes from EASYCAP (Herrsching, Germany), and a chloride-based electrogel was used (Abralyt HiCl, EASYCAP) to achieve impedance below 10 kΩ. The system featured a reference electrode (common mode sense, CMS) at FCz and a driven right leg electrode (DRL) at Fpz. All electrode locations follow the 10–20 system (see **Figure 1B**) and mainly covered occipital and parietal areas. The electrodes at Fp1 and Fp2 were considered to account for artifacts from eye movements.

Markers that indicate the onset of an (audio-) visual event were streamed from Unity using the lab-streaming layer for Unity asset (LSL4UNITY). Furthermore, all streams were recorded and synchronized using the SMARTING built-in streamer v3.3 for the lab-streaming layer. The data was further processed and analyzed via Matlab (Matlab and Statistics Toolbox Release 2020b, The MathWorks, Inc) combined with the toolboxes EEGlab (Delorme and Makeig, 2004) and fieldtrip (Oostenveld et al., 2011).

Experimental Procedure and Stimulus Design

The study was divided into a visual-only and an audio-visual experiment containing additional auditory cues that matched the visual scene. In both experiments, the stimuli were simulated at the same positions in space and time during the trial. Moreover, the sequence of trials was the same for all subjects.

Each experiment (see **Figure 2A**) consisted of 8 blocks with a break of variable duration in between. Each block contained 30

FIGURE 2 | Experimental design and visual scene. **(A)** The experiment was divided into eight blocks of 4 min-recordings. In between, a subject-controlled break was implemented. The total duration of an experiment ranged from 27 to 37 min. **(B)** Each block consisted of 30 trials, either stimulus or control, with a duration of 6 s per trial. Within that period, the box traveled along the conveyor belt, as shown in panel **(C)**. A short break in between trials (between disappearance at iv and entering of a new box at i) of 1.3–2 s was implemented as visual rest time. **(C)** Visual scenery of the experiment. First, the box appears at the right part in the subject's view (i) to subsequently move along the conveyor-belt pathway. At position (ii), the box is subject to either an explosion or ignition event (see **Supplementary Material**), each occurring with a probability of 15%. As the regular or ignited box travels, it reaches a junction with a manual separator, where the participant is supposed to discard the burning box and let all regular boxes pass. Exit points (iv) burning box and (v) regular box represent the spatio-temporal locations where the box disappears and the trial ends.

trials with a fixed duration of 6 s per trial, as shown in **Figure 2B**. In general, three different conditions for the box's pathway were implemented – either the box exploded (a), the box ignited and kept on burning (b), or the box traveled unperturbed along the pathway (c). Regardless of the trial condition, the box initially appeared in the center of the conveyor belt in the right part of the subject's field of view (see (i), **Figure 2C**). Then, the box kept traveling along the conveyor belt for 2 s until it reached point (ii) in **Figure 2C**, where the safety-relevant events occurred with a probability of 33% (equal probability for either a burning or an exploding box) following the oddball paradigm. This probability ultimately leads to 40 stimulus trials for an exploding and 40 stimulus trials for a burning box.

The participants were told to stay seated with a visual point of view, as shown in **Figure 2C**. When a box appeared at point (i), the participant was instructed to track the box along the conveyor

FIGURE 1 | Experimental setup **(A)** Experimental environment. The subject wears a VR lens and is sitting in front of the keyboard and the loudspeaker. **(B)** EEG electrode distribution over the scalp following the 10–20 System.

belt visually. Moreover, a short break in between trials (between disappearance at iv and entering of a new box at i) of 1.3–2 s was implemented as visual rest time.

The deviating stimuli were designed to mimic real-world scenarios, consisting of different visual characteristics (e.g., a light flash, change in size and shape). For instance, the explosion (see the video in the **Supplementary Material**) combined a sudden rapid change in light intensity, a swiftly propagating spherical light wave, and a disappearing flying box that occupies the entire field of view. Contrarily, in case of ignition (see the video in the **Supplementary Material**), the box emitted flames of fire from the center of the box. Compared to the explosion, the ignition only partially affected the scenery and started with a slower change in light intensity. While the box was traveling, the fire intensity increased until a steady state was reached.

For the burning and the control condition, the boxes were traveling past position (ii) in **Figure 2C** to reach the manual separator at location (iii) after 1 s. There, the subject had to manually discard the burning box toward the waste container at location (iv) by pressing the right arrow key on the keyboard. A regular box was directed to the exit (v) by pressing the up arrow key. Depending on the discarding speed, the trial duration was ∼6 s. Then, the subsequent trial started 1.3–1.5 s after the box had exited the scene at locations (iv) or (v).

In an audio-visual experiment, sounds matching the visual impressions were selected from an open-source library (freesound.org, see **Supplementary Material**). The sound source was attached to the traveling box in the virtual scene. However, reverberations usually stemming from walls were disabled in order to keep the acoustic scene simple. Before each experiment, the loudspeaker was adjusted to match a maximum sound level of 67 ± 0.5 dBA for the explosion and 55 ± 0.3 dBA for the burning box sound, respectively. Both sounds featured fast increasing and slowly decaying characteristics (see **Supplementary Material**). In the case of the burning box, the auditory cue was displayed at a constant level of 50 dBA SPL as long as the box traveled. Additionally, background noise was added to mimic a conveyor belt sound (42 ± 0.1 dBA).

Signal Processing

Eight out of the nine subjects per condition were considered while one of each group was excluded for hardware issues. The following signal processing pipeline is depicted in **Figure 3**. First, bad channels due to non-working electrodes were excluded. Thus, all non-working electrode were removed consistently for all participants. Then, notch filters with 50 and 100 Hz cutoff frequencies were applied to remove line noise and its second harmonic. Similar to other work, (Rozenkrants and Polich, 2008; Wang C. et al., 2012; Putze et al., 2014; Tidoni et al., 2014; Chang, 2018; Guo et al., 2019) the signal was subsequently bandpass-filtered using a low-pass FIR filter with a cutoff frequency of 40 Hz and a high-pass FIR filter with a cutoff frequency of 0.5 Hz. Consequently, all frequencies outside the narrow frequency band, such as slow drifts and high-frequency artifacts, were attenuated (Nicolas-Alonso and Gomez-Gil, 2012; de Cheveigné and Nelken, 2019). A re-referencing step was omitted due to the low number of channels and their
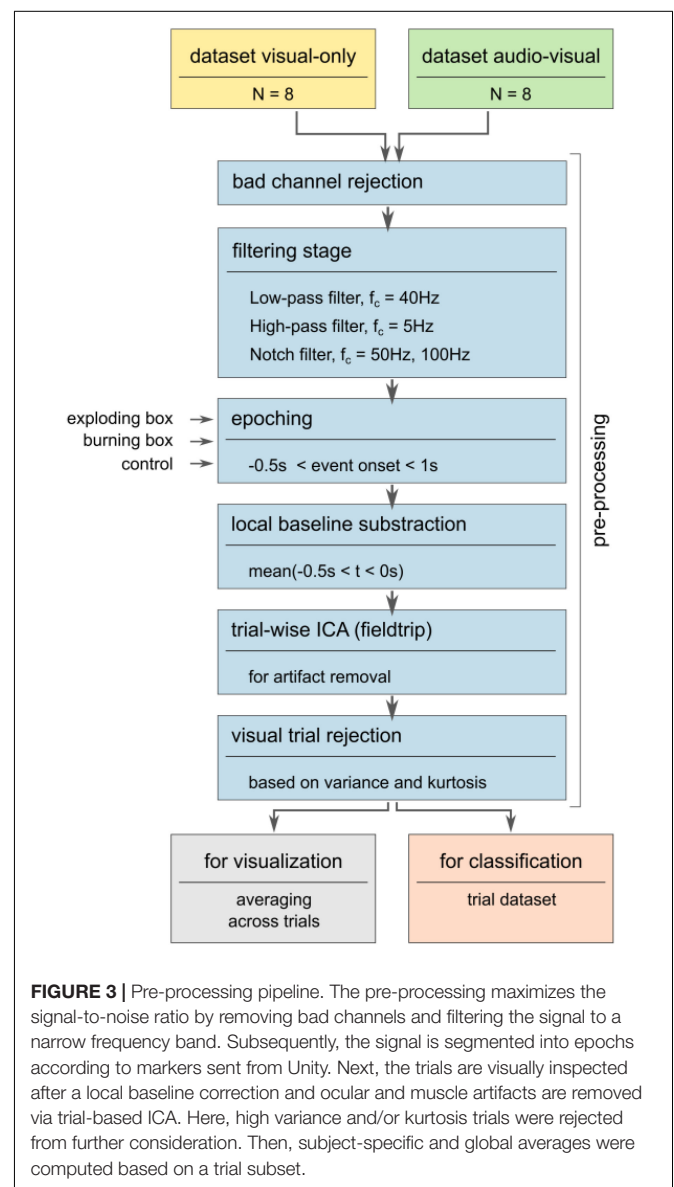
FIGURE 3 | Pre-processing pipeline. The pre-processing maximizes the signal-to-noise ratio by removing bad channels and filtering the signal to a narrow frequency band. Subsequently, the signal is segmented into epochs according to markers sent from Unity. Next, the trials are visually inspected after a local baseline correction and ocular and muscle artifacts are removed via trial-based ICA. Here, high variance and/or kurtosis trials were rejected from further consideration. Then, subject-specific and global averages were computed based on a trial subset.

heterogeneous distribution across the scalp (see **Supplementary Figure 1**). After the filter stage, the recordings were segmented into epochs according to the respective markers sent from Unity at the onset of the stimulus (position (ii) in **Figures 2B,C**). This segmentation resulted in a structural dataset containing all epochs ranging from $t_{(ii)} - 0.5s \leq t \leq t_{(ii)} + 1s$ for all three conditions, explosion (a), burning box (b), and control (c). A local baseline subtraction based on the mean signal before the onset accounted for offset differences. Then, an independent component analysis (ICA) was applied using the logistic infomax approach provided by the fieldtrip toolbox to decompose the signal (Donchin, 1966; Oostenveld et al., 2011; Chang, 2018). Subsequently, the independent components that stem from artifacts such as eye blinking and eye movement, electrode-pops, and muscle movements were visually rejected (Xue et al., 2006; Zhang et al., 2017). Here, the rejected independent

component frequency spectrum and the mixing topographical matrix was inspected to decide which component was identified as an artifact. Lastly, a visual trial rejection removed trials that significantly deviated from the ensemble in terms of variance and/or kurtosis (Oostenveld et al., 2011). In general, the signal processing pipeline was established to maximize the signal-to-noise ratio and, at the same time, to avoid large signal distortions by amplification or attenuation.
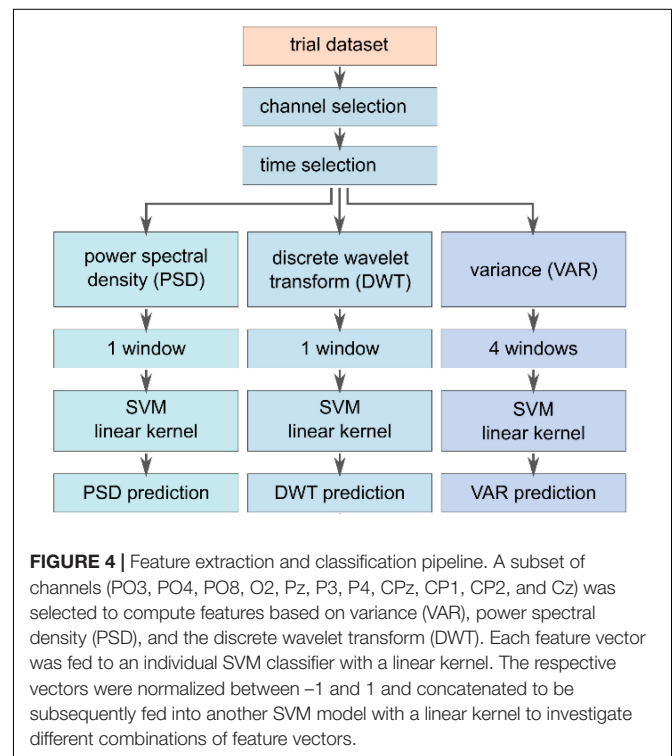
In order to be consistent, subject-specific averages were computed based on 38 out of 40 stimulus trials per subject. Similarly, 38 control trials per subject were randomly selected out of 200 trials. Finally, the global responses shown in the results section were calculated as mean and standard deviation based on the subject-specific characteristics. Hence, the global average indicates the mean neuronal response of the population, whereas the standard deviation visualizes the variability between subjects. Finally, the average control condition was computed based on a random selection of 304 out of 1500 possible trials.

Finally, a statistical analysis on the difference between visual-only vs. audio-visual experiments was performed using a Welch's t-test with a 5% significance level. The evaluation is based on the maximum (P1, P3b) and minimum (N2c) for each subject's average (channel O2) and there latencies. The t-test assumes that both ensembles are sampled from a normally distributed dataset with unequal variance.

Feature Extraction and Offline Classification

In order to assess the influence of additional auditory cues on the classification performance, different feature extraction methods, see **Figure 4**, – based on the variance (VAR), the power at a specific frequency band (PSD), and specific time-frequency characteristics acquired by a discrete wavelet transform (DWT) – are compared using a SVM classifier. The task of the SVM classifier was to detect the safety-relevant event – explosion (a) or ignition (b) – compared to the control condition (c), where the box was regularly traveling the pathway.

The feature extraction methods were evaluated based on the same dataset that was used for averaging. The feature vectors were computed based on channels covering the parietal and occipital lobe, namely PO3, PO4, PO8, O2, Pz, P3, P4, CPz, CP1, CP2, and Cz. Unfortunately, the channels O1 and PO7 had to be excluded due to inconsistency across subjects. The three methods were applied to the previously selected epochs for averaging with yet a smaller timeframe ranging between $t_{(ii)} \leq t \leq t_{(ii)} + 660$ ms. Each feature extraction method resulted in a dataset of feature vectors, as described in the following. The VAR method computes the variance in four different windows that have been chosen to capture the specific characteristics of the response signal, leading to a 44-element (4 values per channel, 11 channels) feature vector per trial. The first window evaluates the entire epoch from 0 ms $\leq t \leq 660$ ms, whereas the other windows split the entire interval into three successive segments of 220 ms without any overlap. Thereby, the VAR method is supposed to extract information of the entire signal and the variance of early and late potential fluctuations. The PSD feature vector of the trial

FIGURE 4 | Feature extraction and classification pipeline. A subset of channels (PO3, PO4, PO8, O2, Pz, P3, P4, CPz, CP1, CP2, and Cz) was selected to compute features based on variance (VAR), power spectral density (PSD), and the discrete wavelet transform (DWT). Each feature vector was fed to an individual SVM classifier with a linear kernel. The respective vectors were normalized between –1 and 1 and concatenated to be subsequently fed into another SVM model with a linear kernel to investigate different combinations of feature vectors.

was computed using the Welch-method from Matlab. Since we expect stimulus-related frequency information between 1 and 30 Hz,[38] all other frequencies outside this window were removed, leading to a vector of length 275 (25 frequency components per channel). The third feature extraction approach, DWT relied on a Matlab discrete wavelet transform decomposition method (Bostanov, 2004; Amin et al., 2015; Cheong et al., 2015; Yahya et al., 2019). In particular, a 3-level decomposition (mother wavelet db8, window size 660 ms) was used to separate the signal in an approximate coefficient vector that extracts low-frequency information and a detail coefficient vector including the high-frequency components. The DWT vector had a length of 341 (31 approximate features per trial). The considered features were normalized and concatenated into a single vector to investigate different feature vector combinations amongst the three approaches. Here, e.g., in the case of the combined VAR-PSD-DWT feature, the vector had a length of 660 elements and ranges between –1 and 1. Subsequently, the feature vectors were individually fed to a support vector machine classifier with a linear kernel to investigate the different extraction methods (Oskoei et al., 2009; Putze et al., 2014; Li et al., 2018). Here, k-fold cross-validation ($k = 10$, 80% training data, 20% testing data) was applied to subject-independent input data stemming from a random selection across the entire dataset. To calculate subject-specific results, an individual SVM classifier for each subject was trained on the combined VAR-PSD-DWT data. Here, similar trial selection and k-fold cross-validation approaches were used as mentioned earlier.

Finally, a statistical analysis on the difference between visual-only vs. audio-visual k-folds classification results was performed

using a Welch's *t*-test with a 5% significance level. The evaluation is based on the accuracy performance for all folds. The *t*-test assumes that both ensembles are sampled from a normally distributed dataset with unequal variance.

RESULTS

Combined Visual Stimuli

The explosion and the ignition event are implemented as a combination of visual effects, see videos in **Supplementary Material**. Thus, we first want to study the neuronal response to such a combinational visual input. For instance, the explosion was mimicked by an upwards flying box and a bright white spherical wave starting at the box and rapidly propagating through space until the entire field of view is filled. Then, the white flash faded out, the box fell downwards until it disappeared at the floor, and the scene stayed blurry until all smoke had vanished. In total, the entire explosion event lasted ∼2 s. Hence, we expect the explosion event to be a spatio-temporal mix of different effects leading to an early visually evoked potential (VEP) induced by the flash at the onset and an event-related potential (ERP) in response to the change of the visual scenery. The global responses to the visual-only exploding and burning box are depicted in **Figures 5A,B**, respectively.

As visualized in **Figure 5A** for channel O2, we found deviations at different time instances in the global average response for an explosion compared to the control condition. First, there was a positive rise in amplitude (P1) at O2 in **Figure 5A**, which started at stimulus onset and peaked with 11.5 ± 9.9 a.u. at ∼125 ms. Then, a negative dip followed, beginning at ∼200 ms and peaking at ∼310 ms to –15 ± 6.9 a.u. Subsequently, a smaller positive rise was observed until a plateau of 4.3 ± 2.8 a.u was reached at ∼430 ms, which decayed slowly afterward. This finding was robust across trials, as the trial colormaps for a single subject show in **Supplementary Figure 2**. The high standard deviations in the global response, especially for the first peak P1, were caused by the subjects' large variability in terms of latency and amplitude, as depicted in **Supplementary Figure 3**. The first rise in amplitude for O2 was also present at the entire parietal-occipital lobe, but with higher amplitude over the primary visual cortex, see topoplots in **Figure 5A** and the average response for all channels of a single subject in **Supplementary Figure 4**.

In contrast to the explosion, the burning box (see videos in **Supplementary Material**) is designed as a progressive rather than a sudden event. Furthermore, it is modeled as less severe since the flames gradually evolve originating at the traveling box. The burning box stimulus was terminated when the box disappeared in the waste container after discarding. The global response to a burning box is visualized in **Figure 5B**. Here, we find a pattern similar to the explosion – a small P1 between 50 and 100 ms, then a N2c at ∼280 ms, followed by a P3b at ∼520 ms.

Additional Acoustic Stimuli

As real-world events naturally lead to a combination of visual and auditory cues, we further investigated the influence of additional

sounds that match the visual experience in the experiment. To this end, background noise (42 dBA SPL) related to the running conveyor belt was implemented. Furthermore, the explosion and the burning box events were synchronized with suitable audio signals (sounds see **Supplementary Material**). Here, we complied with the hierarchical approach and implemented different loudness levels for the explosion and the burning box event. The explosion audio signal had a peak level of ∼65 dBA and faded slowly toward the conveyor belt noise floor, correlating with the visual impression. The burning box audio stimulus consisted of a transient signal (lighting a match) that reached a steady state of 50 dBA (fire) until the subject discarded the box. Apart from the additional sound, the experiment was the same as previously described. The global responses to the audio-visual exploding and burning box are depicted in **Figures 5C,D**, respectively.

In case of an explosion, five characteristic fluctuations at O2 are visible: a positive peak with ∼4 a.u. between 70 and 140 ms (P1), two small-amplitude peaks around 220 ms, followed by a prominent negative peak with −13.0 ± 7.1 a.u. at 320 ms (N2c), and a subsequent positive peak with 7.4 ± 5.2 a.u. at ∼530 ms (P3b). The global response to a burning box with additional auditory cues is shown in **Figure 5D**. Here, three peaks, P1 with 2.6 ± 2.1 a.u. at ∼80 ms, N2c with –4.4 ± 3.9 a.u. at ∼330 ms and P3b with 4.9 ± 2.0 a.u. at 550 ms are visible, similar to the fluctuations in **Figure 5B**.

Offline Classification

Since experiments based on virtual reality nowadays offer a great tool to study the applicability of BCIs, we lastly investigate the detectability of events based on visual-only and audio-visual input. This is particularly interesting, as real-world training data is not always easily accessible – especially if the event is rare and/or severe. Moreover, the implementation of multiple modalities in VR settings can be challenging as well. Thus, we aim to evaluate if the classifier that uses bimodal training data is outperforming the classifier based on unimodal input only. To this end, we tested different feature extraction methods – variance-based (VAR), power-spectral density-based (PSD), and discrete-wavelet-transform based – and performed an offline classification using support vector machines on a subject-independent dataset. Here, all subjects' data was merged to randomly select training and cross-validation trials afterward. The VAR method calculates the variance of four different windows containing the response in the P1-, the N2c- and the P3b-part, and the entire epoch as shown in **Figure 5**. The PSD method analyzes the power within the frequency band of 1–30 Hz. In the DWT method, we used a Daubechies mother wavelet to decompose the signal. Additionally, all three methods were combined by concatenation into a single feature vector (DVP) and assessed. The performance of the methods was evaluated with three indicators: (i) the average accuracy across folds indicating the overall model performance, (ii) the average specificity indicating the model performance toward detecting the control condition, and (iii) the average sensitivity that represents the model performance toward detecting the stimulus. The offline detection results are shown in **Table 1**.
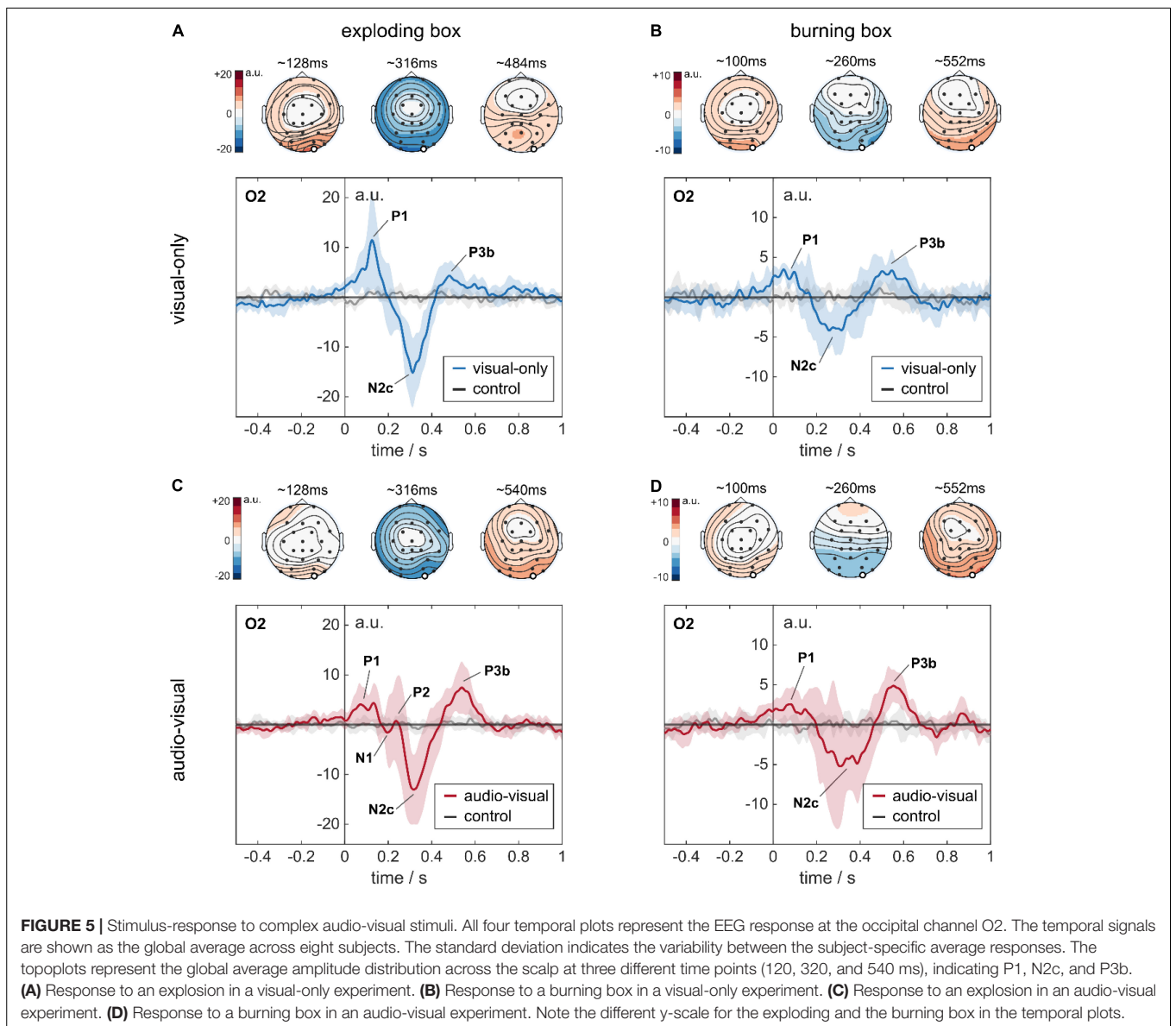
FIGURE 5 | Stimulus-response to complex audio-visual stimuli. All four temporal plots represent the EEG response at the occipital channel O2. The temporal signals are shown as the global average across eight subjects. The standard deviation indicates the variability between the subject-specific average responses. The topoplots represent the global average amplitude distribution across the scalp at three different time points (120, 320, and 540 ms), indicating P1, N2c, and P3b. **(A)** Response to an explosion in a visual-only experiment. **(B)** Response to a burning box in a visual-only experiment. **(C)** Response to an explosion in an audio-visual experiment. **(D)** Response to a burning box in an audio-visual experiment. Note the different y-scale for the exploding and the burning box in the temporal plots.

TABLE 1 | Classification results for the subject-independent dataset.

		Exploding box		Burning box	
		Visual-only	Audio-visual	Visual-only	Audio-visual
Variance method (VAR)	accuracy/%	86.18	87.09	74.01	76.89
	specificity/%	86.5	89.08	79.85	79.27
	sensitivity/%	86.09	85.40	68.39	76.3
Power-spectral density method (PSD)	accuracy/%	82.16	85.58	67.56	76.42
	specificity/%	83.90	87.58	72.6	80.47
	sensitivity/%	80.83	83.02	61.91	72.6
Discrete wavelet transform method (DWT)	accuracy/%	91.16	90.82	78.45	78.73
	specificity/%	90.07	92.36	78.65	79.55
	sensitivity/%	91.70	89.7	79.46	78.66
Feature Fusion Method (DVP)	accuracy/%	**94.56**	92.92	80.78	**86.36**
	specificity/%	96.10	94.25	84.22	89.47
	sensitivity/%	92.84	91.71	78.32	84.25

A support vector machine with a linear kernel was used to detect either the exploding or the burning box with respect to the control condition. The results are provided as mean across 10 folds. The Bold values represent the highest achieved accuracy.

DISCUSSION

In the following, we will first discuss the neuronal activity in response to the combinational visual stimuli of an explosion and burning box (see Section "Combined Visual Stimuli"). Afterward, the changes in neuronal activity for experiments with additional auditory cues are presented in Section "Additional Acoustic Stimuli". Focusing on an industrial BCI application, we lastly compare in Section "Offline Classification" the detectability of an explosion or ignition event based on different feature extraction methods using a support vector machine classifier.

Combined Visual Stimuli

For the explosion box stimulus, we assign this first response P1 to a VEP stemming from a sudden change in light intensity (Connolly and Gruzelier, 1982; Lines et al., 1984; Creel, 1995; Kazai and Yagi, 2003; Sharma et al., 2015; Guo et al., 2019). Further, we associate the negative peak at ~310 ms with the N2c component of an ERP-response, as it is distributed across the occipital/posterior region (see **Supplementary Figure 4A**). The N2c component is generally related to visual attention and the processing of stimulus characteristics, which aligns with our expectations of an early primary reaction (P1) and a later activity that reflects the interpretation of the visual scene (N2c and further peaks) (Ritter et al., 1979, 1982; Folstein and Petten, 2008). Lastly, we identify the positive response at ~430 ms to be a late P300 signal being evoked by the oddball paradigm. Here, the processing in the visual cortex leads to a delayed response, called P3b, which is usually observed after an N2c component (Comerchero and Polich, 1999; Stige et al., 2007). Consistent with other published work, (Katayama and Polich, 1998; Comerchero and Polich, 1999; Stige et al., 2007; Folstein and Petten, 2008) we observed the P3b component to be higher in the posterior region than in the anterior region of the brain, see topoplots in **Figure 5A** and **Supplementary Figure 4A** as well.

In the burning box stimulus, the absolute amplitudes are notably reduced to a range of approx. ± 5 a.u., reflecting the lower degree of severity and/or lower attention accumulation compared to the explosion. Interestingly, the P1 amplitude for the burning box was in the same range as its N2c-P3b complex, which is in stark contrast to the explosion stimulus, where the P1 was significantly higher than the P3b. This difference might be firstly explained by the gradual increase of fire, secondly by its bounded extent, and thirdly by the red-orange color scheme of the fire animation compared to a full-screen white flash for the explosion.

The high standard deviations for both global responses can be explained by significant differences in amplitude and – even more critical – latencies across individual subjects (see **Supplementary Figures 3A,B**). Here, the response variation might also be affected by adaptation and/or the subjects' engagement and focus throughout the experiment. In summary, we observed a similar neuronal activity – a combination of an early visually evoked potential (P1) and a delayed event-related potential (N2c-P3b complex) – in response to our virtual explosion and burning stimuli. Here, the degree of severity is reflected in the signal amplitudes, leading to a generally reduced response for the burning box compared to the explosion. Both events, however, showed clearly differentiable global average responses compared to the control condition where the box simply travels along the pathway.

Additional Acoustic Stimuli

In case of an explosion, we find the characteristics of N2c and P3b to be stable, yet their latencies and amplitudes differ (see **Supplementary Figure 5A**). Surprisingly, the VEP P1 is reduced by a factor of ~3, whereas the N2c component is similar in amplitude. The P3b component is delayed by ~70 ms and increased by a factor of ~2. Consequently, the additional sound had two effects, the primary visual cue is drastically suppressed, and the ERP components are robust (N2c) or enhanced and delayed (P3b) compared to the visual-only findings. Whereas the suppression of the VEP response P1 are suprising, the ERP enhancement seems plausible, as the additional sound provided congruent supplementary information to the subjects' visual impression. Furthermore, the enhanced N2c signals could also be attributed to increased attention during the experiment since participants (that took both experiments in an initial pilot study) reported the audio-visual experiment to be more engaging in the burning box stimuli. Lastly, two new fluctuations around 220 ms appeared in the global averages, see **Figure 5C**. Therefore, in line with our hypothesis, the additional small-amplitude peaks could be interpreted as the N1 and P2 components of a strongly enhanced ERP and were not caused by the additional auditory cues. Generally, the N1 and P2 fluctuations of an ERP can be assigned to sensation-seeking behavior, thus reflecting a stronger focus of the participants (Sur and Sinha, 2009). A closer look at the individual responses (**Supplementary Figures 5A, 6A**) reveals the presence of N1 and P2 in 6 out of 8 subjects that participated in an audio-visual experiment. Surprisingly, the additional P2 is in most cases in the same amplitude range as the visually evoked P1 (see **Supplementary Figure 6A**), which is not visible in the global averages due to latency differences across subjects. However, we found N1-P2 components also in the visual-only experiment for some subjects (see **Supplementary Figure 3A**), yet with smaller amplitude compared to an audio-visual experiment. Thus, we conclude that the additional peaks most probably stem from the ERP, which might be altered in amplitude by attention, focus, severity, and congruent input.

The global response to a burning box with additional auditory cues compared to the visual-only experiment, we find the P1 component also to be suppressed by a factor of ~1.3. However, the N2c and the P3b components are again enhanced by a factor of ~1.25 and 1.5, respectively. Additionally, we also observed a delayed ERP response. This result is in line with the previous findings for the explosion. Moreover, large standard deviations around 300 ms indicate the presence of additional small-amplitude peaks as well, which is supported by inspecting the individual responses in **Supplementary Figures 5B, 6B**.

Statistical analysis based on Welch's t-tests revealed a significant amplitude difference in the mean responses for the P1 ($p = 0.0393$) in the case of the explosion stimulus, and further for the N2c ($p = 0.0412$) in case of a burning box at channel O2. However, the P3b component for both conditions did not yield statistical significance as we calculated $p = 0.0764$, $p = 0.0704$ for the exploding box and burning box, respectively. Moreover, all other differences in amplitude and latencies did

FIGURE 6 | Differences in classification performance parameters **(A)** accuracy, **(B)** specificity, and **(C)** sensitivity for an audio-visual compared to a visual-only experiment.
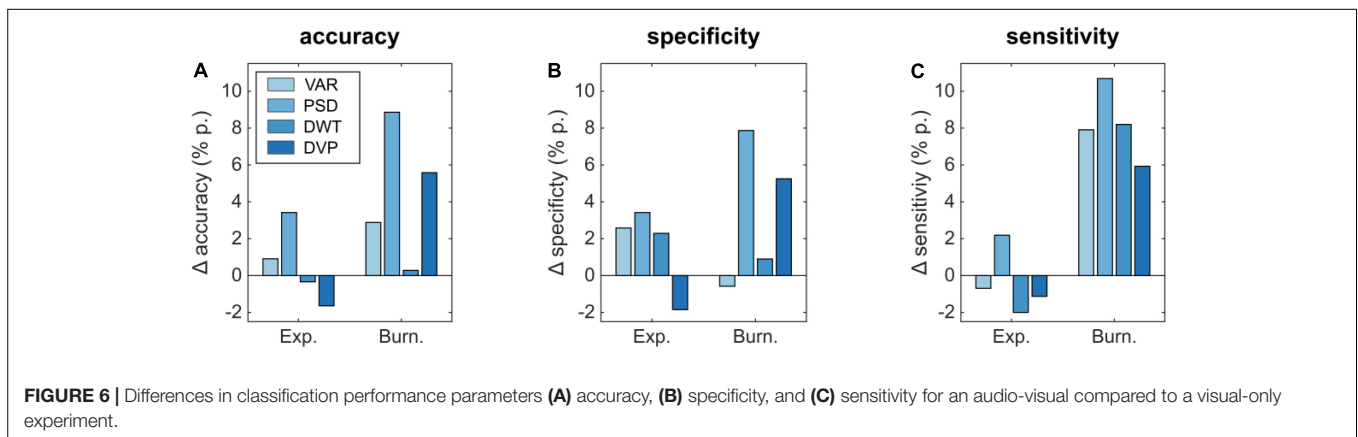
not provide statistical significance, which can be also explained by the small dataset and large deviations across subjects (see **Supplementary Table 1**).

In summary, we noticed two different effects on the neuronal responses if additional matching auditory cues were present (see **Supplementary Figure 7**). Firstly, different levels of severity – explosion versus burning box – were again visible as differences in amplitude. Consistently for both stimuli we found the VEP or primary reaction in the visual cortex to be diminished, whereas the ERP components N2c and P3b were enhanced by the sound. Moreover, two other fluctuations, N1-P2, occurred around 220 ms, which we assign to ERP components prior to the large-amplitude peaks N2c and P3b.

Based on our observations, we conclude that additional auditory cues lead to a suppression of the VEP by inhibitory pathways. This was surprising, as we did not expect the sound to induce changes in the early processing stages of primary visual information. However, recent studies shed light on the complex interplay of the neuronal processing of multisensory input (Driver and Spence, 2000; Calvert, 2004; Marchant and Driver, 2013). Indeed, it has been demonstrated that there is "crosstalk" between modality-specific pathways in the associative cortex (Calvert, 2001; Hidaka and Ide, 2015) as well as the primary sensory cortices (Talsma et al., 2007; Senkowski et al., 2011) leading to an early audio-visual integration (Driver and Noesselt, 2008; Wang Y. et al., 2008; Iurilli et al., 2012; Ide and Hidaka, 2013; Hidaka and Ide, 2015). In line with our data, other groups demonstrated e.g., a decreased fNIRS response in the visual cortex (Wiggins and Hartley, 2015) as well as a suppressed visual perception (Hidaka and Ide, 2015) when sound is presented in a spatially and temporally consistent manner. However, we did not only observe the suppression of the primary reaction in the visual cortex (VEP) but also an enhancement and a delay of the following ERP response for additional sound. This could be caused due to differences in the population for both experimental conditions. However, we experienced the phenomenon on single subjects in pilot studies to be robust. In fact, various effects – both, facilitatory and inhibitory – have been reported for multimodal audio-visual input (Stein et al., 1996; Shams et al., 2005; Hidaka et al., 2009; Meredith et al., 2009; Romei et al., 2009; Gleiss and Kayser, 2013).

For instance, it was shown that a multimodal (e.g., visual, acoustic, and tactile) compared to unimodal (visual) stimulation can lead to a drastic enhancement of the P300 signal. (Wang W. Y. et al., 2012; Marucci et al., 2021). Interestingly, an additional delay of the ERP, as visible in our data, was not explored. One could attribute the ERP delay to originate from weak inhibition effects that eventually lead to longer responses (Wang W. Y. et al., 2012). Yet, we found the ERP responses to be more prominent and robust in the audio-visual experiment. Thus, we conclude that a multimodal stimulus leads to an increased certainty about visual perception. Especially in the case of the burning box, where the unimodal visual perception is less clear, the additional (informative) sound supports the understanding and discrimination of the scene (Stein et al., 1996; Talsma et al., 2007; Senkowski et al., 2011; Gleiss and Kayser, 2013).

Offline Classification

Last, we investigated the effect of multimodal stimuli on their classifiability by using offline classification. In this way, we are able to test different extraction methods in a time effifient manner and apply our findings to online classification schemes.

As expected, detecting an explosion is less challenging than detecting a burning box; see absolute values of all criteria in **Table 1**, both in a visual-only and in an audio-visual experiment. Here, we observe significant amplitude differences between the explosion and the burning box responses. The best single-method detection performance for both a visual-only and audio-visual experiment was achieved with the DWT approach (e.g., 91.16 % for an explosion and 78.45 % for the burning box in a visual-only experiment). In contrast, PSD and VAR-based detection performances were substantially lower. This can also be partially explained by correlations between the mother wavelet of the DWT and the neuronal response (Samar et al., 1999). Furthermore, the concatenation of all three feature vectors (DVP) led to an improvement in both conditions (visual-only and audio-visual) for both stimuli compared to DWT. Again, this was partially expected since a larger feature vector can provide more information to the classifier. In the subject specific classification, we achieved an average detection accuracy of 96.06 and 79.96 % for the explosion and burning box, respectively.

The effect of additional auditory cues on the detectability based on different features is shown in **Figure 6**. Here, the accuracy for the explosion (**Figure 6A**) improves by 0.91 and 3.42% p. for VAR and PSD, whereas the DWT and DVP-based performance decreased by –0.34 and –1.64% p., respectively. In case of the burning box, additional auditory cues lead in all cases to an improvement, most prominent for the PSD (8.86% p.) and the combined DVP (5.58% p.). Similarly, the specificity and sensitivity for the burning box are also increased in all but one method, if additional auditory cues are present. In case of the explosion, there is not always an improvement. Mainly if the extraction method relies on the strong P1-contribution in the visual-only experiment (VAR, DWT, and DVP), the performance is slightly decreased in case of additional sound. Similar to ensemble values, we observed a slightly decreased subject-specific classification accuracy (based on DVP) of 94.53% for the audio-visual explosion compared to the visual-only. Again, the burning box led to opposite results. Here, the accuracy increased to 85.18%.

Statistical analysis based on Welch's t-tests revealed a significant classification accuracy difference in case of the burning box stimulus for the VAR, PSD, and DVP feature extraction methods ($p = 0.0044$, $p < 0.001$, $p = 0.0050$). Moreover, the exploding box stimulus classification accuracy did not yield statistical significance, which can be explained by the small increase or decrease in performance and the overlapping standard deviation between folds.

The results for the burning box highlight that multimodal input can lead to more robust and enhanced ERP patterns that guarantee an enhanced classification performance. In fact, future real-world detection tasks will resemble most likely the burning box-type of situation, where isolated sensory inputs are less severe, hence, attention-grabbing. Here, the consistent multisensory experience leads to a stronger attentional shift and an increased certainty about the (complex) situation. Consequently, we expect that BCIs trained on multimodal input will show an enhanced classification performance in real-world settings compared to BCIs that consider only unimodal input.

CONCLUSION

Within this work, we studied neuronal responses to two complex stimuli – an exploding box and a burning box – with different perceived severities. The response consisted of a strong early VEP component and a smaller delayed ERP complex in the explosion. The burning box evoked a similar pattern consisting of a minor VEP component and the following ERP complex, but significantly smaller amplitudes than the explosion. Thus, the effect of different severity levels was reflected in the signal amplitudes. Surprisingly, the effect of additional auditory input was not consistent for all response components. Most prominently, for the exploding box, the initial VEP was significantly suppressed in the audio-visual experiment. Moreover, we observed additional small-amplitude peaks around 220 ms after stimulus onset, which we attribute to the early small-scale ERP fluctuations N1 and P2. Hence, we conclude that

congruent multimodal sensory input leads to greater attention and/or a more confident evaluation of the input data, resulting in a robust ERP signal.

In summary, experiments in a virtual environment offer great potential to test the potential of BCIs in different applications. However, stimuli that mimic real-world situations elicit complex neuronal patterns that highly depend on the exact stimulus and environment. As shown in this work, step-by-step VR-EEG studies provide means to bridge the gap from experiments under "clean" lab conditions toward specifically tailored BCI systems. Here, we demonstrated that inhibition and facilitation effects alter the signal for a combined audio-visual input. Based on a SVM classifier, we showed an improvement in the detectability of a bimodal audio-visual stimulus compared to a unimodal visual input. As real-world experiences are multimodal by nature, the early integration of multisensory input has a significant impact on the design of future VR BCI studies.

DATA AVAILABILITY STATEMENT

The raw data supporting the conclusions of this article will be made available by the authors, without undue reservation.

ETHICS STATEMENT

The studies involving human participants were reviewed and approved by Ethics Commission of the Technical University of Munich. The patients/participants provided their written informed consent to participate in this study.

AUTHOR CONTRIBUTIONS

FUNDING

ACKNOWLEDGMENTS

SUPPLEMENTARY MATERIAL

The Supplementary Material for this article can be found online at: https://www.frontiersin.org/articles/10.3389/fnhum.2022.809293/full#supplementary-material

REFERENCES

Abdulkader, S. N., Atia, A., and Mostafa, M.-S. M. (2015). Brain computer interfacing: applications and challenges. *Egypt. Inform. J.* 16, 213–230. doi: 10.1016/j.eij.2015.06.002

Adrian, E. D., and Yamagiwa, K. (1935). The origin of the berger rhythm. *Brain* 58, 323–351. doi: 10.1093/brain/58.3.323

Alho, K., Woods, D. L., and Algazi, A. (1994). Processing of auditory stimuli during auditory and visual attention as revealed by event-related potentials. *Psychophysiology* 31, 469–479. doi: 10.1111/j.1469-8986.1994.tb01050.x

Allison, B. Z., Brunner, C., Kaiser, V., Müller-Putz, G. R., Neuper, C., and Pfurtscheller, G. (2010). Toward a hybrid brain–computer interface based on imagined movement and visual attention. *J. Neural Eng.* 7:026007. doi: 10.1088/1741-2560/7/2/026007

Amin, H. U., Malik, A. S., Ahmad, R. F., Badruddin, N., Kamel, N., Hussain, M., et al. (2015). Feature extraction and classification for EEG signals using wavelet transform and machine learning techniques. *Australas. Phys. Eng. Sci. Med.* 38, 139–149. doi: 10.1007/s13246-015-0333-x

Amiri, S., Fazel-Rezai, R., and Asadpour, V. (2013). A review of hybrid brain-computer interface systems. *Adv. Hum.-Comp. Int.* 2013:187024. doi: 10.1155/2013/187024

Belitski, A., Farquhar, J., and Desain, P. (2011). P300 audio-visual speller. *J. Neural Eng.* 8, 025022. doi: 10.1088/1741-2560/8/2/025022

Blankertz, B., Tangermann, M., Vidaurre, C., Fazli, S., Sannelli, C., Haufe, S., et al. (2010). The Berlin Brain–Computer Interface: non-Medical Uses of BCI Technology. *Front. Neurosci.* 4:198. doi: 10.3389/fnins.2010.00198

Bostanov, V. (2004). BCI competition 2003-data sets Ib and IIb: feature extraction from event-related brain potentials with the continuous wavelet transform and the t-value scalogram. *IEEE Transac. Biomed. Eng.* 51, 1057–1061. doi: 10.1109/TBME.2004.826702

Bright, D., Nair, A., Salvekar, D., and Bhisikar, S. (2016). "EEG-based brain controlled prosthetic arm," in *2016 Conference on Advances in Signal Processing (CASP)*, (Piscataway: IEEE), 479–483. doi: 10.1109/CASP.2016.7746219

Brumberg, J., Nieto-Castanon, A., Kennedy, P., and Guenther, F. (2010). Brain-Computer Interfaces for Speech Communication. *Speech Commun.* 52, 367–379. doi: 10.1016/j.specom.2010.01.001

Calvert, G., Spence, C., and Stein, B. E. (2004). *The Handbook of Multisensory Processes*. Cambridge, MA: MIT Press.

Calvert, G. A. (2001). Crossmodal Processing in the Human Brain: insights from Functional Neuroimaging Studies. *Cereb. Cortex* 11, 1110–1123. doi: 10.1093/cercor/11.12.1110

Chang, H. l (2018). *Computational EEG Analysis: Methods and Applications. Biological and Medical Physics, Biomedical Engineering*. Singapore: Springer, doi: 10.1007/978-981-13-0908-3

Cheong, L. C., Sudirman, R., and Hussin, S. s (2015). Feature extraction of EEG signal using wavelet transform for autism classification. *ARPN J. Eng. Appl. Sci.* 10, 8533–8540.

Cincotti, F., Mattia, D., Aloise, F., Bufalari, S., Schalk, G., Oriolo, G., et al. (2008). Non-invasive brain–computer interface system: towards its application as assistive technology. *Brain Res. Bull.* 75, 796–803. doi: 10.1016/j.brainresbull.2008.01.007

Comerchero, M. D., and Polich, J. (1999). P3a and P3b from typical auditory and visual stimuli. *Clin. Neurophysiol.* 110, 24–30. doi: 10.1016/S0168-5597(98)00033-1

Connolly, J. F., and Gruzelier, J. H. (1982). Amplitude and Latency Changes in the Visual Evoked Potential to Different Stimulus Intensities. *Psychophysiology* 19, 599–608. doi: 10.1111/j.1469-8986.1982.tb02510.x

Creel, D. (1995). ""Visually Evoked Potentials,"," in *Webvision: The Organization of the Retina and Visual System*, eds H. Kolb, E. Fernandez, and R. Nelson (Salt Lake City (UT): University of Utah Health Sciences Center).

Davis, H., Davis, P. A., Loomis, A. L., Harvey, E. N., and Hobart, G. (1939). Electrical reactions of the human brain to auditory stimulation during sleep. *J. Neurophysiol.* 2, 500–514. doi: 10.1152/jn.1939.2.6.500

Davis, P. A. (1939). Effects of acoustic stimuli on the waking human brain. *J. Neurophysiol.* 2, 494–499. doi: 10.1152/jn.1939.2.6.494

de Cheveigné, A., and Nelken, I. (2019). Filters: when. *Why, and How (Not) to Use Them. Neuron* 102, 280–293. doi: 10.1016/j.neuron.2019.02.039

Delorme, A., and Makeig, S. (2004). EEGLAB: an open source toolbox for analysis of single-trial EEG dynamics including independent component analysis. *J. Neurosci. Methods* 134, 9–21. doi: 10.1016/j.jneumeth.2003.10.009

Donchin, E. (1966). A Multivariate Approach to the Analysis of Average Evoked Potentials. *IEEE Transac. Biomed. Eng.* 13, 131–139. doi: 10.1109/TBME.1966.4502423

Douibi, K., Le Bars, S., Lemontey, A., Nag, L., Balp, R., and Breda, G. (2021). Toward EEG-Based BCI Applications for Industry 4.0: challenges and Possible Applications. *Front. Hum. Neurosci.* 15:456. doi: 10.3389/fnhum.2021.705064

Driver, J., and Noesselt, T. (2008). Multisensory Interplay Reveals Crossmodal Influences on 'Sensory-Specific'. *Brain Regions, Neural Responses, and Judgments. Neuron* 57, 11–23. doi: 10.1016/j.neuron.2007.12.013

Driver, J., and Spence, C. (2000). Multisensory perception: beyond modularity and convergence. *Curr. Biol.* 10, R731–R735. doi: 10.1016/S0960-9822(00)00740-5

Fatourechi, M., Bashashati, A., Ward, R. K., and Birch, G. E. (2007). EMG and EOG artifacts in brain computer interface systems: a survey. *Clin. Neurophysiol.* 118, 480–494. doi: 10.1016/j.clinph.2006.10.019

Finger, S. (2001). *Origins of Neuroscience: A History of Explorations Into Brain Function*. Oxford: Oxford University Press.

Folstein, J. R., and Petten, C. V. (2008). Influence of cognitive control and mismatch on the N2 component of the ERP: a review. *Psychophysiology* 45, 152–170. doi: 10.1111/j.1469-8986.2007.00602.x

Gleiss, S., and Kayser, C. (2013). Eccentricity dependent auditory enhancement of visual stimulus detection but not discrimination. *Front. Integr. Neurosci.* 7:52. doi: 10.3389/fnint.2013.00052

Gross, C. G. (1999). *Brain, Vision, Memory: Tales in the History of Neuroscience*. Cambridge: MIT Press.

Guo, M., Jin, J., Jiao, Y., Wang, X., and Cichockia, A. (2019). Investigation of Visual Stimulus With Various Colors and the Layout for the Oddball Paradigm in Evoked Related Potential-Based Brain–Computer Interface. *Front. Comput. Neurosci.* 13:24. doi: 10.3389/fncom.2019.00024

Hidaka, S., and Ide, M. (2015). Sound can suppress visual perception. *Sci. Rep.* 5:10483. doi: 10.1038/srep10483

Hidaka, S., Manaka, Y., Teramoto, W., Sugita, Y., Miyauchi, R., Gyoba, J., et al. (2009). Alternation of Sound Location Induces Visual Motion Perception of a Static Object. *PLoS One* 4:e8188. doi: 10.1371/journal.pone.0008188

Hill, D. (1958). Value Of The E.E.G in Diagnosis Of Epilepsy. *Brit. Med. J.* 1, 663–666.

Holper, L., Muehlemann, T., Scholkmann, F., Eng, K., Kiper, D., and Wolf, M. (2010). Testing the potential of a virtual reality neurorehabilitation system during performance of observation, imagery and imitation of motor actions recorded by wireless functional near-infrared spectroscopy (fNIRS). *J. Neuroeng. Rehabil.* 7:57. doi: 10.1186/1743-0003-7-57

Homan, R. W., Herman, J., and Purdy, P. (1987). Cerebral location of international 10–20 system electrode placement. *Electr. Clin. Neurophysiol.* 66, 376–382. doi: 10.1016/0013-4694(87)90206-9

Hong, K.-S., and Khan, M. J. (2017). Hybrid Brain–Computer Interface Techniques for Improved Classification Accuracy and Increased Number of Commands: a Review. *Front. Neurorobot.* 11:35. doi: 10.3389/fnbot.2017.00035

Ide, M., and Hidaka, S. (2013). Tactile stimulation can suppress visual perception. *Sci. Rep.* 3:3453. doi: 10.1038/srep03453

Iurilli, G., Ghezzi, D., Olcese, U., Lassi, G., Nazzaro, C., Tonini, R., et al. (2012). Sound-Driven Synaptic Inhibition in Primary Visual Cortex. *Neuron* 73, 814–828. doi: 10.1016/j.neuron.2011.12.026

Katayama, J., and Polich, J. (1998). Stimulus context determines P3a and P3b. *Psychophysiology* 35, 23–33. doi: 10.1111/1469-8986.3510023

Kazai, K., and Yagi, A. (2003). Comparison between the lambda response of eye-fixation-related potentials and the P100 component of pattern-reversal visual evoked potentials. *Cogn. Affect. Behav. Neurosci.* 3, 46–56. doi: 10.3758/CABN.3.1.46

Kober, S. E., and Neuper, C. (2012). Using auditory event-related EEG potentials to assess presence in virtual reality. *Int. J. Hum.-Comput. Stud.* 70, 577–587. doi: 10.1016/j.ijhcs.2012.03.004

Leeb, R., Sagha, H., Chavarriaga, R., Millán, J., and del, R. (2011). A hybrid brain–computer interface based on the fusion of electroencephalographic and electromyographic activities. *J. Neural Eng.* 8:025011. doi: 10.1088/1741-2560/8/2/025011

Li, J., Yu, Z. L., Gu, Z., Wu, W., Li, Y., and Jin, L. (2018). A Hybrid Network for ERP Detection and Analysis Based on Restricted Boltzmann Machine. *IEEE Transac. Neural Syst. Rehab. Eng.* 26, 563–572. doi: 10.1109/TNSRE.2018.2803066

Lines, C. R., Rugg, M. D., and Milner, A. D. (1984). The effect of stimulus intensity on visual evoked potential estimates of interhemispheric transmission time. *Exp. Brain Res.* 57, 89–98. doi: 10.1007/BF00231135

Lotte, F., Faller, J., Guger, C., Renard, Y., Pfurtscheller, G., Lécuyer, A., et al. (2012). "Combining BCI with Virtual Reality: Towards New Applications and Improved BCI,'" in *Towards Practical Brain-Computer Interfaces*, Chap. Millán, eds B. Allison, S. Dunne, R. Leeb, R. Del, and A. Nijholt (Berlin: Springer), 197–220. doi: 10.1007/978-3-642-29746-5_10

Marchant, J. L., and Driver, J. (2013). Visual and Audiovisual Effects of Isochronous Timing on Visual Perception and Brain Activity. *Cereb. Cortex* 23, 1290–1298. doi: 10.1093/cercor/bhs095

Marucci, M., Di Flumeri, G., Borghini, G., Sciaraffa, N., Scandola, M., Pavone, E. F., et al. (2021). The impact of multisensory integration and perceptual load in virtual reality settings on performance, workload and presence. *Sci. Rep.* 11:4831. doi: 10.1038/s41598-021-84196-8

Meredith, M. A., Allman, B. L., Keniston, L. P., and Clemo, H. R. (2009). Auditory influences on non-auditory cortices. *Hearing Res.* 258, 64–71. doi: 10.1016/j.heares.2009.03.005

Minguillon, J., Lopez-Gordo, M. A., and Pelayo, F. (2017). Trends in EEG-BCI for daily-life: requirements for artifact removal. *Biomed. Signal Proc. Control* 31, 407–418. doi: 10.1016/j.bspc.2016.09.005

Nicolas-Alonso, L. F., and Gomez-Gil, J. (2012). Brain Computer Interfaces, a Review. *Sensors* 12, 1211–1279. doi: 10.3390/s120201211

Oostenveld, R., Fries, P., Maris, E., and Schoffelen, J.-M. (2011). FieldTrip: open source software for advanced analysis of MEG. *EEG, and invasive electrophysiological data. Comput. Intell. Neurosci.* 2011:156869. doi: 10.1155/2011/156869

Oskoei, M. A., Gan, J. Q., and Hu, H. (2009). "Adaptive schemes applied to online SVM for BCI data classification," in *2009 Annual International Conference of the IEEE Engineering in Medicine and Biology Society*, (Piscataway: IEEE), 2600–2603. doi: 10.1109/IEMBS.2009.5335328

Penfield, W., and Evans, J. (1935). The Frontal Lobe in man: a clinical study of maximum removals1. *Brain* 58, 115–133. doi: 10.1093/brain/58.1.115

Pfurtscheller, G., Allison, B., Bauernfeind, G., Brunner, C., Solis Escalante, T., Scherer, R., et al. (2010). The hybrid BCI. *Front. Neurosci.* 4:30. doi: 10.3389/fnpro.2010.00003

Putze, F., Hesslinger, S., Tse, C.-Y., Huang, Y., Herff, C., Guan, C., et al. (2014). Hybrid fNIRS-EEG based classification of auditory and visual perception processes. *Front. Neurosci.* 8:373. doi: 10.3389/fnins.2014.00373

Rebsamen, B., Guan, C., Zhang, H., Wang, C., Teo, C., Ang, M. H., et al. (2010). A Brain Controlled Wheelchair to Navigate in Familiar Environments. *IEEE Transac. Neural Syst. Rehab. Eng.* 18, 590–598. doi: 10.1109/TNSRE.2010.2049862

Ritter, W., Simson, R., Vaughan, H. G., and Friedman, D. (1979). A brain event related to the making of a sensory discrimination. *Science* 203, 1358–1361. doi: 10.1126/science.424760

Ritter, W., Simson, R., Vaughan, H. G., and Macht, M. (1982). Manipulation of event-related potential manifestations of information processing stages. *Science* 218, 909–911. doi: 10.1126/science.7134983

Romei, V., Murray, M. M., Cappe, C., and Thut, G. (2009). Preperceptual and Stimulus-Selective Enhancement of Low-Level Human Visual Cortex Excitability by Sounds. *Curr. Biol.* 19, 1799–1805. doi: 10.1016/j.cub.2009.09.027

Rozenkrants, B., and Polich, J. (2008). Affective ERP Processing in a Visual Oddball Task: arousal. *Valence, and Gender. Clin. Neurophysiol.* 119, 2260–2265. doi: 10.1016/j.clinph.2008.07.213

Samar, V. J., Bopardikar, A., Rao, R., and Swartz, K. (1999). Wavelet Analysis of Neuroelectric Waveforms: a Conceptual Tutorial. *Brain Lang.* 66, 7–60. doi: 10.1006/brln.1998.2024

Senkowski, D., Saint-Amour, D., Höfle, M., and Foxe, J. J. (2011). Multisensory interactions in early evoked brain activity follow the principle of inverse effectiveness. *NeuroImage* 56, 2200–2208. doi: 10.1016/j.neuroimage.2011.03.075

Shams, L., Iwaki, S., Chawla, A., and Bhattacharya, J. (2005). Early modulation of visual cortex by sound: an MEG study. *Neurosci. Lett.* 378, 76–81. doi: 10.1016/j.neulet.2004.12.035

Sharma, R., Joshi, S., Singh, K. D., and Kumar, A. (2015). Visual Evoked Potentials: normative Values and Gender Differences. *J. Clin. Diagn. Res.* 9, CC12–CC15. doi: 10.7860/JCDR/2015/12764.6181

Stein, B. E., London, N., Wilkinson, L. K., and Price, D. D. (1996). Enhancement of Perceived Visual Intensity by Auditory Stimuli: a Psychophysical Analysis. *J. Cogn. Neurosci.* 8, 497–506. doi: 10.1162/jocn.1996.8.6.497

Stige, S., Fjell, A. M., Smith, L., Lindgren, M., and Walhovd, K. B. (2007). The Development of Visual P3a and P3b. *Dev. Neuropsychol.* 32, 563–584. doi: 10.1080/87565640701361096

Strotzer, M. (2009). One Century of Brain Mapping Using Brodmann Areas. *Clin. Neuroradiol.* 19, 179–186. doi: 10.1007/s00062-009-9002-3

Sur, S., and Sinha, V. K. (2009). Event-related potential: an overview. *Ind. Psychiatry J.* 18, 70–73. doi: 10.4103/0972-6748.57865

Talsma, D., Doty, T. J., and Woldorff, M. G. (2007). Selective Attention and Audiovisual Integration: is Attending to Both Modalities a Prerequisite for Early Integration? *Cereb. Cortex* 17, 679–690. doi: 10.1093/cercor/bhk016

Tauscher, J.-P., Schottky, F. W., Grogorick, S., Bittner, P. M., Mustafa, M., and Magnor, M. (2019). "Immersive EEG: Evaluating Electroencephalography in Virtual Reality," in *2019 IEEE Conference on Virtual Reality and 3D User Interfaces (VR)*, (Piscataway: IEEE), 1794–1800. doi: 10.1109/VR.2019.8797858

Tidoni, E., Gergondet, P., Kheddar, A., and Aglioti, S. M. (2014). Audio-visual feedback improves the BCI performance in the navigational control of a humanoid robot. *Front. Neurorobot.* 8:20. doi: 10.3389/fnbot.2014.00020

Vourvopoulos, A., Pardo, O. M., Lefebvre, S., Neureither, M., Saldana, D., Jahng, E., et al. (2019). Effects of a Brain-Computer Interface With Virtual Reality (VR) Neurofeedback: a Pilot Study in Chronic Stroke Patients. *Front. Hum. Neurosci.* 13:210. doi: 10.3389/fnhum.2019.00210

Wang, C., Xiong, S., Hu, X., Yao, L., and Zhang, J. (2012). Combining features from ERP components in single-trial EEG for discriminating four-category visual objects. *J. Neural Eng.* 9:056013. doi: 10.1088/1741-2560/9/5/056013

Wang, W. Y., Hu, L., Valentini, E., Xie, X. B., Cui, H. Y., and Hu, Y. (2012). Dynamic characteristics of multisensory facilitation and inhibition. *Cogn. Neurodyn.* 6, 409–419. doi: 10.1007/s11571-012-9197-x

Wang, Y., Celebrini, S., Trotter, Y., and Barone, P. (2008). Visuo-auditory interactions in the primary visual cortex of the behaving monkey: electrophysiological evidence. *BMC Neurosci.* 9:79.

Wiggins, I. M., and Hartley, D. E. H. (2015). A Synchrony-Dependent Influence of Sounds on Activity in Visual Cortex Measured Using Functional Near-Infrared Spectroscopy (fNIRS). *PLoS One* 10:e0122862. doi: 10.1371/journal.pone.0122862

Xue, Z., Li, J., Li, S., and Wan, B. (2006). Using ICA to Remove Eye Blink and Power Line Artifacts in EEG. in First International Conference on Innovative Computing. *Inform. Contr.* 107–110. doi: 10.1109/ICICIC.2006.543

Yahya, N., Musa, H., Ong, Z. Y., and Elamvazuthi, I. (2019). Classification of Motor Functions from Electroencephalogram (EEG) Signals Based on an Integrated Method Comprised of Common Spatial Pattern and Wavelet Transform Framework. *Sensors* 19:4878. doi: 10.3390/s19224878

Yin, E., Zeyl, T., Saab, R., Chau, T., Hu, D., and Zhou, Z. (2015). A Hybrid Brain–Computer Interface Based on the Fusion of P300 and SSVEP Scores. *IEEE Transac. Neural Syst. Rehab. Eng.* 23, 693–701. doi: 10.1109/TNSRE.2015.2403270

Zander, T. O., and Kothe, C. (2011). Towards passive brain–computer interfaces: applying brain–computer interface technology to human–machine systems in general. *J. Neural Eng.* 8:025005. doi: 10.1088/1741-2560/8/2/025005

Zander, T. O., Kothe, C., Jatzev, S., and Gaertner, M. (2010). ""Enhancing Human-Computer Interaction with Input from Active and Passive Brain-Computer Interfaces,"" in *Brain-Computer Interfaces: Applying our Minds to Human-Computer Interaction Human-Computer Interaction Series*, eds D. S. Tan and A. Nijholt (London: Springer), 181–199.

Zhang, S., McIntosh, J., Shadli, S. M., Neo, P. S.-H., Huang, Z., and McNaughton, N. (2017). Removing eye blink artefacts from EEG—A single-channel physiology-based method. *J. Neurosci. Methods* 291, 213–220. doi: 10.1016/j.jneumeth.2017.08.031

C. Copyright Permissions

Opportunities and challenges of translating direct single impact electrochemistry to high-throughput sensing applications

Author: Lennart J.K. Weiß, Philipp Rinklin, Bernhard Wolfrum

Publication: Current Opinion in Electrochemistry

Publisher: Elsevier

Date: August 2020

Journal Author Rights

Engineering Electrostatic Repulsion of Metal Nanoparticles for Reduced Adsorption in Single-Impact Electrochemical Recordings

Author: Lennart J. K. Weiß, Emir Music, Philipp Rinklin, et al

Publication: ACS Applied Nano Materials

Publisher: American Chemical Society

Date: Aug 1, 2021

PERMISSION/LICENSE IS GRANTED FOR YOUR ORDER AT NO CHARGE

Single-Impact Electrochemistry in Paper-Based Microfluidics

Author: Lennart J. K. Weiß, Georg Lubins, Emir Music, et al

Publication: ACS Sensors

Publisher: American Chemical Society

Date: Mar 1, 2022

Copyright © 2022, American Chemical Society

PERMISSION/LICENSE IS GRANTED FOR YOUR ORDER AT NO CHARGE

This type of permission/license, instead of the standard Terms and Conditions, is sent to you because no fee is being charged for your order. Please note the following:

- Permission is granted for your request in both print and electronic formats, and translations.
- If figures and/or tables were requested, they may be adapted or used in part.
- Please print this page for your records and send a copy of it to your publisher/graduate school.
- Appropriate credit for the requested material should be given as follows: "Reprinted (adapted) with permission from {COMPLETE REFERENCE CITATION}. Copyright {YEAR} American Chemical Society." Insert appropriate information in place of the capitalized words.
- One-time permission is granted only for the use specified in your RightsLink request. No additional uses are granted (such as derivative works or other editions). For any uses, please submit a new request.

If credit is given to another source for the material you requested from RightsLink, permission must be obtained from that source.

BACK   CLOSE WINDOW

On-Chip Electrokinetic Micropumping for Nanoparticle Impact Electrochemistry

Author: Lennart J. K. Weiß, Emir Music, Philipp Rinklin, et al

Publication: Analytical Chemistry

Publisher: American Chemical Society

Date: Aug 1, 2022

Copyright © 2022, American Chemical Society

PERMISSION/LICENSE IS GRANTED FOR YOUR ORDER AT NO CHARGE

This type of permission/license, instead of the standard Terms and Conditions, is sent to you because no fee is being charged for your order. Please note the following:

- Permission is granted for your request in both print and electronic formats, and translations.
- If figures and/or tables were requested, they may be adapted or used in part.
- Please print this page for your records and send a copy of it to your publisher/graduate school.
- Appropriate credit for the requested material should be given as follows: "Reprinted (adapted) with permission from {COMPLETE REFERENCE CITATION}. Copyright {YEAR} American Chemical Society." Insert appropriate information in place of the capitalized words.
- One-time permission is granted only for the use specified in your RightsLink request. No additional uses are granted (such as derivative works or other editions). For any uses, please submit a new request.

If credit is given to another source for the material you requested from RightsLink, permission must be obtained from that source.

BACK   CLOSE WINDOW

Prototype Digital Lateral Flow Sensor Using Impact Electrochemistry in a Competitive Binding Assay

Author: Lennart J. K. Weiß, Philipp Rinklin, Bhawana Thakur, et al

Publication: ACS Sensors

Publisher: American Chemical Society

Date: Jul 1, 2022

Copyright © 2022, American Chemical Society

Issue 8, 2023

From the journal:
Nanoscale

Previous Article | Next Article

About | Cited by | Related

Inkjet-printed 3D micro-ring-electrode arrays for amperometric nanoparticle detection†

Check for updates

Hu Peng, ‡[a] Leroy Grob, ‡[a] Lennart Jakob Konstantin Weiß, ‡[a] Lukas Hiendlmeier,[a] Emir Music,[a] Inola Kopic,[a] Tetsuhiko F. Teshima, [ab] Philipp Rinklin[a] and Bernhard Wolfrum *[a]

⊕ Author affiliations

Abstract

Chip-based impact electrochemistry can provide means to measure nanoparticles in solution by sensing their stochastic collisions on appropriately-polarized microelectrodes. However, a planar microelectrode array design still restricts the particle detection to the chip surface and does not allow detection in 3D environments. In this work, we report a fast fabrication process for 3D microelectrode arrays by combining ink-jet printing with laser-patterning. To this end, we printed 3D pillars from polyacrylate ink as a scaffold. Then, the metal structures are manufactured *via* sputtering and laser-ablation. Finally, the chip is passivated with a parylene-C layer and the electrode tips are created *via* laser-ablation in a vertical alignment. As a proof of principle, we employ our 3D micro-ring-electrode arrays for single impact recordings from silver nanoparticles.

Inkjet-printed 3D micro-ring-electrode arrays for amperometric nanoparticle detection

Login / Register

ADVANCED **MATERIALS** TECHNOLOGIES

Research Article | 🔒 Open Access | (cc) (i)

Low-Cost, On-Site, Nano-Impact Detection of Silver Nanoparticles via Laser-Ablated Screen-Printed Microelectrodes

Leroy Grob, Lennart J. K. Weiß, Emir Music, Ilja Schwertfeger, George Al Boustani, Julian Feuerbach, Marta Nikić, Lukas Hiendlmeier, Philipp Rinklin, Bernhard Wolfrum ✉

Go here for SFX

Figures · References · Related · Information

☰ SECTIONS   📄 PDF   ✎ TOOLS   ⇜ SHARE

Abstract

With the ever-growing presence of silver nanoparticles in consumer products, there is a need for cost-effective and on-site monitoring of their influence on our environment. Herein, we report the use of screen-printed and laser-ablated microelectrode arrays (SPMEAs) for the electrochemical detection of 20 nm-sized silver nanoparticles (AgNPs) via collision electrochemistry. The electrodes' morphology is optically analyzed and their electrochemical properties later characterized using cyclic voltammetry and impedance spectroscopy. The SPMEAs were calibrated using a AgNP concentration range of 1 to 100 pM, resulting in a linear dependency of 22 mHz pM^{-1} for the impact frequency. Finally, to demonstrate the possibility of future on-site applications, an in-house built portable nanoparticle detection (POND) device was used to measure Faradaic AgNP impacts on a

---

*****Correspondence:** Bernhard Wolfrum, bernhard.wolfrum@tum.de

†These authors have contributed equally to this work